

DISS. ETH NO. 23728

**CarbonTracker Switzerland: A high resolution
Ensemble Kalman Filter System to constrain
biospheric CO₂ fluxes in central Europe**

A thesis submitted to attain the degree of
DOCTOR OF SCIENCES of ETH ZURICH
(Dr. sc. ETH Zurich)

presented by

YU LIU

M.Sc. Cartology and Geographic Information System, Beijing Normal
University
born on February 23th, 1985
citizen of Shenzhen, China

accepted on the recommendation of

Prof. Dr. N. Gruber Guyan, examiner
Dr. D. Brunner, co-examiner
Prof. Dr. W. Peters, co-examiner

2017

Contents

1	Introduction	5
1.1	Motivation	5
1.2	Global carbon cycle and its perturbation	7
1.2.1	Global carbon pools, processes, and timescales	7
1.2.2	Global and regional anthropogenic carbon budgets	10
1.2.3	Anthropogenic CO ₂ emission	12
1.2.4	Land biospheric fluxes and dynamics	13
1.3	Quantifying land biospheric fluxes	14
1.3.1	Bottom-up method for carbon fluxes	15
1.3.2	Observations for top-down methods	17
1.4	Atmospheric CO ₂ inversion	19
1.4.1	Global atmospheric CO ₂ inversions	20
1.4.2	Regional atmospheric CO ₂ inversions	22
1.4.3	Challenges in the inversion system	23
1.4.4	The CarboCount CH project	25
1.5	Aim and the structure of this thesis	25
2	CarbonTracker Switzerland: Method and Data	27
2.1	Overview of carbon data assimilation systems	27
2.1.1	Basic concepts in data assimilation	28

2.1.2	Bayesian objective function	29
2.1.3	Data assimilation in carbon cycle research	30
2.2	Kalman Filter Methods for Carbon Cycle Research	31
2.2.1	Ensemble Kalman Filter	31
2.2.2	Generating background and observation error covariances	33
2.2.3	Tuning and regularization of the ensemble Kalman Filter	34
2.2.3.1	Covariance localization	34
2.2.3.2	Covariance inflation	35
2.2.4	Time filtering	36
2.2.5	Diagnostics	36
2.2.5.1	Error reduction	36
2.2.5.2	Chi-square	37
2.2.5.3	Degree of freedom of signal(DFS)	37
2.3	CarbonTracker Switzerland	37
2.3.1	Basic setup and flow chart	38
2.3.2	Atmospheric Transport Model COSMO	39
2.3.3	Fossil fuel Emissions	41
2.3.4	Lateral boundary conditions and background CO ₂	42
2.3.5	Terrestrial biosphere Fluxes	42
2.3.6	Subgrid scale heterogeneity in ecoregions	42
2.4	Atmospheric CO ₂ Observations	43
3	Fossil-fuel CO₂ signal in central Europe	47
3.1	Introduction	48
3.2	Methods and Data	51
3.2.1	Atmospheric transport model	51

3.2.2	Fossil fuel emissions	52
3.2.3	Other CO ₂ component fluxes	54
3.2.4	Simulations	55
3.3	Evaluation	55
3.3.1	Total atmospheric CO ₂	55
3.3.2	Fossil fuel CO ₂ component	56
3.4	The spatiotemporal pattern of the fossil fuel CO ₂	58
3.4.1	The spatial pattern	58
3.4.2	The temporal variability	63
3.5	Discussion	65
3.5.1	The impact of variations in fossil fuel emissions on atmospheric CO ₂	66
3.5.2	Fossil fuel CO ₂ signal from different sources	69
3.5.3	The response of atmospheric CO ₂ to an emission reduction	73
3.6	Summary and conclusions	77
4	Evaluation of COSMO and synthetic tests of CarbonTracker Switzerland	81
4.1	Introduction	83
4.2	Method	86
4.2.1	Forward Simulation	86
4.2.2	Observations and synthetic data	88
4.2.3	Temporal autocorrelations	89
4.2.3.1	Ecoregions	90
4.2.3.2	Prior covariance matrix	90
4.2.3.3	Base inversion	91
4.2.3.4	Sensitivity Experiments	91
4.3	Atmospheric CO ₂ variations over Switzerland and model evaluation	92

4.3.1	Model evaluation with atmospheric CO ₂	92
4.3.2	Spatiotemporal variability of CO ₂	96
4.3.2.1	Contribution of different CO ₂ components	96
4.3.2.2	Diurnal and seasonal cycles	97
4.3.2.3	Vertical distribution	100
4.4	Base run	102
4.4.1	Error reduction	102
4.4.2	Seasonal fluxes and error	104
4.4.3	Time series	106
4.5	Sensitivity studies	106
4.5.1	Control run: only errors in NEE (S2)	106
4.5.1.1	Different network choices (S2.1)	107
4.5.1.2	Different localization method (S2.2)	110
4.5.1.3	Role of subgrids scale ecoregion variations (S2.3)	111
4.5.2	Second set: Sensitivity to background CO ₂	112
4.5.2.1	Background error at 8 sites with 100 km spatial correlation (S3.1)	112
4.5.2.2	Different spatial correlation (S3.2)	113
4.5.2.3	Different temporal correlation (S3.3)	113
4.5.3	Third Set: Sensitivity tests to fossil fuel emissions uncertainties (S4)	114
4.6	Discussion	115
4.6.1	Forward simulation and implication for inverse run	115
4.6.2	Assimilation method, network and correlation length	115
4.6.3	Data error	116
4.7	Conclusions	117

5 Net terrestrial biospheric carbon fluxes in central Europe and Switzerland 121

5.1	Introduction	122
5.2	Method and data	124
5.2.1	CarbonTracker Switzerland	124
5.2.2	Simulations	126
5.3	Results	127
5.3.1	Evaluation	127
5.3.2	Source/sink behavior of CO ₂ in the domain	129
5.3.2.1	Error reduction	129
5.3.2.2	Annual and seasonal average NEE	130
5.3.3	Carbon budget of Switzerland	133
5.4	Discussion	136
5.4.1	Posterior fluxes	136
5.4.2	Uncertainties related to the CarbonTracker CH system	136
5.4.3	Top-down and bottom-up methods	138
5.5	Summary and Conclusion	138
6	Summary, conclusions and outlook	141
6.1	Background	141
6.2	Summary and general conclusions	143
6.3	Caveats and outlook	144
	Bibliography	159

Abstract

The magnitude, distribution, and variability of the CO₂ sources and sinks at regional scales are less constrained compared to those at global scale, irrespective of whether this concerns terrestrial carbon exchange fluxes or fossil fuel emissions. This limits the development of a comprehensive understanding of the mechanisms that control the carbon balance at regional scales. This is a crucial gap, as it hinders us to develop effective policies for managing carbon and negotiating international emissions treaties. Yet, the recent increase in the network density for atmospheric CO₂ observations as well as the recent progress in high-resolution atmospheric modeling now provide novel opportunities to combine the CO₂ observations with regional atmospheric transport models to understand and better constrain the carbon fluxes at regional scales.

The aim of this thesis is to benefit from these developments, especially the establishment of four new atmospheric CO₂ observing sites in Switzerland as part of the CarboCount CH project, and to derive the net CO₂ balance for central Europe and especially Switzerland using CarbonTracker Switzerland, i.e., a newly developed regional atmospheric CO₂ assimilation system. CarbonTracker Switzerland is based on an Ensemble Kalman Filter-based assimilation method and ingests atmospheric CO₂ observations in order to optimally estimate the net biospheric fluxes, i.e., net ecosystem exchange, over its domain. Relative to existing systems, CarbonTracker Switzerland contains several improvements, namely the consideration of high resolution (7 km) atmospheric transport and mixing based on online calculations with the weather model COSMO, the consideration of subgrid scale variations in the underlying ecoregions, and high resolution fossil fuel emissions with hourly time functions.

First, in chapter 3, the European-scale footprint of these fossil fuel CO₂ emissions is investigated using the European domain of COSMO (also at 7km resolution). The evaluation with ¹⁴C and CO observations-based estimates of the fossil fuel footprint reveal excellent agreement across different sites in Europe, suggesting high fidelity in both the emission estimates and the modeling of atmospheric transport. The comparison of a simulation with hourly varying emission with one where the emissions were kept constant reveals a substantial fossil fuel rectifier effect (up to 9 ppm) that emerges from the covariance between emissions and transport. The fossil fuel footprint is characterized by very high spatiotemporal variations. In fact, it contributes in many places in central Europe to more than half of the temporal variability in atmospheric CO₂, mostly on diurnal and synoptic timescales. This is the result of the interaction between strongly spatially patterned emissions and variations in atmospheric transport and mixing. These strong fossil fuel emission induced temporal variations in atmospheric CO₂ offer new opportunities for detecting changes in emissions, especially from satellites.

Second, in chapter 4, the CarbonTracker CH system is evaluated and thoroughly assessed on the basis of comparisons with observations and a number of tests using synthetic data. The evaluation reveals excellent agreement at all CarboCount CH observing sites and Jungfraujoch,

with biases in the annual mean of less than 1 ppm and correlations between 0.85 and 0.9. An important exception is the Gimmiz site, likely owing to this station's location in proximity to strong CO₂ fluxes from agriculture activities and vegetation, and having very strong inversion conditions in wintertime that are not well captured by our transport model. The performance of the assimilation system is affirmed by it being able to reduce the a priori error very substantially, and by retrieving the true fluxes accurately despite strong initial perturbations and the introduction of errors in the background CO₂ and in the fossil fuel CO₂ signals. The sensitivity tests reveal some sensitivity to the many parameterizations and parameters that enter an atmospheric CO₂ assimilation system, but confirm the advantages of considering the subgrid scale variations in the ecoregions.

Third, in chapter 5, CarbonTracker Switzerland is used to assimilate two of the CarboCount CH atmospheric CO₂ observing sites as well as four others in Germany, Austria, and northern Italy to infer the net ecosystem exchange fluxes in central Europe for 2013. Three other sites not used in the inversion are used for independent evaluation. The assimilation of the atmospheric CO₂ data leads to a significant improvement of the fits at the independent evaluation sites. In particular, the negative bias in the prior estimates of atmospheric CO₂ in summertime was removed. Although, the total annual net ecosystem fluxes are not shifted significantly from the prior estimates from a terrestrial ecosystem model, the seasonal cycle is altered substantially. The maximum uptake of the terrestrial biosphere in central Europe is shifted from July to June and the magnitude of seasonal cycle is reduced in the posterior fluxes. The main reason is a substantial reduction in NEE in the cropland regions in late summer, likely associated with harvest, which is a process not considered in the prior. The assimilation system estimates a total biospheric sink for Switzerland of 1.4 Tg CO₂. The largest uptake is driven by croplands, followed by forests and grassland. The bottom-up estimates agree with the country total, but allocate this sink almost entirely to forests, while estimating a neutral balance for the croplands.

In sum, this research developed, applied, and evaluated new methods for detecting the fossil fuel emission and for assessing the limits of a regional high-resolution assimilation system for atmospheric CO₂. This is necessary for improving our understanding of the regional carbon budgets and for the development, assessment and verification of carbon reduction schemes, whether through changes in land management or through reductions in fossil fuel emissions.

Zusammenfassung

Die Grösse, Verteilung und Variabilität der CO₂ Quellen und Senken auf regionaler Skala sind gut bekannt weniger im Vergleich zu denen auf globaler Skala, und zwar unabhängig davon, ob diese terrestrischen Kohlenstoffflüsse oder Emissionen fossiler Brennstoffen betrifft. Dies begrenzt ein umfassendes Verständnis der Mechanismen, die die Kohlenstoffbilanz auf regionaler

Skala zu steuern. Das ist eine entscheidende Lücke, denn es hindert uns, wirksame Strategien zur Minderung von Kohlenstoffemissionen und internationalen Emissionsabkommen zu entwickeln. Doch die jüngste Zunahme der Netzdichte atmosphärischer CO₂ Beobachtungen sowie die jüngsten Fortschritte hochaufgelöster atmosphärischer Modellierung listen jetzt neue Möglichkeiten, die CO₂ Beobachtungen mit regionalen atmosphärischen Transportmodellen zu kombinieren, um besser auf die Kohlenstoffflüsse auf regionaler Skala zu rückschliessen. Das Ziel dieser Arbeit ist von diesen Entwicklungen zu profitieren, vor allem von der Einrichtung vier neuer atmosphärischen CO₂ Messstandorte in der Schweiz im Rahmen des Projekts CarboCount CH um erneut die Netto-CO₂ Bilanz für Mitteleuropa insbesondere für die Schweiz zu bestimmen. Dies erfolgt mit Carbon-Tracker Schweiz, eine weiterentwickelte regionale atmosphärische CO₂ Assimilationssystem. CarbonTracker Schweiz basiert auf einem Ensemble Kalman Filter-basierten Assimilationsverfahren und benutzt atmosphärischen CO₂ Beobachtungen, um die netto biosphärische Flüsse in seiner Domäne optimal zu schätzen. Im Vergleich zu bestehenden Systemen, CarbonTracker Schweiz enthält eine Reihe von Verbesserungen, nämlich die Berücksichtigung hoher Auflösung (7 km) atmosphärischen Transports basierend auf Online-Rechnungen mit dem Wettermodell COSMO, die Berücksichtigung von Variationen in den zugrunde liegenden Regionen innerhalb einer Gitterzelle und, hoch aufgelöste anthropogene Emissionen mit stündlichen Zeitfunktionen.

Erstens wird in Kapitel 3 der Fubdruck fossiler CO₂ Emissionen auf europäischer Skala mit Hilfe von COSMO (in 7km Auflösung) untersucht. Die Evaluierung mit 14C und CO Beobachtungen des fossilen Brennstoffs Fubdruck zeigen eine hervorragende ereinstimmung an verschiedenen Standorten in Europa, was darauf hindeutet, hohe Genauigkeit in den Emissionen und der Modellierung atmosphärischen Transports. Der Vergleich einer Simulation stündlich variierender Emissionen mit einer Simulation konstanter Emissionen zeigt einen wesentlichen Rektifizierungseffekt (bis zu 9 ppm), die wegen der Kovarianz zwischen Emissionen und Transport vorkommt. Der fossile Fubdruck ist mit einer sehr hohen räumlichen und zeitlichen Variabilität versehen. Tatsächlich trägt in vielen Orte in Mitteleuropa mehr als die Hälfte der zeitlichen Variabilität der atmosphärischen CO₂ bei, vor allem auf täglichen und synoptischen Zeitskalen. Dies ist das Ergebnis der Wechselwirkung zwischen stark räumlich gemusterten Emissionen und der atmosphärischen Variabilität. Diese durch fossilen Emissionen verursachten zeitliche Schwankungen des atmosphärischen CO₂ bieten neue Möglichkeiten zur Erfassung Veränderungen in Emissionen, insbesondere mithilfe von Satelliten.

Zweitens in Kapitel 4 wird das CarbonTracker CH-System evaluiert auf der Basis von Vergleichen mit Beobachtungen sowie eine Anzahl von Tests anhand synthetischer Daten. Der Vergleich zeigt eine ausgezeichnete ereinstimmung bei allen CarboCount CH Beobachtungsorte und Jungfraujoch, mit Verzerrungen im Jahresmittel von weniger als 1 ppm und Korrelationen zwischen 0,85 und 0,9. Eine wichtige Ausnahme ist der Gimmiz Messstandort, was auf die Nähe starke CO₂ Flüsse der Landwirtschaft und städtischen Aktivitäten, und sehr starke winterliche atmosphärische Inversion mit Bedingungen im Winter zurückzuführen ist. Dies wird von unserem

Transportmodell nicht gut erfasst. Die Leistung des Assimilationssystems wird durch das Reduzieren von vornherein in biosphärischen Flüssen künstliche eingebrachte Fehler weitestgehend bestätigt. Dies erfolgte durch die Bestimmung der wahren Flüsse trotz starker Anfangsstörungen und die Einführung von Fehlern im Hintergrund CO_2 Mischungsverhältnisse sowie in den fossilen Brennstoffen CO_2 Signale. Die Empfindlichkeitstests zeigen leichte Empfindlichkeit gegenüber den vielen Parametrisierungen und Parameter, die in ein atmosphärisches CO_2 Assimilationssystem einfließen, bestätigen aber die Vorteile der Berücksichtigung der Variationen der Regionen innerhalb einer Gitterzelle.

Drittens wird in Kapitel 5 CarbonTracker Schweiz verwendet, um Beobachtungen von zwei der CarboCount CH Standorten sowie von vier weiteren Standorten in Deutschland, reich und im Norden Italiens die biosphärischen Flüsse in Mitteleuropa zu bestimmen. Drei weitere, bei der Inversion nicht verwendeten Messstandorte wurden für die unabhängige Bewertung verwendet. Die Assimilation der atmosphärischen CO_2 Daten führt zu einer deutlichen Verbesserung anhand der Differenz zwischen simulierter und beobachteter CO_2 Mischungsverhältnisse bei den unabhängigen Evaluierungsstandorten. Insbesondere wurden die negative systematische Abweichung in den a priori Schätzungen des atmosphärischen CO_2 im Sommer entfernt. Obwohl die gesamten jährlichen biosphärischen Flüsse nicht wesentlich von den a priori Schätzungen von einem terrestrischen System Modell sich nicht unterscheiden, der saisonale Zyklus verändert sich wesentlich. Die maximale Aufnahme in terrestrischen Biosphäre in Mitteleuropa ist von Juli bis Juni in den a posteriori Flüssen verschoben und die Größe des saisonalen Zyklus ist reduziert. Der Hauptgrund dafür ist eine deutliche Reduzierung der NEE in den landwirtschaftlichen Regionen im Spätsommer, wahrscheinlich mit der Ernte verbunden, was ein Prozess ist, das nicht im biosphärischen Modell betrachtet wird. Das Assimilationssystem schätzt insgesamt eine biosphärische Senke für die Schweiz von 1,4 Tg CO_2 während 2013. Die größte Aufnahme wird durch Ackerflächen, gefolgt von Wäldern und Wiesen getrieben. Die Bottom-up-Schätzungen stimmen mit dem bestimmten Ländertotal insgesamt überein, aber diese verteilen die Senke fast ausschließlich auf Wälder, während es eine keine Senke für die croplands abschätzt.

Zusammenfassend hat diese Arbeit neue Methoden zur Erfassung der fossilen Brennstoffemissionen und für Prüfung der Grenzen eines regionalen, hoch aufgelösten Assimilationssystems von atmosphärischen CO_2 Beobachtungen entwickelt, angewandt und evaluiert. Dies ist notwendig für die Verbesserung unseres Verständnis des regionalen Kohlenstoffkreislaufs und für die Entwicklung, Bewertung und Überprüfung der Strategien zur Minderung der CO_2 Emissionen, sei es durch Veränderungen in der Landnutzung oder durch Reduzierung der Emissionen fossiler Brennstoffe.

Chapter 1

Introduction

1.1 Motivation

Carbon dioxide (CO₂) and methane (CH₄) are the two most important long-lived greenhouse gases driving climate change (IPCC, 2014). About half of the man-made emissions of CO₂ have been removed from the atmosphere through sink processes on land and in the ocean (Sarmiento and Gruber, 2002; Sabine, 2004; Le Quere et al., 2016; Ciais et al., 2013b), strongly limiting the increase in atmospheric CO₂ since the beginning of the industrial period. Although an additional 10 to 20% will get removed on century timescales, a good fraction of the cumulative emissions will remain there for many centuries, making the CO₂-driven climate change essentially "irreversible" (Solomon et al., 2009). As a consequence of this long-term impact of the human emissions, any climate change target, such as the 2° C target recently agreed upon at the 21st Conference of the Parties (COP21) of the United Nations Framework Convention on Climate Change (UNFCCC) is associated with an emission budget (Meinshausen et al., 2009; Allen et al., 2009; Stocker et al., 2013b; Kolby Smith et al., 2015). The exact magnitude of this budget critically depends on the magnitude of these carbon sinks and on the carbon that might get liberated from the existing carbon pools through carbon-climate feedbacks (Cox et al., 2000; Gruber et al., 2004; Stocker et al., 2013a; Steinacher et al., 2013). It is thus essential to understand the sources and sinks of atmospheric CO₂ in order to provide the foundation of the strategies toward mitigating adverse effects of climate change (Le Quere et al., 2016; Michalak et al., 2011).

The terrestrial biosphere is responsible for about half of the annual removal of CO₂ from the atmosphere (Le Quere et al., 2016) and for the the majority of the atmospheric CO₂ variations on interannual timescales (Rayner, 2005; Keeling and Shertz, 1992). Thus, quantifying these sources and sinks over land is highly demanded in order to predict future atmospheric CO₂ (Pillai et al., 2012). However, there is still tremendous uncertainty in our estimation of the terrestrial carbon sinks. The current general questions about the land carbon sink are the magnitude, distribution, variability, trends and underlying natural and human triggered mechanism in each region

(Ciais et al., 2013b). Resolving surface fluxes to the regional biome level will help us to identify the key driving processes and provide high-resolution flux products that can be used to improve our understanding of the mechanisms of the terrestrial biosphere CO₂ exchange processes. Resolving them to the level of countries will be beneficial for managing carbon and for negotiating international emissions treaties (Canadell and Schulze, 2014; Göckede et al., 2010).

Different approaches have been used to estimate the terrestrial biospheric fluxes, such as forest statistics (Janssens et al., 2003), eddy covariance measurements (Aalto et al., 2004), process modeling (Reichstein et al., 2007), space-borne observations, and atmospheric trace gas monitoring combined with inverse modeling (Rayner, 2005; Rayner et al., 2010). The latter set of method is often referred to as "top down methods", while the former ones are being called "bottom-up methods". Each of these methods has its particular strengths and weaknesses.

Forest statistics methods based on forest inventory data are good at tracking carbon in above-ground biomass, but are less suitable to describe the accumulation of soil carbon (Krinner et al., 2005). In addition, they are, by definition, limited to assess carbon changes in forests. But they have the great advantage of having near global coverage (Pan et al., 2011). Eddy covariance measurements provide detailed and temporally highly resolved estimates of the main terrestrial carbon fluxes, but cannot be used without some form of upscaling (Jung et al., 2011) to determine average fluxes over large regions, as the representative information is constrained to local scales (Göckede et al., 2010). Terrestrial carbon process models combine climate, carbon pools, and carbon dynamics across larger spatial and temporal scales, but most of them do not include land-use history. Further, given the need to parameterize many key processes and interactions, they always just reflect the state-of-the-art in the carbon cycle's community's understanding. Two examples are the ongoing discussions about the strength of the CO₂ fertilization effect (Schimel et al., 2015) and the potential role of nitrogen limiting that effect (Hungate, 2003; Luo et al., 2004; Reich et al., 2006). Space born measurements, from which properties such as land use, leave area index (LAI) and other relevant quantities can be inferred, have proven to be very important for monitoring regions that are otherwise difficult to access (e.g., the Arctic or tropics), but their constraints on carbon stocks and fluxes is modest at best. Atmospheric CO₂ measurements have a long history of being used to infer carbon sources and sinks (Bolin and Keeling, 1963; Keeling et al., 1989; Gurney et al., 2002; Ciais et al., 2010), but their accuracy has remained limited so far, owing to limited observational coverage and the limited accuracy of atmospheric transport modeling (Lin and Gerbig, 2005; Gerbig, C. and Körner, S. and Lin, J. C., 2008).

The gap in scales between the different methods, and particularly between the top-down and bottom-up methods, has been an important reason for the difficulty in achieving full closure of the carbon budget (Wofsy and Harris, 2002). Most atmospheric CO₂ based inversions methods can only determine fluxes at large scales, while the bottom-up estimation methods are often available only at the local to regional scale. In order to close this scale gap, atmospheric inversions need to resolve the local (< 100 km) to regional scales (100-1000 km) e.g. (Gerbig et al., 2009). To obtain

this spatial resolution, daily to synoptic time variability also must be resolved, because these variabilities at different temporal scales contain a lot of information about regional CO₂ fluxes (Geels et al., 2004). In addition, resolving the fluxes diurnally could help separate land biospheric fluxes into their photosynthetic and respiratory components (Braswell et al., 2005). The current atmosphere CO₂ observation network of 200 surface flask sites and ground continuous measurement stations may constrain the carbon budget well for the big continents, such as North America, Europe and Japan. However, the sources and sinks at national, or states/province scale, or at city scale are not well constrained due to the sparseness of the ground-based network of atmospheric stations (Ciais et al., 2013b; Chevallier et al., 2010).

Recognizing this need for higher spatial resolution, denser measurement networks are now being constructed around the world, such as those associated with the European project ICOS. In addition, space based measurements are being pushed, (e.g., OCO-2 (Infrared) and ASCENDS (active)). These measurements will provide new possibilities for extracting information of regional fluxes. To combine the strengths of these methods and make use of large amount of data that is now becoming available (such as tall tower measurements, remote sensing data), one way to make progress is to adopt the method of assimilation. Several efforts have pushed atmospheric inversions to sub-continental and regional scales in the last few years (Peylin et al., 2005; Gerbig et al., 2006; Peters et al., 2010), but only a few groups have attempted to do inversions with spatial resolutions well below 10 km (Lauvaux et al., 2008, 2009; Sarrat et al., 2007, 2009; Göckede et al., 2010; Tolk et al., 2011; Chatterjee et al., 2012).

As part of the interdisciplinary CarboCount CH project (carbocount.ch), this thesis aims to develop, test, and apply a regional high-resolution (~7 km) atmospheric CO₂ inversion system in order to deduce the sources and sinks of the terrestrial biosphere for central Europe, and particularly Switzerland. Our ultimate objective is to understand the magnitude, distribution, and variability of the terrestrial carbon fluxes, and to determine the key factors that limit the estimation of terrestrial biospheric fluxes in this region. Our inversion system is based on the Ensemble Kalman Filter method (Peters et al., 2005) developed originally for the globe with a focus on North America (Peters et al., 2007), and later applied also for Europe (Peters et al., 2010), the Netherlands (Meesters et al., 2012), the Amazon basin (Alden et al., 2016; van der Laan-Luijkx et al., 2015), and most recently southeast Asia (Thompson et al., 2016; Zhang et al., 2014).

1.2 Global carbon cycle and its perturbation

1.2.1 Global carbon pools, processes, and timescales

Carbon dioxide (CO₂) is being mixed within the planetary boundary layer and transported into the free atmosphere within hours after emitted, and then subjected to the large-scale transport

and mixing processes that mix the air within a given hemisphere within a few weeks to months. With an exchange timescale of about one year, the transport across the equator takes the longest. Since the vast majority of the fossil fuel emissions occur in the northern hemisphere, this slow exchange causes the northern hemisphere to have a mean atmospheric CO₂ concentration several ppm higher than that of the southern hemisphere (Keeling et al., 1989; Fan et al., 1999). Even slower is the transport from the troposphere into the stratosphere, causing the stratospheric CO₂ increase to lag that of the troposphere by several years (Andrews et al., 2001)

In comparison to the mixing timescales in the atmosphere that range from hours to several years, the time scales of exchange of CO₂ between atmosphere and ocean, land, soil, or freshwater range over a much wider set of scales, i.e., from minutes, hours, days, years, to decades or even millennia. The speed of exchange between the atmosphere and the geologic reservoirs (such as rocks) is even slower, i.e., has timescales of hundreds of thousands of years. Thus, the latter is usually considered constant for the purpose of the study of the current carbon cycle and its anthropogenic perturbation.

Before the onset of the industrial era in the late 18th century, atmospheric CO₂ varied little for centuries, with only a small increase of about 20 ppm characterizing the last 8000 years, i.e., the entire Holocene (Indermühle et al., 1999). This implies that the exchange fluxes between the different reservoirs of the global carbon cycle must have remained nearly balanced, i.e., that the global carbon cycle operated in steady-state on the multi-decadal timescales recorded in the ice cores. This permitted carbon cycle researchers to reconstruct the so-called natural carbon exchange fluxes between the different reservoirs, i.e., the black arrows shown in 1.1, which presents a baseline, against which the anthropogenic perturbation fluxes (red arrows) can be compared.

Clearly, there had been larger variations in atmospheric CO₂ in Earth's history, with the best recorded being the glacial/interglacial variations that dominated Earth's history during the last million years (Lüthi et al., 2008). During the glacial maxima, the atmospheric CO₂ concentration dropped by about 100 ppm compared to the interglacial periods, for reasons that are still not fully understood, although most researchers would agree that the polar oceans were key in driving these changes (Sigman et al., 2010). In contrast, the terrestrial biosphere likely did not contribute much to the drawdown of atmospheric CO₂ between the interglacial and glacial periods. If anything, it likely lost several hundred Pg of carbon going into a fully glaciated world (Sigman and Boyle, 2000).

On timescales shorter than a few decades, the decadal-term steady state picture shown in Figure 1.1 may look rather different. The most prominent variations in atmospheric CO₂ are caused by the El Niño/Southern Oscillation (ENSO), first described by Bacastow (1976). ENSO causes anomalies in atmospheric CO₂ of several ppm, implying anomalous exchange fluxes of several Pg C yr⁻¹ (Keeling and Revelle, 1985). Later research has shown that most of these variations stem from the tropical land, which tends to dry out during El Niño events, leading to a

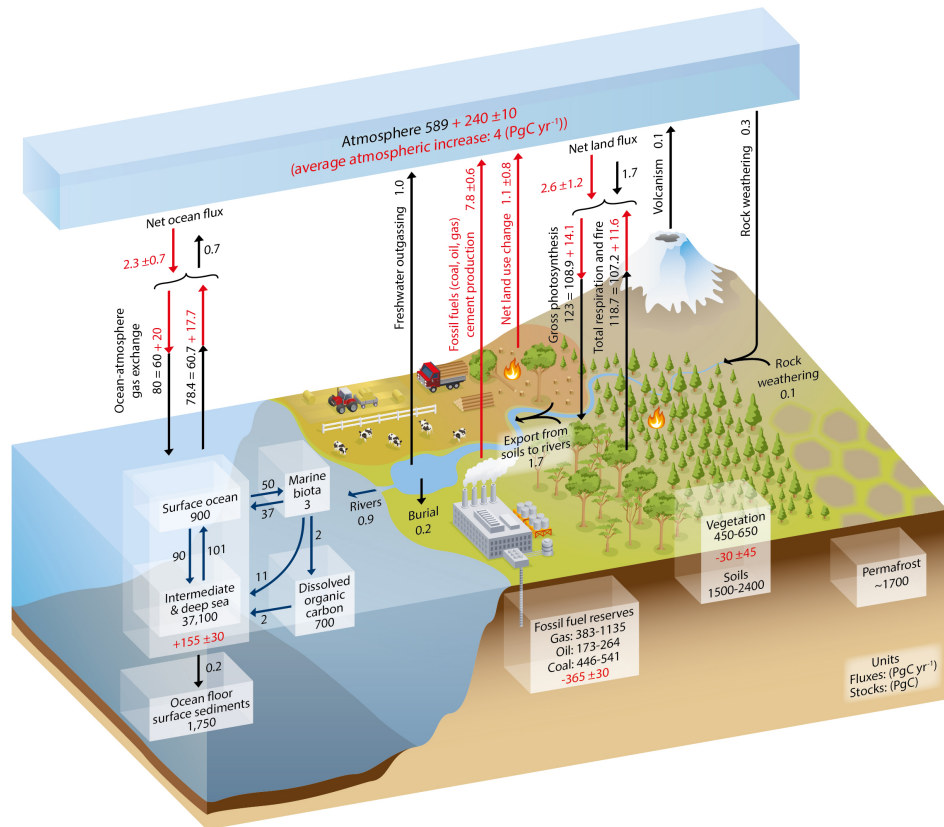


Figure 1.1 Schematic of the global carbon cycle taken from Ciais et al., (2013). The numbers are the stock of carbon (Pg C) in each reservoir, while the arrows show the fluxes (Pg C yr⁻¹). The red arrows and numbers refer to the anthropogenic fluxes, while the black ones denote the "natural" fluxes.

massive loss of carbon. Another prominent example are volcanic eruptions, of which the Pinatubo event in the early 1990s has attracted most attention (Keeling et al., 1996; Jones and Cox, 2001; Sarmiento et al., 2010; Frölicher et al., 2011, 2013). Also this event is mostly driven by the terrestrial biosphere, likely a response to the cooler and more moist conditions that prevailed as a result of the increased loading of aerosols in the upper atmosphere (Jones and Cox, 2001; Frölicher et al., 2011).

On even shorter timescales, the pronounced seasonal cycle in atmospheric CO₂ reflects the exchange of several tens of Pg C yr⁻¹ back and forth between the atmosphere and the Earth's surface, with a clear tendency for an increase in recent decades (Graven et al., 2013b). The seasonal cycle as well as its increasing amplitude are almost entirely caused by the terrestrial biosphere (Forkel et al., 2016; Heimann and Reichstein, 2008), as the timescale for the exchange of CO₂ between the surface ocean and the atmosphere is too slow to leave a strong imprint of the seasonal cycle in the ocean on the atmosphere (Sarmiento and Nicolas, 2006). During the growing season, the strong excess of photosynthesis over respiration on land leads to a massive net removal of carbon from the atmosphere. During the dormant season, most of this carbon is respired back to the atmosphere, leaving a relatively small net flux into the terrestrial biosphere.

1.2.2 Global and regional anthropogenic carbon budgets

Starting in 2001, the Global Carbon Project has issued an annual global anthropogenic carbon budget based on the best available knowledge (Le Quere et al., 2016). So far, it established the land carbon balance, i.e., S_{land} , by difference from the other terms in the global budget of anthropogenic CO_2 , i.e., by using observations for the rate of increase in atmospheric CO_2 (G_{atm}), estimates of the emissions from fossil fuel burning and cement manufacturing (E_{ff}), estimates of the emissions from land use change (E_{LUC}), and observation and model-based estimates for the ocean sink for anthropogenic CO_2 (S_{ocean}). This gives:

$$S_{\text{land}} = E_{\text{ff}} + E_{\text{LUC}} - S_{\text{ocean}} - G_{\text{atm}} \quad (1.1)$$

The input from chemical reaction from other gases, i.e., the production of CO_2 by oxidation of methane and any possible lateral fluxes of anthropogenic CO_2 from land to the ocean are ignored in this calculation (Le Quere et al., 2016). Fig 1.2 shows the inferred partitioning of anthropogenic CO_2 emissions to the different components, revealing the steady increase in emissions, but also the corresponding increase in the sinks by the atmosphere, land and ocean. Particularly impressive is the strong increase in the sink strengths of the land and ocean, as they have kept up in relative terms with the strong growth in emissions, so that the fraction of emissions staying in the atmosphere has not changed in a substantial manner through time, even though there is much debate about a small decrease in this ratio (Raupach et al., 2014). Very notable are also the strong interannual variations in the atmospheric growth rate, which have their corresponding variations in the land sink, largely driven by variations in ENSO (Note that these variations are present in the budget only after 1959 due to the fact that the annual data needed to determine the interannual variations in atmospheric growth are available only since the start of the direct atmospheric CO_2 measurements at the Mauna Loa and South Pole stations.)

For the last decade available (2004–2013), the Global Carbon Project estimated E_{ff} as $8.9 \pm 0.4 \text{ Pg C yr}^{-1}$, E_{LUC} $0.9 \pm 0.5 \text{ Pg C yr}^{-1}$, G_{atm} $4.3 \pm 0.1 \text{ Pg C yr}^{-1}$, S_{ocean} $2.6 \pm 0.5 \text{ Pg C yr}^{-1}$, and S_{land} $2.9 \pm 0.8 \text{ Pg C yr}^{-1}$, i.e., both land and ocean are responsible for about a quarter of the total anthropogenic carbon sink.

While the uncertainties of the global anthropogenic CO_2 sinks are relatively modest, resulting in an inferred land sink that is uncertain only within $\pm 30\%$ (Le Quere et al., 2016), the spatial attribution of this sink is very uncertain, with some studies emphasizing the sinks in the northern hemisphere, while others tend to locate it more in the tropics (Ciais et al., 2013b; Sarmiento et al., 2010; Pan et al., 2011; Ballantyne et al., 2015). For Europe, initial assessments suggested a very small sink (Fan, 1998), although this estimate was later shown to be biased by the choice of transport models. More recent assessments put the land carbon sink of Europe anywhere between about 0.2 Pg C yr^{-1} (Peters et al., 2010) and 0.9 Pg C yr^{-1} (Luyssaert et al., 2012). With the

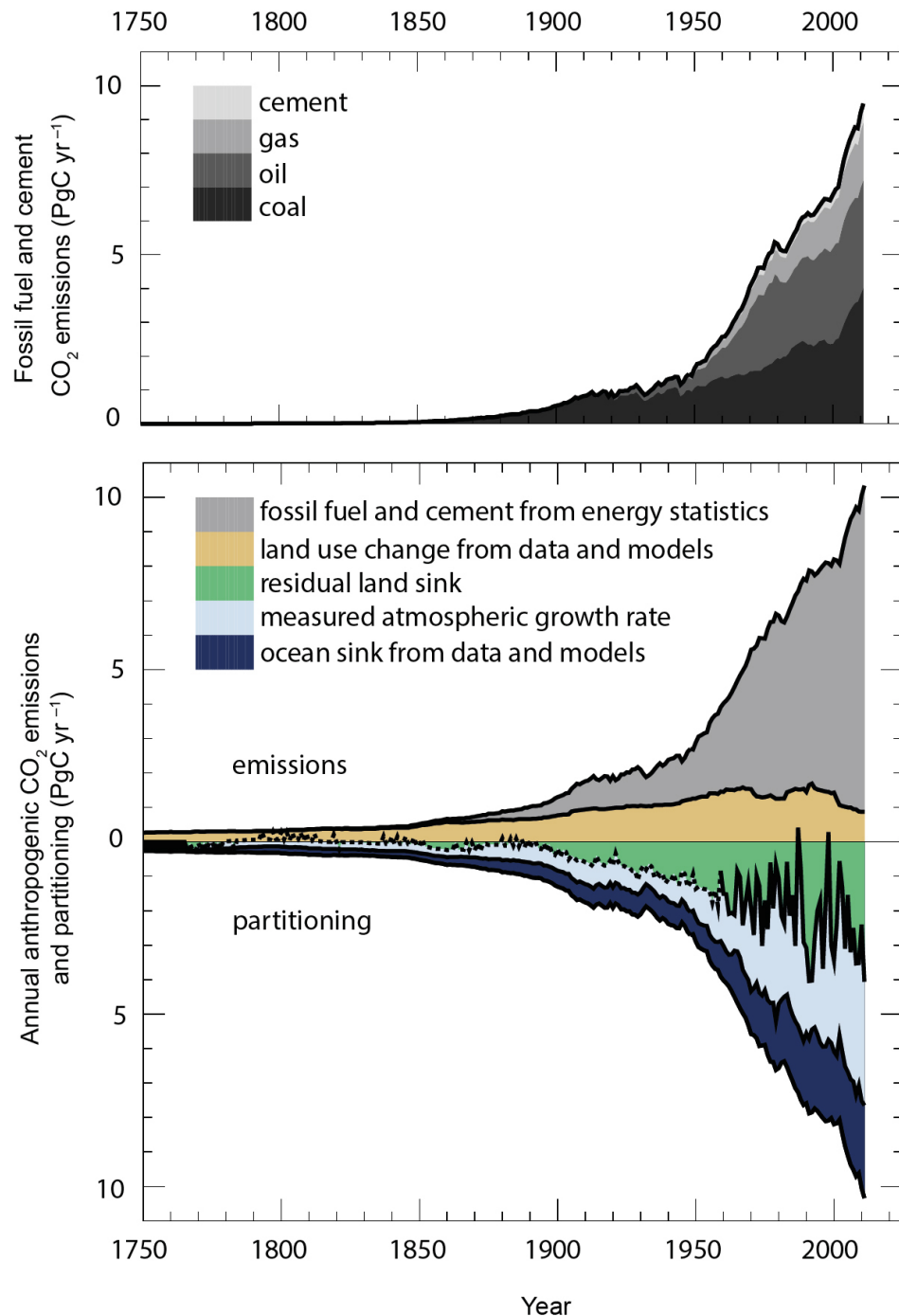


Figure 1.2 Annual anthropogenic CO₂ emissions and their partitioning among the atmosphere, land and ocean (Pg C yr⁻¹) from 1750 to 2011. See Ciais et al. (2013b) for details.

help of satellite CO₂, the Europe uptake more CO₂ than former studies as shown in Reuter et al. (2014, 2016, in press).

This sink applies to CO₂ only. If the balance of all greenhouse gases is taken into consideration, i.e., also that of methane and nitrous oxide, then a more neutral or even a slightly positive balance emerges (Schulze et al., 2009). This is because the trend towards more intensive agriculture and relatively large number of livestock leads to strong emissions of nitrous oxide and methane that offsets the carbon sequestration in forests and grasslands. In addition, forest distur-

bance in Europe has continued to increase in the first decade of this century (Seidl et al., 2014).

The land carbon sink of Europe has been shown to vary from year to year quite substantially, mostly in response to variations in soil moisture conditions during the growth season (Peters et al., 2010; Bastos et al., 2016; Mystakidis et al., 2016). Bastos et al. (2016) showed that the strongest land sink occurs when the North Atlantic Oscillation and the East-Atlantic pattern are both in negative phase, associated with cool summers with wet soils that support plant growth.

1.2.3 Anthropogenic CO₂ emission

The rise in the atmospheric CO₂ concentration is a consequence of the cumulative anthropogenic CO₂ emissions since the beginning of the industrial era. The average growth rate of the emissions during the last decade (2005-2014) was 2.2% yr⁻¹, reaching a level of 9.8 ± 0.5 Pg C yr⁻¹ for 2014, slightly lower than 2013 (Le Quere et al., 2016). The majority of these emissions stem from the burning of fossil fuel and cement manufacture, i.e., 8.9 ± 0.4 Pg C yr⁻¹, while land use change is responsible for 0.9 ± 0.5 Pg C yr⁻¹. The latter emissions stem almost entirely from tropical deforestation (Houghton et al., 2012).

As one of the biggest contributors to fossil fuel CO₂ emissions, the European Union (EU) (> 11 %) promised to reduce its emissions by 2020 by 20% relative to the level in 1990, with deeper cuts planned for the future. The tracking and verification of this pledge requires accurate information about the fossil fuel emissions. Currently, these emissions are estimated primarily from statistics of fossil fuel consumption and cement production, using well known fossil fuel inventories, such as IEA (Andres et al., 2012). But these statistics can be biased (by error or as a result of manipulation), thus raising the need for independent methods to assess the veracity of a given emission reduction pledge.

Different methods have been developed to determine and/or verify anthropogenic CO₂ emissions. One method, for example, involves the tracer sulfur hexafluoride (SF₆), which is associated with the CO₂ emissions from fossil-fuel fired power plants, thus providing a distinct fingerprint (Turnbull et al., 2006). Another commonly used tracer for fossil fuel carbon is carbon monoxide (CO), i.e., a side-product from fossil fuel burning, especially if the combustion process is not complete. Thanks to its relatively ease of measuring, CO is a very powerful tracer of the fossil fuel signature in atmospheric CO₂ (Oney, 2016; Turnbull et al., 2015), but its main disadvantage is the varying ratio to the fossil fuel CO₂ depending on the source process. Another powerful tracer for tracking fossil fuel CO₂ is radiocarbon, since the burning of fossil fuel adds radiocarbon "dead" CO₂ to the atmosphere, thus reducing the relative abundance of radiocarbon in the atmosphere, the so called Suess effect (Keeling, 1979). Since there is very little interference by other processes (except for the production of radiocarbon by nuclear power plants (Graven et al., 2013a)), this tracer is fundamentally very useful for tracking fossil fuel derived CO₂, and thus has

been used extensively (Graven, 2015; Levin and Rödenbeck, 2008; Turnbull et al., 2011). But making these measurements at the required precision and accuracy is a challenge, so that they mostly tend to be used together with CO, with radiocarbon providing the basis for computing the CO:CO₂ emission ratios, and then the CO providing the detailed evolution of the fossil fuel signal (van der Laan et al., 2010; Vogel et al., 2013).

1.2.4 Land biospheric fluxes and dynamics

Each year, the global land ecosystem fixes CO₂ at a rate of 120 Pg C per year, corresponding to Gross Primary Production (GPP), of which half is emitted back into the atmosphere by plant respiration. This results in a net primary production (NPP) of about 60 Pg C yr⁻¹ (see also Figure 1.2). The decomposition by heterotrophs consumes another 50 Pg C yr⁻¹ stored by ecosystem, leading to a global net ecosystem production (NEP) of approximately 10 Pg C yr⁻¹. A positive NEP corresponds to a medium-term carbon storage (Peh et al., 2015). Net biome production (NBP) is then the carbon that enters the longer-term storage. It emerges from NEP after taking into consideration irregular loss events such as forest fires and insect invasions that temporarily enhance the loss. Net biome production (NBP) corresponds ultimately also to the number required to establish the global budget of anthropogenic CO₂, i.e., roughly to the net land sink of 2 to 3 Pg C yr⁻¹ (Le Quere et al., 2016).

A large range of different model approaches have been developed and used to simulate the land ecosystems and to investigate their dynamics. Along an axis of simplicity, simple statistic models sit at the beginning. They are easy to apply by assuming that the relationship between the local climate and the species abundance are in some form of equilibrium. However, under future climate changes, competition and disturbances will play an important role in the forest models, making statistical models less helpful. Forest succession models (or gap models) were developed to simulate the complex processes in forests, such as the essential processes of establishment, growth, light competition and mortality. The European mountain forests, for example, were simulated using the forests model FORCLIM (Bugmann and Solomon, 1995), and hardwood forests were applied to different latitudes with model SORTIE (Pacala et al., 1996).

At a higher level of sophistication, the most recent land surface models, Dynamic Global Vegetation Model (DGVM), consider more ecosystem processes, such as stomatal conductance, and better resolve the ecosystem processes, such as soil moisture, exchange of carbon, water cycles, as well as implement some disturbance processes, such as harvesting, management, mortality, some nutrient limitations, and permafrost (Jiang et al., 2016; Sitch et al., 2007; Quillet et al., 2010). However, the current generation of coupled biosphere-atmosphere models still have many gaps that can be improved, such as including physiological effects of high ozone concentration, photosynthetic enhancement due to diffuse radiation, influence from the nitrogen cycle, more realistic modelings of disturbances, vegetation dynamics (mainly the response of vegeta-

tion to disturbances), fires and aerosols, and how the combination of all these processes impacts on carbon cycle. Coupling DGVM could also improve the performance of climate models (e.g, carbon, water cycles) (Levis, 2010; Seneviratne et al., 2006; Davin et al., 2016).

Process-based ecosystem models and forest inventories suggest that CO₂ fertilization, nitrogen deposition and forest regrowth are largely driving a long-term increase in the land biosphere sink (Houghton et al., 2012; Zaehle, 2013; Thornton and Zimmermann, 2007). Plants will uptake more CO₂ under increasing atmospheric CO₂ through photosynthetic enhancement, which has a negative feedback to rising atmospheric CO₂ concentration. However, as the atmospheric CO₂ increases beyond the optimal level for the plant, that effect has been shown to saturate (Canadell et al., 2007).

In order to assess the future source-sink balance of the terrestrial biosphere, more processes than just CO₂ fertilization need to be considered. An interesting example is ozone, which has a negative effect on vegetation productivity owing to its easy diffusion through the stomata openings and its strong oxidative potential that tends to destroy cellular structures. If a future warmer world comes with higher levels of near-ground ozone, then this will act as an additional positive feedback between climate change and the global carbon cycle. An additional process is fire. However, while it has an effect on GPP and autotrophic respiration, as well as on interannual variations in the atmospheric CO₂, it appears that its influence on the average annual net carbon balance is limited (Arneeth et al., 2010). Further, the exact role played by nitrogen in terrestrial ecosystems is still to be explored (Gruber and Galloway, 2008). While some experiments and coupled carbon-nitrogen models suggest that nitrogen availability severely limits the fertilization of terrestrial biosphere response to elevated CO₂ (Reich et al., 2014), others argue that this effect is not as important, particularly not in tropical forests, owing to the very high C:N ratio of wood, and the competitive advantage of trees to allocate a fraction of their energy into growing tall (Ray et al., 2015). Finally, there is a key role of temperature in controlling all the processes determining NBP. Warming enhances GPP, but also all the respiration terms, with the overall balance on NBP critically depending on the relative temperature sensitivity of the different processes. Further, temperature affects also plant growth indirectly, through impacts on soil moisture, for example. In general, the consensus is that globally, warming tends to lead to a loss of carbon from terrestrial ecosystems. This does not apply on a regional level, however (Ciais et al., 2013b; Mystakidis et al., 2016), as many regions reveal a positive response, particularly at higher latitudes, where the plants can benefit from a longer growing season.

In summary, while there are many climate feedbacks associated with the carbon cycle, nitrogen and atmospheric chemistry in response to anthropogenic warming, the exact sign and magnitude of these feedbacks remain ill constrained. Further, the effects of extreme events on this carbon balance has only been partially quantified. This is critical, since droughts and heat waves are a substantial contributor to interannual variability and possibly trends of regional land carbon fluxes (Ciais et al., 2005; Lewis et al., 2011).

1.3 Quantifying land biospheric fluxes

As introduced above, the quantification of the land biospheric fluxes has relied on two sets of approaches, i.e., those that are based on local measurements of fluxes or biomass, commonly are referred to as the bottom-up approaches, and those based on remote observations of effects of these fluxes on atmospheric concentration, commonly referred to as the top-down approaches. While both sets of approaches have been used successfully, the most promising method to determine the terrestrial carbon fluxes is to combine the bottom-up methods with top-down methods (Wofsy and Harris, 2002; Gerbig et al., 2009).

Right now, only a bottom-up method based on the forest inventory exists to estimate the carbon budget for Switzerland (FOEN, 2015).

1.3.1 Bottom-up method for carbon fluxes

In the bottom-up approaches, information obtained at local scale is used to derive either changes in carbon stocks or net CO₂ exchanges between the land surface and the atmosphere on regional or global scales. This local information can be flux measurements from eddy covariance towers, or carbon stock measurements from forest inventories, which are then scaled up using empirical or process-based models in conjunction with maps of land cover and biophysical parameters (Dolman et al., 2009; Pan et al., 2011; Jung et al., 2011).

The eddy covariance fluxes are obtained as the products of the co-variation of the temporal anomalies atmospheric CO₂, C' and vertical wind speed, w' , i.e., $w'C'$. The eddy covariance measurements are very powerful for the understanding of the processes governing the terrestrial carbon cycle. For example, the nighttime measurements of NEE have been used to separate GPP from community respiration (Reichstein et al., 2005), permitting to use the eddy covariance data to produce a global GPP dataset with monthly resolution on a 1 by 1 degree grid (Jung et al., 2011). This development was greatly aided by the homogenization of the data from all the global sites through the FLUXNET project (Baldocchi et al., 2001), and the public access to these data through the FLUXNET data portal alongside with other meteorological data at these sites. The FLUXNET data have produced numerous insights, such as the impact of the 2003 heat wave on European plant productivity (Ciais et al., 2005; Teuling et al., 2010; Finnigan and Brunet, 1995; Baldocchi, 2003; Friend et al., 2007). Still, known issues with the eddy covariance technique introduce large uncertainties in the measurements. This includes, for example, the difficulties to constrain the fluxes during night-time, when the vertical turbulence is very small, or when there is considerable lateral flow (e.g. Saleska et al. (2003); Alfieri et al. (2011)). By virtue of the sheer number of plot sites across the globe, forest inventories have proven to be among the most powerful methods to constrain the terrestrial carbon sink, at least that associated with forested lands. In the most extensive synthesis to date, Pan et al. (2011) collected forest inventory data

from across the globe and determined for 1990 to 2007 a total forest sink of $2.4 \pm 0.4 \text{ Pg C yr}^{-1}$ globally. Regionally, they suggest the strongest sink for the tropical forests ($1.19 \pm 0.41 \text{ Pg C yr}^{-1}$), followed by the temperate forests ($0.72 \pm 0.08 \text{ Pg C yr}^{-1}$), and then the boreal forests ($0.50 \pm 0.08 \text{ Pg C yr}^{-1}$). Taking into account the substantial amount of deforestation still occurring in the tropics, i.e., about 1.3 Pg C yr^{-1} , the overall balance of the tropical forests is about neutral, consistent with the inversion estimate of tropical atmosphere-land CO_2 fluxes (Stephens et al., 2007; Steinkamp and Gruber, 2013; Ciais et al., 2013b).

Forest inventories are also one of the few methods that provide detailed estimates for individual countries. As a consequence, the results of these inventories provide also the basis for the individual nations reporting their forest sinks to the UNFCCC. For Switzerland, this forest inventory is the only bottom-up method based result currently available (FOEN, 2015).

An alternative way to estimate land carbon fluxes relies on process-based models, such as the land surface models that not only include all the biophysical fluxes between the land surface and the atmosphere, but incorporate all the processes controlling the major land carbon fluxes. Among the most advanced of them are the Dynamic Global Vegetation Models (DGVMs), as they also simulate the relative abundance of the major plant functional types in response to changes in the environment. Thus, these process-based models determine the terrestrial carbon cycle and the response of carbon and vegetation patterns to climate change based on the understanding of the underlying processes or dynamics that are temporally or spatially relevant to the global carbon cycle (Friedlingstein et al., 2014). The biggest advantage of the process-based models is that they allow for an easy understanding of the processes driving the carbon cycle (Piao et al., 2009; Thonicke et al., 2010). However, as discussed above, these models are highly sensitive to the particular parameterizations that they employ, making their predictions not really robust. Thus, a lot of work is still needed in order to identify the key representative ecological processes, and to find ways to implement them in a more robust and fundamental manner (McGuire et al., 2001; Cramer et al., 2001; Friedlingstein et al., 2014).

There are other methods used for constraining the land carbon fluxes, such as the Normalized Difference Vegetation Index (NDVI), or oxygen isotopes (Welp et al., 2011), both of which contain information about GPP. Vegetation fluorescence from remote sensing (such as GOSAT) also provides a relatively direct way for constraining GPP (Frankenberg et al., 2011). Finally, measurements of the atmospheric concentration of carbonyl sulphide (COS) has recently emerged as a novel tracer constraint for GPP, based on the quantitative correlation between GPP and COS plant uptake (Hilton et al., 2015; Campbell et al., 2017).

The accuracy of any estimate based on a bottom-up approach relies on the representativeness of the local measurement sites. Hence, a common challenge to all such bottom-up based measurements is that there may be significant uncertainties due to the need to extrapolate the local data to at least regional scales. However, modern non-linear statistical models have proven to be

very powerful in overcoming some of these challenges (Jung et al., 2011).

1.3.2 Observations for top-down methods

As the variations in atmospheric CO₂ reflects the spatially and temporally integrated signal from different CO₂ sources and sinks, atmospheric CO₂ measurements have been used for determining the biospheric fluxes already for a long time. The very basis of any inversion is the availability of high quality atmospheric CO₂ data.

The first modern, high-quality CO₂ concentration measurements were conducted by Charles D. Keeling at Mount Mauna Loa in Hawaii and at the South Pole Station in the late 1950s (Keeling, 1960). These in-situ data combined with other coastal measurements showed for the first time that the atmospheric CO₂ concentration is increasing in response to the emissions of fossil fuel derived carbon. This insight provided the very foundation for the first concerns about global warming. Since then, many new observing stations have been added, including those at mountain tops, on tall towers, on remote islands, and in the middle of major cities, greatly expanding the global network of atmospheric CO₂ data. These measurements are being collected world wide through various programs and projects, such as, the Global Atmosphere Watch (GAW) program with data archived at the World Data Centre for Greenhouse Gases (WDCGG; www.gaw.kishou.go.jp/wdcgg/). The major challenge has been data quality, and in particular the tracing of any measurement back to a particular standard (Ciais et al., 2014). While this standard was originally provided by Charles D. Keeling based on this manometric measurement technique, this was taken over by the World Meteorological Organization (WMO) in the 1980s. This ensures that all high quality measurements of atmospheric CO₂ are traceable back to the WMO standards, i.e., comply with their dry mole fraction.

The advent of the new laser-based instrumentation such as Cavity Ring-Down Spectroscopy-based Picarro has substantially alleviated the measurement challenges, as these instruments tend to produce very precise and accurate measurements with little drift. Nevertheless, measurements to the WMO standard still require carefully calibrated data. With proper working standards and calibration, this is now more commonly achievable, so that data with precisions of 0.1 ppm or less and accuracies approaching the precision level are available from a rapidly growing number of stations around the world, which represents a significant expansion with respect to the previous existing networks (Andrews et al., 2014; Buchwitz et al., 2013). For example, the U.S. plans to establish 60 new sites as part of the National Ecological Observatory Network (NEON) (<http://www.neoninc.org/>), and in Europe, the plan is to maintain the existing sites and to establish a few more in order to have a total of about 35 sites as part of the European Infrastructure program ICOS (<http://www.icos-infrastructure.eu/>) (Ciais et al., 2014). However, there is no monitoring system in place to guarantee that each site is compatible to the WMO standards. Further, few sites have guaranteed long-term funding, while the monitoring of

the global carbon cycle is critically tied to sustained observations (U.S. Carbon Cycle Science Plan) (Michalak et al., 2011).

Aircraft measurements provide essential information about the vertical distribution of atmospheric CO₂, particularly because they provide strong constraints on the vertical transport, which is one of the Achilles heels of atmospheric transport modelling. In fact, Stephens et al. (2007) showed that none of the global transport models used in the Transcom project is able to successfully reproduce the vertical gradients when comparing to the measurements over the U.S.. To date, the only regular measurements are with dedicated aircraft those from the National Oceanic and Atmospheric Administration (NOAA) (www.esrl.noaa.gov/gmd/ccgg/aircraft/). Several projects included aircraft campaigns, such that data are available from Siberia, California Nexus (CalNex), the Amazon (Gatti et al., 2010; Miller et al., 2007), and from a series of global meridional flights as part of the HIPPO project (Graven et al., 2013b; Wofsy, 2011).

Measurements on commercial aircrafts, such as the Japanese CONTRAIL project (<http://www.cger.nies.go.jp/contrail/>), or the German IAGOS-CARIBIC project (In-service Aircraft for a Global Observing System, while IAGOS-CORE provides in-situ measurements of the atmospheric chemical species (O₃, CO, CO₂, CH₄, NO_x, NO_y, H₂O), aerosols and cloud particles) provide another avenue to extend the surface measurement network aloft (Petzold et al., 2012). Some of these aircraft measurements have already been used in atmospheric inversions, although with higher observation error compared to the in-situ measurements (Peters et al., 2010). Some scientists also applied the aircraft measurements for correcting the boundary conditions in regional inversions, as boundary conditions constitute an important source of error (Lauvaux et al., 2012). Aircraft profile data could also potentially correct the satellite observation, as suggested by Kulawik et al. (2010).

Space-based observations of the column CO₂ dry mole fraction XCO₂ have opened another window to constrain the atmospheric CO₂ distribution (Crisp et al., 2004; Reuter et al., 2016, in press). The first attempt, SCanning Imaging Absorption spectroMeter for Atmospheric CHartographY, (SCIAMACHY), used the solar infrared wavelength to measure the whole atmospheric column, but these data suffered from interference by aerosols and clouds, resulting in a relatively poor precision of around 3 ppm (Reuter et al., 2011). Later, another satellite to monitor atmospheric CO₂ and methane was successfully launched in 2009 by Japan, Greenhouse gases Observing Satellite (GOSAT), which could provide more accurate XCO₂ data. However, it has proven difficult to realize its full potential, requiring extensive correction of the retrieval biases in order to produce results that can be used in conjunction with surface-based measurements (Wunch et al., 2011). Nevertheless, atmospheric inversions that make use of the GOSAT data have demonstrated substantial error reductions, especially once they were combined with surface measurements (Chevallier et al., 2010; Miller et al., 2007). The precision might be improved further by aggregating SCIAMACHY and GOSAT data, and hence help reduce the uncertainties related to the limited spatiotemporal coverage of either satellite (Ciais

et al., 2014). The recently (2014) launched satellite Orbiting Carbon Observatory 2 (OCO-2) carries high expectations from the CO₂ community. Other satellite products include those from the Atmospheric Infrared Sounder (AIRS) on EOS-Aqua (Liu et al., 2012), the hyperspectral Infrared Atmospheric Sounding Interferometer (IASI) (<http://www.ospo.noaa.gov/Products/atmosphere/soundings/iasi/>) and the Thermal Emission Spectrometer (TES) on EOS-Aura (Kulawik et al., 2010), but all products struggle from their low precision and accuracy relative to the other elements of the global atmospheric CO₂ observing network (Kulawik et al., 2010). An important role for improving the satellite retrievals is being played by the ground-based network for the measurement of the total air column of CO₂, i.e., the Total Carbon Column Observing Network (TCCON). It has a precision of around 1 ppm, i.e., substantially better than that of the current suite of satellites, and by measuring essentially the same quantity, i.e., the weighted average column dry air mixing ratio of CO₂, it can provide calibration observations during overflights as well as improve the detailed spectroscopic information needed to invert the retrieved radiance. Although not at the level to be compatible with the WMO measurement standards, the measurement quality of TCCON has been proven to be good enough to be used in atmospheric inversions (Chevallier et al., 2011). Nevertheless, there are still some uncertainties when calibrating the TCCON data to WMO rules (Wunch et al., 2010), and with its relative sparse density (only 18 stations in 2012).

In summary, the global atmospheric CO₂ measurement network has greatly expanded since Charles D. Keeling began his first systematic measurements on Mauna Loa and the South Pole in the late 1950s. The observing system has also become much more diverse not only with regard to the measurement systems, but also with regard to the aim of the measurements. While Keeling's measurements aimed at documenting the global-scale rise in atmospheric CO₂, today's networks aim to cover also much more detailed and regional aspects, including the wish to track changes in fossil fuel emissions (Ciais et al., 2014).

1.4 Atmospheric CO₂ inversion

The term atmospheric CO₂ inversion describes not a single technique, but rather a whole suite of approaches that share the common goal of "inverting" atmospheric CO₂ observations in order to determine the CO₂ fluxes between the atmosphere and Earth's surface (Peylin et al., 2013). These include the classical Bayesian synthesis inversion methods (Enting et al., 1995), but also carbon data assimilation systems of various flavors (Rayner et al., 2010). Such carbon assimilation systems can serve for more than the determination of the carbon fluxes. They can also be used to generate consistent 4-dimensional fields of atmospheric CO₂ concentrations (Liu et al., 2012) or to estimate parameters of biogeochemical models (Rayner, 2005). The carbon data assimilation system is a framework that puts atmospheric, terrestrial and (when needed oceanic) data together, with the goal to find optimal solutions that fulfill all available constraints (model and observa-

tions) in an optimal manner, often employing methods that are common in other fields, such as signal processing (Rayner et al., 2011; Chatterjee, 2012; Steinkamp and Gruber, 2013).

1.4.1 Global atmospheric CO₂ inversions

Many studies have used atmospheric inversions to estimate CO₂ fluxes on the global scale in the last decade (Gurney et al., 2002; Rayner, 2005; Liu et al., 2009; Feng et al., 2009; Chevallier et al., 2007, 2009; Piao et al., 2009; Rödenbeck et al., 2003; Patra et al., 2005; Peters et al., 2007; Steinkamp and Gruber, 2013; Jacobson et al., 2007). These inversion systems were developed by different groups based on very different methods, such as Bayesian synthesis inversion (Chevallier et al., 2006; Bocquet and Wu, 2011; Göckede et al., 2010) maximum likelihood estimate methods (Michalak et al., 2005; Gourdjji et al., 2010), 4-D variational methods, such as CCDAS (Rayner, 2005), Ensemble Kalman Filter (EnKF) Methods (adapted from Bayesian method), such as CarbonTracker (Peters et al., 2005), Markov chain Monte Carlo (MCMC) methods (Miller et al., 2013) and several hybrid methods, such as the hybrid method between EnKF and maximum likelihood (Zupanski et al., 2007), or that between EnKF and the 4-D Variational method. Michalak et al. (2004) applied a geo-statistical approach based on the Bayesian method, in which the prior probability density function is based on an assumed form of the spatial and temporal correlation and prior flux estimates are required. It optimizes the prior error covariance parameters, the variance and the spatial correlation length by maximizing the probability density function of the observations with respect to these parameters. Rayner (2005) developed a terrestrial carbon cycle data assimilation system (CCDAS) with EnKF and found that on interannual timescales, net primary productivity (NPP) is the controlling process.

Peters et al. (2005) introduced an ensemble Kalman Filter-based assimilation system, i.e., CarbonTracker, that was later expanded and improved upon by Peters et al. (2007) and Peters et al. (2010). This system used the atmospheric transport model TM5, and the prior land surface fluxes from the Carnegie Ames Stanford Approach (CASA) biosphere model as well as a number of additional data sets to constrain the atmosphere-Earth surface fluxes globally. In these versions of CarbonTracker, weekly scaling factors for the terrestrial biospheric and ocean carbon fluxes are estimated across a set of pre-defined ecoregions. The estimated total uptake in North America and Europe matched well with results from previous work, but substantial differences were found for cropland. The low resolution of the atmospheric model, poorly constrained soil moisture, phenology and errors in the vertical mixing above this ecoregion have been suggested as reasons for the poor behavior on cropland. In addition, unrealistic diurnal cycles of CO₂ flux were found in these initial versions of CarbonTracker due to the fact that the optimization was done only for the net CO₂ flux, i.e., the sum of GPP and respiration. In recent years, CarbonTracker has been adapted for different applications, such as for multi-tracer inversions (van der Velde, 2015), for different regions (e.g., China, Amazon(CT-SAM))(Jiang et al., 2016; Laan-Luijkx et al., 2015),

or combined with different transport models (such as the Stochastic Time-Inverted Lagrangian Transport model), or for different tracers (CH₄) (Tsuruta et al., 2017).

Joint assimilation of data from different observation platforms has also been attempted, such as combining the space and surface networks. Peng et al. (2014) developed a regional assimilation system CFI-CMAQ (Carbon Flux Inversion system and Community Multi-scale Air Quality) by combining the RAMS-CMAQ (Regional Atmospheric Modeling System and Community Multi-scale Air Quality) and EnKF. Basu et al. (2013) used a joint inversions of surface and corrected GOSAT XCO₂ and found that the terrestrial uptake are mainly from subtropical regions. Peylin et al. (2013) collected around 13 inversion systems and most of them could be found at <http://www.globalcarbonatlas.org/?q=en/content/atmospheric-inversions>. The comparison of the inversion systems reveal that the biggest differences from inversion systems exists in the tropical and southern land balance, while the interannual variability (IAV) in land carbon fluxes are consistent among these systems. Markov chain Monte Carlo (MCMC) is rarely used in the former inversion system in the past until Miller et al. (2013).

The currently most common assimilation methods are the Kalman filter and the four-dimensional variational assimilation (4D-var) methods. The Ensemble Kalman Filter (EnKF) was first introduced by Evensen (1994) and first applied to an atmospheric system by Houtekamer and Mitchell (1998) (Evensen, 2009). As neither an adjoint model nor full linearity are required, and since uncertainties can propagate forward directly inside the EnKF, it has become popular among many assimilation systems. For example, the Canadian Meteorological Centre has applied an EnKF method to its operational ensemble prediction system (EPS) in 2005. Further, the method has seen many developments and improvements. For example, Whitaker and Hamill (2002) proposed a square root filter (EnSRF) method of EnKF to avoid the source of sampling errors generated from perturbed observation. Ott et al. (2004) proposed a local ensemble Kalman filter (LEKF, a kind of EnSRF) for parallel implementation to reduce the computational cost in EnSRF. Hunt et al. (2007) extended the ETKF method to a local ensemble transform Kalman filter (LETKF) to further accelerate the LEKF. More recent developments include a no-cost smoother, i.e., using the same weight for different time steps; using spin-up, dealing with forecast sensitivity to observations; and the simultaneous estimation of the optimal inflation and observation errors. Yang et al. (2011) also showed that EnKF has advantages over 4D-var for short assimilation windows.

Popular transport models used in global atmospheric inversions are Eulerian transport models, such as TM3, TM5, LMD, etc. In Eulerian models, the CO₂ concentration is simulated in the 3-dimensional boxes that represent the discretised space. Generally, Eulerian models suffer from numerical diffusion, limiting the resolution to scales larger than the grid size in the underlying meteorology. But they have the advantage of simulating the space-time distribution of CO₂ everywhere, providing the opportunity to analyze the distribution of CO₂ in both forward and inverse mode. Some inversion systems started to use a Lagrangian transport model, such as a new version of CarbonTracker, CarbonTracker-Lagrange (CT-L). Lagrangian models can represent the

atmospheric transport with high accuracy owing to their following the air parcels and therefore not being subject to excessive diffusion and easily run backward in time, but they require good parameterizations of the sub-grid scale processes, particularly in the planetary boundary layer. Further, owing to their relatively low computational cost, Lagrangian inversion systems tend to do well in regional inversions with a limited number of observing sites, but they tend to lose this advantage on global scales with the corresponding increase in the number of observations.

Pillai et al. (2012) compared these two different frameworks (Eulerian (WRF) versus Lagrangian (STILT)), and found the representation of details in the interaction between turbulent mixing and advection through wind shear as the main cause of discrepancies between the two. Combining Lagrangian and Eulerian transport models in DA might be conducive to reduce the transport model errors.

1.4.2 Regional atmospheric CO₂ inversions

There are at least two important differences between global and regional inversions of atmospheric CO₂. First, regional inversions require information about the CO₂ concentration at their lateral boundaries, i.e., the so-called background component. In addition, given their higher spatial resolution, they require correspondingly more highly resolved surface boundary conditions, such as the fossil fuel emissions and prior biospheric fluxes. Further, they are more susceptible to the specific regional transport and mixing characteristics, such as sea-breezes, flows around and over mountain ranges, and other small-scale, but persistent flows. Thus, the resolution and fidelity of the transport models needs to be higher than that in the models used for global-scale inversions.

A large number of inverse modeling studies have been conducted at continental scales, such as for Europe (Bergamaschi et al., 2010; Rigby et al., 2011), or for some regional domains in the US at moderate resolution (Brioude et al., 2013; Miller et al., 2014). Also studies at higher resolution exist. For example, Göckede et al. (2010) undertook high-resolution inversions for the state of Oregon in the northwestern U.S, with a horizontal grid size of 6 km. They revealed that dividing biome types by ecoregions could capture their different biogeochemical responses to external forcings across climatic gradients. They also emphasized that the precise definition of the advected background CO₂ mixing ratios is paramount for inverse modelings frameworks operating on regional to continental scales, as systematic mixing ratio offsets can cause significant shifts in the inversely estimated flux fields.

Tolk et al. (2011) suggested to re-evaluate the inverse methods for regional scales that were simply transferred over from global inversion systems, after they found the inaccurate carbon exchange at local scale using the different inversion methods in Netherlands. Tolk et al. (2009), Tolk et al. (2011) and Meesters et al. (2012) found that optimising the scaling factors separately

for GPP separating and respiration for every grid box instead of whole eco-regions works quite well on short time scales for the regional scale based on tests with synthetic data and field measurements. They also pointed out that on regional scale, inversions appear to be quite sensitive to the precise specification of the land surface properties in the assimilation system.

Another issue is the selective use of observations. With inversions increasingly aiming to use all available observations, the question arises whether night-time observations can be assimilated. But the use of night-time measurements exposes the inversion system much more to the often problematic night-time prediction of PBL height in the transport models (Gerbig, C. and Körner, S. and Lin, J. C., 2008). In addition, night-time measurements from short towers within the nocturnal boundary layer also provide information of limited spatial representativeness due to the stable boundary layer. Gourdji et al. (2010) checked the night time measurements and found that including nighttime measurement worsened the optimization not only at sites based on short towers, but also those on tall towers.

1.4.3 Challenges in the inversion system

The first challenge is the density and coverage of the observation network. The number of unknowns in the inversion often exceeds the number of available independent observations, i.e., the problem often tends to be underconstrained. This is especially the case for global inversions on the basis of the existing surface observation network, as many regions of the world have only sparse coverage. One solution to this problem is to reduce the number of unknowns by aggregating the surface regions into larger spatial patterns based on some rules, such as similar ecosystems (Peters et al., 2010), or spatial proximity (Bousquet et al., 2000). This clearly reduces the degrees of freedom of the statistical problem at hand, but it introduces aggregation errors, i.e., errors that arise because all the fluxes within such a region are now forced to have the same variations through time, i.e., are forced to be fully correlated, even if this is not the case in reality (Kaminski et al., 2001). The aggregation error can be reduced by grouping elements with correlated errors (Turner and Jacob, 2015). This can be achieved by using some form of a tree aggregation method, or through a clustering method based on prior error patterns (Wu et al., 2011; Turner and Jacob, 2015; Wecht et al., 2014). Another problem in this aggregation is that it tends to suppress variability in the true fluxes, as it fails to take into consideration the considerable variability that occurs on local to sub-regional scales.

The second important problem is the transport model error. The perfect model of the circulation and air movement in the atmosphere does not exist, because the errors from spatiotemporal resolution, incorrect vertical transport, systematic errors in the meteorological forcing data, imperfect parameterizations for convection, etc., will cause unrealistic model samples (Basu et al., 2013). The impact of this error has been well illustrated in the results from the TransCom Standard Inversion Experiments, where the in-between model error was often as large or even larger

than the within model posterior error (Gurney et al., 2002; Baker et al., 2006). The transport error does not only cause a spread between the models, but also a bias in the results because of the systematic nature of these errors. Of particular concern is the simulation of the vertical atmospheric transport, which has been shown to be particularly ill simulated by most global transport models (Stephens et al., 2007). Different methods were used for calculating or reducing transport error (Miller et al., 2015), e.g., Lin and Gerbig (2005) used the uncertainties in the wind speed to estimate the transport error, while Broquet et al. (2013) used a relative error based on the assessment of the performance of the tracer Radon to track the transport model error. Chan et al. (2015) treated the difference between individual runs from prior mole fractions and the sampled synthetic observations. The project ACT-America aims at solving the problem of transport model error at regional scale, in which one example is that assimilated observed wind profiles from lidar to provide accurate meteorological forcing which results in decreased model error within the boundary layer (Deng et al., 2015).

The third challenge is the need to provide accurate information about the background CO₂ at the boundaries of the regional inversion model. This has been shown to cause as much uncertainty in the posterior flux estimates as the spread of the prior estimates of the ecosystem fluxes (Lauvaux et al., 2012). Different methods have been tested to address this issue, for example, constraining the inverted land ecosystem fluxes together with the measured background CO₂ (Lauvaux et al., 2012), or improving the inverted land ecosystem fluxes by assimilating the background CO₂ as well (Alden et al., 2016).

A further challenge is the representation error, i.e., the mismatch of spatial scales between the model and the observations (Peylin et al., 2013). Eulerian inversion systems assume that a point observation can be represented by the average CO₂ mixing ratio in a model grid box. However, coarse resolution transport models can have substantial mismatches between the observed and simulated CO₂ concentrations that are not caused by erroneous surface fluxes, but by specific local features not captured in the transport model, such as local wind pattern associated with unresolved topographic features. For example, the representation errors were estimated to be 1-2 ppm at mesoscale, around half ppm at continent scale (Gerbig et al., 2003; Lin and Gerbig, 2005). Transport models with higher resolution are adopted to reduce the representation errors due to their stronger capability of modelling small scale (Tolk et al., 2008).

In addition to above challenges, there are some other problems in multi-data inversion systems that assimilating data streams from different sources, such as, incompatibilities between model and data, mismatch between different data. Bacour et al. (2015); MacBean et al. (2016) proposed data calibration and preliminary sensitivity analyses for model parameters that need to be improved.

In summary, atmospheric inversions are a powerful, but also somewhat fickle method, as the quality of the results critically depends on many aspects of the system, ranging from the

transport model to the statistical method employed to find the optimal solution. Often, the impact of the many choices that have to be made along the way are not very obvious, requiring detailed sensitivity studies to fully expose these dependencies. Yet, unlike no other data-driven method, these inversion methods provide an integrated and consistent view of the land carbon fluxes.

Some projects have already made efforts towards filling the gap between bottom-up and top-down method, such as North American Carbon Program (http://nacp.ornl.gov/int_synthesis.shtml), REgional Carbon Cycle Assessment and Processes (<http://www.globalcarbonproject.org/reccap/overview.htm>), or reconcile the estimated fluxes from these different methods (Turner et al., 2011; Gourdjji et al., 2012; Dolman et al., 2012) Reconciling the results from these 2 approaches favor for robust results from these 2 methods, because the uncertainties could be reduced when reconciling the results, such as (Jiang et al., 2016) found very close estimation from these methods that both methods indicated the increased trend of sinks in China.

1.4.4 The CarboCount CH project

To fill the gap between the different spatial scales and to better understand CO₂ and CH₄ fluxes and their sensitivity to recent and current climate variability, the project CarboCount CH was proposed to develop a prototype modelling and observing system for CO₂ and CH₄ at the regional scale. In the project, top-down methods based on atmospheric measurements were proposed to be combined with "bottom-up" methods based on fluxes measurements, process-based models of natural fluxes, and statistical information on anthropogenic emissions. This project focuses on central Europe and especially central Switzerland where rich and detailed data sets are available to provide input and independent verification. The heterogeneity and complex topography of the region provide the challenge and the need that avoided by other regional system.

To achieve the goal, first, an integrated atmospheric CO₂/CH₄ measurement network are developed in central Switzerland with four new representative sites on hill tops and towers all equipped with continuous instruments measuring (at least) CO₂, CH₄, and water vapor, augmented existing flux and concentration measurement sites and Second, the establishment of high resolution bottom-up driven data products based on process-based ecosystem modeling, direct flux measurements, forest inventories, and geostatistical data of anthropogenic CO₂ and CH₄ emissions. Third, the development and application of high-resolution regional to local models of atmospheric transport and atmosphere-biosphere exchange of CO₂ and CH₄, used in forward and inverse (data assimilation) modes.

1.5 Aim and the structure of this thesis

The specific aim of this thesis is to develop, test, and apply a new regional high-resolution atmospheric inversion method on the basis of an Ensemble Kalman Filter method, taking advantage of the newly acquired CO₂ observations from the CarboCount CH network. The particular questions I will try to answer in this thesis are: How well can the high resolution transport model with the newly built-in tracer module reconstruct the atmospheric CO₂ concentration and its fossil fuel components? How to port the global inversion system to regional inversion system with high resolution transport model given current cluster and computational capability and what are the proper settings for this regional inversion system? What are the key sources of error in the estimates of CO₂ concentration for the inversion system, and how much do the input data uncertainties or biases, mainly background CO₂ contribute to the uncertainties of inverted fluxes? What are the difference between top-down and bottom-up method, and the reason leading to these difference?

As this method builds on the various CarbonTracker versions, we name the resulting assimilation system CarbonTracker Switzerland. This is not the first time a high resolution atmospheric CO₂ inversion is conducted in Europe (Tolk et al., 2011), but this is the first time such a system is being developed for complex mountainous terrain and for a region with rather fine-grained patterns of ecosystem structure. I will be using an ecoregion-based aggregation, which has its disadvantages owing to the implied strong aggregation, but I will alleviate this by allowing for sub-grid level patterning of the ecoregions.

My work encompasses the two major components of top-down methods, and is structured as: the introduction (Chapter 1) is followed by the method and data of the thesis (Chapter 2). We tested the transport model and fossil fuel CO₂ in Europe domain (Chapter 3) and then test the data assimilation system in the central Europe using synthetic data from a forward simulation (Chapter 4), following by the assimilation of the real data in order to quantify the biospheric carbon budget for central Europe and Switzerland (Chapter 5). The last chapter (Chapter 6) summarizes the conclusions and provides an outlook into the future topics.

Chapter 2

CarbonTracker Switzerland: Method and Data

Abstract

This chapter first briefly introduces the basic concept of data assimilation and the Bayes' perspective on the cost function, and then provides the background and the core elements of an Ensemble Kalman Filter (EnKF) that underpins much of this thesis. It then describes the tuning methods as well as the diagnostics that are being used to determine the quality of an EnKF. The core part of this chapter is then the introduction and description of the CarbonTracker Switzerland inversion system for atmospheric CO₂. This high-resolution inversion system for central Europe and particularly Switzerland is based on the coupling of the CarbonTracker (Peters et al., 2005) EnKF code with the atmospheric weather forecast model COSMO that we use as a transport model, set up at a resolution of 7 km for the COSMO-2 domain covering central Europe. The goal of CarbonTracker CH is to optimally estimate a small set of scaling factors for the prior net terrestrial CO₂ fluxes taking advantage of a suite of 9 CO₂ observing sites in central Europe, three of them taken from the newly established CarboCount CH network. This chapter describes the general setup of CarbonTracker CH, while the specific applications are thoroughly introduced and described in the following chapters.

2.1 Overview of carbon data assimilation systems

The broad set of methods summarized under data assimilation (DA), also known as model-data fusion, are an analysis tool that uses different statistical methods based on information theory, control theory, optimization theory and inverse problem theory to project observations into a background field in order to approximately reproduce or represent a true physical state of a system

from the real world (Rayner P. and Chevallier, 2016; Bouttier and Courtier, 1999; Tarantola, 2005). The first application of data assimilation dates back to the time when Gauss and Legendre used an early version of the least squares method to calculate the orbits of heavenly bodies. Such data assimilation methods are used particularly in cases, when there is incomplete information about a system, providing an opportunity to improve the description or understanding of this system by using observations of this system. Such an incomplete understanding can stem from a deficient model (owing to, for example imperfect knowledge of the governing equations), or poorly known parameters, or incorrect estimates of the current state, and/or noisy or imperfect observations. Thus DA optimizes the prior information by combining model and data to generate the ‘truth’, or analysis, or posterior, which could then be useful as initial state for the forecast in the next step. An alternative application of DA is to generate merged data-model products in order to assess the quality of observations due to instrumental, or other sources of errors (Bouttier and Courtier, 1999).

2.1.1 Basic concepts in data assimilation

A data assimilation system has three core elements: i.e., a state vector that describes the state of the unknowns, a measurement vector, and an observation operator.

The basic problem in any inversion is formed by a set of measurements Y (with dimension of N), from which we would like to infer a true state vector λ with a set of M parameters (e.g., CO_2 fluxes, soil moisture, etc.) using an observation operator H (a dynamic model, in our case an atmospheric transport model, or a radiative transfer model). This observation operator acts upon the state vector to produce a model-based set of observations, i.e., forecast, that then can be compared to the real observations:

$$Y = H(\lambda) + \epsilon, \quad (2.1)$$

where ϵ represents the misfit between the measurements and the model forecast. The observation operator H may be linear or nonlinear, depending on the complexity of the system, but its quality is critical in order to estimate the best guess of the observation. The goal of the inversion system is to estimate the parameters λ and the error structure using the observations. If the system is linear and of manageable size, the observation operator H can be directly inverted, as done in so called synthesis inversions (Enting et al., 1995). But in many cases, the observation operator H is sparse, ill conditioned and often very large, so that other methods are often being used to “invert” the problem (see below).

In the end, all inversions aim to minimize a cost function J that quantifies the model-data mismatch:

$$J = \|(H(\lambda) - Y)\|^2 \quad (2.2)$$

which is equivalent to stating that the inversion seeks to make ϵ as small as possible.

However, due to the often sparse observations, the inverse problem is often underdetermined. This requires us to provide some extra information for the parameters, known as prior information. The prior information is usually the information at the initial step of each assimilation cycle, while the background field is the forecast from the dynamic model, which we also call as background state vector). After introducing the prior information, the goal of inverse problem is to find the optimal parameters that balance the prior information error and the model-data mismatch.

2.1.2 Bayesian objective function

The Bayesian framework assumes that all the processes follow a Gaussian distribution so that the data information and the observations can be represented as probability density functions (PDF) and combined in a joint PDF (i.e., the joint probability that the λ and Y occur together), described by the following equality:

$$P(\lambda, Y) = P(\lambda|Y) \cdot P(Y) = P(Y|\lambda) \cdot P(\lambda), \quad (2.3)$$

where $P(\lambda, Y)$ is the joint PDF for prior (or background) information λ and observation data Y . $P(Y|\lambda)$ is the conditional probability of the observation given the prior information, determined from λ and the observation operator. $P(Y)$ is the PDF of the observation. In the analysis procedure, we know that that a measurement has been taken, so that $P(Y) = 1$. This gives then:

$$P(\lambda|Y) = P(Y|\lambda) \cdot P(\lambda). \quad (2.4)$$

This means that the key term, the posterior $P(\lambda|Y)$ is equal to the background PDF $P(\lambda)$ times $P(Y|\lambda)$. The aim is to find the maximum for $P(\lambda|Y)$. Next we will derive how to generate the cost function under Bayes' rule to solve this problem.

Although there is no specific limit for the probability in Bayes Theory, a Gaussian PDF is assumed for the sake of algebraically convenience and often a good approximation, particularly for the atmospheric CO₂ inverse problem. In addition to the assumption of Gaussian distribution, we make two additional assumptions for the atmospheric CO₂ inversion system: First, we assume that the forward dynamic model H is linear, so that $H(\lambda - \lambda^f)$ is the same as $H(\lambda) - H(\lambda^f)$, where the symbol f denotes the prior from the model forecast, or background. Since atmospheric CO₂ is essentially an inert gas in the atmosphere (we neglect here the production of CO₂ from methane and other organic substances) and atmospheric transport and mixing are linear by definition, this assumption is very closely fulfilled. The second assumption is the expectation that the background errors and the observation errors are entered around 0, i.e., that they are unbiased ($E[\epsilon^f] = E[\epsilon^o] = 0$). We further assume that these two errors are mutually uncorrelated ($E[\epsilon^f, \epsilon^o] = 0$). Their

variance are noted as $var(\epsilon^f) = P^f$, $var(\epsilon^a) = R$.

The Gaussian PDF of the observations and parameters are calculated using the equations for a bell-shaped curve:

$$P(\lambda) = e^{(-1/2)(\lambda - \lambda^f)^T P^{f-1} (\lambda - \lambda^f)} \quad (2.5)$$

$$P(Y|\lambda) = e^{(-1/2)(H(\lambda) - Y)^T R^{-1} (H(\lambda) - Y)}. \quad (2.6)$$

Inserting function (2.6) and (2.5) into (2.4), and taking the logarithm gives:

$$-\log P(\lambda|Y) = C1((1/2)(H(\lambda) - Y)^T R^{-1} (H(\lambda) - Y) + (1/2)(\lambda - \lambda^f)^T P^f$$

Rewriting this in terms of the cost function $J(\lambda)$ gives:

$$J(\lambda) = (1/2)(H(\lambda) - Y)^T R^{-1} (H(\lambda) - Y) + (1/2)(\lambda - \lambda^f)^T P^{f-1} (\lambda - \lambda^f) = J^o + J^f, \quad (2.8)$$

where J^o is the contribution from the observation data, and J^f is the part from the background part. The optimal λ is to make the cost function J minimal.

2.1.3 Data assimilation in carbon cycle research

After several decades of development in DA, there are two basic data assimilation methods commonly used in the atmospheric field, with the two methods being distinguished based on their sequence to incorporate the observation information: The first one is called sequential assimilation, as it uses observations from the past until the time of analysis. This method is further differentiated according to its dimensionality into 3 or intermittent 4 dimensional variational assimilation methods (3D-Var or intermittent 4D-Var). The second method is called retrospective assimilation, as it uses observations from the future as well (Bouttier and Courtier, 1999). The Ensemble Kalman Filter belongs to this second group.

In terms of data assimilation in carbon cycle research, two fundamentally different approaches have been taken to improve the carbon sources and sinks depending on the observation operator: This goal is achieved by either optimizing the 4-dimensional fields of atmospheric CO₂ concentrations (e.g.(Peters et al., 2007; Liu et al., 2012; Michalak et al., 2005)) (see Fig 2.1), or by improving parameters in biogeochemical models (Gao et al., 2011). The latter has the advantage that it provides for a system that is fundamentally capable of making also predictions. But it comes at the cost of being highly dependent on the fidelity of this model, i.e., structural problems in the underlying model will lead to a strongly distorted set of optimized parameters.

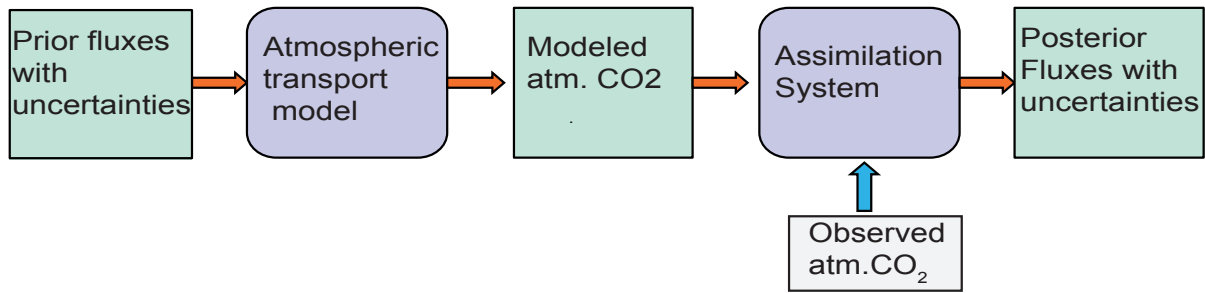


Figure 2.1 A schematic flow diagram of a carbon data assimilation system using observed CO_2 concentrations.

2.2 Kalman Filter Methods for Carbon Cycle Research

2.2.1 Ensemble Kalman Filter

The Ensemble Kalman Filter methods can be divided further into two sets of methods depending on how the errors are considered in the observations: In the stochastic Ensemble Kalman Filter, the observations are perturbed by their errors, while this is not the case in the deterministic Ensemble Kalman Filter methods. In both methods, there are two steps in each time period, i.e., a forecast step before the observations are introduced and an analysis step thereafter (see Fig 2.2). Lei and Bickel (2011) argued that the behavior of these two different methods depends on the observations: the stochastic filter is more stable if it is provided with observations of good quality or with observations that have a high information content. As this is not necessarily the case here, we use a deterministic Ensemble Kalman Filter (Ensemble Kalman Smoother) to incorporate the observations and transport model. But as it turns out, if the forecast or background state vector is Gaussian distributed, these two methods behave quite consistently (Furrer and Bengtsson, 2007).

Concretely, in this thesis we are following Peters et al. (2005), and use an Ensemble Square Root Filter (EnSRF) method, which is a subclass of the deterministic EnKF methods (Whitaker and Hamill, 2002). In EnSRF, the prior parameter error distribution is known and the total analysis error variances need to be minimized. With the given background(or prior) covariance P^f , the square root of this matrix can be calculated through either a Cholesky decomposition or a singular value decomposition method to get the deviation of the parameters, which are then added to the parameters in the background state vector to obtain the ensemble members.

There are many other flavors of Ensemble Kalman Filters, such as ensemble adjustment Kalman filter(EAKF) (Anderson, 2001), the local Ensemble Kalman Filter (LEKF) (Ott et al., 2004), and the local ensemble transform Kalman filter (Miyoshi and Kunii, 2012), with the main differences being their update scheme. More advanced data assimilation methods that emerged in recent studies attempt to account for the non Gaussian feature. These methods include particle filtering methods, or combinations of the filtering method with variational methods, or with other

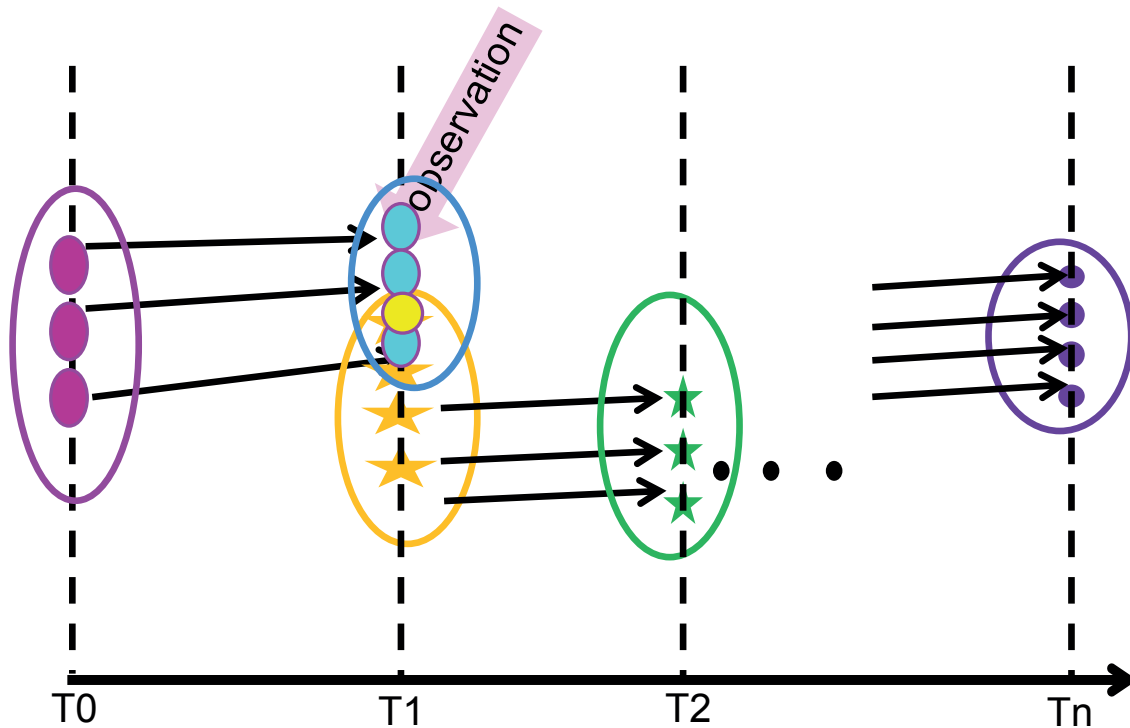


Figure 2.2 Schematic drawing of the time stepping used in an Ensemble Kalman Filter.

machine learning methods, for example, with the non parametric Kernel method, or Gaussian mixture models (Sondergaard and Lermusiaux, 2013; Anderson, 2010; Liu et al., 2016).

In this thesis, the parameters that we are trying to solve are flux scaling factors λ , which are optimized by the following Kalman filter function:

$$\bar{\lambda}^a = \bar{\lambda}^f + \mathbf{K}(Y^o - H(\bar{\lambda}^f)), \quad (2.9)$$

where $\bar{\lambda}^a$ represents the optimized ensemble mean scaling factor, $\bar{\lambda}^f$ the mean background scaling factor, Y^o the observed CO_2 , and \mathbf{K} the Kalman Gain. As before, $H(\cdot)$ is the observation operator (normally a model if the unit of background state vector is different from the observation, otherwise H is just identity matrix, such as some data assimilation in hydrology, e.g., soil moisture). In this study, H is an atmospheric transport model that converts prescribed CO_2 fluxes at the surface into observation space, i.e., atmospheric CO_2 concentrations. The Kalman gain \mathbf{K} is computed as follows:

$$\mathbf{K} = \mathbf{P}^f \mathbf{H}^T (\mathbf{H} \mathbf{P}^f \mathbf{H}^T + \mathbf{R})^{-1}, \quad (2.10)$$

where \mathbf{R} is the error covariance matrix of the measurements. It includes measurement (instrument + retrieval) error, model (transport) error and a representation error (Peylin et al., 2002). In the case of atmospheric CO_2 observations from a high quality network the instrument error is negligibly small. In the case of observations retrieved from satellites, this error is actually quite substantial. Here, we assign the instrument error just a small value. Since it is difficult to calculate the atmospheric model transport error, the model transport error is implicitly contained in the

matrix of observation error matrix \mathbf{R} . Finally, the symbol $()^T$ is the matrix transpose. The two matrix products are computed as follows:

$$\mathbf{H}\mathbf{P}^f\mathbf{H}^T = \frac{1}{N-1} \sum [\mathbf{H}(\lambda'_1), \mathbf{H}(\lambda'_2), \dots, \mathbf{H}(\lambda'_N)][\mathbf{H}(\lambda'_1), \mathbf{H}(\lambda'_2), \dots, \mathbf{H}(\lambda'_N)]^T. \quad (2.11)$$

Where N is the number of ensemble members.

$$\mathbf{P}^f\mathbf{H}^T = \frac{1}{N-1} \sum [\lambda'_1, \lambda'_2, \dots, \lambda'_N][\mathbf{H}(\lambda'_1), \mathbf{H}(\lambda'_2), \dots, \mathbf{H}(\lambda'_N)]^T. \quad (2.12)$$

where λ' represents deviations from mean values:

$$\lambda' = \lambda - \bar{\lambda}, \quad (2.13)$$

The posterior covariance is calculated by:

$$\mathbf{P}^a = (1 - \mathbf{K}\mathbf{H})\mathbf{P}^f. \quad (2.14)$$

When the ensemble size is big enough, the posterior covariance converge to $(\lambda^a - \bar{\lambda}^a)(\lambda^a - \bar{\lambda}^a)^T$

In the Ensemble Square Root Kalman Filter (EnSRF), the ensemble is broken into a mean and into an anomaly part, and the anomalies (λ') are updated using a reduced gain:

$$\lambda'^a = \lambda'^f - \hat{\mathbf{K}}\mathbf{H}(\lambda'^f) \quad (2.15)$$

$$\hat{\mathbf{K}} = \mathbf{K}(1 + (R/(\mathbf{H}\mathbf{P}^f\mathbf{H}^T + \mathbf{R}))^{-1/2})^{-1} \quad (2.16)$$

The Kalman gain has the dimension of the number of parameters times number of observations, such that $\mathbf{K}(Y^o - H(\bar{\lambda}^f))$ has the same dimension as $\bar{\lambda}^f$.

2.2.2 Generating background and observation error covariances

The background or prior covariance matrix \mathbf{P}^f contains the prescribed uncertainty of each parameter, multiplied by the correlation between different parameters in horizontal space using the Schur product. Here, we assume that the spatial correlation decreases exponentially with distance ($L=100\text{km}$), calculated as

$$\mathbf{P}^f = \mathbf{P} \cdot e^{-d^{ij}/L} \quad (2.17)$$

where the same ecosystems are assumed to behave approximately the same, as shown by Peters et al. (2010); van der Laan-Luijkx et al. (2017). In addition, the ecoregions in the same grid cell

Table 2.1 Summary and notation of variables used in the Ensemble Kalman Filter. M is the

Variables	Meaning	Dimension or dimension changes
λ^a	Analysis of the model state	m
λ^f	Forecast or background model state	m
λ^t	True model state	m
K	Kalman gain	$m \times n$
Y^o	Vector of observations	m
H	Observation operator	$m \times n$
R^f	Covariance matrix of observation errors	$n \times n$
P^f	Covariance matrix of background errors $\lambda^f - \lambda^t$	$m \times m$
P^a	Covariance matrix of analysis errors $\lambda^a - \lambda^t$	$m \times m$

have higher correlation than those that are located in different grid cells.

The observation error covariance is a diagonal matrix, with the diagonal values obtained from the error between the forecast and the observed CO_2 concentration. Here we do not consider any possible correlations between the different observation sites, so the off-diagonal values are set to 0.

2.2.3 Tuning and regularization of the ensemble Kalman Filter

Many choices have to be made when building an atmospheric CO_2 inversion system based on an EnKF, such as the finding of a proper ensemble size, defining appropriate spatial and temporal correlation lengths for the covariance matrix, and reducing the potential error arising due to inefficient sampling, or systematic errors. Tuning can help us to identify the best choices.

2.2.3.1 Covariance localization

If the ensemble size N is not big enough given the unknown variables, then the sampling covariance might be biased, and cannot be considered as a correct prediction sampling (Frei and Künsch, 2013). Covariance localization and inflation are used to avoid huge ensemble sizes that brings along a heavy computational cost (Peters et al., 2005; Chatterjee et al., 2012). Peters et al. (2005) introduced the localization in the CarbonTracker, i.e., first, the site with high observation errors are chosen, then the correlation coefficients (CR) of the $H(\lambda^f)$ and λ^f are calculated, then the probability of the these scalars are inferred based on the the correlation coefficients:

$$Pro = CR / \sqrt{(1 - CR^2) / (n-2)} \quad (2.18)$$

If this calculated Pro is smaller than the t-test value based on the degrees of freedom and p value (degrees of freedom is 8 in our case and $p=0.02$), then the localization is applied.

Zupanski et al. (2007) applied a covariance localization method in the Maximum Likelihood Ensemble Filter using the distance function defined in the information space and found that the system works very well even with small ensemble sizes. In chapter 4, we adopted similar covariance method, i.e., first, we calculated the ratio(R_t) of prior covariance to the posterior covariance:

$$R_t = P_f / P_a \quad (2.19)$$

If the ratio is larger than the limit number, then the influence of the observation is localized within this area.

The covariance localization might destroy the autocorrelation structure(Chatterjee, 2012). Other localization methods, such as spectrum regularization, balance-aware localization schemes, or dynamic or covariance schemes were created to better suppress such spurious errors(Buehner, 2012; Anderson, 2012; Leng et al., 2013).

The above addresses just the issue of horizontal localization, while we have not addressed the issue of the vertical localization at all. The latter is not particularly relevant for our surface observation based inversion, but might become highly relevant in the future in the context of the use of satellite-based or ground-based total column measurements.

2.2.3.2 Covariance inflation

If the ensemble size is small, the analysis covariance will be significantly underestimated. In such cases, the filter may diverge, because the ensemble spread is too small, resulting in the model rejecting observations and sticking to its prior (Furrer and Bengtsson, 2007; Chatterjee et al., 2012). Thus the covariance need to be enlarged when using varying background covariance

matrix, which is achieved by an inflation following:

$$\lambda_j^{f,a} = \bar{\lambda} + \alpha^{0.5}(\lambda_j - \bar{\lambda}), \quad (2.20)$$

where the subscripts f, a means different processes when dealing with inflated ensemble members, either before (f) the update step, or after (a) the update but before the propagation step, j the calculated covariance based on the posterior analysis. Anderson (2007) suggested to conduct the inflation after the assimilation due to errors in assimilation that might results in too small variance in the analysis. Different methods were used to calculate the factor α . Anderson (2007) and Anderson (2009) discussed the use of observations and the observational error variance to update α temporally and spatially. Chatterjee et al. (2012) inflated the background error of both the concentrations and the surface fluxes of CO₂. Miyazaki et al. (2011); Chatterjee et al. (2012) applied this method to CO₂ fluxes inversion, i.e., using random variables and then updated using Bayes theorem. Here, we tested the system with constant values inflation, and found that the covariance is still too small, or too high that is out of our knowledge. Hence, we still adopted the constant prior covariance in the later chapters.

2.2.4 Time filtering

There is a time lag before the CO₂ emitted by the vegetation or any other surface process reaches the receptor at the observation site. In addition, mixing occurs along the way, so that any given observation represents the weighted sum of surface fluxes over a time interval. As we are using high-frequency observations (daily), the observation frequency is shorter than the atmospheric transport process, requiring us to take the time lag and mixing into consideration. This is ensured in the EnSRF by using a time filter to account for the different response of CO₂ to the fluxes in former time steps. The length of this filter is referred to as the smoother window. The time filtering is implemented in such a manner that information from previous steps is used alongside the new observations. Concretely, Concretely, this means that the state vector at time t is constrained by observations from different times between time t and time t plus the lag time, in consecutive cycles of the filter.

2.2.5 Diagnostics

The essential step when building a data assimilation procedure is the diagnostic step, which allows monitoring the performance of the filter and ensure that the posterior error remain in a proper range.

2.2.5.1 Error reduction

Reducing uncertainty is the goal of EnKF, hence error reduction is one of most important ways to judge the behavior of the system. The error reduction can be computed as:

$$\text{Error reduction} = 1 - \sigma_{\text{opt}}^2 / \sigma_{\text{prior}}^2 \quad (2.21)$$

σ^2 is the variance. Generally, we expect an optimal system to have higher error reduction.

2.2.5.2 Chi-square

$$\chi^2 = (\mathbf{y} - \mathbf{H}(\lambda))^2 / (\mathbf{H}\mathbf{P}\mathbf{H}^T + \mathbf{R}) \quad (2.22)$$

In a Bayesian framework, the chi-square using posterior information ($\mathbf{H}(\lambda)^a$) should converge to the number of observations (Steinkamp, 2011), while the chi-square using prior information ($\mathbf{H}(\lambda)^f$) requires the chi-square to go towards the degrees of freedom (Zupanski et al., 2006). However, in the framework of a data assimilation system, this rule does not always work. For example, Peters et al. (2005) found that synthetic tests violate this rule, and Chevallier (2014) demonstrated that the results from the simulation with chi-square around 1 was the worst among all the configuration. In the sensitivity test, we found the system behaves better when the chi-square is higher than the degree of freedom. However, the chi-square converges towards the number of observation when using the real in-situ measurements.

2.2.5.3 Degree of freedom of signal(DFS)

The Degrees of Freedom of Signal (DFS) can be used to measure the contribution from the observations sites Lauvaux et al. (2012); Kim et al. (2014). Lauvaux et al. (2012) computed the DFS with the prior covariance matrix to evaluate the weight of the observation constraints from different correlation structures. We used the sensitivity matrix of analysis to the observation, then summing the off-diagonal elements of this matrix, resulting in the following function:

$$\text{DFS} = \text{Trace}(\mathbf{H}\mathbf{P}^a\mathbf{H}^T/\mathbf{R}). \quad (2.23)$$

For more details about the diagnostic and error characteristics, please refer to chapters 2 and 3 of Rodgers (2000) and Chevallier (2014). Weston et al. (2014) and Pinnington et al. (2016) also checked the basic assumption that the correlation in prior and observation error, and found that the root mean square error of NEE could be reduced after considering the correlation of observation error.

2.3 CarbonTracker Switzerland

CarbonTracker Switzerland represents the regional adaptation of the global CarbonTracker atmospheric inversion system (Peters et al., 2005, 2011), which is based on an Ensemble Square Root Kalman Filter (EnSRF). This required several adaptations, the most important of which is the explicit consideration of CO_2 at the lateral boundaries, which was avoided in the other CarbonTracker implementations by using an atmospheric transport model covering the globe. Here, we introduce the basic elements of the model, but refer the reader to chapters 4 and 5 regarding the specific implementations.

2.3.1 Basic setup and flow chart

Figure 2.3 illustrates the basic flow chart of CarbonTracker CH, i.e., the flow of information and the basic two step approach typical of an Ensemble Kalman Filter system. The initial step consists of the computation of an ensemble of forecasts with an observation operator. These results are then compared with the observational constraints in the second step, out of which a set of optimized parameters emerges plus a new set of ensembles, which then can be used to start the whole process again. At its core, CarbonTracker CH follows the EnSRF system outlined above.

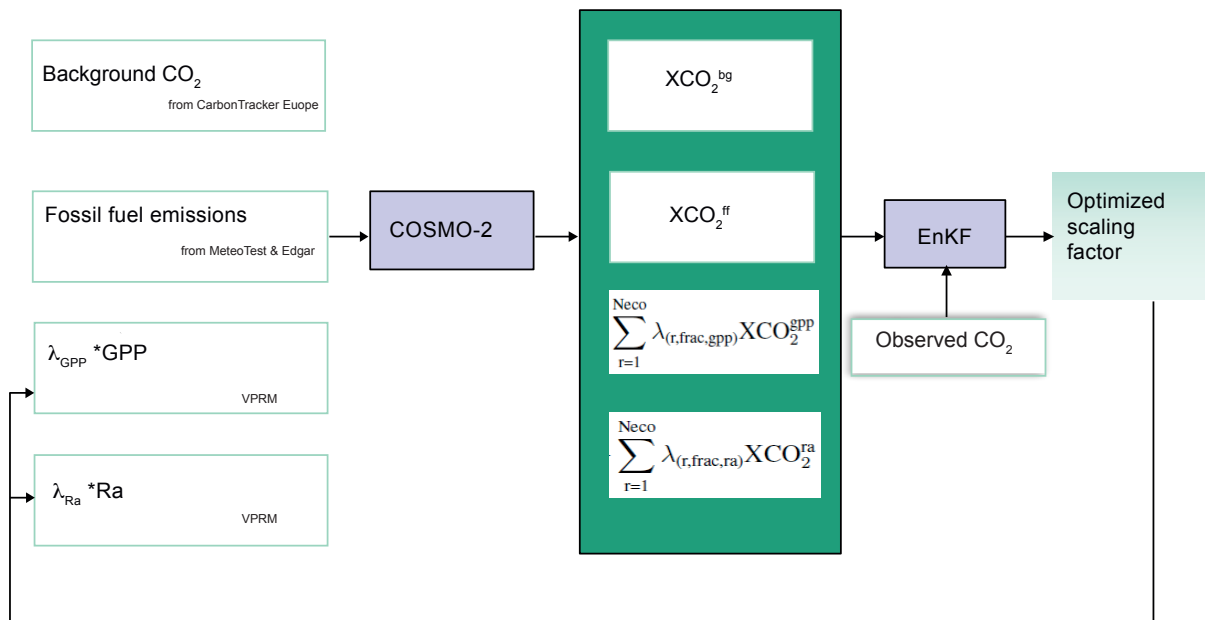


Figure 2.3 The schematic draw of the assimilation system using observed CO_2 concentration.

We use the high resolution atmospheric weather forecast model COSMO as the observation operator in this paper to convert the modelled CO_2 fluxes into observation space. In the model, we separately consider 53 tracers, each of them reflecting a particular process, and together making up the total atmospheric CO_2 dry air mole fraction, $X\text{CO}_2$. Concretely, we consider (i) the advection and mixing of the lateral background information into the domain, i.e., the so called

background CO₂ signal, (XCO_2^{bg}) (ii) the fossil fuel signal, (XCO_2^{ff}) (iii) the oceanic CO₂ signal (XCO_2^{oce}), (iv) the signal of GPP from each considered ecoregion, i.e., $XCO_2^{gpp,r}$, and (v) the signal of total ecosystem respiration from each considered ecoregion, i.e., $XCO_2^{ra,r}$. The atmospheric CO₂ mole fraction can then be computed by the sum of all components, with the GPP and respiration components being scaled with the respective scaling factors, $\lambda_{(r,frac,gpp)}$ and $\lambda_{(r,frac,ra)}$. This gives for the total dry air mole fraction of CO₂:

$$XCO_2 = \sum_{r=1}^{Neco} \lambda_{(r,frac,gpp)} XCO_2^{gpp} + \sum_{r=1}^{Neco} \lambda_{(r,frac,ra)} XCO_2^{ra} + XCO_2^{bg} + XCO_2^{ff} + XCO_2^{oce} \quad (2.24)$$

The evaluation of the modelled with the observed CO₂ concentration is based on equation (2.24), based on the modelled 3-D XCO₂ field for each ensemble member.

2.3.2 Atmospheric Transport Model COSMO

The initial version of the COSMO-Model (former name was Lokal Modell (LM)) was developed by the Deutscher Wetterdienst (DWD), but its further development is now organized through the Consortium for Small-scale Modelling (COSMO)(Baldauf et al., 2011). It is a non-hydrostatic regional weather model designed for high resolution regional forecast requirements of weather services, and used by different meteorological institutions worldwide.

The COSMO consortium and CLM-Community released unified versions of COSMO. The version used in this thesis is COSMO4.23, a numerical weather prediction (NWP) version. Further information about COSMO is provided on www.cosmo-model.org and www.clm-community.eu. The COSMO model has been configured and evaluated for different European countries extensively.

The model's grid is based on rotated geographical coordinates, that is geographical coordinates by tilting the north pole, and a generalised terrain following height coordinate, on which the dynamical core, hydrodynamical equations are built to describe atmospheric transport in a non-hydrostatic and fully compressible form, with different applicable spatial scales. We adopted the Runge Kutta core in this thesis, which uses the 3rd-order Runge-Kutta scheme from Wicker and Skamarock (2002) (Optionally a Leapfrog scheme could be used in COSMO). A level 2.5 turbulent closure is used for parameterizing the vertical turbulent mixing, which treats Turbulent Kinetic Energy as a prognostic variable. For radiation, a sigma-two-stream radiation scheme is adopted from Ritter and Geleyn (1992). Cloud processes with prognostic equations for water vapor, cloud water, cloud ice, rain and snow, are dealt with using a bulk microphysics scheme. The cloudiness at sub-grid scale is an empirical function of relative humidity and height. A fully 3-dimensional semi-Lagrangian scheme and a direction split finite volume differencing scheme are adopted inside COSMO model. In this thesis, we use the semi-Lagrangian scheme method for

the tracers due to problems encountered with the other scheme with negative CO_2 concentration for sinks (GPP).

MeteoSwiss has configured COSMO for its weather prediction needs for two domains, the COSMO-7 domain covering most of Europe with a resolution of 7 km (see chapter 3), and the COSMO-2 domain covering Switzerland and most of the surrounding countries at a resolution of 2 km (Figure 2.4). The model domain for CarbonTracker CH is the same domain at that of COSMO-2 but with a resolution of 7 km, covering the region from $42.72^\circ \text{ N } 2.25^\circ \text{ E}$ (lower left) to $49.76^\circ \text{ N } 17.25^\circ \text{ E}$ (upper right) with Switzerland in the center of the domain (Figure 2.4). The model is configured with 60 vertical geometric hybrid levels.

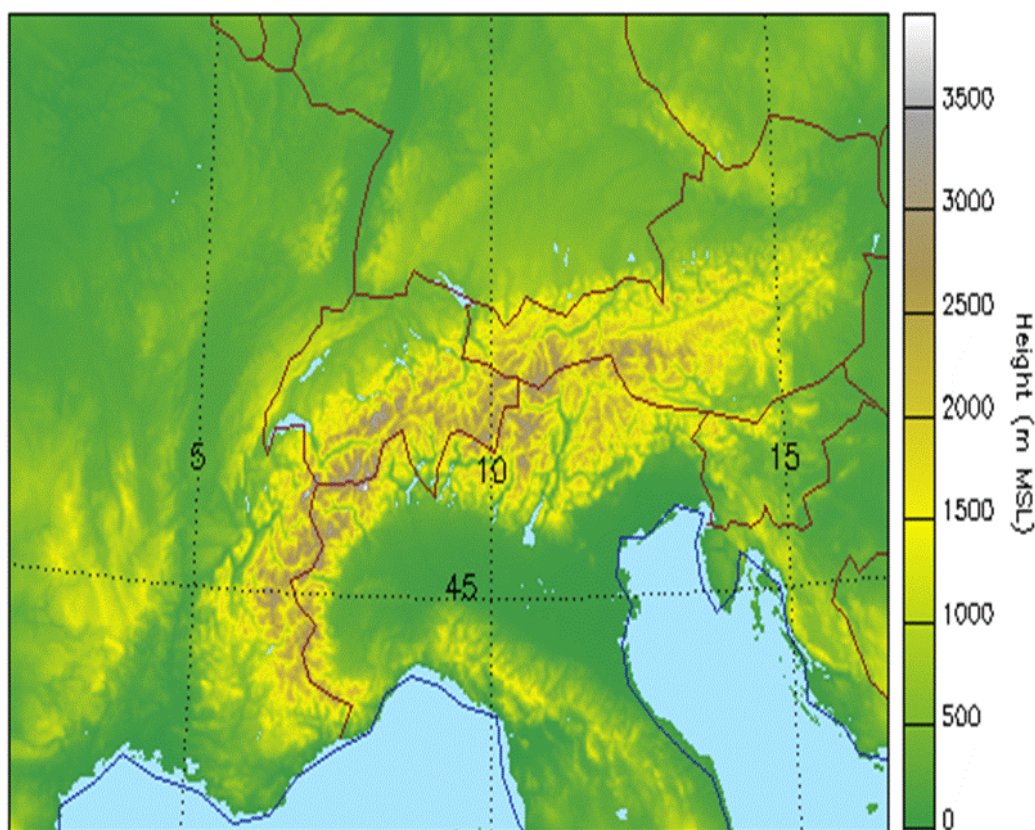


Figure 2.4 The geographic domain of CarbonTracker Switzerland. The domain is the same as that of the COSMO-2 setup used by MeteoSwiss, but with a resolution of 7 km.

A generic tracer transport module was developed by ETH's Center for Climate Systems Modeling (C2SM) and MeteoSwiss and added to COSMO as part of the CarboCount CH project (Roches and Fuhrer, 2012). At the lateral boundaries, the boundary conditions are given through a relaxation scheme, with the boundary condition values for each prognostic variable being read in from a file. For fossil fuel tracers, we implemented a semi-Lagrangian scheme with clipping processes to ensure strictly positive concentration.

2.3.3 Fossil fuel Emissions

The fossil fuel emissions for CO₂ were generated by merging a relatively coarse emission inventory for the regions outside Switzerland (EDGAR v4.2, 10 km (Janssens-Maenhout et al., 2012)) with a high-resolution (0.5 km) emission inventory for Switzerland. The latter was produced by the company MeteoTest, specifically for the CarboCount CH project.

We merged the emission categories from the two inventories to 5 large emission categories, i.e., power generation, residential heating, road transport, industrial processes, and others. Even though each of these different categories have a distinct emission pattern, many of them co-occur in the large metropolitan areas, leading to a very patchy emission pattern with strong emission hotspots, and extensive regions with relatively low emissions (More detail see Chapter 3).

These emissions inventories are given for each emission category as annual totals for each grid cell, requiring us to multiply them with time functions to generate hourly time series of the fossil fuel emissions at each location (Nassar et al., 2013). The time functions we employed were originally generated by the University of Stuttgart (Institute für Energiewirtschaft und Rationelle Energieanwendung, IER) (Friedrich and Reis, 2004) and had been used in several air quality modeling studies. The time functions are comprised of diurnal, weekly and seasonal components and are specific to each of the main economic sectors (activities collected in the Selected Nomenclature for Air Pollution (SNAP) codes) (Kuenen et al., 2014). The time functions (except for the daily one) vary also by country, and are locally adjusted to reflect local time. Some small reassignments were necessary to align the categories used for the emission inventories with the SNAP categories.

The time functions differ greatly between the various categories, reflecting their very different time course of activities over the average day, week or year. Among all diurnal time functions, road transportation has the largest diurnal variability and is characterized by two peaks during the day reflecting the rush hour periods (local time 8:00-9:00 and 17:00-18:00). Also residential/commercial combustion has a distinct diurnal cycle with two peaks but lagged compared to the road transportation. In contrast, the emissions from industrial processes and fossil-fuel fired power plants vary less over the course of the day and also have only one peak. The time functions for the day-of-week primarily reflect the lower industrial and traffic activities during the week end, while most other sectors continue to emit at only slightly smaller rates. Nevertheless, combining all the sectors together, emissions during the weekend are 15-20% lower than during the week. The seasonal time functions depend primarily on the local climatic conditions, with northern and central European countries having a clear maximum in winter due to their heating requirement, while there is little seasonality in emissions in the southern European countries.

2.3.4 Lateral boundary conditions and background CO₂

The meteorological forcing data are from MeteoSwiss COSMO-7 analysis hourly data with 150 2D or 3D fields. The boundary concentrations for the background CO₂ are provided by the post-assimilation results of CarbonTracker Europe (Peters et al., 2010) (with a resolution of 1°). The 3-hourly CO₂ fields were cropped and interpolated to the COSMO-7 and COSMO-2 domains using the COSMO preprocessing tool INT2LM at 7km. As the vertical coordinate systems are different, i.e., CarbonTracker Europe uses pressure levels, we interpolated these data to the hybrid height level of COSMO. This required knowledge of the hybrid coefficients for the center of each layer in the CarbonTracker output as well as surface pressure, which we took from the COSMO model.

2.3.5 Terrestrial biosphere Fluxes

The terrestrial biospheric exchange pattern is used for prescribing the flux patterns within the regional basis functions (figure 2.3). The flux pattern is purely seasonal (annual mean flux is zero for every pixel).

The Gross Primary Production (GPP) in VPRM is calculated by using the MODIS land surface water index, enhanced vegetation index, near surface temperature and shortwave radiation, while total ecosystem respiration fluxes (R) are calculated based on temperature (Mahadevan et al., 2008) (<http://modis.gsfc.nasa.gov/>). The terrestrial biospheric CO₂ is the sum of the CO₂ concentration from GPP and R, representing net ecosystem exchange (NEE) of CO₂ between the atmosphere and the terrestrial biosphere. Eight vegetation classes are used in VPRM with different parameters, which are the combination of 22 sub-classes, in which parameters controlling these classes had been optimized using CarboEurope-IP eddy covariance flux observations at various sites as described in Pillai et al. (2012). After converting to a surface mass flux and reprojecting to the simulation domain, the hourly NEE fields were read in by COSMO.

2.3.6 Subgrid scale heterogeneity in ecoregions

The ecoregion maps are from the VPRM percentage information, with detailed percentage information kept inside each pixel. In this paper, we ignore the ecoregions in one grid with area less than 10% and replace them with the dominant ecoregion. As the 4 new measurement sites have distinct sensitivity region (result from a Lagrangian model), we separate their main sensitivity region from the rest of the domain, and call this inside the footprint. The croplands dominate other species, with total fluxes about 2 times as the sum of the forests. The original croplands were decomposed into 4 different regions, due to similar behaviour and species at different regions. The grassland is kept as 1 ecoregion in the whole domain due to the small contribution to the total

NEE fluxes.

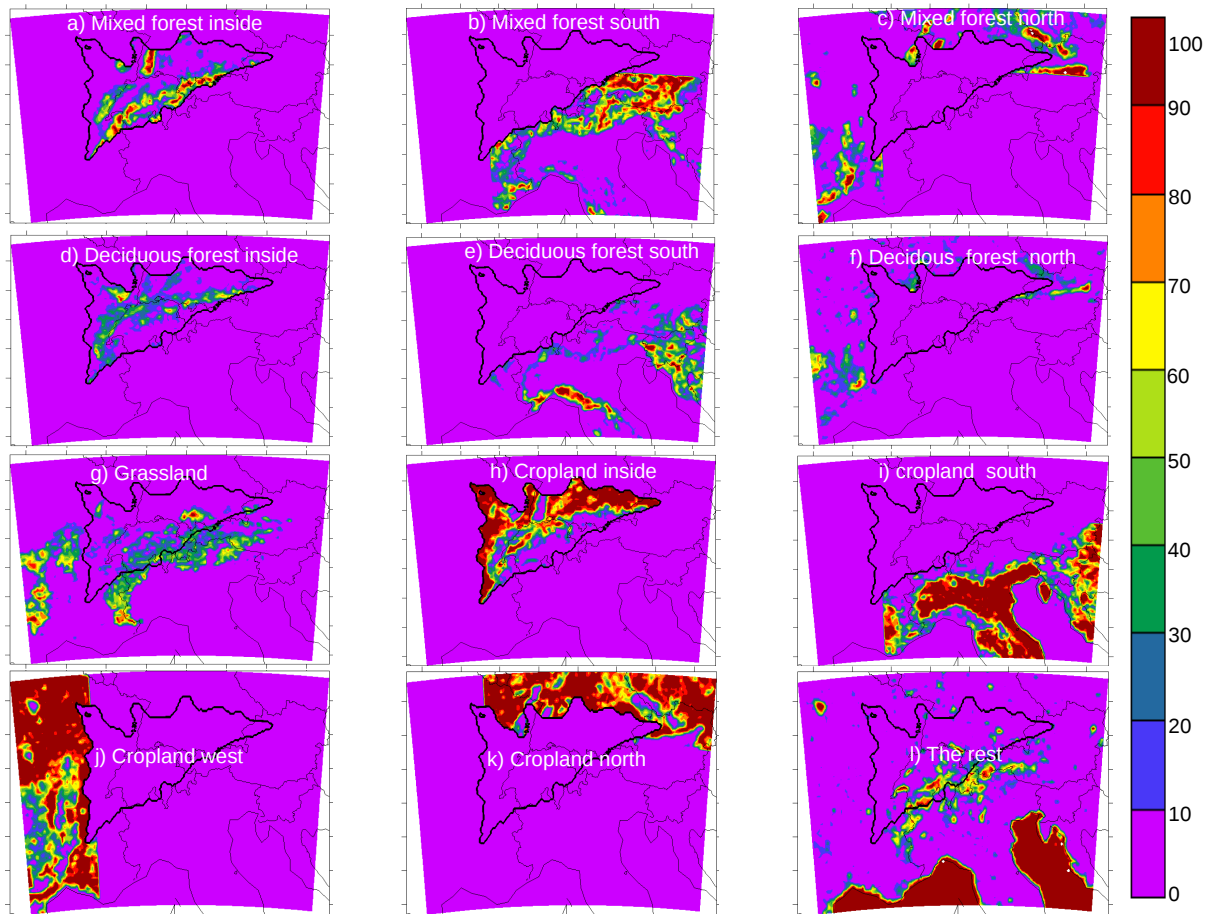


Figure 2.5 The distribution of different eco regions: percentage of area in each pixel(%).

2.4 Atmospheric CO₂ Observations

Table 2.2 lists all the atmospheric CO₂ measurement sites used in this study (either used for evaluation or for assimilation). These observation sites all adhere to the WMO standards and record the atmospheric CO₂ concentrations at high frequency, from which hourly means are generated. Most of the sites have complete daily coverage with the exception of Monte Cimone, where a substantial period is missing in the summer and fall in 2013.

Four of the sites are new and have been added thanks to the CarboCount CH project (Oney et al., 2015) (see Fig. 2.6), i.e., Beromünster, Frübüehl, Lägern Hochwacht, and Gimmiz.

The Beromünster measurements sensor are located on a tall tower (217 m above ground) located on a gentle hill in Switzerland, with Alps in the south and the Jura Mountains in northwest, with sampling from 5 different elevations. We choose the observation at the highest level due to less exposure to the local fossil fuel emissions and bigger concentration footprint (more details see(Satar et al., 2016)). The Frübüel site measurements are made 4 m above ground on the flank

of a gently sloping mountain (we treat it as continental site where the uncertainty is relatively high), with influence from nearby (< 50 km) pasture and forest fluxes during most days, and mainly influenced by the eastern Swiss Plateau during convective days in summertime. The measurements at Gimmiz are made on a small tower (32 m) in flat terrain, and mainly inform on the CO₂ from nearby (< 50 km) crop and anthropogenic fluxes. The site Gimmiz is only used in the pseudo-inversions, but excluded in the real observation inversions due to the too high errors with observations. For more detail information on the specifics of each site, the reader is referred to Oney et al. (2015).

In addition, we use one more site from Jungfrauoch (JFJ, Switzerland) that is a high elevation site that mainly records the large-scale variations in the free troposphere, and 4 more sites outside Switzerland. Please consult Schöner et al. (2012), Ferrarese et al. (2015) and Geels et al. (2007) for more information about these sites.

For the inversion, we subselect the data based on the degree of vertical mixing. At the mountain sites, i.e., SNB, CMN, and PRS, where the site is above the PBL for most of the day, we use the observation data at 0-6:00 AM. For the other sites, we use the data in the afternoon from local time (UTC) 12:00-15:00 PM.

Table 2.2 The CO₂ concentration measurement site information.

Station(code)	Location	Altitude a.s.l.	characteristics
Lägern Hochwacht (LHW)	47.48° N, 8.4° E	860m	continental
Beromünster (BRM)	47.19° N, 8.18° E	797(base), 1009m(highest level)	continental
Früebüel (FRU)	47.12° N, 8.54° E	982 m	continental
Gimmiz (GIM)	47.05° N, 7.25° E	443 m	continental
Monte Cimone (CMN)	44.20° N, 10.70° E	2165 m	mountain site
Schauinsland (SSL)	47.92° N, 7.92° E	1205 m	continental
Plateau Rosa (PRS)	45.93° N, 7.70° E	3482 m	mountain site
Sonnblick (SNB)	47.05° N, 12.95° E	3106m	mountain site
Jungfrauoch (JFJ)	46.55° N, 7.98° E	3580 m	mountain site

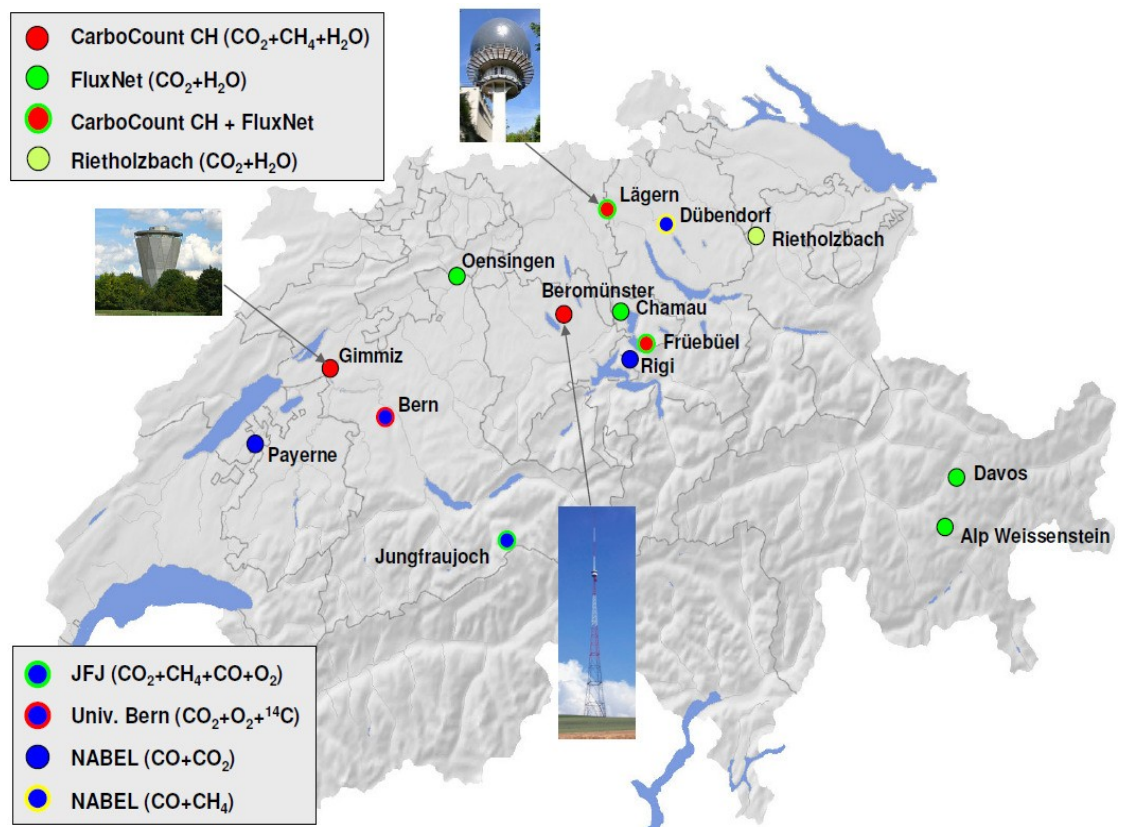


Figure 2.6 Map showing the CarboCount CH measurement sites for atmospheric CO₂ in the context of other carbon related activities in Switzerland, such as FluxNet (Eddy Covariance Measurements) and the NABEL network (air quality).

Chapter 3

Spatiotemporal patterns of the fossil-fuel CO₂ signal in central Europe: Results from a high-resolution atmospheric transport model

abstract

The emission of CO₂ from the burning of fossil fuel is a prime determinant of variations in atmospheric CO₂. Here, we simulate this fossil fuel signal together with the natural and background components with a regional high-resolution atmospheric transport model for central and southern Europe considering separately the emissions from different sectors and countries on the basis of emission inventories and hourly emission time functions. The simulated variations in atmospheric CO₂ agree very well with observation-based estimates, although the observed variance is slightly underestimated, particularly for the fossil fuel component. Despite relatively rapid atmospheric mixing, the simulated fossil fuel signal reveals distinct annual mean structures deep into the troposphere reflecting the spatially dense aggregation of most emissions. The fossil fuel signal accounts for more than half of the total (fossil fuel + biospheric + background) temporal variations in atmospheric CO₂ in most areas of northern and western central Europe, with the largest variations occurring on diurnal timescales owing to the combination of diurnal variations in emissions and atmospheric mixing/transport out of the surface layer. Their co-variance leads to a fossil-fuel diurnal rectifier effect with a magnitude as large as 9 ppm compared to a case with time-constant emissions. The spatial pattern of CO₂ from the different sectors largely reflects the distribution and relative magnitude of the corresponding emissions, with power plant emissions leaving the most distinguished mark. An exception is southern and western Europe, where the emissions from the transportation sector dominate the fossil fuel signal. Most of the fossil fuel

CO₂ remains within the country responsible for the emission, although in smaller countries, up to 80% of the fossil fuel signal can come from abroad. A fossil fuel emission reduction of 30% is clearly detectable for a surface-based observing system for atmospheric CO₂, while it is beyond the edge of detectability for the current generation of satellites with the exception of a few hotspot sites. Changes in variability in atmospheric CO₂ might open an additional door for the monitoring and verification of changes in fossil fuel emissions, primarily for surface based systems.

3.1 Introduction

With annual CO₂ emissions from fossil fuel burning and cement production having soared in the recent decades and approaching 10 Pg C yr⁻¹ (Raupach et al., 2007; Friedlingstein et al., 2014; Le Quere et al., 2016), these fluxes have reached the same order of magnitude as the natural exchange fluxes between the atmosphere and land surface and between the atmosphere and the ocean, respectively (Sarmiento and Gruber, 2002; Le Quere et al., 2016). Thus, the fossil fuel emissions have become a key driver for the spatiotemporal dynamics of atmospheric CO₂, not only close to major sites of emissions, but also far downstream (Peylin et al., 2011; Keppel-Aleks et al., 2013; Nassar et al., 2013). This represents simultaneously a challenge and an opportunity. It is an opportunity since the substantial and growing size of this fossil fuel CO₂ signal facilitates the use of variations in atmospheric CO₂ to monitor and verify changes in fossil fuel emissions (Bovensmann et al., 2010; Velazco et al., 2011; McKain et al., 2012; Ciais et al., 2014; Shiga et al., 2014). At the same time, the large fossil fuel CO₂ signal complicates the use of atmospheric CO₂ observations to determine sources and sinks of CO₂ driven by the land biosphere through atmospheric inverse modeling methods. This requires the separation of the biospheric signal in atmospheric CO₂ from the total signal, which is usually accomplished by subtracting an estimate of the fossil fuel component from the measured atmospheric CO₂ concentration. This implies that any error in the fossil fuel component tends to be projected directly onto the inversely estimated biospheric fluxes (Nassar et al., 2013; Peylin et al., 2011). Thus, in order to benefit from the monitoring and verification opportunity as well as to minimize the magnitude of the challenge associated with atmospheric inversions, it is paramount to well characterize the fossil fuel component in atmospheric CO₂ in time and space.

Two sets of approaches have been developed to determine this fossil fuel component in atmospheric CO₂. A first set of approaches relies on concurrent observations of carbon monoxide (CO) and/or radiocarbon to determine the fossil fuel component in the observed atmospheric CO₂ variations (Breon et al., 2015; Ciais et al., 2013a; Levin and Karstens, 2007; van der Laan et al., 2010; Turnbull et al., 2011; Newman et al., 2013; Vogel et al., 2013; Lindenmaier et al., 2014; Vardag et al., 2015; Oney, 2016). A major advantage of these observation-based methods is that they do not require any atmospheric transport modeling, and thus are not sensitive to any errors in the modeled atmospheric transport. A major disadvantage is that these observation-based es-

timates are available only at a relatively small set of observing sites, providing a very limited picture of the spatiotemporal dynamics of the fossil fuel signal for larger areas. Further complications may arise from e.g., poorly known and varying ratios of the emissions of CO and CO₂ in the case of CO-based methods (Oney, 2016), or the emission of radiocarbon from nuclear power and reprocessing plants in the case of radiocarbon-based methods (Graven and Gruber, 2011).

In the second set of approaches the fossil fuel CO₂ signal is modeled, starting from the specification of fossil fuel emissions as a bottom boundary condition in an atmospheric transport model, and then running this model forward in time (Peylin et al., 2011; Ogle et al., 2015). A key advantage of this set of approaches is that the spatiotemporal dynamics is fully resolved. But this comes at the disadvantage that the resulting accuracy of the modeled fossil fuel CO₂ signal not only depends on the quality of the fossil fuel emissions data, but also on that of the transport model. The latter disadvantage is well illustrated by the results of a recent model intercomparison study, where inter-model differences in the simulated spatiotemporal pattern of the fossil fuel CO₂ were 2-3 times larger than the differences resulting from the use of different emission inventories (Peylin et al., 2011). Of particular relevance is the resolution of the atmospheric model, as this is key to better resolve the topography and land surface contrasts that govern much of the atmospheric circulation and mixing in the lower atmosphere.

The challenge associated with the modeling of atmospheric transport is particularly acute for the fossil fuel component, since fossil fuel emissions are distributed in time and space in a highly heterogeneous and non-Gaussian manner (Ray et al., 2014). This reflects the nature of the processes underlying these emissions, ranging from the point source nature of the emissions from coal-fired power plants, whose emissions vary in response to changing needs for electricity, to the strong diurnal fluctuations of the dispersed emissions associated with road transportation (Nassar et al., 2013). This strong spatial and temporal patterning of the fossil fuel emissions interacts with the spatiotemporal variability of atmospheric transport, forming distinct patterns of the fossil fuel signal in atmospheric CO₂ (Feng et al., 2016c). Of particular relevance are the diurnal and the seasonal changes in emissions, since they tend to co-vary with atmospheric transport, which can lead to atmospheric CO₂ concentration gradients due to a rectification effect (Denning et al., 1995; Zhang et al., 2016). Such unaccounted for variations in the fossil fuel signal would bias the biospheric signal in atmospheric inversion frameworks, hindering us from developing a better understanding of the role of the land biosphere as a carbon sink. At the same time, this strong temporal patterning of the emissions creates also distinct signals that might be used to detect or track the fossil fuel signal.

In fact, several studies already explored the possibilities to detect the fossil fuel signal (Ciais et al., 2014; Nassar et al., 2013). These include a range of methods and systems, including bottom up methods based on surface observation systems (Shiga et al., 2014; McKain et al., 2012; Keller et al., 2016), CO and radiocarbon based methods (Levin and Karstens, 2007; van der Laan et al., 2010; Vogel et al., 2013), airborne measurements (Turnbull et al., 2011), satellite constraints (Kort

et al., 2012), and top-down approaches on the basis of atmospheric inversions (Ogle et al., 2015; Lauvaux et al., 2016; Brioude et al., 2013). Spatially, the focus ranges from point scale emissions (Bovensmann et al., 2010; Velazco et al., 2011; Turnbull et al., 2016), or urban-scale (Newman et al., 2013; Breon et al., 2015; Turnbull et al., 2015; Pillai et al., 2016) to regional and global (Keppel-Aleks et al., 2013; Basu et al., 2016).

A necessity to successfully deploy any of these different detection approaches is a good understanding of the spatiotemporal dynamics of the fossil fuel signal over a scale that is sufficiently large in order to avoid an unacceptably high sensitivity to the lateral boundary conditions, i.e., over scales exceeding a few 100 km. A successful detection also requires a good understanding of the contribution of the other processes affecting atmospheric CO₂ variations, namely the exchange fluxes with the land biosphere and with the ocean, respectively. Further, often it would be quite useful to know the source processes responsible for the fossil-fuel CO₂ signature, i.e., what fraction of the signal stems from emissions from a coal-fired power plant and what part from road transportation. This helps, e.g., with the assessment of how the implementation of a particular policy affects the fossil fuel signature, such as e.g., the shutting down of coal-fired power plants.

Few studies have taken a continental to global perspective on the fossil fuel signal (Keppel-Aleks et al., 2013), as the focus in the last few years had been on urban areas (McKain et al., 2012; Newman et al., 2013; Kort et al., 2012), or just whether the emissions in the city be detected or not (Hase et al., 2015; Pillai et al., 2016). In addition, comparatively less work has been carried out in Europe (Schneising et al., 2008), and the majority of those used relatively coarse resolution atmospheric transport models, resulting in relatively washed-out gradients of the fossil fuel signal over Europe (Keppel-Aleks et al., 2013; Peylin et al., 2011), or few of them focused on whether the potential reduced emissions could be discerned by current observation methods in this region or not (Levin et al., 2011). Furthermore, little consideration has been given to the temporal variations of the emissions.

The main objective of this work is to fill these gaps, and to develop a quantitative understanding of the fossil fuel CO₂ signal in Europe. To this end, we employ a forward modeling approach using a high resolution atmospheric transport model for Europe, forced with finely resolved fossil fuel emission fluxes in time and space. In this paper, we will (i) investigate the magnitude of the contribution of the fossil fuel CO₂ signal to the variations in total CO₂; (ii) understand how the high temporal resolution considered in the fossil fuel emissions affect the fossil CO₂ signal; and (iii) determine the detectability of a reduction of fossil fuel emissions from different sources through changes in the column mean CO₂ as seen, e.g., by a satellite-based observing system. We first describe the model and methods, followed by the evaluation of the model in the third part. We then present the results, followed by a discussion of each of the aforementioned three main topics, and then conclude with a summary and an outlook.

3.2 Methods and Data

To simulate the fossil-fuel CO₂ over central and southern Europe in the context of the variations in total atmospheric CO₂, we employ a regional high-resolution atmospheric transport model for the European domain and prescribe lateral and boundary conditions for the various components that constitute atmospheric CO₂. These include the fossil fuel emissions, the CO₂ exchange fluxes with the land and ocean surfaces, and the lateral atmospheric CO₂ boundary conditions. The simulations cover the period April 2008 until April 2009. The following subsections describe the methods and data in more detail.

3.2.1 Atmospheric transport model

The simulations were undertaken with the limited-area atmospheric prediction model COSMO (Consortium for Small-scale Modeling) (Baldauf et al., 2011) Version 4.23. We employed the COSMO-7 setup developed by the Swiss Federal Office for Meteorology and Climatology (MeteoSwiss) for the purpose of providing boundary conditions for the inner COSMO-2 grid used for forecasting the weather in Switzerland. The COSMO-7 setup has a grid spacing of 6.6 km and its domain covers central and southern Europe (35.16°N/9.80°E (lower left) to 56.84°N/23.02°E (upper right) (see Fig. 3.1).

The COSMO model is based on the primitive hydro-thermodynamical equations describing compressible non-hydrostatic flow in a moist atmosphere without any scale approximations. The model equations are solved numerically on a rotated latitude-longitude grid, with terrain-following coordinates in the vertical (60 vertical levels, and lowest level at 10 meters), using an Eulerian finite difference method. Parameterization schemes are used to resolve the sub-grid scale physical processes such as vertical diffusion (turbulence), convection, radiation, and soil processes. A tracer transport module was recently added to the COSMO model, permitting the online transport of passive tracers in a manner that is fully consistent with the physics of the model (Roches and Fuhrer, 2012). In our setup, advective transport was accomplished with a 3-dimensional semi-Lagrangian scheme. The tracers are transported in the model as moist air mass mixing ratios q_{CO_2} . Values reported here are provided as dry air mole fractions χ_{CO_2} , calculated as $\chi_{CO_2} = q_{CO_2}/(1 - q_{H_2O})M_{dry}/M_{CO_2}$, where q_{H_2O} is the specific humidity and M_{dry} and M_{CO_2} are the molar masses of dry air and CO₂, respectively. The dry air column average mixing ratio is calculated as $X_{CO_2} = (\sum_{k=1}^K (p(k + 1/2) - p(k - 1/2))q_{CO_2}(k))/(\sum_{k=1}^K (p(k + 1/2) - p(k - 1/2))(1 - q_{H_2O}(k))) * M_{dry}/M_{CO_2}$. K is the vertical level, and p pressure, which is at the staggered level (Baldauf et al. (2011) is recommended for more information).

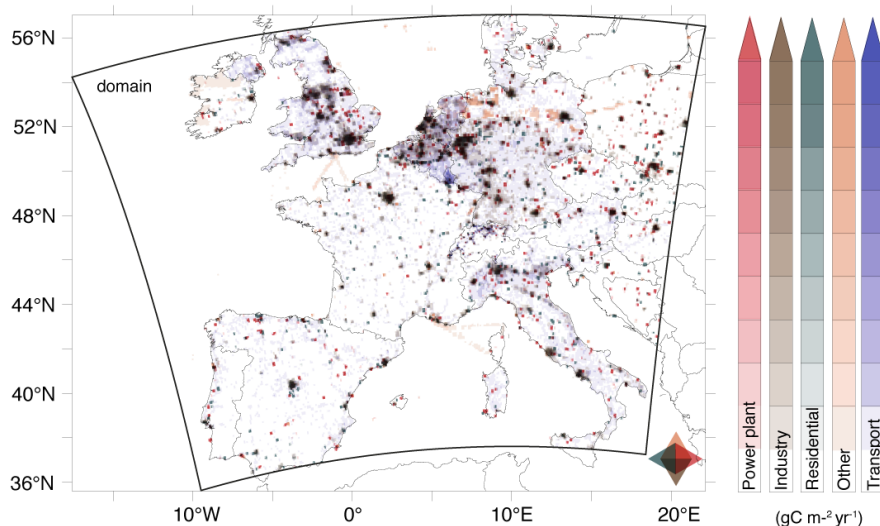


Figure 3.1 Map of the fossil fuel emissions used in this study. Also depicted is the domain of the COSMO-7 setup employed here. Shown in transparent color are the fossil fuel CO₂ emissions for different sectors in units of $\text{gC m}^{-2} \text{yr}^{-1}$. The colors from the different sector blend to a darker color when they are co-located as shown by the color mixing star at the bottom right.

3.2.2 Fossil fuel emissions

The fossil fuel emissions for CO₂ were generated by merging a relatively coarse emission inventory for the regions outside Switzerland (EDGAR v4.2_FT2010, approx. 10 km, (Janssens-Maenhout et al., 2012)) with a high-resolution (0.5 km) emission inventory for Switzerland. The latter was produced by the company Meteotest specifically for the CarboCount CH project. The annual emissions from this merged product for the year 2008 amount to 2.54 Pg CO₂ over the domain, representing about 10% of the global emissions of that year (Le Quere et al., 2016). We merged the emission categories from the two inventories to 5 large emission categories, i.e., power generation, residential heating, road transportation, industrial processes, and others. Even though each of these different categories have a distinct emission pattern, many of them co-occur in the large metropolitan areas, leading to a very patchy emission pattern with strong emission hotspots, and extensive regions with relatively low emission densities (Fig. 3.1).

These emission inventories are given for each emission category as annual totals for each grid cell, requiring us to multiply them with time functions to generate hourly timeseries of the fossil fuel emissions at each location (Nassar et al., 2013). The time functions we employed were originally generated by the University of Stuttgart (Institute für Energiewirtschaft und Rationelle Energieanwendung, IER) for the GENEMIS project (Friedrich and Reis, 2004) and have been used since in several air quality modeling studies. The time functions are comprised of diurnal, weekly and seasonal components and are specific to each of the main economic sectors (activities collected in the Selected Nomenclature for Air Pollution (SNAP) codes) (Kuenen et al., 2014). The time functions (except for the daily one) vary also by country, and are locally adjusted to reflect local time. Some reassignments were necessary to align the categories used in EDGAR v4.2

and the CarboCount CH inventory (both following IPCC guidelines) with the SNAP categories as described in the supplementary material.

The time functions differ greatly between the various categories, reflecting their very different time course of activities over the average day, week or year (see Fig. 3.2a,b). Among all diurnal time functions, road transportation has the largest diurnal variability and is characterized by two peaks during the day reflecting the rush hour periods (local time 8:00-9:00 and 17:00-18:00). Also residential/commercial combustion has a distinct diurnal cycle with two peaks. In contrast, the emissions from industrial processes and fossil-fuel fired power plants vary less over the course of the day and also have only one peak. The time functions for the day-of-week reflect primarily the lower industrial activities and traffic during the week end, while most other sectors continue to emit at only slightly smaller rates (see Fig. 3.2a). Combining all the sectors together, emissions during the weekend are 15-20% lower than during the week. The seasonal time functions depend primarily on the local climatic conditions (see Fig. 3.2b), with northern and central European countries having a maximum in winter due to their heating requirement, while there is little seasonality in emissions in the southern European countries.

In order to be able to trace the fossil fuel signature in atmospheric CO₂ back to the emitters, we consider separate fossil-fuel tracers for ten different countries (or groups of countries) in our atmospheric transport model (see Fig. 3.1). Each of these tracers receives only the emissions from its respective country or group of countries, while elsewhere, the emissions are set to zero. Due to the linearity of atmospheric transport and the absence of any transformation of CO₂ in the atmosphere, the individual country-based tracers can then be summed to obtain the total fossil fuel CO₂ signal. In addition, in order to determine the contribution of the different CO₂ emission categories to the total fossil fuel CO₂, we also included five additional fossil fuel tracers, one each for the five categories we consider, i.e., power generation, residential heating, road transportation, industrial processes, and others. For these 5 tracers, we used time-invariant emissions, permitting us to assess also the role of the time variations in emissions on the fossil fuel CO₂ signal. In total, we included 17 fossil fuel tracers (10 countries, 5 sectors, and total fossil fuel CO₂ with time varying emission, and total fossil fuel CO₂ with time constant emission) in our high-resolution simulation study.

3.2.3 Other CO₂ component fluxes

In order to simulate the distribution of total atmospheric CO₂, we also include in our model three other CO₂ components, namely background CO₂, the terrestrial biospheric CO₂ and the oceanic CO₂ components. The background CO₂ represents that part of the atmospheric CO₂ that enters the domain through its boundaries. These boundary concentrations are provided by the post-assimilation results of CarbonTracker Europe (Peters et al., 2010). For the terrestrial biospheric CO₂ component, we used the hourly terrestrial biospheric fluxes from the Vegetation Photosynthesis

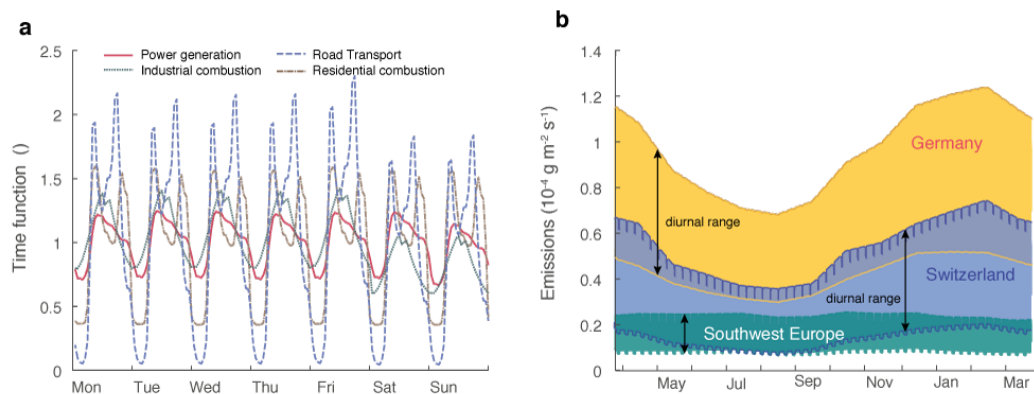


Figure 3.2 Time dependence of fossil fuel CO₂ emissions for different sectors and countries. (a) Time functions for the diurnal and weekly emissions for four sectors. (b) Annual evolution of the CO₂ emission intensity for three different countries or group of countries. Shown are the daily minima and maxima for each country.

and Respiration Model (VPRM) (Mahadevan et al., 2008). For the oceanic CO₂ component, we combined the monthly air-sea CO₂ flux estimates for the Atlantic from Landschützer et al. (2013) with the annual mean flux estimates for the Mediterranean by DOrtenzio et al. (2008). As the oceanic flux contribution is small, no attempt was made to add higher frequency variability.

3.2.4 Simulations

The hindcast simulation started on March 1, 2008, with the initial and boundary conditions for meteorology taken from the operational hourly COSMO-7 analyses of MeteoSwiss and the initial and boundary conditions for atmospheric CO₂ provided by CarbonTracker Europe (Peters et al., 2010). The model was then run for 13 months until April 30, 2009. No assimilation of any meteorological data was performed. The lateral and boundary conditions for the total of 18 CO₂ tracers considered (15 fossil fuel, 3 other components) were prescribed as described above. We consider the first month as a spinup, and use the subsequent 12 months for our analyses.

3.3 Evaluation

3.3.1 Total atmospheric CO₂

We evaluate our COSMO-based results for the total atmospheric CO₂ concentration (computed by summing the fossil fuel component with the three others) by comparing them to the measurements from four sites in central Europe, namely Mace Head (MHD, 3.33°N, 9.90°W, 5m above ground, coastal site, 15 m a.s.l.), Cabauw (CBW, 51.97°N, 4.92°E, 20m, 60m, 200m above

ground, flatland, near urban site, 0 m a.s.l.), Hegyhatsal (HUN, 6.95°N, 16.65°E, 10m, 48m, and 115m above ground, continental site, 248 m a.s.l.) (Geels et al., 2007), Puy de Dome (PUY, 45.46°N, 2.58°E, mountain site, 1480 m a.s.l.). In order to minimize the impact of local influences, we use the average CO₂ concentrations between 12:00 and 18:00 local time, i.e., the time of day of maximum vertical mixing.

The modeled atmospheric CO₂ records at these four sites agree well with the observed ones (see Table 3.1). The correlation between the modeled and observed values exceed 0.7 at all sites and heights. The highest correlation is found at Mace Head (MHD) (>0.81). This is due to the relatively steady conditions that characterize this relatively clean coastal site. Influence from air pollution is only observed during episodes of transport from the United Kingdom and continental Europe, which are very well captured by the model. The correlations are somewhat lower at the more polluted and more continental sites, i.e., between 0.72 and 0.78 at the coastal tall tower station Cabauw (CBW) in the Netherlands, and around 0.8 at the continental tall tower station Hegyhatsal (HUN) in Hungary. Even the atmospheric CO₂ variations at the mountain top site Puy de Dome in France are well captured ($r = 0.75$).

COSMO tends to systematically underestimate the observed CO₂ concentration at most of the stations and levels, except at the coast of Ireland (MHD), where it is overestimated by 0.3 ppm (Table 3.1). The biases tend to get larger with increasing continentality of the sites, and the associated higher complexity of the surrounding terrain and other influencing factors. At the Cabauw site (CBW), the biases amount to between -0.8 and -1.6 ppm, while in central Hungary (HUN) the biases are already more than -4 ppm at all vertical levels. In general, this may be related to COSMO-7 ventilating the planetary boundary layer too strongly, particularly in winter time under weakly stratified conditions. This is especially acute for the HUN site, because the air in the lowest atmospheric levels tends to get trapped at this site owing to the winter-time prevalence of anticyclonic conditions in the Carpathian Basin (Haszpra et al., 2012). An alternative explanation is that the biospheric sink simulated by VPRM is too strong, as discussed later.

Even though COSMO exhibits some biases in the mean, it captures the observed variability generally well (Table 3.1). In particular, COSMO reproduces the strong gradient in variability between the coastal site Mace Head (~6 ppm) and the continental site in central Hungary (~12 ppm), reflecting primarily differing contributions of synoptic variations on atmospheric CO₂. However, the absolute magnitude of the variations are not matched by our simulations, with COSMO consistently underestimating the observed variability.

Overall, the evaluation of the total atmospheric CO₂ concentration reveals a good agreement with the observations, both in terms of mean and variability. The low and positive bias at the Mace Head site, where the contribution of the background CO₂ component dominates, suggests that this component is overall well modeled and likely not responsible for the bias at the other sites. This bias is likely due to the superposition of biases in atmospheric transport (as argued

for the HUN site) and biases in the underlying boundary conditions for the fossil fuel emissions and/or terrestrial fluxes. Since the contribution of the oceanic fluxes is very small, this component can be excluded as an explanation. Unfortunately, we do not have observationally-based estimates of the fossil fuel or terrestrial biosphere components at the four sites discussed so far, requiring us to use data from other sites for further evaluation.

3.3.2 Fossil fuel CO₂ component

Estimates of the fossil fuel component in atmospheric CO₂ are available for our model simulation period from Lutjewad in the Netherlands (LUT, 6.35° E, 53.4° N, 1 m a.s.l.) (van der Laan et al., 2010; Bozhinova et al., 2014) and from Heidelberg (HEI, 49.417°N, 8.675°E, 116 m a.s.l.) (Levin and Karstens, 2007). Both estimates are based on a combination of concurrent CO and ¹⁴CO₂ measurements and represent the fossil fuel induced offset relative to a regional background. They are thus comparable to our modeled fossil fuel component, as this reflects the offset relative to the domain-wide background induced by the lateral boundary conditions. Lutjewad is located on the Waddensea dike in the north of the Netherlands, influenced by the highly populated and industrialized areas in the Netherlands and in northwestern Germany (Ruhr area). The Heidelberg station is located near an urban center with considerable fossil fuel emissions.

At the Dutch site LUT, the daily average fossil fuel CO₂ component simulated by our model compares well with the observations ($r = 0.73$, mean bias -4 ppm) (see Fig. 3.3a). Generally, the model reproduces the observed variability, especially in summer, when the fossil fuel CO₂ component is low owing to the deep mixing in the atmosphere. But the model underestimates the estimated fossil fuel CO₂ component substantially in winter. This may be due to several reasons. First, the model may transport signals too quickly out of the planetary boundary layer, which is a known problem of many atmospheric transport models under stratified conditions typical of wintertime (see also above) (Holtslag et al., 2013). Second, our wintertime emission inventory in the region might be too small, owing to, for example, our underestimating the strength of the seasonal signal in the time functions. Third, the observations might be biased high. One reason is that these reconstruction rely on a constant ratio between CO and ¹⁴CO₂, which may lead to an underestimation of the ¹⁴C-CO ratio compared to real values at some time of the year, and subsequently overestimation of the inferred fossil fuel CO₂ (van der Laan et al., 2010; Bozhinova et al., 2014).

At Heidelberg, our model captures the fossil fuel CO₂ component even better, particularly since the model has a very small mean bias of 0.75 ppm. Also the day- to-day and the seasonal variations are well represented with a correlation coefficient of 0.72. The model's (small) overestimation of the fossil fuel component may be due to our prescribing all emissions at the surface, while the fossil-fuel fired power plants that contribute substantially to the fossil fuel CO₂ at this site tend to have an effective emission height quite some distance above the ground due to the

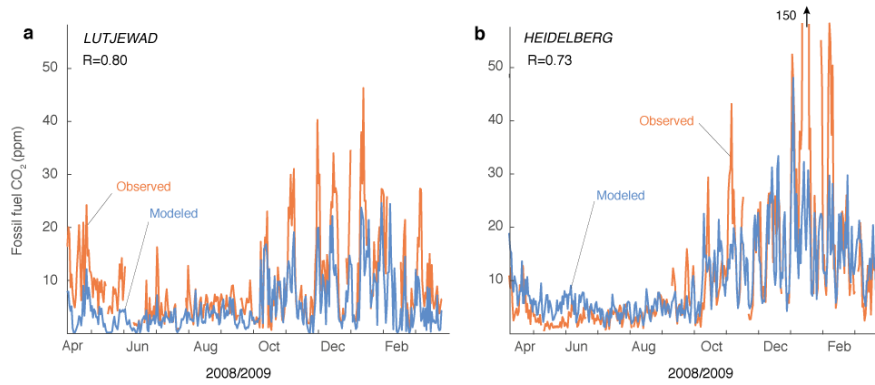


Figure 3.3 Comparison between modeled and observation-based estimates of the fossil fuel CO₂ component. (a) Comparison at the Lutjewad site in the Netherlands (LUT, 6° 21'E, 53° 24'N, 1 m a.s.l.) (van der Laan et al., 2010; Bozhinova et al., 2014). (b) Comparison at Heidelberg (HEI, 49.417° N, 8.675° E, 116m a.s.l.) (Levin and Karstens, 2007). The observational estimates are based on concurrent observations of CO and ¹⁴CO₂.

height of the stacks and the additional rise of the buoyant plumes (Vogel et al., 2013). Another reason might be an overestimation of the emissions in our emission inventory EDGAR - an explanation furthered by EDGAR's emission being higher than those of IER (Peylin et al., 2011). Especially assuring, and particularly so in comparison to the situation at LUT, is the COSMO model's ability at HEI to capture most of the variability and amplitude of the fossil fuel component in winter. An exception are the observations from late December and early January, where the data include a number of exceptionally high peaks. These peaks may be the result of very strong local trapping of the emitted fossil fuel CO₂ by e.g., a local inversion situation, i.e., a process that our model cannot properly resolve.

Despite these discrepancies, the good to excellent evaluation results provide us with good confidence to use our COSMO-7 based system to investigate the spatio-temporal variability of the fossil-fuel CO₂ in central and southern Europe. It is particularly encouraging to note the good agreement not only for the fossil fuel CO₂ component, but also for total atmospheric CO₂. The presence of an overall negative bias in the total atmospheric CO₂ in the absence of such a bias in the fossil fuel component suggests that the bias comes from the terrestrial biospheric component. This could be due to our VPRM-based estimates of the net fluxes being too negative as suggested by Oney (2016), i.e., suggesting a too strong sink for central and southern Europe, or for our model simulating a too small diurnal and/or seasonal rectification effect (Denning et al., 1995), i.e., a too small correlation between the time variations in the terrestrial exchange fluxes and atmospheric transport/mixing. This deficiency does not impact our results much, since our focus will be on the spatio-temporal variability of the fossil fuel CO₂ signal.

Table 3.1 Evaluation of COSMO-7 based simulations of the atmospheric CO₂ concentration at 4 European sites (locations are shown in Figure 1). The comparison are shown for the 3 hourly means between 12 to 18 PM local time for the period April 2008 through April 2009. m.s.a.g.is the height above ground or relative height.

Station	characteristics	m.s.a.g(m)	S.T.D. obs(ppm)	S.T.D. mod(ppm)	Correlation	Bias(ppm)
Cabauw (CBW, Netherlands)	tower	20	11.46	11.80	0.78	0.72
Cabauw (CBW, Netherlands)	tower	60	10.86	11.06	0.77	0.27
Cabauw (CBW, Netherlands)	tower	200	9.35	8.19	0.74	0.88
Puy de Dome (PUY, France)	mountain top	10	7.83	7.65	0.75	0.85
Hegyhatsal (HUN, Hungary)	continental	10	12.08	9.42	0.8	4.0
Hegyhatsal (HUN, Hungary)	continental	48	11.51	9.32	0.8	4.04
Hegyhatsal (HUN, Hungary)	continental	115	10.69	8.72	0.8	3.86
Mace Head (MHD, Ireland)	coastal	15	6.26	3.87	0.81	-0.34

3.4 The spatiotemporal pattern of the fossil fuel CO₂

3.4.1 The spatial pattern

In the annual mean, computed from data from all times of the day, the fossil fuel component of atmospheric CO₂ in the surface layer (~10 m above ground) amounts to more than 10 ppm across wide swaths of central Europe (Fig. 3.4a). In large metropolitan areas, such as in western Germany (Ruhrgebiet), Berlin, London, Paris, and Milan, the annual mean fossil fuel component exceeds even 30 ppm. To first order, the distribution of the surface fossil fuel CO₂ reflects the distribution of the emissions (see Fig. 3.1), suggesting a somewhat limited efficiency of atmospheric transport and mixing to disperse the signal laterally. In mountainous regions this is clearly

a consequence of topographic constraints; elsewhere this is largely a result of the strong spatial gradients in emissions, which remain conserved in the annual mean due to the overall diffusive nature of the dispersion. Nevertheless, a substantial amount of the emitted CO₂ is being transported away, leading to a sizeable fossil fuel CO₂ signal extending far into the oceans surrounding Europe, especially the North Sea.

Despite this lateral transport, the relatively good conservation of the spatial gradients in emissions sets our results distinctly apart from previous studies, where the fossil fuel CO₂ signal was modeled to be very smooth in space and on average also substantially smaller. For example, compared to the results obtained with the medium-resolution (0.5°) Regional Model (REMO) (Peylin et al., 2011), one can detect in our simulations nearly all major metropolitan regions and other fine-scale features, such as individual fossil-fuel fired power plants (e.g., in eastern Germany). This is primarily the result of the high horizontal and vertical resolution of COSMO permitting this model to conserve the spatial gradients well. This good conservation is particularly well illustrated when considering snapshot distributions of the fossil fuel CO₂ for individual seasons (Fig. 3.5). This figure also shows the strong impact of the transport and dilution by the diurnal variations of the planetary boundary layer, whose impact is particularly strong in summer.

For much of Europe, the fossil fuel component is the dominant contributor to the spatial gradients in annual mean atmospheric CO₂ (Fig. 3.4b-d). In many places it accounts for nearly all of the spatial gradients, with the contribution of the background and the terrestrial biospheric component being substantially smaller. The latter shows gradients up to 10 ppm (Fig. 3.4c), while the background signal does not exceed a few ppm (Fig. 3.4d). In the big cities, the fossil fuel CO₂ component represents even a sizeable fraction (10%) of the total CO₂ concentration. This dominance of the fossil fuel component together with its highly patterned nature owing to the many point sources leads to a hotspot pattern in the near surface map of total atmospheric CO₂ over much of Europe (Fig. 3.4b). However, due to lower emissions in southwestern Europe, the fossil fuel CO₂ signal is less strikingly visible there compared to central Europe, while the biospheric signal is stronger. This results in a relatively uniform spatial pattern of atmospheric CO₂ across Europe (Fig. 3.4b). Also the relatively low CO₂ concentrations in the mountain regions, such as the Alps, Apennines, Pyrenees and central France, reflect the much lower contribution from the fossil fuel component.

Naturally, when investigating the column averaged dry air mole fractions (X_{CO_2}), i.e., the property typically measured by remote sensing from a satellite, the annual mean gradients of the fossil fuel component are much smaller than those seen at the surface (see Fig. 3.6a). This is a consequence of the lateral gradients being much weaker aloft, owing to a more effective transport and mixing. As a result, most of the hotspot nature seen in the surface concentration pattern is blurred in X_{CO_2} . Also the magnitude of the signal is much weaker. While the surface signal of the fossil fuel CO₂ signal amounted to more than 30 ppm in strong emissions regions, the signal in the column averaged annual mean X_{CO_2} hardly exceeds 2 ppm. The impact of

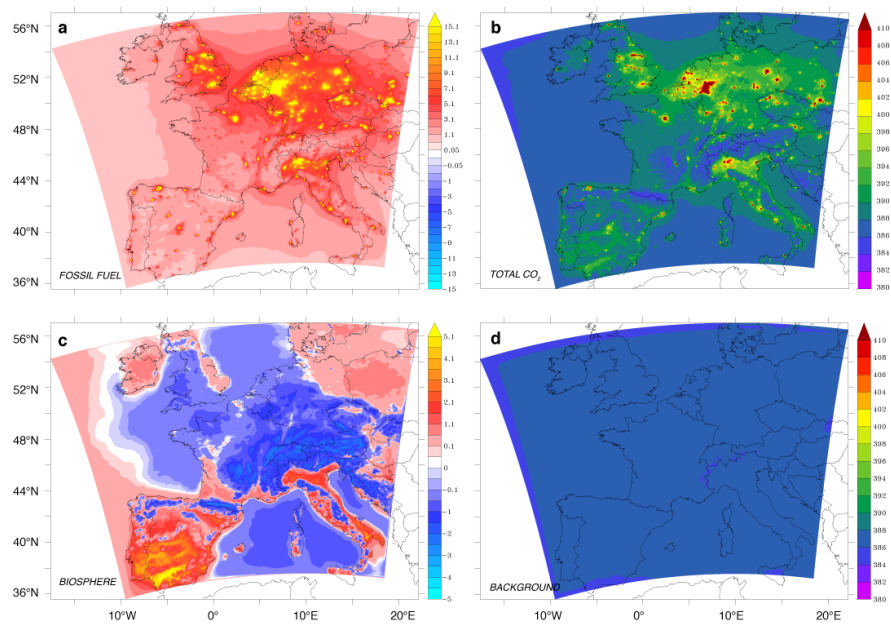


Figure 3.4 Maps of the model simulated annual mean components of atmospheric CO₂ in the surface layer (10 m above ground). (a) fossil fuel component, (b) total atmospheric CO₂, (c) terrestrial biosphere component, and (d) background CO₂ component. The results are shown as dry air mole fraction with units of ppm.

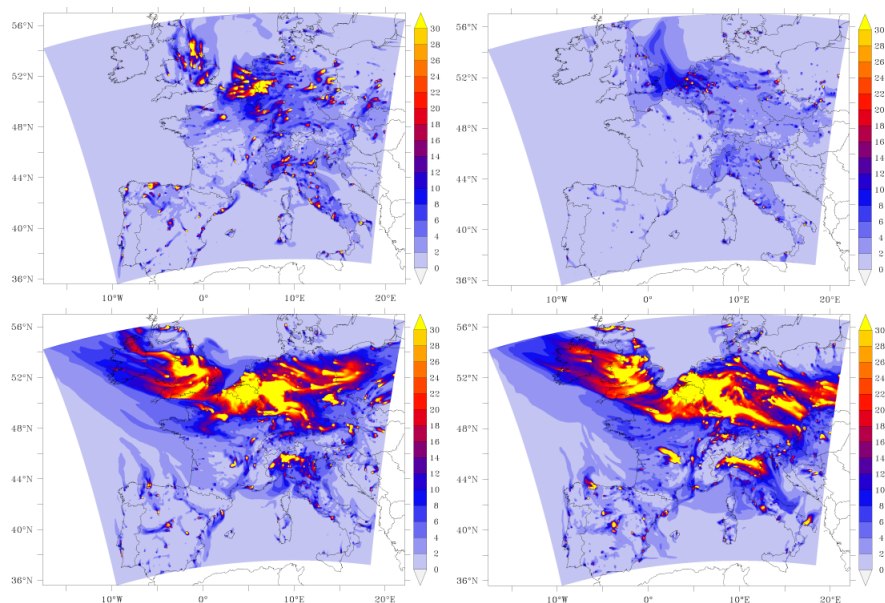


Figure 3.5 Instantaneous snapshot of the model simulated fossil fuel CO₂ in the surface layer. (a) Snap shot on July 1st at 06 00 GMT, (b) as (a) but at 18 00 GMT, (c) snapshot on January 1st at 06 00 GMT, (d) as (c) but at 18 00 GMT.

the predominant westerly air-flow becomes much more obvious in the column averaged dry air mole fraction X_{CO_2} , with the fossil fuel component revealing a clear eastward increase that is substantially stronger than the gradient in the underlying emissions.

The relative dominance of the fossil fuel component over the other components of atmo-

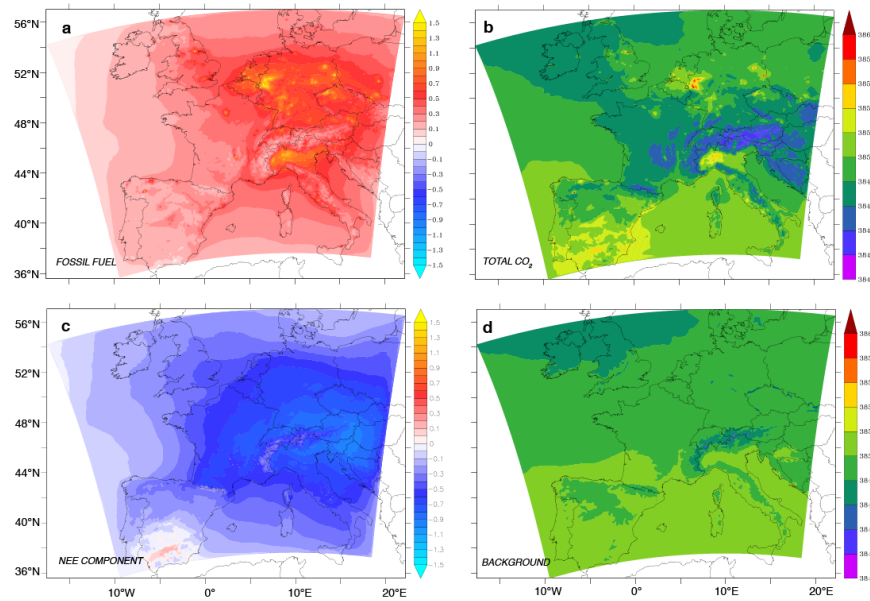


Figure 3.6 As Figure 3.4, but for whole air column averaged dry air mole fraction in units of ppm

spheric CO₂ is much weaker when considering the column averaged dry air mole fraction of CO₂ (see Fig. 3.6b-d). As a result, the total X_{CO_2} is made up of three relatively equally sized contributions, with the fossil fuel CO₂ signal continuing to dominate the X_{CO_2} variations in the major metropolitan areas. Contrary to the annual surface pattern, where CO₂ tends to increase eastward, the highest X_{CO_2} are found in southwestern Europe with a trend toward lower values going eastward. This is partly a consequence of the lateral boundary conditions for atmospheric CO₂, which tend to lead to the advection of high background CO₂ into the domain from the southwest. But the most important reason is the strong negative terrestrial biosphere signal over Europe, reflecting the sizeable carbon sink in European forests in the last decade (Reuter et al., 2016, in press). Interestingly, the relatively uniform negative distribution for X_{CO_2} contrasts with a more patterned biospheric signal in the lowest atmosphere (Figure 3.4c), where the strong negative signal is restricted to central Europe, while much of southern Europe has a positive annual mean biospheric signal. The likely reason for this difference is the biospheric rectification effect (Denning et al., 1995), which tends to lead a vertical redistribution of CO₂, i.e. positive values in the lower atmosphere and negative ones aloft. In most of Europe, this rectification signal is relatively small in comparison to the annual mean biospheric component, so that the latter determines the overall signal. But in southern Europe, where the biospheric fluxes tend to be smaller in magnitude and in the annual mean to be near zero, the rectifier effect can dominate, explaining the positive signals in the surface layer (Figure 3.4c) and simultaneously the negative signals when the biospheric signal is integrated vertically (Figure 3.6c).

3.4.2 The temporal variability

The temporal variability of the fossil fuel CO₂ signal at the surface is very large, leading to a standard deviation around the annual mean of 30 ppm or more in the hotspot regions (Figure 3.7a). These hotspots correspond largely to the regions of highest emissions (Figure 3.1). But this high variability is not only a result of the temporal variability of the emissions, but arises also from the interaction of variability in atmospheric transport and mixing with the strong lateral gradients seen in the snapshot figures (see Fig. 3.5).

A similar pattern of variability is seen in surface atmospheric CO₂ (Figure 3.7b), suggesting that the fossil fuel CO₂ is a major determinant not only of the annual mean spatial distribution of atmospheric CO₂, but also of its temporal variability. This is confirmed by Figure 3.8a, which shows the relative contribution of the fossil fuel CO₂ signal to the temporal standard deviations of atmospheric CO₂. In many places, particularly in Europe's major metropolitan areas, but also in many urban areas across Europe, the fossil fuel signal dominates the variability in atmospheric CO₂. But the high fossil fuel contribution is not limited to the urban areas. In fact, the region delineated by having a 50% contribution or more extends over much of northern central Europe, including the North Sea (see Fig. 3.8a).

In order to better understand the origin of the strong variability, we decomposed the variability into seasonal, synoptic and diurnal contributions. The seasonal variation component was derived by averaging the data on a monthly basis and by subtracting the annual mean. The synoptic component was then computed by subtracting from the data the time series of the monthly means and then forming daily averages of these deseasonalized data. Finally, the diurnal variability was derived by subtracting the seasonal and synoptic components from the data.

This decomposition reveals that the contribution of the fossil fuel CO₂ to the total variability of atmospheric CO₂ varies greatly depending on the temporal scale considered (Figure 3.8). While the fossil fuel contribution is comparably small on seasonal timescales (Figure 3.8b), the contribution on synoptic and particularly on diurnal timescales is actually very large, exceeding 60% across nearly the entire northern part of central Europe (Figure 3.8c-d). The small contribution on the seasonal timescales is the result of the dominance of the seasonal cycle of the biospheric fluxes in most of Europe. An exception are a few places in northern Europe and in the very south of our European domain. We interpret this to be caused primarily by the relatively strong seasonality of the fossil fuel emissions in these regions, owing to the strong summer-time requirement for cooling in the south and the strong winter-time demand for heating in the north.

The pattern of the fossil fuel contribution on synoptic timescales is very similar to that of the total contribution, meaning its contribution is one of the dominant contributions to the total temporal variability. This is consistent with synoptic variations also being among the strongest contributors to atmospheric variability, owing to baroclinic waves and frontal systems being formed

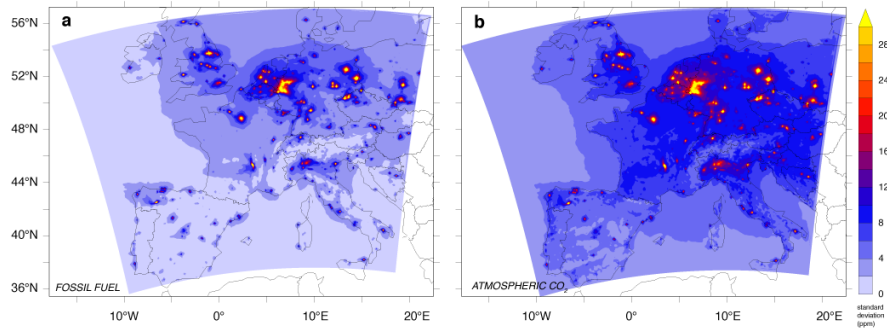


Figure 3.7 Maps of the annual standard deviation of (a) the fossil fuel component and (b) atmospheric CO₂ in the surface layer.

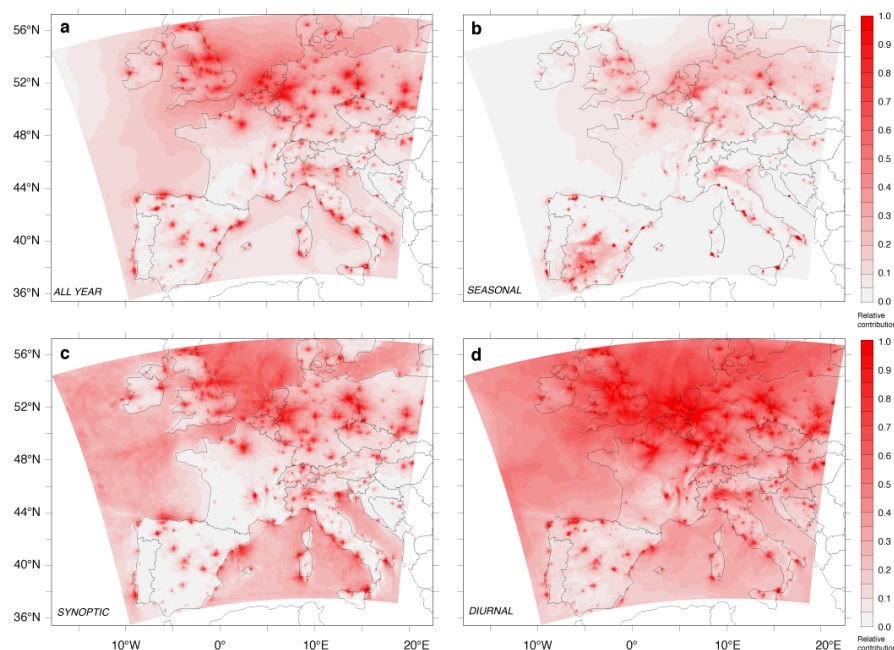


Figure 3.8 Maps of the contribution of fossil fuel CO₂ variability to total atmospheric CO₂ variability on various timescales in percent. (a) Contribution over all timescales; (b) contribution for the seasonal timescale only; (c) contribution for the synoptic timescale only; (d) contribution for the diurnal timescale only.

out of the strong baroclinicity that characterize the mid-latitudes. These synoptic weather events transport the emitted CO₂ also quite efficiently outside the main metropolitan areas, explaining the widespread signal of the fossil fuel contribution to the total variance of atmospheric CO₂. Even larger than the fossil contribution to synoptic variability is the contribution on the diurnal timescale, with the fossil fuel CO₂ contributing more than half of the variability over most of Europe. This high variability comes from the interaction of the diurnal variability of the fossil fuel emissions, with the strong diurnal variability of atmospheric transport, particularly the diurnal mixing of the planetary boundary layer. This co-variability between fossil fuel emissions and atmospheric transport exceeds that between the biospheric fluxes and atmospheric transport over the entire year, owing to the latter fluxes being large and relevant only during the spring/summer period, while the fossil fuel emissions are relatively high during most of the months of the year,

particularly close to the sources.

3.5 Discussion

The analyses of the results raise a number of questions that we would like to discuss next. First, why is the diurnal variability so high, and in particular, what is the contribution of our consideration of diurnal (and seasonal) variations in CO₂ emissions on the simulated fossil fuel CO₂ signal? Further, is there an impact beyond the variability, e.g., on the mean fossil fuel CO₂ signal? Second, what is the contribution of the various sectors on the fossil fuel CO₂ signal and in what way do emissions from one country influence the fossil fuel CO₂ signal in another country? Third, how can we use the insights gained from the study of the fossil fuel CO₂ signal to develop optimal strategies for detecting changes in fossil fuel CO₂ emissions? We discuss each of these three questions next.

3.5.1 The impact of variations in fossil fuel emissions on atmospheric CO₂

In order to elucidate the role of the temporal variations in fossil fuel emissions on the fossil fuel CO₂, we contrast the results of our standard simulation with time-varying emissions with those where the fossil fuel emissions were kept constant over time. The annual emissions are identical for the two cases, but the time constant case has, on average, considerably higher emissions in summer and at night.

The contrast between these two cases shows only a small change in the high diurnal variability of atmospheric CO₂ seen in Figure 3.8d, implying that the contribution of the diurnal variations in fossil fuel emissions is less important than other factors (results not shown). The largest contributions are found around some of the large metropolitan areas (e.g., London, Paris, Milan), but they do not exceed 10%. Thus the majority of the diurnal variability in the fossil fuel CO₂ stems from the diurnal variations in atmospheric transport and mixing acting on the strong horizontal gradients in emissions.

While not contributing much to the diurnal variability in the fossil fuel CO₂, the consideration of the time-varying emission matters quite substantially for the annual mean distribution of the fossil CO₂ signal. Figure Fig. 3.9a reveals that the annual mean fossil CO₂ signal in the simulation with time varying emissions is substantially lower over wide swaths of Spain, Italy, the Benelux countries, (western) Germany and the UK compared to the simulation where fossil fuel emissions were kept constant. The strongest negative signals are found close to the strongest emitters in these countries, with magnitudes exceeding several ppm. But the magnitude of the signal does not correspond to the magnitude of emissions, since regions with comparably low

emissions such as Spain, have signals that are as large as those in high emission regions of the Netherlands. The relatively large signals in southern Europe are likely due to the stronger PBL dynamics in these regions throughout the year in comparison to central and northern Europe. Some regions also have a positive signal from the time-varying emissions, such as parts of France and northeastern Germany. Thus the interaction between the variations in fossil fuel emissions and the variations in atmospheric transport and mixing leads to a substantial net signal in atmospheric CO₂, even though the total emissions in both cases are identical.

This net signal represents a fossil fuel-driven rectification effect (Zhang et al., 2016) in analogy to the rectification effect associated with the terrestrial biosphere (Denning et al., 1996; Larson and Volkmer, 2008), i.e., a signal that is due to the co-variance of emissions and atmospheric transport/mixing. Its (mostly) negative sign emerges from the fact that when the emissions are large, e.g., during the day, the transport and mixing away from the surface is strong, diluting the fossil fuel signal in atmospheric CO₂. In contrast, when the emissions are small, e.g., during the night, the transport and mixing tends to be weak. Taken together, this results in a more efficient dilution of the emissions in the time-varying emission case compared to the time-invariant case, thus explaining the mostly negative sign of the fossil fuel rectification effect.

This explanation is supported by the mostly positive correlation between the height of the planetary boundary layer (PBL) and the fossil fuel emissions, since the height of the PBL is a direct measure of the magnitude of the dilution in the lowest levels of the atmosphere (Figure Fig. 3.9b).

But there are a number of notable exceptions. For example, wide swaths of northeastern Germany and Poland and some places in central France have a positive rectification signal. Further, there are places where the co-variation of fossil fuel emission and the PBL is negative, yet the fossil-fuel rectification effect is still negative (e.g. the Ruhr valley region in western Germany), suggesting that our explanation does not cover all aspects. In response, one first needs to recognize that not only PBL but also other temporally varying phenomena, such as local atmospheric circulation patterns (e.g. mountain winds, sea-breezes) can lead to co-variability between emissions and transport/mixing, creating a rectification signal that can differ in sign. The contribution of the sea-breeze can be identified quite clearly by the strong negative sign along most of the coastline between southern Europe and the Mediterranean. Second, the local timing between the growth and decay of the PBL and the emissions can be quite different, owing in part, to the substantially different time functions for the different emission categories and their different local contributions (Figure 3.1). For example, in regions with a large contribution from road transportation, the local emissions have a strong peak in the early morning hours, when the PBL is still shallow, leading to a high signal there, while emissions are lower when the PBL is at its maximum in the early afternoon. This would create a positive rectification signal. Finally, in certain places, also the seasonal rectification appears to play a role, i.e., the seasonal co-variations of the emissions with the PBL height. In fact, in many places the magnitude of the correlation between

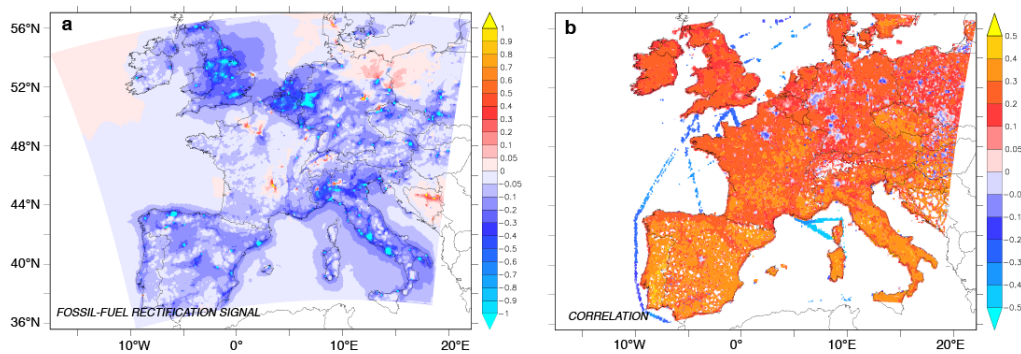


Figure 3.9 Maps of the impact of the consideration of time-varying fossil fuel emissions. (a) Difference in annual mean surface CO₂ between the case with time varying and time-constant fossil fuel emissions. This difference represents the fossil fuel rectification effect. (b) Linear correlation between the fossil fuel emissions and the height of the planetary boundary layer height in the COSMO-7 model. Pixels with emissions smaller than $0.06 \text{ gC m}^{-2} \text{ yr}^{-1}$ are not plotted. The positive correlation implies high emissions when the PBL is deep, and vice versa. Most of this correlation stems from the diurnal time-scale, but the correlation is enhanced through the (mostly) positive correlation also on seasonal timescales.

emission and PBL height on seasonal timescales exceeds that on diurnal timescales. This seasonal variation is particularly large for residential heating, which is maximum in winter when the PBL is low, leading to a positive seasonal rectification. This effect likely contributes to the negative correlations between emissions and PBL height in large urban centers such as Paris (Figure Fig. 3.9b). We suspect that such seasonal effects are also the primary reason for the positive rectification signal in northeastern Germany and northern Poland. In southern Europe, these seasonal co-variations tend to lead to a negative fossil-fuel rectification effect, since the emissions peak in summer (Figure 3.2b), when the PBL height is at its seasonal maximum.

The magnitude of the fossil fuel rectification effect is smaller than the rectifier effect induced by the exchange fluxes with the terrestrial biosphere (Zhang et al., 2016), but still quite substantial. Thus, the fossil fuel rectification effect clearly needs to be taken into consideration when modeling the atmospheric fossil fuel CO₂ signal, highlighting the need to use and apply accurate time functions. Our results thus clearly support the results of Nassar et al. (2013), who demonstrated the substantial impact of the consideration of time-varying emissions on atmospheric CO₂. We extend their result by demonstrating an effect on the annual mean fossil fuel CO₂, suggesting that special attention needs to be given to the relative timing of variations in atmospheric transport and mixing and fossil fuel emissions. Our results confirm the recent findings by Zhang et al. (2016) who demonstrated the fossil fuel rectification effect for the first time in a global model. Their signal is locally smaller than ours, owing to their using a much coarser resolution model, but they also show that the sign of the fossil fuel rectification effect tends to vary between timescales, with the diurnal being primarily negative, while the seasonal rectification effect being positive. This supports our explanation for the positive signals in northeastern Germany and northern Poland.

3.5.2 Fossil fuel CO₂ signal from different sources

Near the surface, the fossil fuel emissions from a particular region create a distribution that stays mostly within the region of origin (see Fig. 3.10 a,b). The fossil fuel CO₂ is highly concentrated near the localized areas of high emissions and then drops off quickly by distance with an e-folding spatial scale of a few hundred kilometers. As a result, the fossil fuel signal tends to be relatively small outside the region of origin, rarely exceeding 1 ppm in contrast to the > 20 ppm signal close to the sources. The different magnitudes of the fossil fuel CO₂ signals from different regions largely reflects the total emissions, but also the emission intensity, i.e., the emission per unit area. For example, with a total emission of 0.59 Pg CO₂ yr⁻¹, Germany is the biggest source of fossil fuel CO₂ within Europe, nearly double that of the second biggest emitter, i.e., France, yet Germany is almost half the size of France, resulting in a considerably higher emission intensity over Germany.

A different picture emerges when considering $X\text{CO}_2$, i.e., the column averaged dry air mole fraction CO₂. After having been transported aloft, where the fossil fuel signal can be much more readily dispersed, the imprint of the emissions of any particular region to the fossil fuel CO₂ within another region is actually quite large (Figure 3.10 c,d). In a small country, such as Switzerland, only 20% of the fossil fuel signature in $X\text{CO}_2$ above its territory stems from emissions within, while the contribution of Germany alone is 21% and that of France 18% (Figure 3.10). A similar distribution of sources is found for other small countries, such as Austria. In contrast, the fraction of the territorial emissions to the total fossil fuel signal is quite a bit larger for large countries/regions, such as France or Germany. In the latter case, more than 50% of its total fossil fuel CO₂ signal stems from emissions within, with 4 countries contributing most of the remainder. The countries/regions with high overall emissions contribute, of course, also most strongly to the fossil fuel CO₂ signal in other countries, with Germany contributing 18% to the signal in France, 11% to that in Italy and 20% to that in the Netherlands. Owing to its lower total emissions, France just contributes 9% to the signal in Germany and 8% to that in Italy. Thus, as is the case with classical air pollution, the fossil fuel CO₂ does not stop at the national borders, but extends to continental scales.

Among all the processes, the CO₂ emissions from power plants dominate the fossil fuel distribution, with concentrations reaching up to 16 ppm in the northern part of the domain (see Fig. 3.12). The point-source nature of this emission sector is clearly visible in the surface distribution, as is the spatially distinct distribution owing to the large differences in power production in the different countries of central Europe. While France has very few fossil-fuel fired power plants as a result of its high reliance on nuclear and hydroelectric power plants, Germany, Italy, the Netherlands and Poland rely strongly on coal- and gas-fired power plants for their electricity production. This leads to a highly heterogeneous fossil fuel CO₂ signals of the power plant sector. In total, this sector contributes 31.8% to the total fossil fuel CO₂ signal in central Europe, which is slightly smaller than its contribution to emissions (32.8%). This small difference emerges from

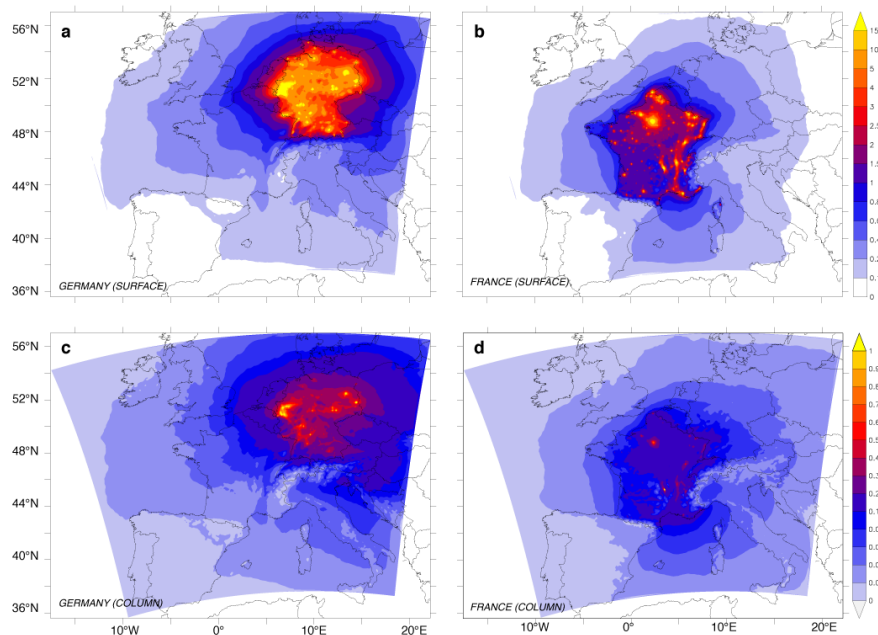


Figure 3.10 Maps of the annual mean fossil fuel CO₂ generated by different countries/regions. (a) Surface pattern created by the emissions from Germany, (b) as (a), but for the France. (c) Column averaged pattern created by the emissions from Germany, and (d) as (c), but for France.

the somewhat stronger loss of the signal across the lateral boundaries from this sector relative to the signal from the other sectors.

The second largest fossil fuel CO₂ signal is generated by the emissions from the road transportation sector (22.0%) (Fig. 3.12d), with this share actually being somewhat larger than its share in total emissions (21.1%). The transportation sector signal is very smooth, owing to the distributed nature of the emissions from this sector (see also Fig. 3.1).

The CO₂ signal from the industrial and residential sectors are more granular than that from the transportation sector, but still not as distinct as the power plant sector, as there are less country specific policies impacting the CO₂ emissions from these sectors. The emissions and consequently the CO₂ signal largely follow population density. The residential sector (mostly heating) contributes 18.1% to the total fossil fuel signal in atmospheric CO₂, slightly larger than the emissions from the industrial sector (17.4%). These two shares in the signal very nearly reflect their shares in total emissions. The emissions from the ‘other’ sectors (e.g., shipping, waste incineration, etc) is smaller, in comparison (10.7%), but not negligible.

The relative contribution of the emissions from the different sectors to the fossil fuel CO₂ vary strongly by region (Fig. 3.13). Clearly, close to major fossil-fuel fired power plants, this sector dominates, but elsewhere, any of the four major sources can take the leading role. For example, in Switzerland, Paris, and London, the emissions from the residential sector dominate the signal, while over much of southern and western Europe, the transportation sector dominates. The industrial sector dominates the signal in a few hotspot areas, where its emissions are high, but where there is no major fossil fuel fired power plants nearby.

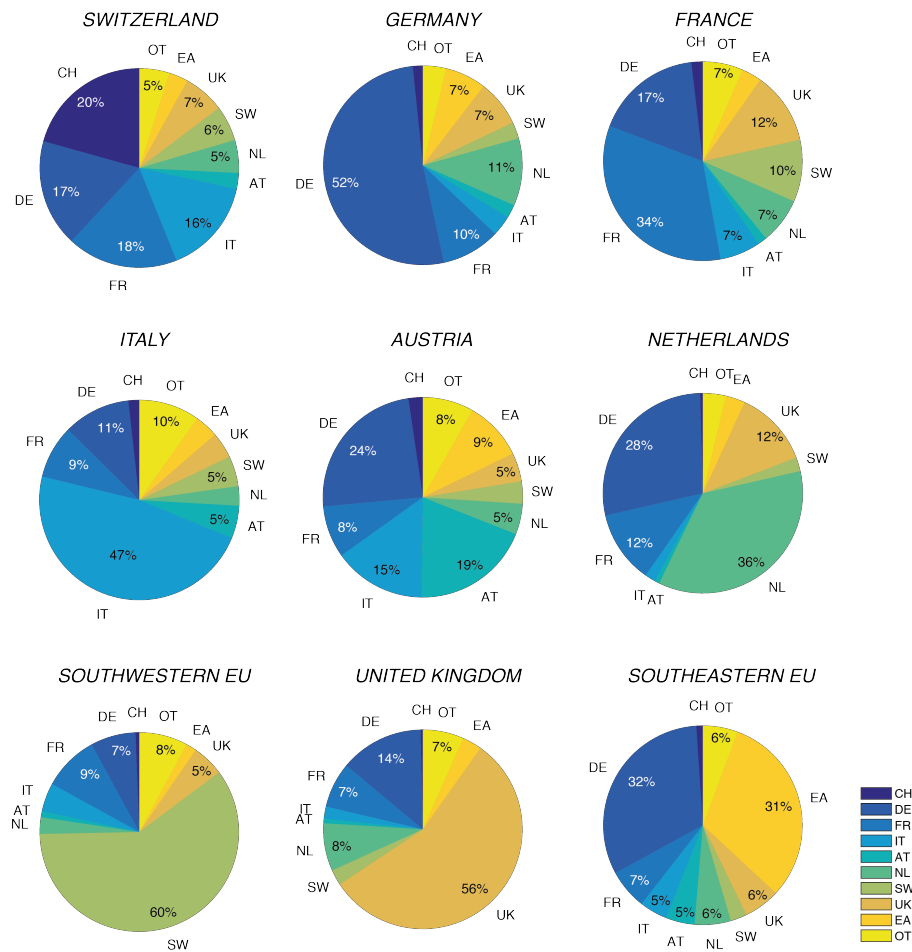


Figure 3.11 Pie charts depicting the origin of the fossil fuel CO₂ signal for each country/region. The percentages represent the contribution of each country/region of origin to the total fossil fuel signal in the averaged over the air column. The pie chart for Switzerland reveals, for example, that only 20% of the fossil fuel CO₂ signal over its territory stems from its territorial emission. Here, CH: Switzerland; DE: Germany; FR: France; IT: Italy; AT: Austria; NL: Netherlands; SW: countries in southwest of the domain; UK: United Kingdom; EA: countries in eastern domain; OT: the rest of countries.

These high spatial variations in the relative contribution puts the findings of Vogel et al. (2013) into a spatial context, as they reported for the Heidelberg site a dominance for emissions from power plants (28%), while the transportation sector contributed only 15%. This is a typical value for much of western Germany, reflecting the relative contribution of the different emission sectors (see also Fig. 3.1). But the contributions are very different, for example, for the CarbCount CH sites in Switzerland (Oney et al., 2015). At Beromünster, the transportation sector dominates over the other sectors, with nearly 70% stemming from this sector alone, while the contribution from power plant emissions is very low at this site, since Switzerland does not operate any fossil fuel power plants.

These large differences in the relative contribution from the different emission sectors have major implications for the analysis of the fossil fuel CO₂ and how it may change in response to mitigation measures. For example, these large differences will lead to substantial spatial gradients in the CO to CO₂ ratio in the fossil fuel signal, as the different emission sectors have very different

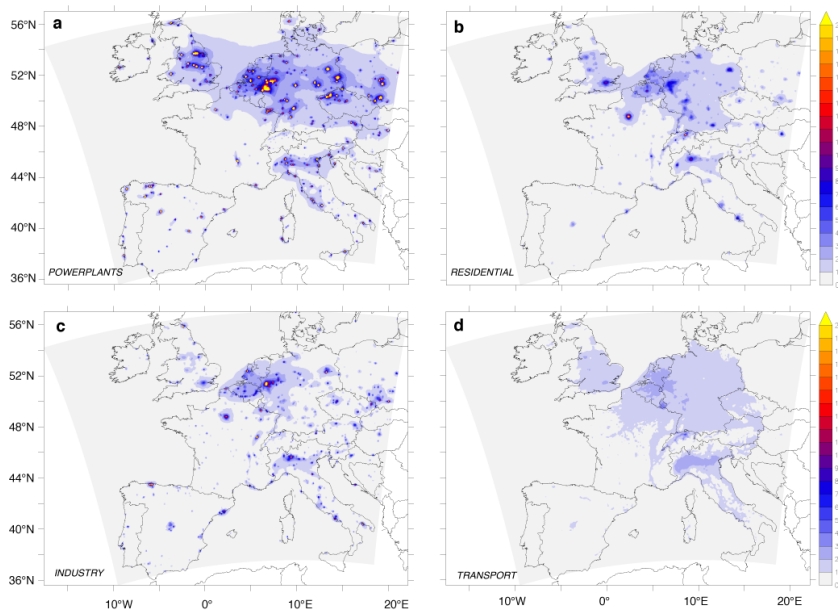


Figure 3.12 Maps of the annual mean surface fossil fuel CO₂ stemming from different sectors in units of ppm. (a) fossil-fuel fired power plants, (b) residential heating, (c) industrial processes, and (d) road transportation.

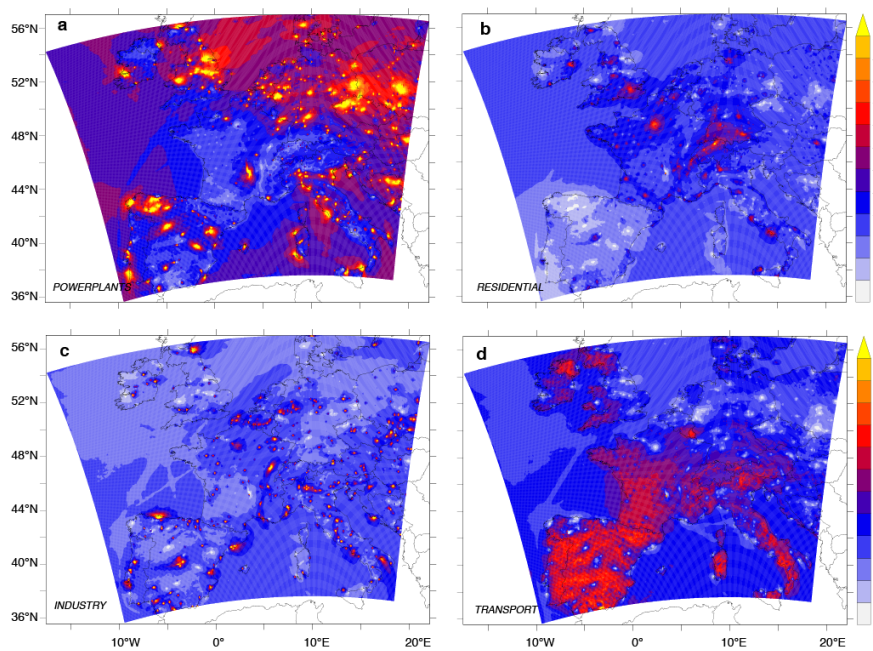


Figure 3.13 Maps of the annual mean relative contribution of each sector to the total surface fossil fuel CO₂. a) fossil-fuel fired power plants, (b) residential heating, (c) industrial processes, and (d) road transportation.

CO to CO₂ emission ratios. Since CO is often used to identify the fossil fuel component from atmospheric CO₂ observations, these variations need to be carefully disentangled in order to properly diagnose the fossil fuel component. The strong variations in the contributions from the different sectors thus adds a substantial amount of uncertainty to the CO method (Oney, 2016; Vardag et al., 2015). A second consequence concerns the detection of changes in emissions from

the different sectors. Thus, with the transportation sector contributing little to the very large fossil fuel signal in much of the northeastern part of our domain, reductions in this sector will be difficult to discern in that region. In contrast, the high relative contribution of the transportation sector to the total signal in southwestern Europe makes it actually quite feasible to detect mitigation measures in this sector in that part of Europe, even though the overall signal might not be that high.

An important caveat of our simulations is the fact that the effective height of the emissions above surface was not considered, but rather all CO₂ was released into the lowest model level. As a consequence, the surface CO₂ signals from elevated stack emissions from power plants and residential heating are likely biased high relative to those from the transportation sector. Given the large contribution from power plant emissions, it will be important to accurately consider the effective emission height (including plume rise) in future simulations, a point that was also raised by Vogel et al. (2013).

3.5.3 The response of atmospheric CO₂ to an emission reduction

According to their intended nationally determined contributions filed with the United Nations Framework Convention on Climate Change (UNFCCC) in late 2015, the European Union and its member states have agreed to a binding target of an at least 40% domestic reduction in greenhouse gases emissions by 2030 compared to 1990 (<http://www4.unfccc.int/Submissions/INDC/Published%20Documents/Latvia/1/LV-03-06-EU%20INDC.pdf>). A major question driving international policy making is to what degree such a reduction can be verified through independent means, such as through the monitoring of atmospheric CO₂ (Ciais et al., 2014, 2015). To address this question, we conducted several sensitivity experiments to investigate how various reductions in the magnitude and types of emissions affect not only the annual mean fossil fuel CO₂ signal, but also its variability. The goal is to determine whether reduced fossil fuel emissions might be detectable by current and future observing systems, especially satellites.

Since CO₂ is a conservative tracer in the atmosphere at the time scales considered here, a uniform reduction in the emissions leads to a uniform and directly proportional reduction of its current distribution, i.e., a 30% reduction of total fossil fuel emission would simply lead to a 30% reduction of the fossil fuel CO₂ signal at the surface (Fig. 3.4a) and throughout the atmospheric column (Fig. 3.6a). Concretely, the fossil fuel CO₂ would be reduced by more than 4 ppm near the surface for vast stretches of central and northern Europe, with maximum reductions of 10 ppm or more in the emission hotspots (Figure 3.14a). This contrasts with the reduction in the averaged column annual mean XCO₂ amounting to just over 0.2 ppm in the regions where the surface decreases by 4 ppm or more (Figure 3.14b). A reduction of 0.5 ppm is reached in just a few isolated locations, generally characterized by a high density of point sources, primarily fossil-fuel fired power plants. Thus, given current measurement accuracies of better than 0.1

ppm for a ground-based observing network (Zellweger et al., 2016), a 30% reduction in the fossil fuel emissions is fundamentally easily detectable for such a system, although one needs to bear in mind the non-trivial task to separate the signal from the background variability. In contrast, such a reduction in the fossil fuel emissions is not trivial to detect by satellite observations for most regions (except around the big power plants) as it is very challenging to obtain and maintain accuracies better than 0.5 ppm by current space-based observing systems (Buchwitz et al., 2015). Furthermore, such high accuracies are only achieved when the data are averaged over large scales, i.e., order of 1000 km or more. Nevertheless, taking 0.5 ppm as the threshold for detection within a single pixel, a 30% reduction in fossil fuel emissions thus appears to be beyond the detectability, except for a few hotspot regions (Figure 3.14b). Even a 50% reduction would not be trivial to detect for a satellite-based system on the basis of changes in the column averaged dry air mole fraction.

Given these challenges, a potentially attractive second avenue for determining changes in fossil fuel emissions is the reduction in temporal variability of atmospheric CO₂ that goes alongside the reduction in the mean signal. This is particularly promising given the very high contribution of the fossil fuel CO₂ signal to the variability in atmospheric CO₂ (see Fig. 3.8). As is the case for the mean, the conservative nature of atmospheric CO₂ implies that a uniform reduction of the emissions will lead to a uniform and proportional reduction of the variability of the fossil fuel signal as well. However, this is not the case for the variability in total atmospheric CO₂, since co-variations between the fossil fuel signal and the signal from e.g., the terrestrial biosphere can lead to non-linear effects. For example, a negative correlation between the two components would lead to a situation where the variability of atmospheric CO₂ was smaller than that of the individual components. In such a case, a reduction of the fossil fuel emission would lead to a smaller decrease in variability than expected. If the two components were positively correlated, the opposite would occur, i.e., the variability in atmospheric CO₂ would decrease more than expected.

Near the surface, the reduction in the temporal standard deviation and in the mean have nearly the same amplitude for most places (Figure 3.14c). This makes the analysis of changes in the temporal variability indeed an attractive option to enhance the detectability of changes in fossil fuel emissions. This is much less the case for the annual mean XCO₂, where the standard deviation changes are in general much smaller than the changes in the mean, with just a few isolated places revealing changes in the standard deviation of 0.5 ppm or more that might be discerned by the current generation of satellites.

But in these isolated places, the analysis of the temporal variability might be an interesting option even for satellite-based measurement systems (Fig. 3.15). In those places, indicated by the green circles in (Figure 3.14c), the changes in the temporal standard deviation are very large. Even for changes in emissions of around only 30%, the changes would be detectable for current satellites (Fig. 3.15). But the number of such sites is very low across Europe, making this not a general, but rather a specialized option.

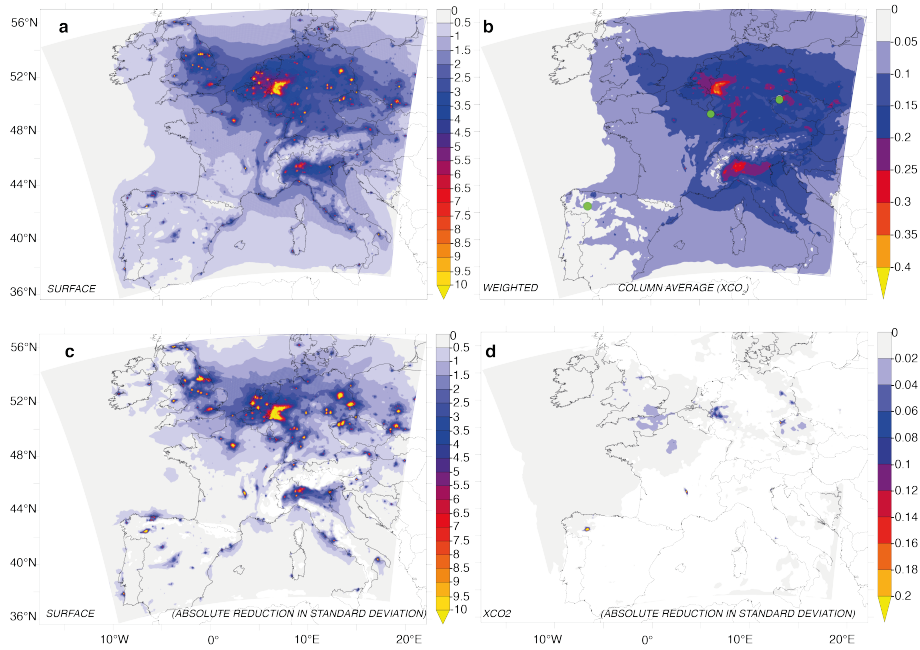


Figure 3.14 Changes in annual mean atmospheric CO₂ and its standard deviations resulting from a 30% reduction in the fossil fuel emissions from all sectors. (a) Change in surface mean CO₂. (b) Change in the column averaged CO₂, i.e., XCO₂. (c) Change in the standard deviation of surface CO₂ (all seasons). (d) Change in the standard deviation of the column averaged CO₂, i.e., XCO₂. The standard deviation refers to the differences of the afternoon data (at 1:00 PM) to the annual afternoon average.

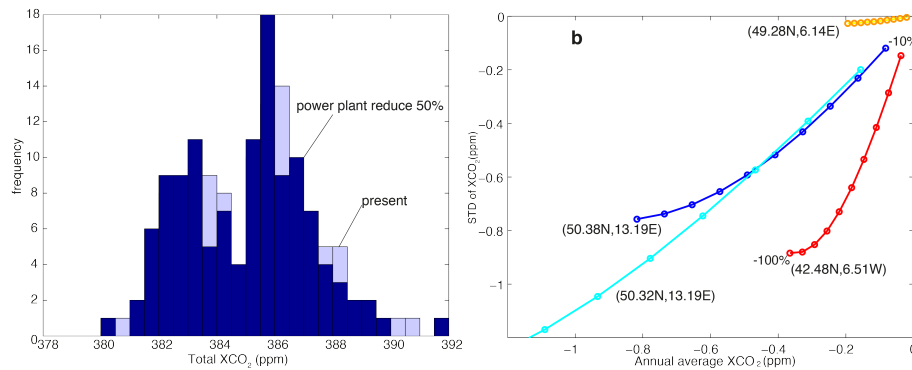


Figure 3.15 Impact of reductions in power plant emissions on the mean and standard deviation of the fossil fuel CO₂ signal . (a) probability density distribution of the surface atmospheric CO₂ for the present and for a case when the power plant emissions were reduced by 50% at a site in eastern Germany (50.32°N,13.19°E). (b) Relationship between the changes in the mean and the standard deviation of the column averaged CO₂ for a given reduction in power plant emissions, with different color representing representing different sites with different characteristics in their response to this reduction in emission: Blue (50.32°N, 13.19°E), Cyan (50.32°N, 6.59°E), Red (42.48°N, 6.51°W), Orange (49,28°N, 6.14°E) (Locations shown in Figure 14b with green circles).

The detection challenge is not simpler for other potential emission reduction scenarios, as outlined, for example in the EU roadmap (http://ec.europa.eu/clima/policies/strategies/2050/index_en.htm). A 50% reduction in the emissions from power plants alone (representing a reduction of the overall emissions by 16%), results in the mean surface concentration of atmospheric CO₂ going down by more than 2 ppm over large parts of northwestern

Europe, following the pattern of the surface signal of this sector (cf. Fig. 3.12a). Alongside we find a substantial reduction of the standard deviation of surface atmospheric CO₂ by more than 2 ppm in these regions, with the hotspots of power plant emissions seeing a reduction in the standard deviation of atmospheric CO₂ of 5 ppm or more. The reduction of the average annual mean column XCO₂ is much smaller than that of atmospheric CO₂ at the surface, amounting to little more than 0.2 ppm over wide swaths of northern Europe. The maximum reductions are of the order of 0.5 ppm in the proximity of large clusters of fossil-fuel fired power plants, i.e., generally too small to be detected. But, in these regions, the changes in the variability in XCO₂ is quite high, making this method again potentially attractive for detecting changes. In fact, in several regions, including some major cities, a 19% reduction of the fossil fuel emissions would result in a change of more than 0.5 ppm in the standard deviation, i.e., above detection level. This thus supports the findings of Pillai et al. (2016) that changes in fossil fuel emissions are fundamentally detectable over major cities or major point sources, but it also shows that this detection is very challenging.

The signals get even more difficult to discern if the emission reductions occur in individual sectors other than the power plants. For example, detectable signals by current generation satellites occur only if industrial emissions are cut by more than 80% or if residential emissions are cut by more than 90%. Also country level emissions are not trivial to be clearly detected. A reduction in Germany by 50% is potentially detectable by current satellites, with a maximum reduction of XCO₂ by 0.95 ppm. For most other countries, however, a 50% reduction in emissions is difficult to be detected.

All the analyses here relied on using the model output on all available days, i.e., we assumed perfect temporal coverage. This is overly optimistic, since cloud cover and other complicating factors (e.g., aerosol layers) will cause the coverage to decrease considerably, complicating the detection.

But regardless of this additional challenge, there is much additional information contained in high frequency observations of atmospheric CO₂. As we demonstrated above, the temporal variations are potentially highly useful for detecting fossil fuel emissions changes from various sources, especially those with a strong spatial granularity such as power plants or individual cities. For a routine monitoring of strong point sources, Velazco et al. (2011) therefore proposed a constellation of 5 satellites of type CarbonSat that combine imaging capability with a relatively wide swath (Bovensmann et al., 2010). Such a constellation would offer daily global coverage, though the presence of clouds would reduce the effective coverage considerably. As the precision and accuracy of satellite retrieved XCO₂ will improve in the future, that minimum change will go down as well.

3.6 Summary and conclusions

We have investigated the fossil fuel signal in atmospheric CO₂ over southern and central Europe using a regional high-resolution atmospheric model forced with temporally and spatially highly resolved variations in the fossil fuel emissions. The assessment of the modeled atmospheric CO₂ with in-situ measurements across multiple sites across Europe reveals good to excellent agreement on all timescales considered with biases of less than 1 ppm, with the exception of the tall tower site Hegyhatsal in central Hungary. The model is also able to capture the reconstructed fossil fuel component at two sites quite successfully. Although the model tends to underestimate the amplitude of the daily averaged fossil fuel CO₂ in winter, the simulation matches fossil fuel CO₂ from both sites very well most of the time, revealing the high quality of the transport model and reasonable time profiles of the fossil fuel emissions used as input.

Over much of Europe, the fossil fuel CO₂ is a dominant component of the spatial variability of atmospheric CO₂, particularly near the surface. In some places, it even contributes significantly to the total (including background) CO₂, up to 110% in large urban centers and power plant plumes. Also the contribution to the temporal variability is very substantial. Fossil fuel CO₂ makes a particularly large contribution at synoptic and diurnal time scales whereas the seasonal variability is dominated by biospheric activity. The influence is not only large over the hot spot regions of fossil fuel emissions, but also over large areas downstream. In case of diurnal variability, fossil fuel CO₂ is the dominant component over wide areas of northern and western Europe.

Temporal variability of the emissions has a non-negligible influence on annual mean fossil fuel CO₂ mole fractions near the surface, due to diurnal and seasonal rectifier effects. Differences between annual mean values with temporally variable and constant emissions can be up to a few ppm in the hot spot regions, but are mostly below 1 ppm elsewhere. This implies that temporal variability of fossil fuel emissions needs to be accurately represented for realistic simulations, confirming the results of Zhang et al. (2016). It is also important for reliably detecting fossil fuel emission changes from specific sources since different sources have different temporal profiles.

Simulating fossil fuel emissions from different countries and sectors suggests that the major part of the signal near the surface remains in the country of origin. Ground-based in situ observations are thus most sensitive to fossil fuel emissions from the country where they are located. A different picture emerges for column averaged dry air mole fractions (X_{CO_2}) as measured by satellites, for which the signal is much more dispersed. Only over Germany, the contribution from emissions within the country is larger than 50%, whereas over France the signal from neighboring countries dominates (66%). An important reason for these contrasting results seems to be the differences in electricity production, which mostly relies on nuclear power in France but on fossil fuels in its neighboring countries including Germany, UK and Italy. Over small countries such as Switzerland or the Netherlands, the contribution from abroad is typically the dominating component. Among all the processes, fossil fuel emissions from power plants contributes the most

(approx. one third) to the total fossil fuel signal of CO₂ both at the surface and in the column. However, the power plant signal at the surface is likely overestimated in our simulations, since all emissions were released into the lowest model level without considering the true elevation of the source. The signal from power plant emissions has a pronounced and distinct spatial pattern that provides us an opportunity to discern changes in from power plant emissions from changes in other sources.

Based on a number of sensitivity studies, we show that reductions in fossil fuel emissions not only leave a distinct signal in the time mean distribution of atmospheric CO₂, but also in its temporal variability. This opens potentially additional ways to detect and verify emission reductions. But this opportunity exists primarily for surface based measurement networks, while the satellite based systems that measure the column-averaged XCO_2 will see too small changes, in general, relative to their current measurement capabilities. An important exception are a few hotspot sites, where the satellites will be able to detect fairly modest changes of about 30% when assuming an accuracy of the satellite observations of 0.5 ppm.

As both satellite and surface measurements have advantages and disadvantages, combining surface measurements with satellite data and increasing the frequency and coverage of the latter will be the optimal path forward to enhance the possibility of detecting future changes in fossil fuel emissions.

Acknowledgements

This study was funded by the Swiss National Foundation (SNF) as part of the CarboCount CH Sinergia Project (Grant Number: CRSII2 136273). Additional funding was provided by ETH Zürich (YL and NG) and Empa (DB). We thank the Center for Climate Systems Modeling (C2SM) and especially Anne Roches for providing extensive support. We acknowledge MeteoSwiss for the provision of their operational COSMO analysis products. The computations were done on the supercomputers of the Swiss National Supercomputing Centre (CSCS). We are very thankful to the principal investigators responsible for the Mace Head (MHD) station in Ireland, for the SNO-ICOS-France station Puy de Dome (PUY) in France, for the Hegyhatsal station (HUN) in Hungary, and for the Cabauw station (CBW) in the Netherlands for making their data publically available. We are also grateful to Dr. Sander van Der Laan and Dr. Felix Vogel for sharing their estimates of the fossil fuel component at Lutjewad and Heidelberg, respectively. Furthermore, we are very grateful to Prof. Woulter Peters, Wageningen University, for providing the CO₂ global model boundary conditions and to Dr. Christoph Gerbig for providing the VPRM biospheric flux data.

Chapter 4

CarbonTracker Switzerland: Evaluation of the transport model COSMO and tests of the high-resolution atmospheric CO₂ inversion system with synthetic data

Abstract

The confidence one has in the biospheric flux results from an atmospheric CO₂ inversion hinges critically on two aspects: Fidelity of the atmospheric transport model, and robustness of the method. The latter requires a well-tested inversion system, whose critical elements are well identified and understood. In this chapter, we pursue these two tasks by first evaluating the high-resolution atmospheric transport model COSMO using observed CO₂ at a diverse set of central European sites, and then testing thoroughly the CarbonTracker Switzerland system with synthetic data.

To evaluate the model, we simulate atmospheric CO₂ for the year 2013 using the central European COSMO-2 grid with 7 km resolution. As boundary conditions, we use the fossil fuel emissions from MeteoTest and EDGAR with the time functions developed in chapter 3, hourly resolved land biosphere flux estimates from the Vegetation Photosynthesis and Respiration Model (VPRM) model, and background CO₂ data from CarbonTracker EU. The modeled atmospheric CO₂ matches the observed CO₂ from the four CarboCount CH sites, from Jungfraujoch and from two sites in southern Germany and northern Italy excellently, both in amplitude and variability with biases of less than 1 ppm, and correlations exceeding 0.8 for all seasons. An important exception is the Gimmiz site, whose location makes it prone to very local influences that are not well captured by our model. This good agreement in CO₂ across several sites suggests that COSMO is a well suited transport model for atmospheric CO₂ inversion studies.

In the second part of the study, the ensemble Kalman filter-based CarbonTracker Switzerland system is then thoroughly assessed and tested with synthetic observations obtained from the forward simulation conducted in the first part. In the standard setup, despite strong perturbations to the initial prior flux estimates, CarbonTracker Switzerland is able to recover the "true" fluxes in most of the regions in the domain, i.e., the biospheric fluxes used in the forward simulation. Alongside, the inversion was able to reduce the error by 80%. Next, we tested the system with regard to the following elements: (i) network size, (ii) localization methods, (iii) inversion method, (iv) errors in the fossil fuel footprint, (v) errors in the background CO₂, and (vi) errors in both background and fossil fuel. The background errors were not added in a random manner, but using an autoregressive model whose parameters were fit from the mismatch between the observations and the model results analyzed in the first part.

Regarding the network size, the results reveal that 5 sites are enough for retrieving fluxes with less than 10% error inside the footprint, and 8 sites are enough for removing most of the prescribed error from scaling factors or uncertainties of fluxes in the domain except for the western region. The tests for different localization methods reveal very little impact. Nevertheless, for a more robust result for the cropland ecoregion inside the footprint, the CT2007 localization method is recommended.

In contrast, the fluxes inside and outside of the footprint are much more sensitive to the inversion method, with the percentage based inversion giving around 20% more error reduction and 10% less posterior error than an ecoregion dominant based inversion.

Results from the sensitivity tests to assess the impact of the background biases indicate that the cropland ecoregion inside the footprint and the deciduous forest ecoregion in the northern part of the domain suffer the most from background CO₂ biases. For more robust posterior fluxes, especially for the cropland ecoregion, longer spatial and temporal correlations (1 month) are needed in order to remove the biases in the background CO₂. Under current settings, i.e., not adopting longer correlations, the percentage inversion method (optimizing the fluxes eco regions based on their coverage of percentage in the pixel) was able to correct for a background error with a standard deviation 2 ppm very well.

The biases from fossil fuel have an influence on the posterior biosphere fluxes only in summer (with an error of around 8% of the true fluxes), with less to no influence in the other seasons. However, this influence from fossil fuel uncertainties is relatively weaker than the influence from background CO₂ biases. The tests of combining NEE error, fossil fuel error and background error imply that the fossil fuel error and background error dominate the NEE error in the posterior results.

4.1 Introduction

While atmospheric CO₂ inversion-based estimates of the global land uptake and its large scale distribution tended to converge in recent years (Ciais et al., 2010; Peylin et al., 2013), large uncertainties exist with regard to the fluxes at the regional scale, with different estimates showing substantial discrepancies. Perhaps this is, in part, a result of this being a newer type of inversion for which the community has gained less experience so far. But there are several distinct elements that differentiate regional inversions from global ones (see also introduction), making them more demanding on the one hand, while making them also possibly less error prone, on the other hand.

The first differentiation is the error associated with the atmospheric transport model, which tends to be accentuated on regional scales compared to global ones. But the much higher resolution transport models that are being used for regional inversions tend to reduce also the spatio-temporal representation error, i.e., the mismatch between the modeled spatial and observation scales (Peylin et al., 2013). Nevertheless, the transport error tends to dominate. In response, several methods have been developed for dealing with this source of error (see (Ciais et al., 2010; Carouge et al., 2008; Baker et al., 2006; Steinkamp, 2011; Kretschmer et al., 2012)). Of particular importance is the work from high resolution atmospheric transport models at regional scale in the framework of ACT-America (<http://act-america.larc.nasa.gov/science.html>), which has focused on the quantification of the transport uncertainties in atmospheric models and on developing methods to decrease them. They show in a synthetic experiment, for example, that the transport model error could be controlled artificially and that the impact of errors in the background or fossil fuel on the inverted result could be separated and investigated. Also Lauvaux et al. (2009) and Broquet et al. (2011) recommended methods for calculating the model error or uncertainties by using result from ensemble statistics or stable tracers as reference for model transport errors.

Modeling the atmospheric transport is particularly challenging in complex terrain where the topography requires the model to adequately reconstruct mesoscale flow patterns around mountains and valleys, or along coastline. Historically, and particularly in global-scale inversions, atmospheric CO₂ data from mountain tops tended to be excluded, or statistically less weighted (larger uncertainty). Also a stronger temporal data filtering was applied to these sites, making the improvement in the mismatch between observation and model mainly restricted to the flat regions (Geels et al., 2007). But this is clearly not an option for regional scale inversions, where the objective is to estimate fluxes also in regions with mountainous terrain. In a method called spatial localization and widely adopted in the weather forecasting community, some of the problems arising from transport errors have been addressed by decreasing the background error covariance terms, such that at some good distance, the errors at two sites are no longer correlated (Gaspari and Cohn, 1999) or there is no correction from the system (Lauvaux et al., 2012) in order to extract the correct information from observation sites. Kang et al. (2011) extended on this concept

and showed that their variable localization algorithm is able to improve estimations, especially when the surface fluxes change with time and when the transport model error becomes significant. Zupanski et al. (2007) introduced the covariance localization method into a Maximum Likelihood Ensemble Filter using a distance function defined in the information space and claimed that the system could work very well even with a small ensemble size. These methods were primarily applied over flat regions with rather homogenous land cover, not over complex mountain regions. We will test different localization methods at complex mountain region in this study.

The second major problem that gives rise to inconsistencies at the regional scale are the errors associated with the CO₂ boundary inflow conditions as they have been shown to substantially shift the posterior spatial pattern and amplitude (Göckede et al., 2010; Gourdjji et al., 2012). In certain cases, biases in this signal, commonly referred to as the background CO₂, rival the magnitude of uncertainty due to the posterior fluxes. Thus, the precise definition of the advected background CO₂ mixing ratios is paramount for inverse modeling frameworks operating on regional to continental scales (Lauvaux et al., 2012). Various methods were adopted to alleviate the bias from background CO₂ in regional inversion systems, pre-processing of the boundary conditions or the use of observed boundary conditions directly as observations in the inverse system. A mean correction could be applied to remove this background error, or the sensitivity to error was simply tested by adding arbitrary values to test the potential limits of the influence (Göckede et al., 2010). Using a constant correction can not capture the dynamics of the variability of the background CO₂ error, which might bias the inverted fluxes at short time scale, and potentially at longer time (synoptic scale) periods for the regional inversion system. In other studies, aircraft profile measurements were used to correct potential biases in the lateral background conditions (Lauvaux et al., 2012; Schuh et al., 2013). The fast and slow changes in the inflow errors were considered in these studies, i.e., the hourly correction, or the correction at the synoptic scale. However, the aircraft measurements are generally available for only short time period. In addition, none of these studies consider the autocorrelation of the residuals between the modeled and observed background CO₂ at the scale of the these inflow errors and calculate their influence of the carbon budget.

Another issue in the regional inversion system is the error or influence from fossil fuel emissions, because global or continental inversion systems could avoid the influence of fossil fuel emissions by choosing far field measurements site. However, regional inversions are more sensitive to errors in fossil fuel emissions, particularly given its fine-grained pattern and its temporal evolution (see also chapter 3). Although some studies show that different time profiles for the fossil fuel emissions do not affect the inverted fluxes (Göckede et al., 2010), these results were obtained for a region with relatively low emission intensity. In contrast, Peylin et al. (2011) showed that for a region like Europe, where the emission intensity is generally high (chapter 3), different fossil fuel inventories substantially affected the inverted net biospheric flux results. To investigate whether the fossil fuel CO₂ errors have influence on the inverted net biospheric fluxes, we use ensemble of fossil fuel CO₂ with a spread that represents their uncertainty to investigate

the influence of fossil fuel CO₂ emission errors on posterior fluxes.

Finally, there is uncertainty associated with the assimilation method itself, largely the aggregation error originating from the tiling of the land surface into a number of discrete regions (irrespective of whether these are based on geography or ecoregions or something similar) (Kaminski et al., 2001). The solutions for this problem are either the adoption of smaller tiles, e.g., going all the way to a pixel-based assimilation, or the balancing between smoothing error and aggregation error, or using a similarity matrix to reduce the aggregation error (Turner and Jacob, 2015). Tolk et al. (2011) and Meesters et al. (2012) highlighted the importance of a pixel-based inversion and the precise specification of the land surface properties for a local scale inversion system. But the very large degrees of freedom of a pixel-based inversion would lead to instabilities in the solutions without some form of regularization. This is achieved by the definition of covariances between the pixels, i.e., by generating off-diagonal structures in the prior error correlation or error covariance matrix (Wu et al., 2011). This effectively reduces the degrees of freedom substantially, but does not solve the issue that a pixel-based inversion has a very large covariance matrix that leads to the need for very substantial computational resources in order to minimize the cost function.

Despite the fundamental superiority of a pixel-based inversion, at the end result might not be that different at regional scale. For example, Tolk et al. (2011) compared a pixel-based inversion for the Netherlands with one that tiled the land surface into ecoregions and showed that there is no significant difference of the mismatch between modeled and observed CO₂ between the two inversion systems. That is why we will not use pixel method given the no significant improvement and smoothing error brought by too many unknowns. Instead, we limited ourselves to an eco region based inversion.

A further issue to which regional-scale atmospheric inversion systems are likely more sensitive to than global-scale inversions is how subgrid scale variations in vegetation (eco)types or plant communities are dealt with. In most inversions undertaken so far, the flux in a grid cell was assigned to the dominant plant community, disregarding the contribution of the other plant communities in that grid cell. In coarse resolution inversion, this results in a nearly complete loss of important ecotypes, but rarely dominant ecotypes. This issue is somewhat alleviated in the regional inversions by the smaller sizes of the grid cells, but given the fine-grained patterning of the plant communities in many regions, these grid cells are still much larger than the typical length scale of a patch of a particular plant community. So far, it has not been determined, how large the potential error of this simplification is.

The objectives of this chapter are: i) to assess the fidelity of the high resolution transport model by evaluating the results with the observations from the CarboCount CH network in a complex topographic environment and quantify the transport and measurement error; ii) to assess how the assimilation system behaves at regional scale and how sensitive the system is to the various EnKF settings; and iii) to check how the background and fossil fuel error affects the

spatial and temporal error of the posterior fluxes.

First, we introduce the method and data, followed by the evaluation of the forward run. Then we show the results from sensitivity tests. Finally, we come to discussion and conclusion.

4.2 Method

4.2.1 Forward Simulation

The numerical weather prediction model COSMO is used as the observation operator, i.e., transport model, to convert the fluxes into the high resolution observation space. We provide a short summary here, while the reader is referred to chapter 2 for details. The model domain for CarbonTracker Switzerland is the same domain as the central European domain of MeteoSwiss, i.e., that of COSMO-2 but with a resolution of 7 km, covering the region from 42.72° N 2.25° E (lower left) to 49.76° N 17.25° E (upper right) with Switzerland in the center of the domain (Figure 4.1).

CarbonTracker Switzerland separately models the atmospheric distribution of a total of 53 CO₂ tracers, each covering one piece of the total information, and expressed as dry air mole fractions, i.e., CO₂. These tracers separately represent (i) the background CO₂ signal, (CO₂^{bg}) (ii) the fossil fuel signal, (CO₂^{ff}) (iii) the oceanic CO₂ signal (CO₂^{oce}), (iv) the signal of GPP from each considered ecoregion, i.e., CO₂^{GPP,r}, and (v) the signal of total ecosystem respiration from each considered ecoregion, i.e., CO₂^{ra,r}. The atmospheric CO₂ mole fraction is then computed by the sum of all components, with the GPP and respiration components being scaled with the respective scaling factors, $\lambda_{(r, \text{frac}, \text{GPP})}$ and $\lambda_{(r, \text{frac}, \text{ra})}$ (see equation 2.24).

The CO₂ concentration from CarbonTracker Europe (Peters et al., 2010) were used for the lateral boundary conditions, i.e., to constrain CO₂^{bg} at the boundaries. The fossil fuel emissions for CO₂ were generated by merging a relatively coarse emission inventory for the regions outside Switzerland (EDGAR v4.2, 10 km, (Janssens-Maenhout et al., 2012)) with a high-resolution (0.5 km) emission inventory for Switzerland. We used the same sector-based set of time functions described in chapter 3 to produce hourly emission flux densities for each grid cell of the model domain. These emission databases were developed for the year 2009. We scaled them uniformly in order to match the total fossil fuel emissions for the year 2013. Given the relatively flat emissions in the recent years, the required scaling was small. Not considered in our scaling are the potential shifts in the different sectors, leading to different spatial and temporal distributions. As the contribution of the oceanic CO₂ in our domain was very small, we set it as 0. For the different biospheric fluxes, i.e., GPP and total ecosystem respiration, we used the hourly terrestrial biospheric fluxes from the Vegetation Photosynthesis and Respiration Model (VPRM) (Mahadevan et al., 2008) with all optimization parameters, λ set to 1. The net biospheric flux, i.e., GPP minus

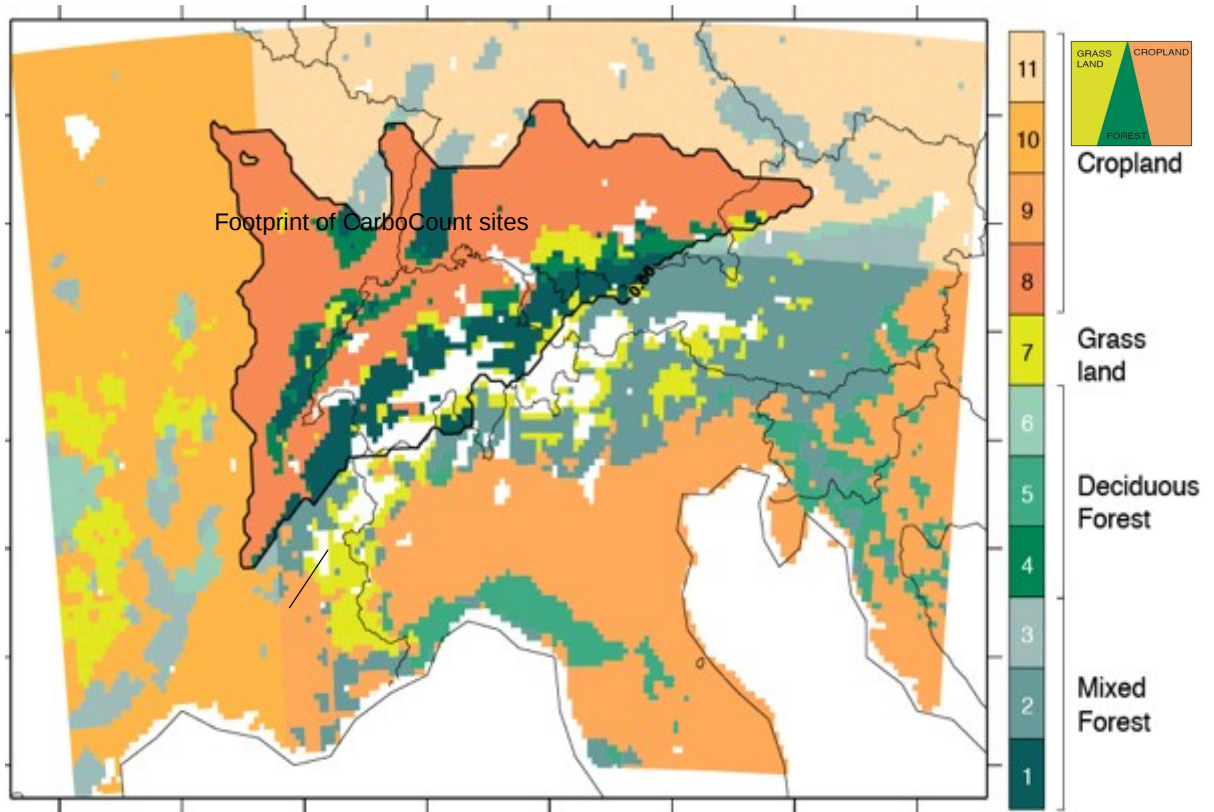


Figure 4.1 Map showing the simulation domain of COSMO-2 and the dominant ecoregions at each grid cell of the model: 1-3: Mixed Forest; 4-6: Deciduous Forest; 7: grassland; 8-11: croplands, white area: others. The darker colors indicate the ecoregions that are inside the footprint of the observing sites of the CarboCount CH network, with the footprint boundary shown as a black line. While only the dominant ecoregion is shown, the inversion actually considers the relative contribution of each ecoregion present in a grid cell. The white areas belong to the group of 'others', which is not solved for in the inversion as their CO₂ fluxes are very small.

total respiration corresponds to the net ecosystem exchange (NEE) flux.

The meteorological model was initialized with the archived COSMO-7 analyses undertaken by MeteoSwiss as part of its operational weather forecasting, and then the meteorological model was run forward without assimilation of any meteorological data, but using the lateral boundary conditions from the same COSMO7 analyses. The inverse simulation covers the period from Jan 1, 2013 until December 31, 2013 to coincide with the first year with full observations of the CarboCount CH network. The CO₂ tracers were transported online as passive tracers, with the initial fields taken from CarbonTracker EU.

4.2.2 Observations and synthetic data

In order to assess the model, we are using the atmospheric CO₂ observations for the year 2013 from the four CarboCount CH sites, i.e., Beromünster (BRM), Lägern Hochwacht (LHW), Fruebuehl (FRU), Gimmiz (GIM) (Oney et al., 2015). In addition, we will be using high quality observations from the other 5 CO₂ sites within our domain, namely Jungfrauoch (JFJ) (Oney et al., 2015), Schauinsland (SSL) in southern Germany, Monte Cimone (CMN) and Plateau Rosa (PRS) in northern Italy, and Sonnblick (SBN) in Austria (see Table in chapter 2 for details).

The synthetic data needed for testing the CarbonTracker Switzerland inversion system were generated by sampling the results from the forward simulation at the observing sites and heights in the same manner as the observations would do. To obtain the relevant atmospheric CO₂ concentration, we used equation 2.24 and set the scaling factors λ for each ecoregion r to unity. The sampled synthetic CO₂ data are assimilated using the CarbonTracker Switzerland system with the goal to optimize the biospheric scaling factors λ . These optimized λ are then compared with the "true" state, i.e., the $\lambda = 1$ value used to generate the synthetic data. This will permit us to directly evaluate the performance of the system with regard to the many decision elements that go into the inversion. The fundamental details of the system are described in chapter 2.

In order to better mimic reality and to challenge the inversion system in a more realistic manner, we added errors to the fossil fuel and the background signals. The error we added to the fossil fuel signal at each observing site was estimated on the basis of the spread of observation-based estimates of the fossil fuel signals (Oney et al., 2016, in review). Concretely, these authors estimated the fossil fuel signature at the CarboCount CH sites Beromünster and Lägern Hochwacht on the basis of the concurrently observed carbon monoxide (CO), using the CO observations from Jungfrauoch as an estimate of the background. The ensemble was generated on the basis of different assumptions about the CO:CO₂ ratio and different ways to generate the background signal. The uncertainty was estimated from the spread of this ensemble (Oney et al., 2016, in review). We took the fossil fuel CO₂ concentration at Lägern and Beromünster and fit the mean and standard deviation of the all the fossil fuel CO₂ concentration with a linear function at each site. The regression function at 2 sites are $\sigma_{\text{BRM}} = \mu_{\text{BRM}} * 0.07 + 0.52$ and $\sigma_{\text{LHW}} = \mu_{\text{LHW}} * 0.2 + 0.407$. σ and μ are the standard deviation and mean of the ensemble runs at different sites calculated by Oney et al. (2016, in review). Then the slope 0.07 and 0.2 are served as the standard deviation of the white noise at the measurement sites. We assume the uncertainties include the fossil fuel CO₂ uncertainties both from the transport models and the inventory dataset.

The error for the background CO₂ signal was estimated based on the model's performance at the Jungfrauoch site, whose elevation results in its CO₂ variations to reflect primarily variation of the background signal. Concretely, we simulated the error to mimic the statistics of the residual between the forward simulation and the observations at JFJ for 2013, i.e., the error is modeled to have the same variance and temporal autocorrelation. Concretely, the background biases were

generated by the following steps: 1) Calculate the residuals between the forward model and observations at JFJ; 2) Generate an ARIMA process for the error to get the variance, temporal autocorrelation length (5 days) and parameters ($P < 0.05$) based on the residuals from former step; 3) Simulate the error structure at other sites using the autocorrelation length and parameters from the former step. The resulting error estimate was then added to the synthetic observations.

4.2.3 Temporal autocorrelations

The scaling factors, λ in equation 2.24 are calculated based on the analysis from previous steps and the a-priori:

$$\lambda_t^f = \sum_{t=n-T+1}^{t=n} W_t(\lambda_t^a + \lambda^p) + G \quad (4.1)$$

where superscript a refers to the analyzed quantities from previous steps, superscript f refers to the background values for the new step, and superscript p refers to real a-priori values. λ^p is set to make sure the first term on the right side of function equals to 1.0 to ensure that the parameters in the system eventually revert back to the predetermined prior values when there is no information coming from the observations (Peters et al., 2005, 2007). n is the current time step (the time cycle relate to the very initial step of the simulation). Here T is determined by the temporal autocorrelation in the prior fluxes error structure, not just based on ad hoc method. Kountouris et al. (2015) and Broquet et al. (2013) showed that the temporal autocorrelation error of NEE in Europe is usually around 1 month. Hence, we adopted 1 month as the temporal correlation length, which is divided by the time cycle 4 days, resulting in $T=6$ in the 2-month test (the 7th 4-day time cycle is for λ^p). In former studies, a uniform weight was assigned to different time cycles, or the weights following some bias errors (Peng et al., 2014). Here we set W as the weight for different time cycle, based on the different contribution from different time cycle. In the base run, we follow what Peters et al. (2007) did, but tested additionally different weights from improvement or information from different cycles, where the total cycle number was deduced from the temporal autocorrelation window. G is the white noise for all ecoregions, with standard deviation of 0.9, except for the 12th ecoregion that contains the urban, snow, water, built-up, tree & grasses, and shrubs ecotypes, i.e., what we summarized as 'others'. This category is not optimized because of its low contribution to the prior terrestrial biospheric fluxes.

Next we elaborate on the specific choices made for the application of this system to invert atmospheric CO_2 observations from the CarboCount CH network. These choices include: (i) tiling the land surface into ecoregions, (ii) parameter settings with regard to the assimilation system, (iii) generation of the covariance matrices, etc.

4.2.3.1 Ecoregions

In order to tile the land surface into ecoregions, we used the same set of ecoregions as VPRM model with resolution of 12 KM. Since this land cover map used a different classification scheme from other methods, with the same ecoregion appeared in different patchy ecoregion types, some remapping was necessary. We merged the evergreen forests with the mixed forests since the former represents only a small fraction of the land cover in the domain. Further, we grouped a number of ecoregions with a very small land cover and very small biospheric CO₂ fluxes, such as lakes and cities into the group 'others'. In the end, we only retained the following five ecoregions: Mixed forest, deciduous forest, grassland, croplands and others. Taking advantage of the much higher resolution of the land cover map, we first created the ecoregion map at the full resolution of the land cover map, and then aggregated the information to the 7 km resolution of our inversion system, while retaining the relative contribution of each ecoregion to each grid cell, i.e., we explicitly account for the subgrid scale heterogeneity of the land cover.

We then split the broadly distributed ecoregions also geographically in order to reflect the fact that the four measurement sites of the CarboCount CH network, i.e., BRM, LHW, FRU, and GIM, have a footprint that can likely constrain only a part of the overall domain. We thus divided each ecoregion into a part inside the footprint of the CarboCount CH network, and a part that is outside. The boundary for this footprint was taken from the Lagrangian model-based footprint analysis of Oney et al. (2015). We further separated some forest types and the croplands outside the footprint into a northern, western, and southern part, in order to reflect the fact that the impact of fluxes from these regions barely overlap, i.e., to avoid the generation of an overly strong aggregation error. This resulted in the generation of 12 ecoregions (see Figure 4.1). The CO₂ fluxes from croplands dominate in our domain, with their contribution being almost 4 times larger than the second largest one from the deciduous forests.

4.2.3.2 Prior covariance matrix

Different methods have been used to calculate the prior error covariance for the scaling factors, including information from models, observations, and statistical considerations (Chatterjee et al., 2012; Chatterjee, 2012; Wecht et al., 2014; Turner and Jacob, 2015).

Here, we follow a spatial and ecoregion-based approach similar to the method of Lauvaux et al. (2009). Namely, we give a high correlation between the ecoregions inside the footprint and inside the same grid cell, or to the same ecoregions in different grid cells, but separated geographically. For example, a high correlation is assigned between the northern croplands (eco 10) and the western croplands (eco 11), while a low correlation is assigned between the northern croplands and the northern deciduous forests. To calculate the spatial correlation, we assumed that the correlation decreases exponentially with a scaling distance of 100km, which is on the

long side compared to other studies (Kountouris et al., 2015).

Lauvaux et al. (2009) kept one with minimum ecosystem fraction in the same grid for calculating the ecosystem-based correlation. As the minimum percentage in our grid is quite small, we keep the fraction parameters as 1 in the correlation function, which also help avoiding double counting the fraction parameters during the process of inversion.

We apply a space localization method in the construction of the prior covariance matrix, as this avoids spurious correlations between distant locations in the background covariance matrix caused by the limited ensemble size (Hunt et al., 2007; Peng et al., 2014). This method also reduces the impact of transport errors (Kang et al., 2011). Here, we compare two different localization methods and contrast them also with a case where no localization is used: the first method is that employed in CarbonTracker (van der Laan-Luijkx et al., 2017) (referred as CT2007), while the second method is the covariance localization method of Zupanski et al. (2007). A covariance localization means that the influence of any observation is confined to the area wherein the posterior covariance remains within a certain level of the prior covariance. Diverging from Zupanski et al. (2007), we do not consider the covariance inflation here.

4.2.3.3 Base inversion

In the base inversion, the synthetic data from the 8 observations sites within the domain are being used in order to recover the "true" biospheric fluxes, i.e., BRM, LHW, FRU, GIM, CMN, SSL, PRS, and SNB. To perturb the initial guesses for the scaling factors, we added a random perturbation (with standard deviation of 0.9 following a Gaussian distribution) to the scaling factors due to the much higher biospheric fluxes comparing to other data sources. In order for the base run to match the real case as closely as possible, we also added the errors for the fossil fuel and background components to the synthetic observations. This synthetic inversion was then run for one year with an ensemble size of 25 and with the other settings (such as smoother windows, etc.) given in Table 4.1.

Table 4.1 Settings of the base inversion.

Time cycles	7 days	Smoother window	2 days
Ensemble members	25	Unknown parameters	11
Time period	2013.01 - 12	Localization method	CT2007
Spatial correlation	100km	Prior Covariance error	0.64
Stddev. of perturbation	0.9	Number of sites for inversion	8

4.2.3.4 Sensitivity Experiments

Table 4.2 provides an overview of the sensitivity simulations that we explored in order to test the CarbonTracker Switzerland system thoroughly and to explore its sensitivity to the many choices associated with an atmospheric inversion. We ran the majority of the sensitivity cases for the 2 months of July and August 2013 only, to make use of the computational resources as efficiently as possible. Further, the NEE is largest during these months, so that we expect to see the biggest impact during these months.

For all simulations, biases and root mean squared error (RMSE) between the prior/posterior and the truth are used for judging the quality of the inversions. Overall, we ran three sets of sensitivity cases. In the first set, we did not consider the error in the background and the fossil fuel signal, permitting us to isolate the particular issue at hand in more detail. In the second set, we added just the background error, and in the third set, we just considered the fossil fuel error.

4.3 Atmospheric CO₂ variations over Switzerland and model evaluation

The forward simulation of atmospheric CO₂ and of its components reveals rich spatiotemporal variations both at the surface and aloft. In this first part, we investigate these variations and use them to evaluate the high resolution atmospheric transport model.

4.3.1 Model evaluation with atmospheric CO₂

To evaluate the model, the simulated results are compared with the four observation sites of the CarboCount CH network as well as with the 5 additional observing sites located within our domain, i.e., SSL, CMN, PRS, SNB, and JFJ. Here we choose only afternoon observations for the evaluation because this is the time of the maximum height of the planetary boundary layer. We thus minimize the potential transport error stemming from problems with the diurnal cycle in the PBL. This is standard practice, as the modeling of the PBL height is one of the persistent areas of model problems (Brunner et al., 2015).

The model captures the mean observed atmospheric CO₂ at the CarboCount CH sites very well with the exception of Gimmiz. At the well matched sites, i.e., at BRM, LHW, and FRU, the annual mean bias is less than 1 ppm (see Table 4.3 and Fig 4.2). The model is also able to capture the variability very well, with excellent agreement regarding the magnitude of the standard deviations, although with a very small tendency to underestimate it. Also the seasonal variations are mostly captured very well, leading to high annual correlations of between 0.86 to

Table 4.2 Summary of inversions with CarbonTracker Switzerland, including control and sensitivity tests.

Experiment	code	background error	fossil fuel error	site number	period(2013)	Comment
Control(with Background error, fossil fuel errors and NEE errors)	S1	standard	standard	8	Jan-Dec 26	standard simulation
Base:only NEE errors	S2	no	no	8	Jul-Aug 26	baseline with no error
Only NEE errors	S2.1	no	no	1-8	Jul-Aug 26	baseline to study network size
Only NEE errors	S2.2	no	no	8	Jul-Aug 26	baseline to study localization methods
Only NEE errors	S2.3	no	no	8	Jul-Aug 26	baseline to study no ecoregion subgridscale variations
Background NEE errors	and S3.1	standard	no	8	Jul-Aug 26	Background only, 100 km correlation
Background NEE errors	and S3.2	short/long corr	no	8	Jul-Aug 26	Background only, 30 (S3.21),300 (S3.22)km correlation
Background NEE errors	and S3.3	standard	no	8	Jul-Aug 26	Background only, 1 month temporal correlation,
Fossil fuel and NEE errors	S4	no	yes	8	Jan-Dec 26	Fossil fuel error only

0.90 (Table 4.3).

The model behaves best in spring, with smaller RMSE than other seasons at all measurement sites. In summer, all the new measurement sites have relative high RMSE comparing to JFJ, due to the strong local influence. The RMSE at BRM is almost the same as at FRU, might due to the

well mixed CO₂ at these two size in the summer afternoon that their influence overlay each other. The high RMSE in autumn and winter time are mainly from the not well captured fossil fuel CO₂ signals during this time period (see chapter 3).

The exception is the Gimmiz (GIM) site, where the annual bias is more than 4 times larger than at the other sites (not shown here), i.e., more than -4 ppm (not shown here). Due its location on top of a short water tower within a relatively flat area, this site has the smallest footprint of all sites (Oney et al., 2015). Further, due to its location within an area of intense agricultural activity and its proximity to urban emissions (the town of Aarberg is located only 2km away), this site is strongly influenced by rather local processes, making it the least representative site in our network to reflect the larger scale fluxes over the Swiss plateau (Oney et al., 2015). The role of the near field signals is readily seen in the higher standard deviation at this site, but particularly in the seasonal biases. In winter, the model has a mean bias of more than -17 ppm, reflecting primarily the underestimating of the local fossil fuel signal, likely owing to its underestimating the strength of the local stratification during this season, i.e., the model is not able to capture the very strong inversion conditions that often characterize this region in the fall and winter. Given this strong local nature of the signals at Gimmiz, we focus our evaluation subsequently on the other sites. We also will not include Gimmiz later in the inversion (see chapter 5).



Figure 4.2 Comparison of average CO₂ concentration in the afternoon (from 12:00 to 15:00 UTC) between observation and model in 2013 at 8 different sites.

The substantially better performance at the other CarboCount CH sites is also seen in their

Table 4.3 Comparison between observations and modeled CO₂ concentration in the afternoon (from 12:00 to 15:00 UTC). Unit for RMSE and std are ppm.

Site	LHW	BRM	FRU	CMN	SSL	PRS	SNB	JFJ
Lat	47.48	47.19	47.12	44.20	47.92	45.93	47.05	7.99
Lon	8.4	8.18	8.54	10.70	7.92	7.7	12.95	46.55
Height used(masl)	860	797	982	2165	1205	3480	3106	3580
Correlation Coefficient	0.86	0.89	0.9	0.78	0.89	0.94	0.90	0.88
Annual mean bias	-0.73	-0.43	0.98	-2.06	0.32	0.48	0.41	-0.23
Annual RMSE	6.5	4.98	5.55	3.9	4.94	2.04	2.64	2.27
Spring RMSE	4.90	4.14	4.78	3.75	3.63	1.76	2.1	1.76
Summer RMSE	6.32	5.35	5.41	4.9	5.49	2.77	3.41	2.86
Autumn RMSE	6.61	4.51	5.45	/	4.8	2.23	2.8	2.0
Winter RMSE	7.9	5.74	6.41	3.79	5.69	1.36	2.11	2.26
Annual std of model	12	10.33	11.68	4.95	9.77	4.84	5.05	4.49
Annual std of obs	12.32	10.86	11.9	5.5	10.47	5.52	5.90	4.75
Spring std of model	7.51	7.87	8.34	3.67	/	1.84	2.79	1.80
Spring std of obs	8.79	8.33	9.04	4.44	7.29	2.35	3.35	2.16
Summer std of model	5.15	4.59	5.20	6.99	5.48	4.52	4.25	4.31
Summer std of obs	6.09	4.78	4.92	3.2875	5.50	4.70	4.234	3.81
Autumn std of model	9.6	9.17	10.48	/	7.30	2.87	3.19	2.91
Autumn std of obs	11.07	10.61	11.54	/	8.95	3.96	5.15	3.68
Winter std of model	6.32	6.41	6.95	2.68	6.29	2.53	2.40	2.32
Winter std of obs	8.92	10.27	10.04	4.62	9.16	3.14	3.41	3.62

having much smaller seasonal biases compared to Gimmiz. But it is of note that the model tends to underestimate consistently the summer CO₂ concentrations at all CarboCount CH sites. As demonstrated also by Oney (2016), at least part of this comes from our employed ecosystem model (VPRM) likely overestimating net ecosystem exchange during summer.

The model performance at the other CO₂ observation sites within the model domain, i.e., at JFJ, SSL, CMN, PRS, and SNB is comparable to that at the CarboCount CH sites (BRM, LHW, and FRU), with also these additional sites confirming the negative model bias in summer, while not showing a comparable bias in the other seasons. This confirms our previous interpretation that most of the summer mismatch seems to stem from the biospheric signal, while the background and fossil fuel signals that dominate the winter variability are well captured. Further confirmation comes from the analysis of the modeled signal at Jungfrauoch, whose variability is primarily determined by the background signal (see below).

4.3.2 Spatiotemporal variability of CO₂

4.3.2.1 Contribution of different CO₂ components

To illustrate the relative importance of the contribution of the different components to the total CO₂ concentration, we show the time series at the Beromünster site, but note that the picture is very similar at the other sites (see Fig. 4.3). While the fossil fuel contribution clearly dominates in winter, the biospheric signal dominates the summer time variations, but with opposite signs. The figure also reveals the importance of the background signal, having a similar level of variability as both the fossil and the biospheric fluxes, highlighting how critical the accuracy of the boundary data is, especially as our model domain is relatively small.

The annual spatial pattern of the total CO₂ in central Europe is dominated by the fossil fuel CO₂ signal, as the magnitude of this component exceeds 5 ppm not only in the urban areas, but also across wide swaths of the domain (see Fig. 4.4) (cf. chapter3). In contrast, the distribution of the background CO₂ is rather homogeneous, although with substantial gradients. The reduction of the background signal toward the center of the domain is due to an increasing contribution of the background CO₂ from air aloft, which tends to have lower CO₂ concentrations (see below). The annual mean biospheric signal has a distinct bimodal distribution, with net negative signals over much of Switzerland, and the alpine arc, and net positive signals over much of the rest of the domain. This reflects not only the net annual fluxes that were prescribed by VPRM, but also the interaction between the seasonal cycles of the fluxes and the seasonal cycle of transport and mixing, i.e., the seasonal rectifier effect (see discussion of vertical distribution below).

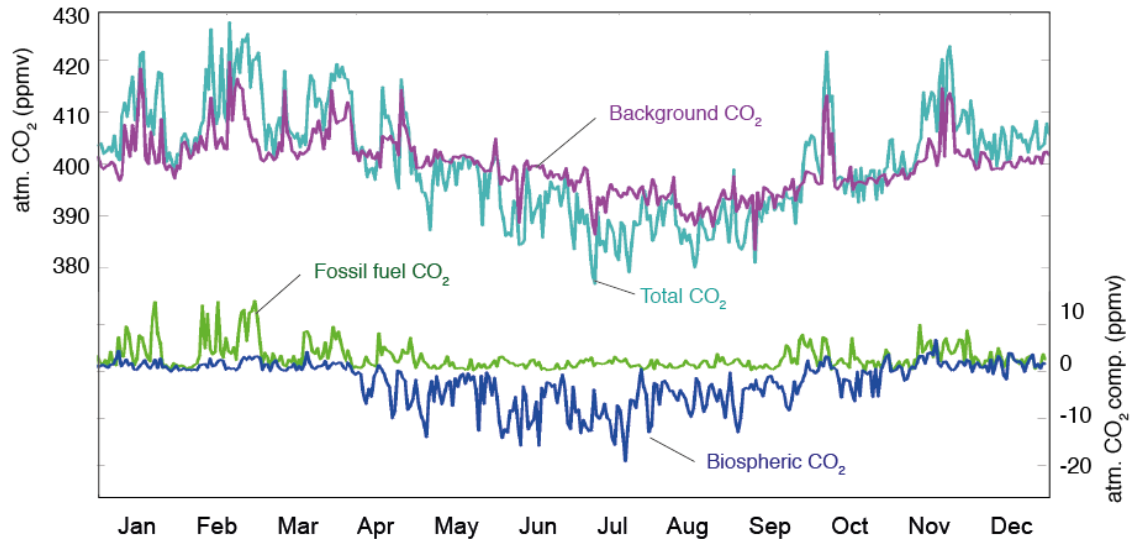


Figure 4.3 Time series of the different component contributing to atmospheric CO₂ (ppm) at daytime at the Beromünster site (selected from 12:00 to 15:00 UTC).

4.3.2.2 Diurnal and seasonal cycles

The dominant modes of variability in atmospheric CO₂ are the diurnal and the seasonal cycle. While we will not make use of the former in the atmospheric CO₂ inversion, it is nevertheless instructive to investigate how well the model is able to capture the diurnal ups and downs of atmospheric CO₂. We determined the mean diurnal cycle in the model and observations by simply bin averaging the data over the respective seasons. The seasonal cycle was determined by smoothing the daily averaged time series with a 1 month running mean filter. We depict the diurnal and seasonal cycles relative to Jungfrauoch (JFJ), as this permits us to retain the mean gradients between the different sites.

The modeled annual mean diurnal cycle of total CO₂ has the highest diurnal cycle at Lägern (~ 7 ppm, might be due to the underestimated sampling height from the model) and Gimmiz (~ 6 ppm), but the diurnal cycles at Beromünster and Frübüehl are also substantial (Figure 4.5a). The majority of the annual mean diurnal signal stems from the summer (Figure 4.5b), reflecting not only the very strong diurnal signal of the biospheric fluxes, but also the strong diurnal variations of the PBL, which tends to create concentration differences simply by controlling the degree of dilution of the surface signal with the concentrations aloft.

The stronger diurnal cycles at Lägern and Gimmiz likely reflect their higher exposure to the local biospheric fluxes, as discussed already for Gimmiz above. For Lägern, this is likely a consequence of it being located in the middle of a forest, i.e., its direct exposure to the strong variations in photosynthesis and respiration.

Overall, the modeled mean diurnal cycles compare reasonably well with those discussed by Oney et al. (2015), but also with some distinct differences. In summer, the model overestimates

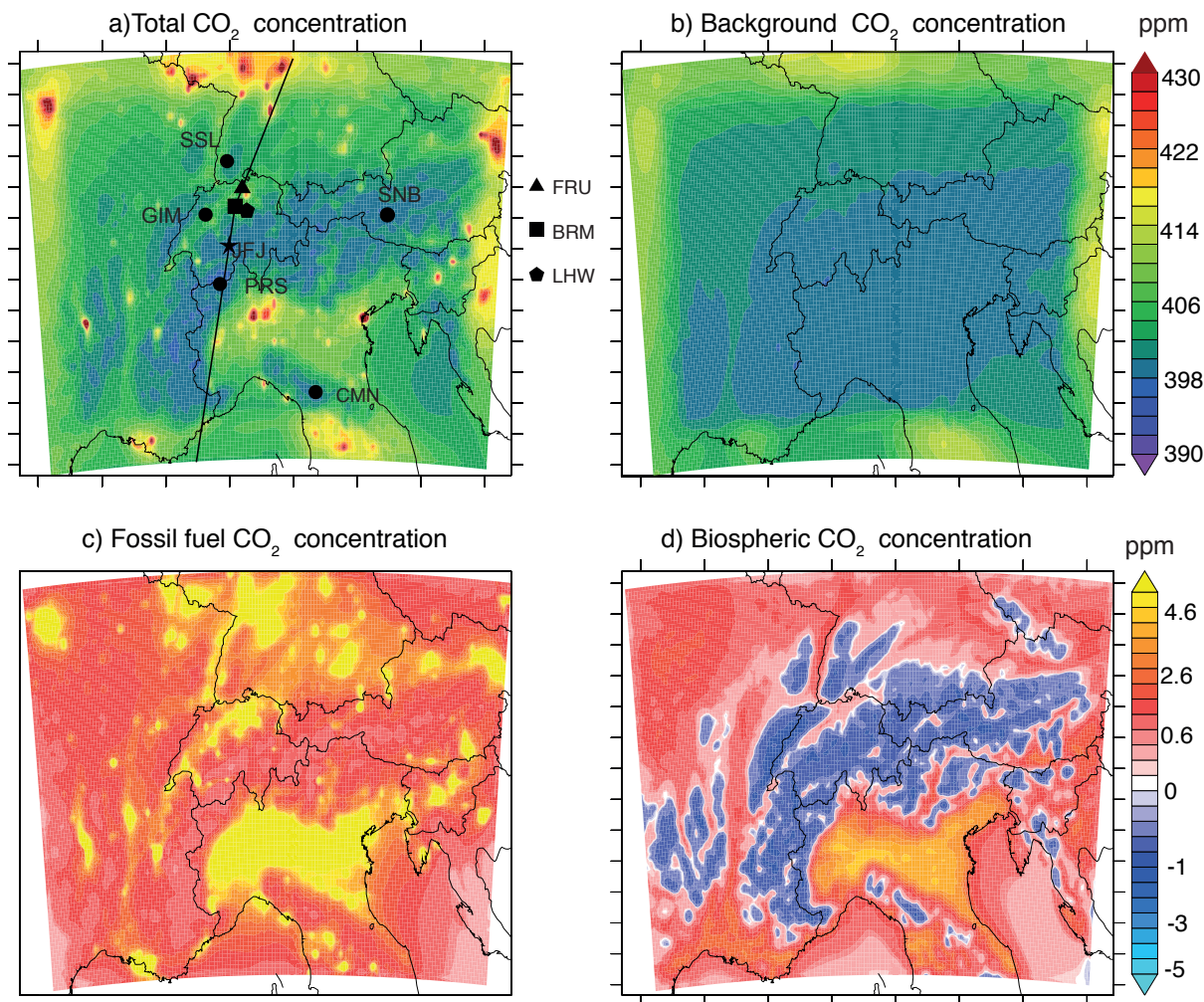


Figure 4.4 Spatial distribution of annual mean total CO₂ mole fraction (ppm) at height 10 meter (lowest level in the model) in 2013, with the 9 measurement sites indicated by symbols, i.e., 5 sites inside Switzerland (LHW, FRU, BRM, GIM, JFJ), 2 in Italy (PRS, CMN), 1 in Austria (SNB), and 1 in Germany (SSL). The solid line indicates the path for the north-south cross section along LHW, BRM and JFJ.

the diurnal cycles at Beromünster compared to Oney et al. (2015) and underestimates the diurnal cycle at Gimmiz and Fruebuel. At Lägern, the model simulates the amplitude of the diurnal cycle very well.

The CO₂ observations at the CarboCount CH sites reveal a distinct seasonal cycle in their gradient relative to JFJ with an amplitude of 10-15 ppm (Figure 4.6). At the sites outside Switzerland, i.e., at SSL and CMN, the seasonal cycles relative to that at JFJ are smaller (about 10 ppm). The lower seasonal amplitude at SSL is likely due to a stronger dilution of the biospheric signal owing to it being a mountain top site and thus being more exposed to the large-scale flow. The lower amplitude at CMN is likely due to a similar reason, although this being a high altitude sites, the dilution likely occurs with air from aloft, which carries essentially the hemispheric scale seasonal cycle also recorded at JFJ.

The low altitude sites in Switzerland as well as SSL have their seasonal minima relative to

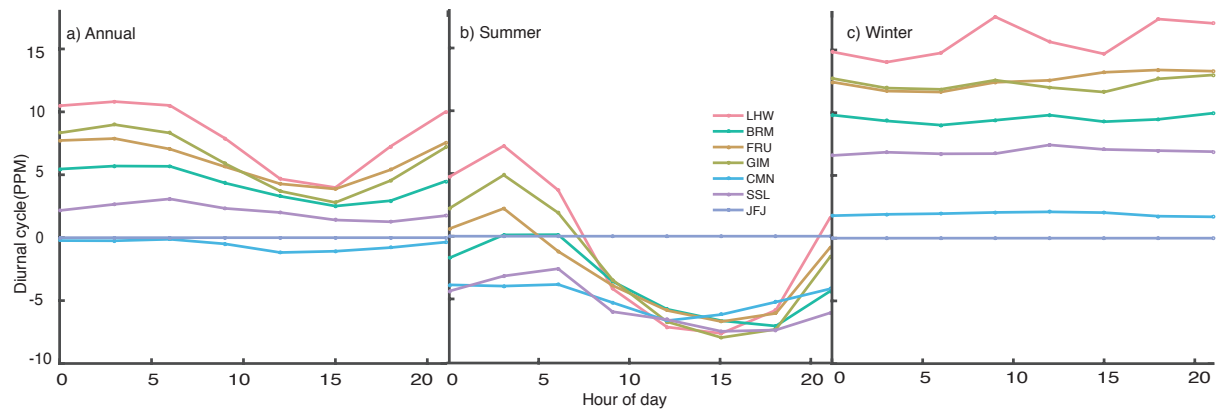


Figure 4.5 Modeled diurnal cycles of CO₂ concentration (ppm) from model simulation: difference between each site and site JFJ. a) annual mean diurnal cycle (January to December in 2013); b) Summer mean diurnal cycle (June to August in 2013); c) winter mean diurnal cycle (December, January and February in 2013).

JFJ in June, while the minimum occurs slightly later at the high altitude site CMN. Again, this is likely a result of the different degree of dilution of the local/regional signal with the large-scale hemispheric signal aloft, which tends to be delayed relative to the period of maximum CO₂ uptake by the land biosphere. The relative timing at the different CarboCount CH sites also depends on the fossil fuel signal, which is in relative terms the weakest in summer at BRM, while it is stronger at FRU and LHW. Particularly the latter site has a rather strong summer-time signal from fossil fuel, resulting in its CO₂ concentration taking an upswing in late summer, when CO₂ at BRM still stays low.

4.3.2.3 Vertical distribution

The vertical north-south cross section of atmospheric CO₂ reveals strong vertical gradients in the annual mean, most of which is generated by the fossil fuel component and the background CO₂ (Fig. 4.7). Since the latter includes a strong vertical gradient in the fossil fuel signal as well, this vertical gradient is actually almost entirely driven by the fossil fuel emissions at the surface. The fossil fuel signal that stems from emissions within the domain contribute a substantial fraction of the signal at all sites, as was already seen in the horizontal cross section in Figure 4.4. Even Jungfrauoch is modeled to have an annual mean signal from fossil fuel emissions within the domain of 0.6 ppm. Although the altitude difference between Lägern and Beromünster is small (860 m versus 1009 m a.s.l. (highest observation), the Lägern site is exposed to a substantially higher fossil fuel signal. This is, of course, also due to the Lägern site being closer to the most intense fossil fuel emissions in Switzerland, i.e., the Zurich metropolitan area (see also Fig. 4.4). This implies that attention may need to be paid when using this site for data assimilation, since it makes it more prone to biases in the fossil fuel CO₂ signal.

The strong vertical gradient in the background signal confirms our prior interpretation of its horizontal gradients being caused by dilution from air aloft (Fig. 4.4). This dilution is actually

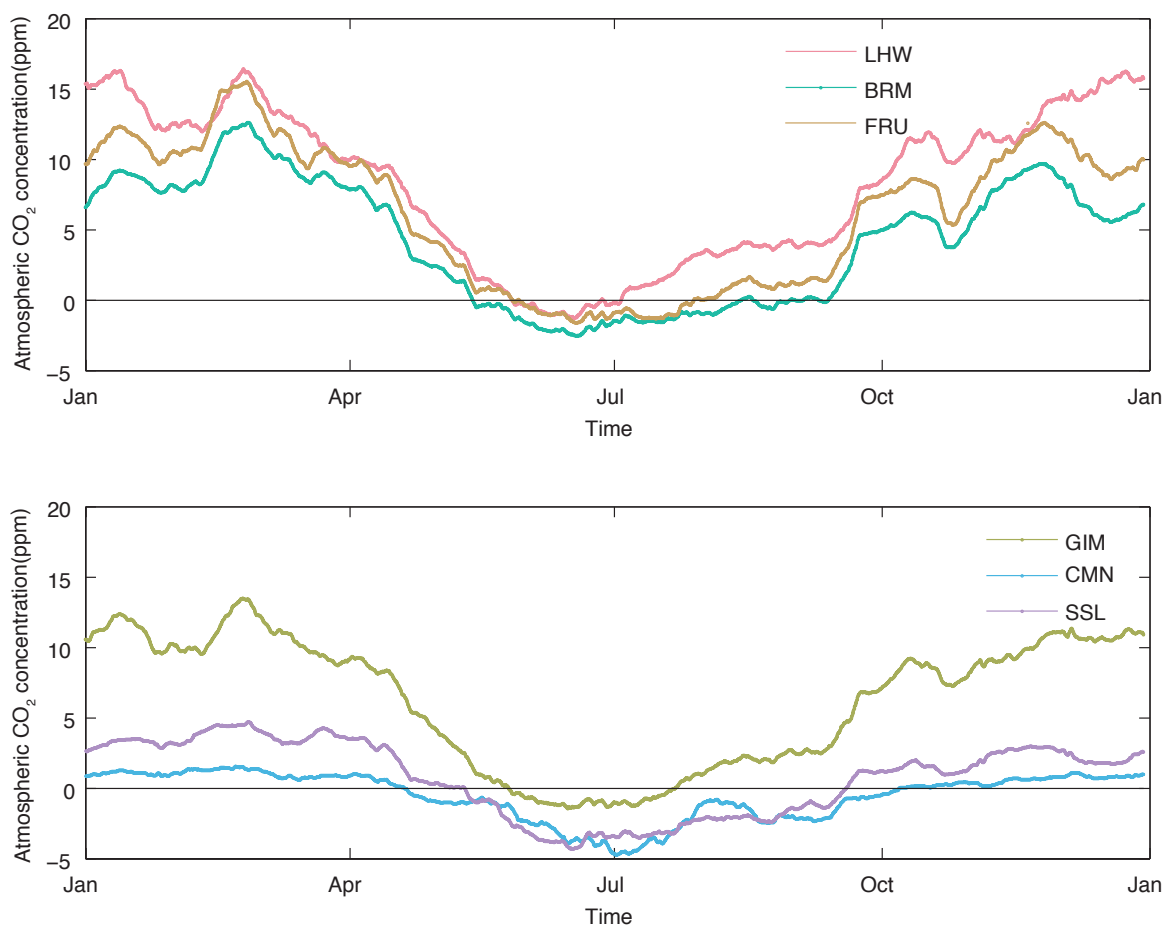


Figure 4.6 Modeled seasonal cycle of atmospheric CO₂ at 6 sites within the model domain for the year 2013 (ppm). Shown is the difference between each site and JFJ. To emphasize the seasonal cycle, the records were smoothed with 1 month running mean filter.

quite effective so that the strong vertical gradients present at the boundaries are relatively quickly diluted, so that the vertical gradients are substantially smaller inside the domain, resulting in our CarboCount CH sites seeing, in the annual mean, more or less the same background as JFJ. This is much less the case for the Schauinsland site.

The biospheric CO₂ component contributes overall little to the annual mean vertical gradients, but with a somewhat unexpected distribution. Rather than having the strongest signal where the fluxes are being generated, the strongest (negative) signals are found aloft, well recorded by our high altitude site JFJ. This vertical distribution is the vertical expression of the seasonal biospheric rectifier. In winter, the high biospheric CO₂ signal caused by the excess of respiration over photosynthesis tends to be trapped near the surface due to inefficient vertical transport. In summer, the low biospheric CO₂ signal caused by the excess of photosynthesis over respiration tends to be transported aloft. This causes a positive rectification signal at the surface, while at the same time creating a negative signal aloft. This pattern is particularly strong in the inneralpine valleys with its topographically more strongly restricted vertical exchange.

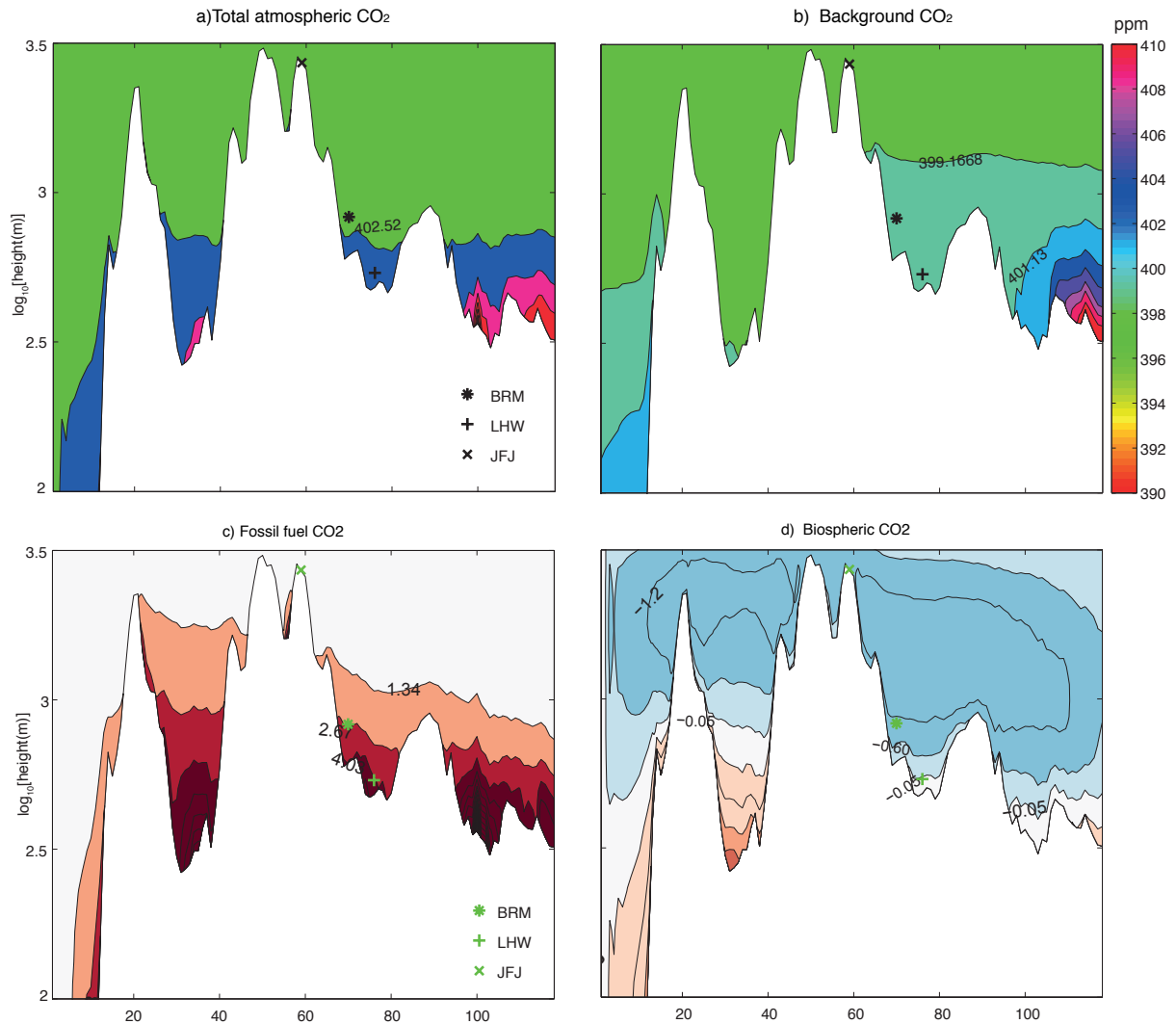


Figure 4.7 North-south vertical section of the annual mean total CO_2 and its components along the line shown in Figure 4.4, i.e., connecting Lägern (LHW), Beromünster (BRM), and Jungfraujoch (JFJ) (ppm). (a) Total CO_2 , (b) Background CO_2 component, (c) fossil fuel CO_2 component, and (d) biospheric CO_2 component. The vertical axis is plotted logarithmically to emphasize the strong vertical gradients in the lowest layers of the atmosphere.

4.4 Base run

The base inversion is the case that aims to simulate most closely an inversion of true observations. Namely, it includes the consideration of all major sources of errors, namely the potential biases emanating from fossil fuel and the background CO_2 components. This inversion was run over the full annual cycle of the year 2013, with a cycling time step of 7 days and a 2 day smoother window (see Table 4.1). We use 8 sites to constrain the system, i.e., all observing sites inside the domain. The prior biospheric fluxes were perturbed by drawing a random number from a Gaussian distribution with a standard deviation of 0.9 and assigning this to the scaling factor. This resulted in a relative error of about 50% to 60% in the regions located inside the footprint (see Fig. 4.8 b) and c)) relative to the true biospheric fluxes. The relatively low prior error in central Switzerland is due to the low biospheric flux values in the Alps.

4.4.1 Error reduction

The CarbonTracker Switzerland assimilation system is able to reduce the prior error in the domain substantially, achieving an error reduction in the inner part of the domain of more than 80%, and a reduction of over 50% nearly everywhere else (see Fig. 4.8). The small uncertainty reduction in the southern part of the domain is due to the presence of only one observing site with a footprint in this area.

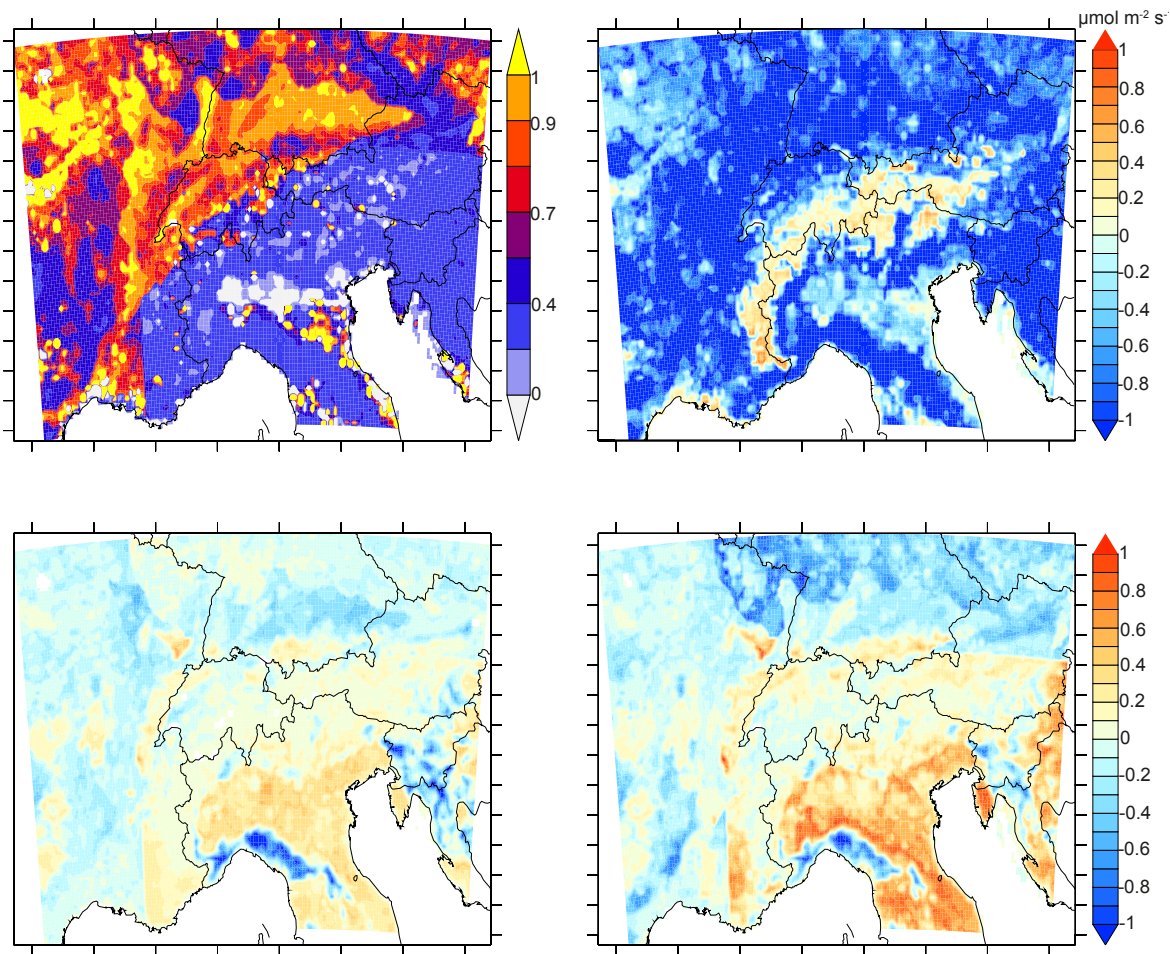


Figure 4.8 Results from the base run for the period of the whole year in 2013. (a) Map of error reduction, calculated from the ratio between the posterior and prior variances, i.e., $1 - (\text{posterior variance} / \text{prior variance})$; (b) Map of mean NEE fluxes from VPRM, taken here as the true fluxes $\mu\text{mol m}^{-2}\text{s}^{-1}$; (c) bias of prior fluxes relative to true fluxes, calculated as $\text{prior} - \text{truth}$; (d) bias of posterior fluxes relative to true fluxes: calculated as $\text{posterior fluxes} - \text{truth fluxes}$.

The net fluxes we imposed from the VPRM model (corresponding to NEE) and that we use as the true fluxes here show in the annual mean strong sinks (around $2 \mu\text{mol m}^{-2}\text{s}^{-1}$) over most of the domain (Figure 4.8b), with the exception of the Alpine arc and a few other regions. In the inner part of the domain, the small prior biases remain largely unchanged. In the regions outside the footprint of the CarboCount CH observing sites, the posterior bias turns out to be actually larger than the prior ones. This is the result of the addition of the error in the background and in

the fossil fuel emissions that tend to pull the posterior fluxes away from the truth in regions with relatively weak constraints, i.e., the outer parts of our domain. In contrast, for the inner parts of our domain, and particularly for Switzerland, CarbonTracker Switzerland is able to recover the true fluxes despite the large perturbations. This demonstrates that the system works overall well. A similar analysis for the summer time reveals an even larger error reduction (not shown).

Fig 4.9 shows the true, prior, and posterior fluxes from 12 ecoregions in the domain, in which the mixed forests and deciduous forests inside the footprint have almost the same amount of NEE as grassland over the whole domain, which is around 1/3 of NEE fluxes from croplands inside the footprint. This means the perturbations are mainly added to the croplands and that any uncertainty associated with this ecoregion will bring strong biases towards the result. This figure shows that the system drags posterior mean from the prior mean towards the true mean significantly in cropland inside the footprint.

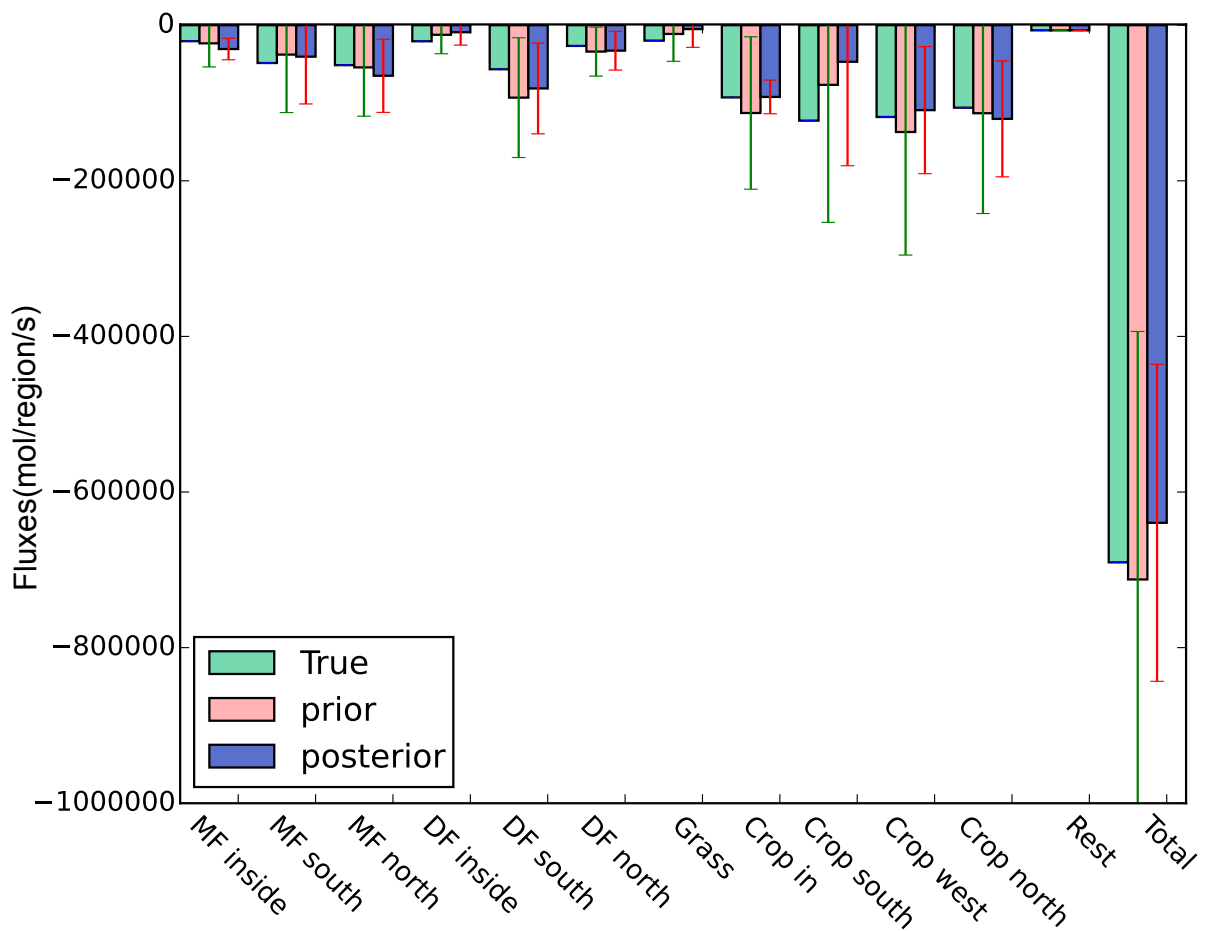


Figure 4.9 Integrated fluxes per ecoregions for of the whole year in 2013 estimated by the base run in units of mol/region/s.

4.4.2 Seasonal fluxes and error

In order to look into the details of the NEE fluxes and attribute the annual flux error to smaller scales, we analyze the flux errors from the base inversion in different seasons. The system behaves quite well in spring, with reduced flux errors in the western part of the domain. In addition, the sources in the northern part of Italy are well recovered given the underestimated sources in the a prior. However, the system fails to catch the strong sink in central Italy (see Fig. 4.10). The underestimated NEE in spring is mainly due to an underestimation of GPP, implying that a higher weighted GPP over Ra for calculating NEE might be better in the assimilation system if trying to fit to the truth, i.e., smaller ratio of Ra to GPP brought less biases to posterior fluxes (Tolk et al., 2011).

As expected, the system could not recover NEE in the northern part and southern part outside the footprint, and the posterior pattern does not change much relative to the a prior. This is due to the sparse network and high background CO₂ biases in these regions in summer. The system could resolve the error inside the footprint and the eastern part of the domain very well. The high uncertainties of the fluxes are related to the high fluxes, both in GPP and Ra. The sources dominate Italy and France in autumn are due to the strong respiration and weak photosynthetic activities. As a result of the biases of background, the assimilation system removes the sources in northern France, while it attributes sinks to the southern France and northern Germany, reiterating the importance of prior information once more. In winter, the NEE is mainly dominated by respiration. Due to small NEE, the system underestimates NEE in small part of the domain, even though the perturbation of fossil fuel is quite high in winter (see Fig. 4.10).

The system could reduce the summer and autumn biases, especially in summer. However, the amplitude of increased bias in summer might be partly due to the large fossil fuel error (as shown in Fig. 4.19).

4.4.3 Time series

In order to check the performance of the base inversion at individual locations, we compare the prior and posterior fluxes at 5 FLUXNET measurement sites where eddy covariance towers are located. The time series of the prior and posterior flux errors are compared with true fluxes at 5 sites. At 3 sites (from 1.20 $\mu\text{mol m}^{-2}\text{s}^{-1}$ to 1.03 $\mu\text{mol m}^{-2}\text{s}^{-1}$ at OE2, 1.26 $\mu\text{mol m}^{-2}\text{s}^{-1}$ to 0.99 $\mu\text{mol m}^{-2}\text{s}^{-1}$ at LAE, from 0.38) the posterior NEE is improved, while degraded at Davos (see Fig. 4.11).

In summer, when the fossil fuel error is relatively small and the background CO₂ error is high, the system could still resolve these errors quite well, except at times when the fluxes are degraded by the optimization process.

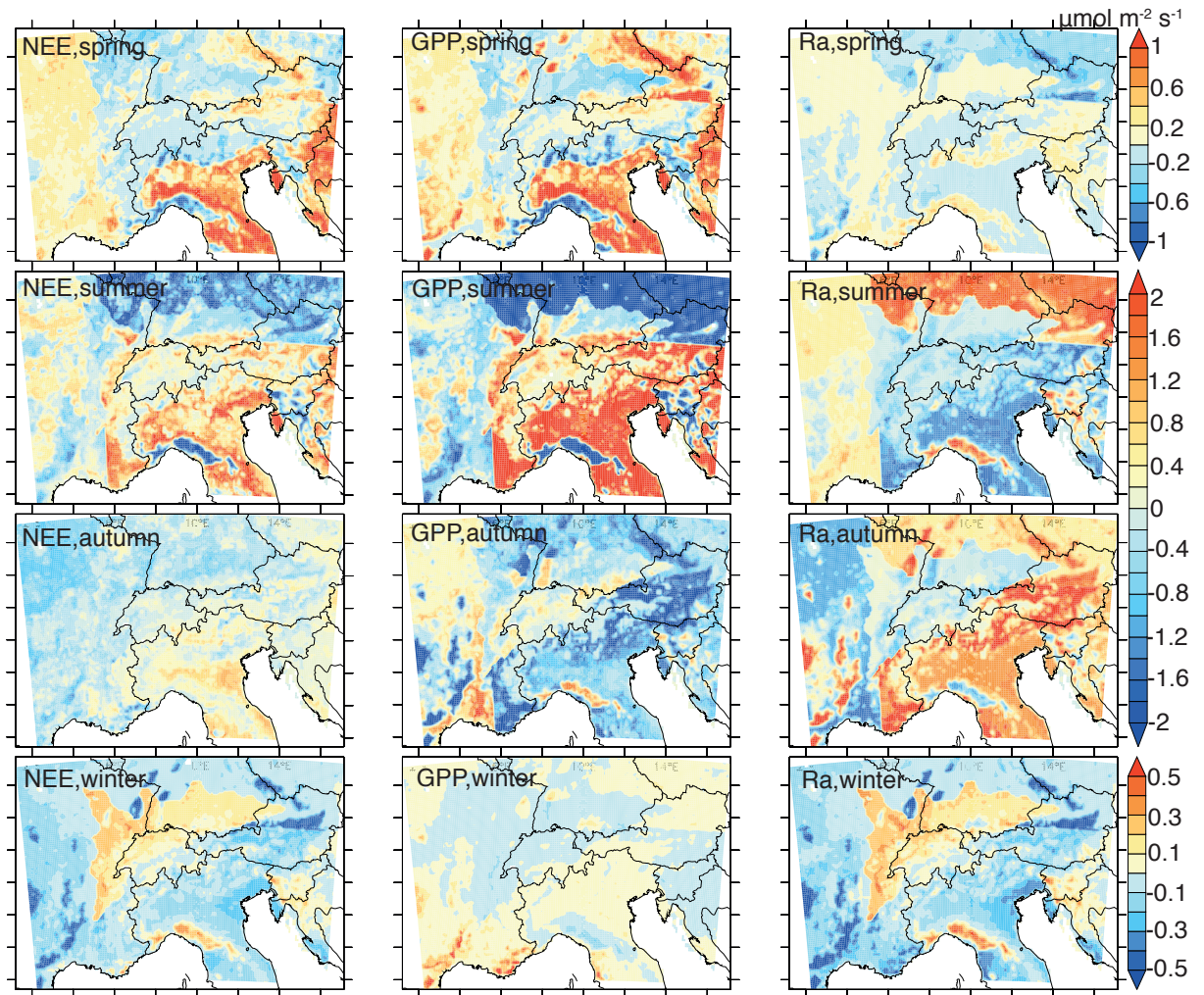


Figure 4.10 Seasonal mean flux biases relative to the truth (unit: $\mu\text{mol m}^{-2}\text{s}^{-1}$): the first row are errors of NEE, GPP, Ra in spring (March-May of 2013); the second row are errors of NEE, GPP, Ra in summer (June-August of 2013); the third row are errors of NEE, GPP, Ra in autumn (September-October of 2013); the fourth row are errors of winter (December, January, February of 2013).

In autumn, the system could correct the wrong prior from sources into sinks. Compared to other sites, the system does not change much at DAV, due to the large contribution of unimproved eco regions (over 80%) for this grid. However, if we only used the dominated eco regions, then there would be no optimization at all, implying that the percentage assimilation method offers more realistic conditions.

In the system there is more uptake at site OE2 due to the added background and fossil fuel CO_2 biases that the system attributes erroneously to biosphere fluxes. This results in underestimated posterior fluxes at these sites, or even a change of the NEE from sources into sinks at some sites. Another possible reason for the unrealistic uptake is the higher standard deviation of the initial error (around 1) than the standard deviation of the spread of the ensembles (0.8), which allows the correction factors to change sign and the ensemble assimilation could not drag this back to the original sign given the perturbed fossil fuel CO_2 error and background CO_2 error. This shows the disadvantage of the arbitrary set of the covariance matrix of the prior.

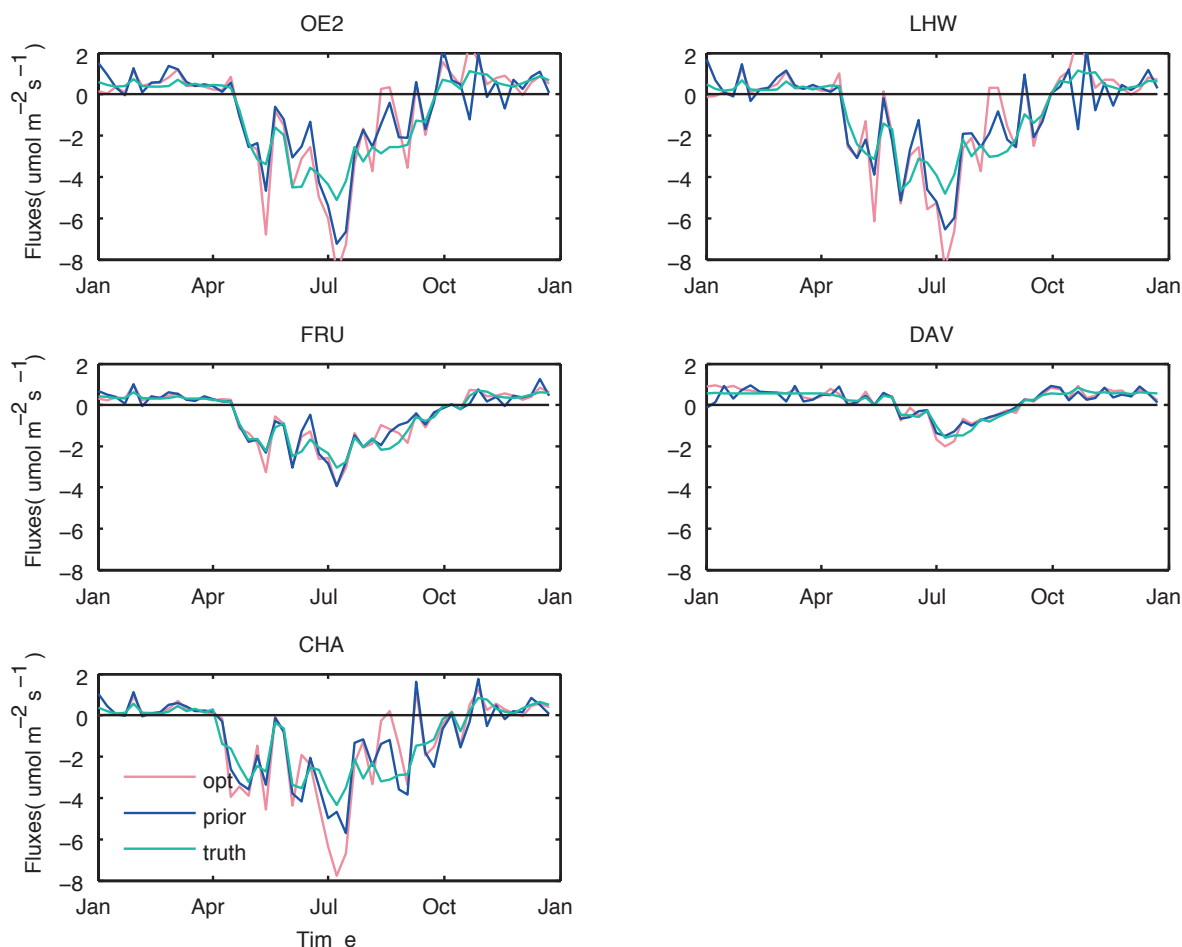


Figure 4.11 Time series of weekly NEE fluxes at 5 measurement sites in 2013: unit ($\mu\text{mol m}^{-2}\text{s}^{-1}$).

4.5 Sensitivity studies

4.5.1 Control run: only errors in NEE (S2)

To set the stage for the subsequent sensitivity cases, we first run a control case (S2), where we only considered the errors in NEE, i.e., the errors in fossil fuel and background were eliminated. The resulting maps of error reduction are overall similar to those of the base run, but reveal a better performance of the system, particularly for the summer (Figure 4.12). This is as expected given the fewer perturbations added in the synthetic inversion.

A similar conclusion can be drawn from the consideration of the ecoregion wide integration of the NEE fluxes (Figure 4.13).

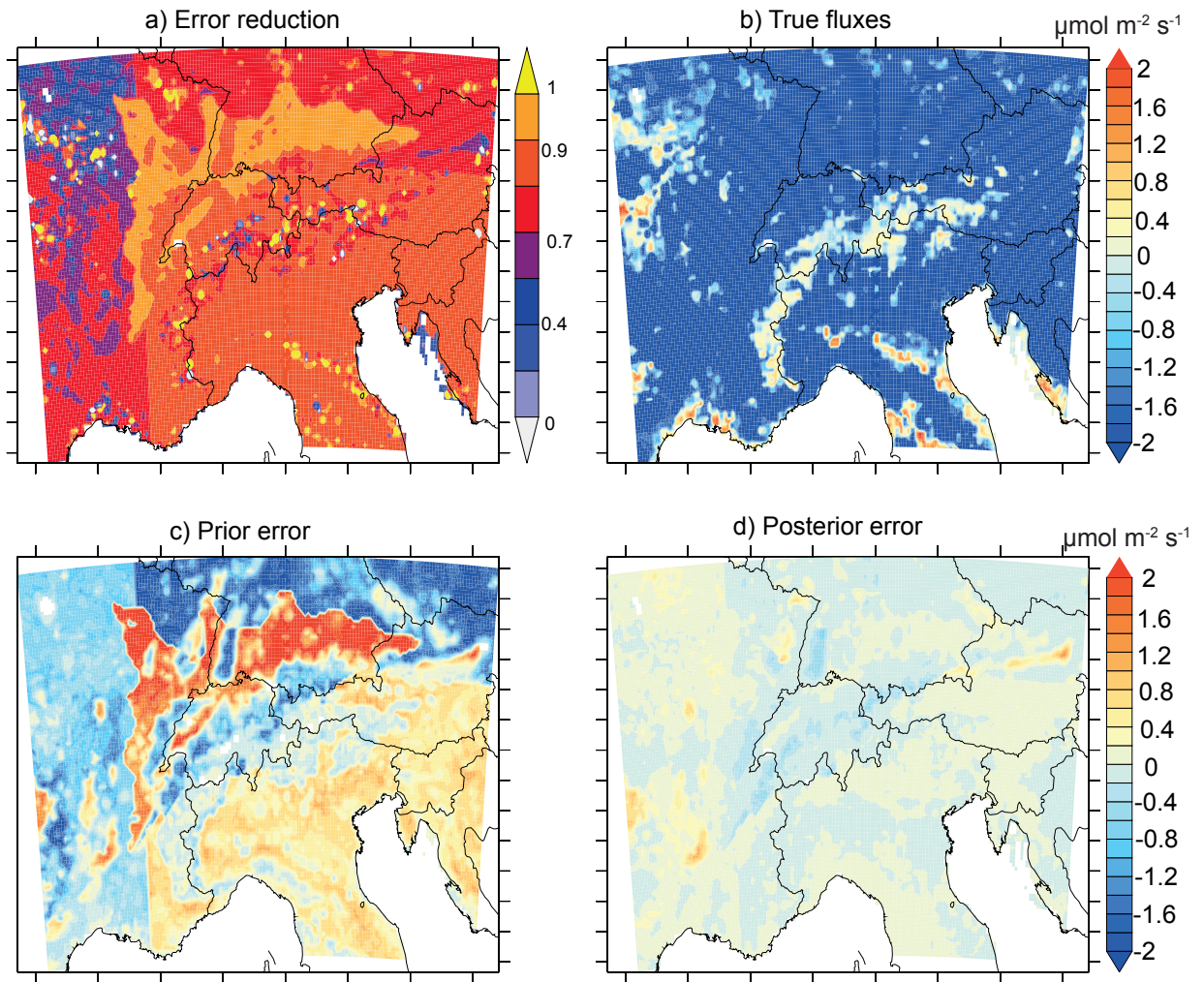


Figure 4.12 Results of the control run (S2) for July to August, 2013. a) Map of error reduction, calculated as $1 - (\text{posterior variance} / \text{prior variance})$; b) Map of mean true fluxes $\mu\text{mol m}^{-2} \text{s}^{-1}$; c) bias of prior fluxes relative to true fluxes, calculated as $\text{prior} - \text{truth}$; d) bias of posterior fluxes relative to true fluxes: calculated as $\text{posterior fluxes} - \text{truth fluxes}$.

4.5.1.1 Different network choices (S2.1)

In order to understand how different network choice affect the posterior errors and the contribution from different sites, we start with 1 site, and then add sites one by one to trace each site's contribution or influence. More sites generally favour more uncertainty reduction, such as 1 site could only reduce the uncertainty by 20-30% in the footprint region, no matter if it was a tall tower site (BRM, 121m), or a short tower site (LHW, 32 m), due to their similar sensitivity region in summer. Combining these 2 sites together eliminates 10-15% more uncertainty, while the total RMSE is still worse than using LHW alone, and this condition does not change until we increase the number of sites to 4. The 4 added measurement sites provide an improvement of the error by 30-40% inside the footprint and north part of the domain. Five sites inside the footprint could reduce the uncertainty by over 80% inside the footprint whereas the rest of the 3 sites mainly help decrease the uncertainties outside the footprint.

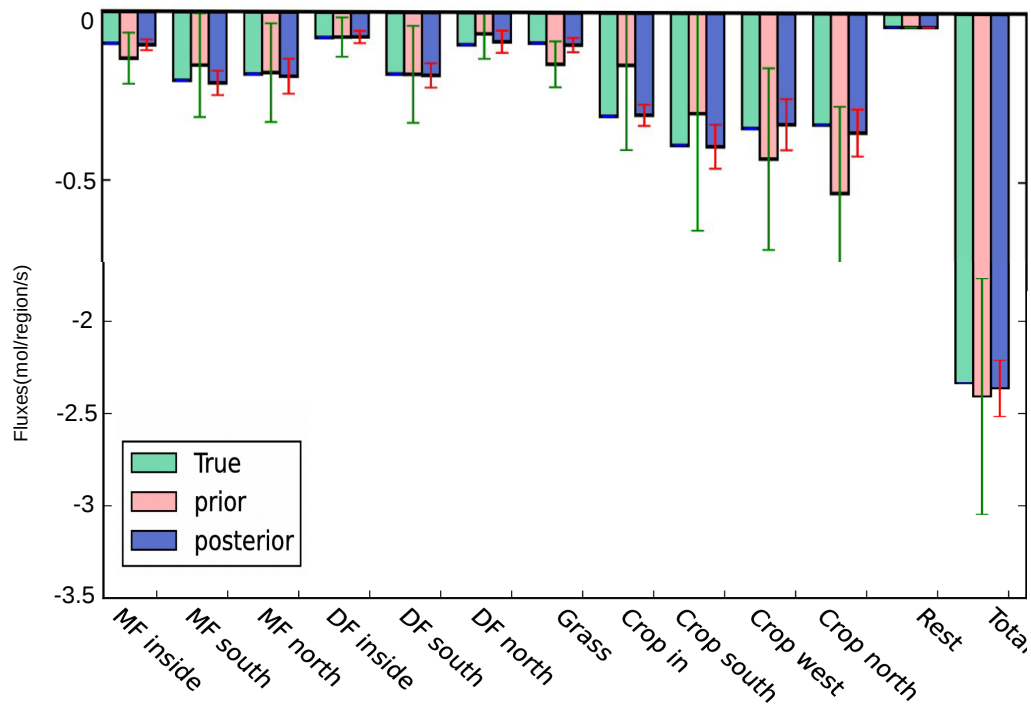


Figure 4.13 Integrated fluxes per eco regions, unit mol/region/s: over July to August in 2013.

Very few sites are not enough for generating robust result for different eco regions, but to have more sites is not always critical for reducing the biases of posterior fluxes (see Fig. 4.14).

With one site only, the posterior NEE fluxes from croplands are still biased (negative inside footprint and in the southern domain, positive in the northern and western part of the domain). Both mixed and deciduous forests inside footprint are well constrained even by only one site. One reason might be the relatively low prior error compared to the croplands as shown by Fig 4.9.

Another reason might be that these sites already reflect proper information from forests due to the location of these sites (Oney et al., 2015), when comparing the posterior and posterior fluxes error from grassland. This test also shows that under perfect transport conditions, short towers perform almost the same as the tall towers when comparing RMSE of the total or different ecoregion posterior fluxes. The total RMSE when using both LHW and BRM is still worse than just using LHW.

With the added site FRU, the RMSE of posterior CO_2 fluxes of most eco regions, such as, cropland inside footprint, or cropland in northern domain still have the same magnitude of bias as those from the 2-site inversion. This situation improved by adding GIM site, for most of the eco regions, e.g. cropland inside footprint, grassland, mixed forest inside footprint, suggesting a significantly benefit from this site under the perfect transport conditions. The only eco region not

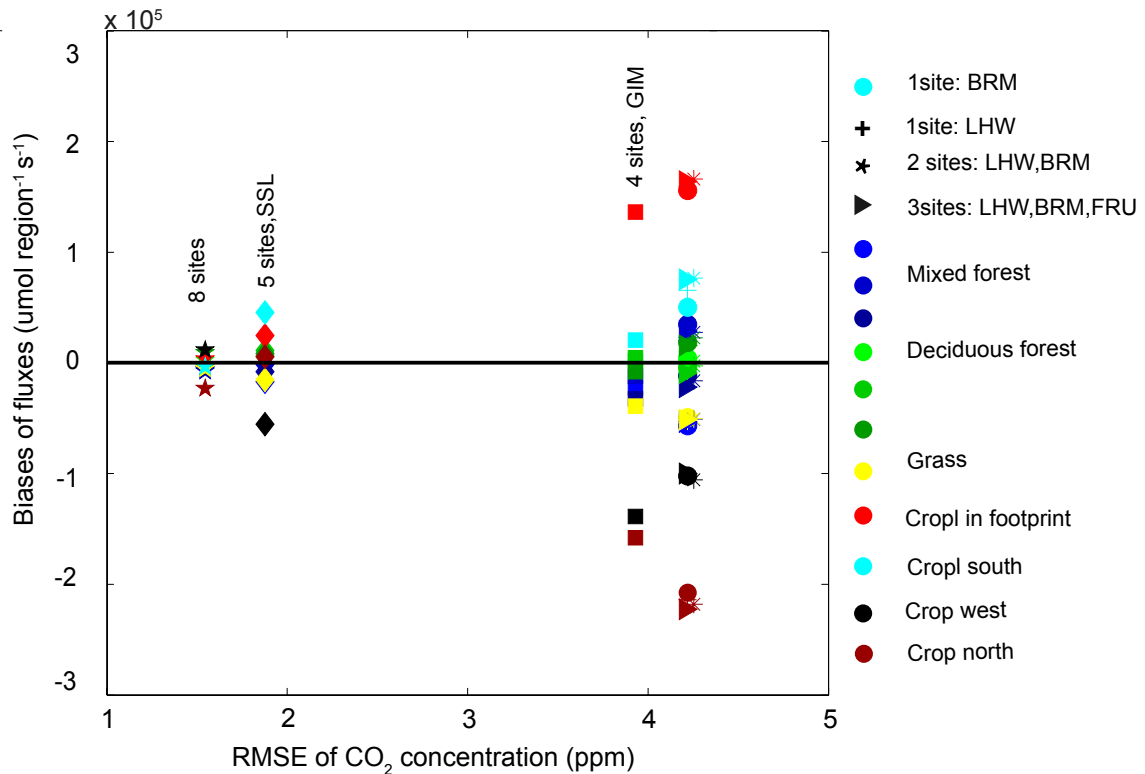


Figure 4.14 Sensitivity test to different network choices from July to August. Different shape are from different simulations, and different color representing different eco regions.

improved is the cropland in the western domain, which could be constrained partly by the 5th site SSL.

Five sites resolve almost half of the error in the western and northern part of the domain, while there is not much improvement in the southeast of the domain due to the low influence of the sites here. The RMSE of integrated fluxes over the whole domain is reduced from 0.76 mol s^{-1} to 0.27 mol s^{-1} , with posterior errors or RMSE from all the eco regions significantly small enough, meaning 5 sites are enough to accurately invert the NEE fluxes in the middle of the footprint. The test with 8 sites shows that both the RMSE of posterior CO_2 concentration and biases of fluxes are less spread among different eco regions, indicating the additional 3 sites outside of the footprint reduce the biases of fluxes of cropland outside the footprint significantly and help reducing RMSE to half of the RMSE from 5 sites simulation (see Fig. 4.14).

4.5.1.2 Different localization method (S2.2)

Among all the localization methods, the 50% cut-off covariance method performs most poorly with regard to RMSE of posterior CO_2 concentrations. Compared to the CT2007 localization (which is the method used for base run), the system with 50% cut-off performs better for the biases of the ecoregions, such as, the posterior fluxes from cropland in the northern domain, mixed forest, cropland in west domain are better simulated under 50% cut-off than CT 2007,

while the fluxes from cropland in the southern domain are worse under this method. Generally, these 2 methods behave similar with both cropland and deciduous forest inside the footprint.

The 10% cut-off covariance method works better than the CT2007 localization, with slightly better RMSE of posterior CO_2 concentrations and half of total RMSE less than the CT2007 localization, and smaller optimized CO_2 RMSE. In addition, due to the complex topography and small eco regions compared to other studies, CT2007 might cutoff some useful information in the central Italy, which results in slightly less uncertainty reduction. While 10% cut off method catches the information in the middle Italy, and resulting in better results. Eco regions behave differently under these 2 localization methods due to the correction of the Kalman gain based on different rules, such as cropland in northern domain is strongly negative biased under CT2007 simulation, but slightly positive biased with the covariance 10% cut-off localization method. In addition, most eco regions perform better under the covariance 10% cut-off localization than the CT2007 localization, e.g., the biases of deciduous forests in northern domain, mixed forest inside footprint and grassland are just half of biases under CT2007 localization (see Fig. 4.15). However, the 10% cut-off covariance method does not work well as CT2007 method in the posterior fluxes from cropland inside footprint and in western and southern domain, which might due to a too strict cut off in the cropland from these 2 regions with 10% cut-off method, because fluxes from these 2 regions are almost the same as the no localization method.

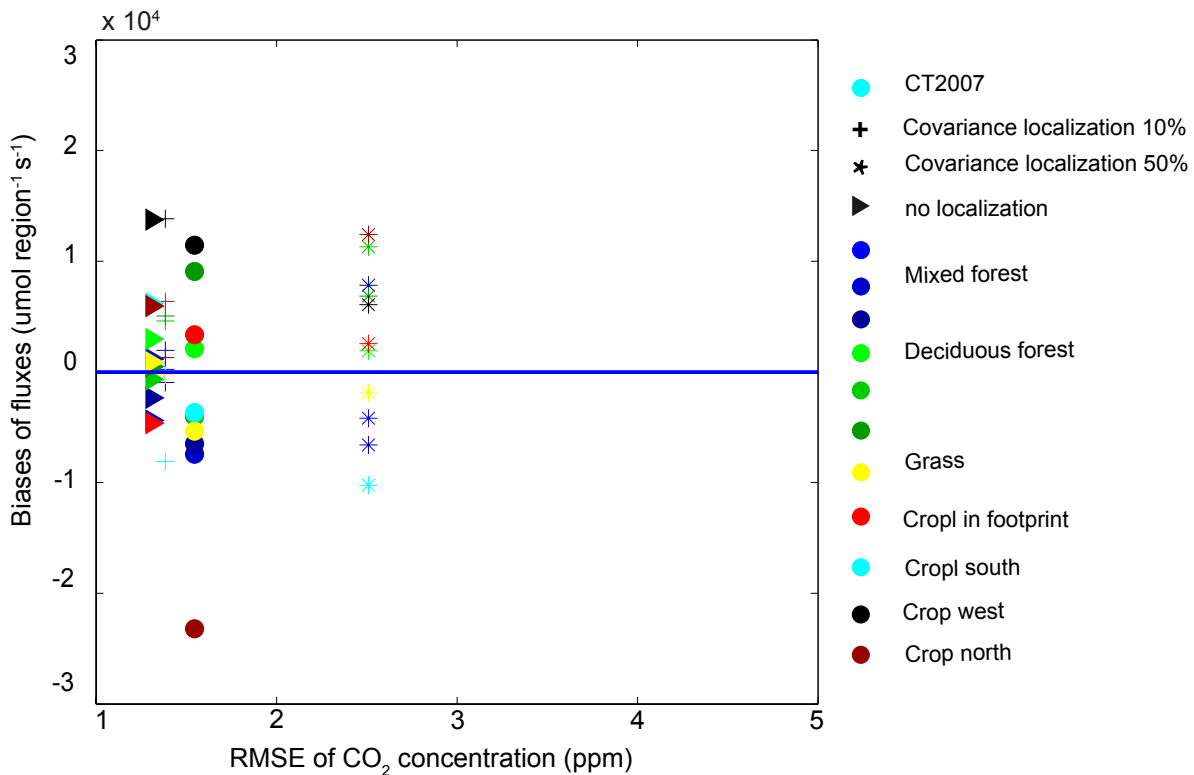


Figure 4.15 Sensitivity tests to different localization methods for the months July to August. Different symbols indicate different simulations, and different colors represent different eco regions.

Although cut-off should decrease with the increasing ensemble size (Zupanski et al., 2007),

we tested different cut-off ratio with the same ensemble size, and these 2 methods behave differently in both RMSE of posterior CO₂ concentration and on biases from different eco regions as well. 10% cut-off localization performs better than 50%, implying the ensemble size is enough for these simulations.

No localization is slightly better than 50% cut-off and CT2007, implying that the measurement sites are enough for the domain and separated eco regions and that we do not need the localization for the spurious error for most of the eco regions, except cropland in the western domain. But generally, all these localization methods could catch the error, and estimate good results with high confidence (see Fig. 4.15). For robust fluxes for cropland inside the footprint, the CT2007 and 50% cut-off method are better choices than others, while covariance localization with 10% cut-off for forest and grassland. As fluxes from cropland are much higher than grassland inside footprint, we would recommend CT2007 localization method in this system.

4.5.1.3 Role of subgrids cale ecoregion variations (S2.3)

The percentage inversion provides more robust results than the dominant eco region inversion due to the more realistic consideration of the eco types in each grid cell. The percentage inversion reduces uncertainties by more than 80% in most of the domain (as discussed in the base run), while the uncertainty reduction from dominant ecoregion inversion has the same amount as the percentage eco region method in 1 ecoregion inside the footprint. The rest of the domain has 10% higher uncertainties than the dominant method, with almost 70% more error in south of Switzerland. The reason for the difference is that in the percentage inversion system, the information that retrieved fluxes locally for an ecosystem type is now available and is applied far away from that location. However, in the dominant eco region inversion system, the ecosystem was restricted to only grids where it is dominant. This means that the the correlations in space have been significantly increased and the information have been spread more widely in the percentage inversion system.

In addition, the system using dominant eco region maps can not remove all the error compared to the truth. There are still around 10-20% of error compared to the truth, while the error from percentage eco region inversion has less than 5% error in most of the regions. Furthermore, the dominant method underrepresents the ecoregion that are less dominant, leading to a patchy uncertainty reduction map and posterior biases map. In contrast, the more homogenous structure from the percentage results are due to the smoothing effect from different eco regions in the pixels. In sum, the fractional grid information help the system achieve a downscaling of the (same) available observational constraints.

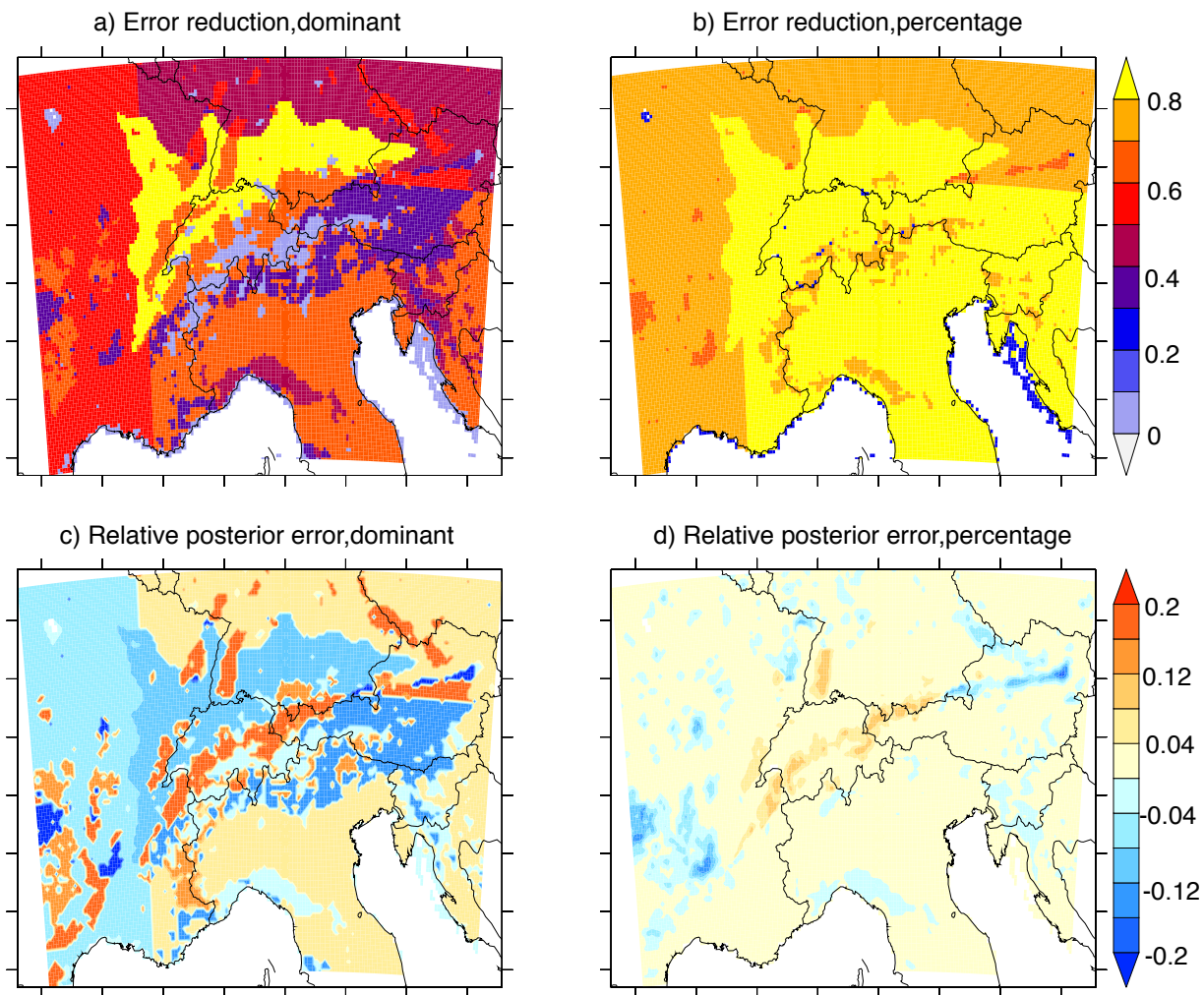


Figure 4.16 Sensitivity test to different eco region map: a) and c) error reduction from dominant or percentage eco region maps) and d) relative improvement comparing to the truth from dominant or percentage eco region maps, relative improvement is calculated as the $(\text{posterior} - \text{truth})/\text{truth}$, unitless.

4.5.2 Second set: Sensitivity to background CO₂

Here all the posterior errors are the difference between posterior fluxes in each simulation and in base run, meaning that there is no impact from NEE error, only the influence from background CO₂ biases.

4.5.2.1 Background error at 8 sites with 100 km spatial correlation (S3.1)

The assimilation system could remove all the error substantially in the southern and the eastern part of domain compared to the truth (see Fig. 4.17 a)), which is essentially due to the well simulated eco regions, such as forest, grassland and croplands in the southern domain. The mean posterior biases in southern and eastern domain are less than $0.4 \mu\text{mol m}^{-2}\text{s}^{-1}$, i.e., less than 10% relative to the truth, mainly from the overestimated deciduous forest. The assimilation system

has difficulties in the prediction in the northern part of the footprint and northern domain, owing primarily to the unrealistic overestimation in cropland (with posterior error around $-1.4 \mu\text{mol m}^{-2}\text{s}^{-1}$), while the dramatic underestimation in footprint is from the cropland, even though 5 sites are adopted here to constrain NEE inside the footprint that results in 90% reduction of uncertainty. By virtue of the perturbed background CO_2 , the system overestimates the total average fluxes, following the same sign as the prior fluxes (overestimated prior), with high uncertainty.

4.5.2.2 Different spatial correlation (S3.2)

Longer spatial correlation resolves the background CO_2 biases far better than shorter spatial correlation. Fig 4.17 b) shows that the posterior error from 300 km (S3.22) spatial correlation in the western part of domain, such as i.e., posterior fluxes from inside footprint and western domain, are very well modeled comparing to simulation with 100km (S3.1) and 30km (S3.21), with posterior error $1 \mu\text{mol m}^{-2}\text{s}^{-1}$ in the footprint in S3.22, almost half of the posterior error from S3.1 and S3.21. In addition, the RMSE of posterior CO_2 concentration also demonstrate that 300 km performs better.

The posterior fluxes of eco regions benefits from longer spatial correlation, such as the bias of posterior fluxes of cropland inside the footprint is significantly improved by around 1/3 in S3.22 than S3.1 and S3.21, although still far from 0. In addition, fluxes of cropland in western domain could even be recovered with almost no bias, compared with are overestimated by S3.1 and S3.21. Longer spatial correlation does not improve the performance of cropland in southern domain, might due to the already low bias in this ecoregion. Higher spatial correlation results in better results might due to the separation of inside and outside the domain, that the higher spatial correlation could spread the information from the measurement site to more eco regions. Here the 30 km (S3.21) works slightly better than 100km (S3.1), when considering the RMSE of posterior CO_2 concentration, and also the cropland in northern domain, This might be due to the balance of spatial correlation and localization method, as the shorter spatial correlation in the prior covariance matrix also spread less uncertainties in the prior knowledge (Kadygrov et al., 2015).

In summary, for the area inside footprint, a higher spatial correlation (300km) gives more robust results.

4.5.2.3 Different temporal correlation (S3.3)

Longer temporal correlation behaves better than shorter temporal correlation by reducing the average posterior NEE error, mainly in the western and southern domain (Fig 4.17d). Although the posterior CO_2 concentration is not improved relative to S3.1, longer temporal correlation reduces the biases of posterior fluxes from inside footprint, western and northern part of cropland,

due to the spread of smoothing effect along time that might bring more prior knowledge to the posterior fluxes.

In addition, higher temporal correlation generates more homogeneous error structure between southern and western domain, indicating there are some spatial smoothing effects from long temporal correlation. The temporal correlation has less effect on improving the biases of posterior fluxes, compared to the improvement brought by longer spatial correlation. But generally, the 1 month fluxes correlation is important for both inside footprint and total fluxes in the whole domain, similar to other research that we should consider the fluxes error correlation.

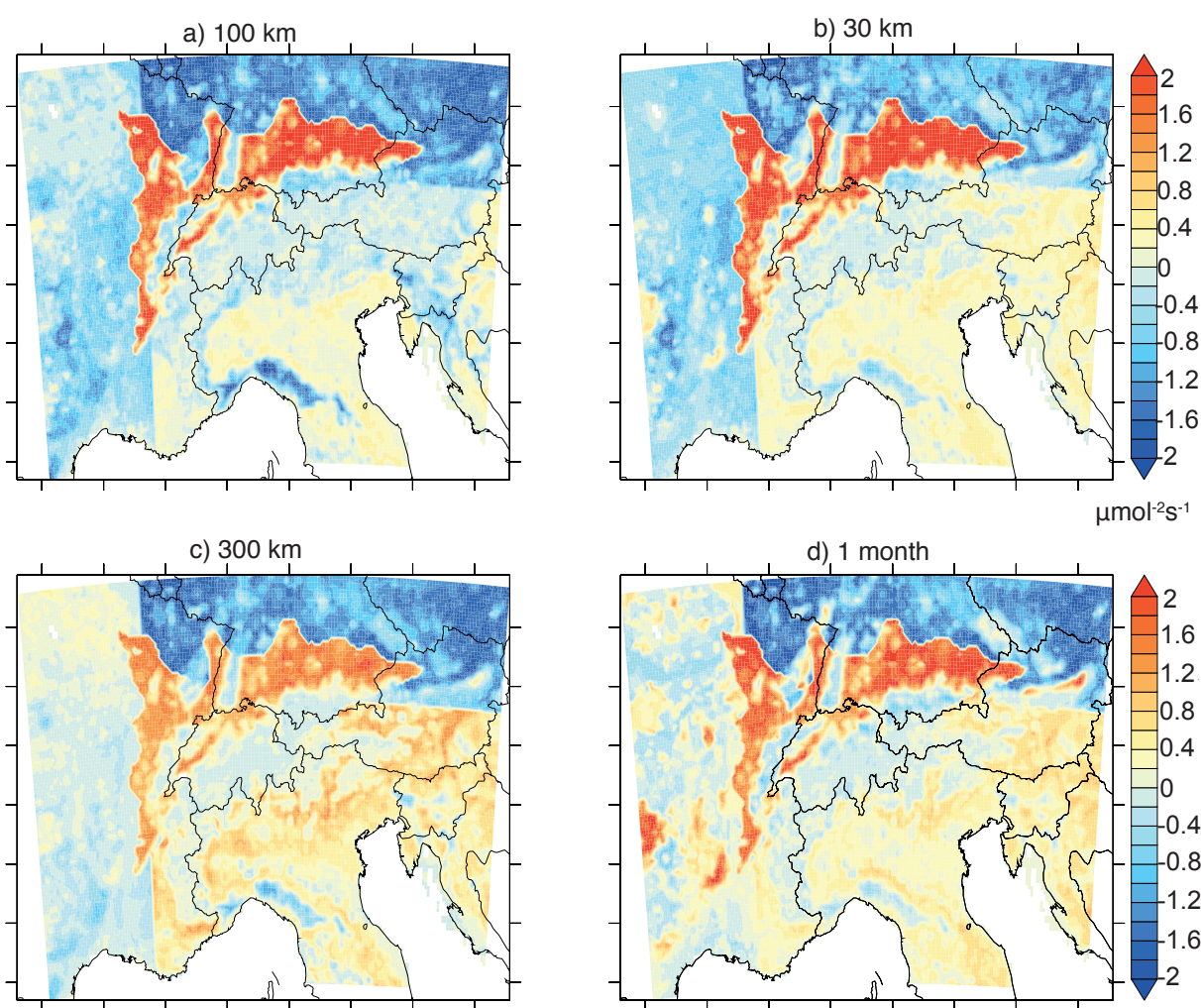


Figure 4.17 Sensitivity test to background CO₂ biases with 8 sites: unit: $\mu\text{mol m}^{-2}\text{s}^{-1}$: a) 100km spatial correlation and 8 days temporal correlation; b) 30km spatial correlation and 8 days temporal correlation; c) 300km spatial correlation and 8 days temporal correlation; d) 100km spatial correlation and 30 days temporal correlation.

4.5.3 Third Set: Sensitivity tests to fossil fuel emissions uncertainties (S4)

The fossil fuel biases have small impact on the annual posterior NEE fluxes, such as, the posterior error is less than $0.1 \mu\text{mol m}^{-2}\text{s}^{-1}$, less than 5% error in most of the region, as shown in Fig 4.18. One must pay attention that the prior error is quite low, such as, the prior error inside footprint is around $-0.3 \mu\text{mol m}^{-2}\text{s}^{-1}$, but the high prior error is relatively high in southern domain, where the NEE fluxes are underestimated by around $1 \mu\text{mol m}^{-2}\text{s}^{-1}$. The system behaves different at different season, due to the combination of fossil fuel and fluxes error combination at different time scales.

In spring, the prior underestimates the NEE by $0.4 \mu\text{mol m}^{-2}\text{s}^{-1}$ inside the footprint (see Fig. 4.19). The small prior error is partly due to the low photosynthesis. There are high prior errors in northern domain and southern domain. After inversion, there is less than 1% error in the domain. These results show that when fossil fuel uncertainties are relatively high the system is able to still remove the error due to the small NEE fluxes error. In summer, the prior error is relative high in most of the area (overestimated by $0.6\text{-}0.8 \mu\text{mol m}^{-2}\text{s}^{-1}$ inside footprint, and underestimated in southern domain by more than $1.5 \mu\text{mol m}^{-2}\text{s}^{-1}$), the system is able to remove most of the NEE prior fluxes error and fossil fuel error in southern domain, but only remove part of the biases from cropland inside the footprint. This leaves some error in the middle of the footprint where the mixed forest is located, even when the fossil fuel uncertainties are low in summer. This means the posterior fluxes from mixed forest in the footprint might be biased by the fossil fuel CO_2 concentration. The system could remove the fossil fuel biases in autumn (see Fig. 4.19) and winter, due to the low NEE fluxes error, even though the fossil fuel biases are relatively higher in winter. Here we consider both fossil fuel error and fluxes error.

Note that the error of perturbed fluxes is not excluded here. As the control simulation just was run from May to December, we could only know the pure effect of fossil fuel error in summer and autumn, when the photosynthesis are most active, and as discussed in the former part, the prior error in most of the domain are from the perturbed fluxes. While the system could remove the fluxes error quite well, it performed poorly for the fossil fuel in the mixed forest in the southern domain. This uncertainty should be considered in the inversion system with observation data.

4.6 Discussion

4.6.1 Forward simulation and implication for inverse run

The good modeled results from the forward simulation allow us to trust the transport model in the Alpine regions. Among all the 4 CarboCount CH sites in Switzerland, the Beromünster has the smallest influence from fossil fuel CO_2 , making it a good site for estimating the land uptake.

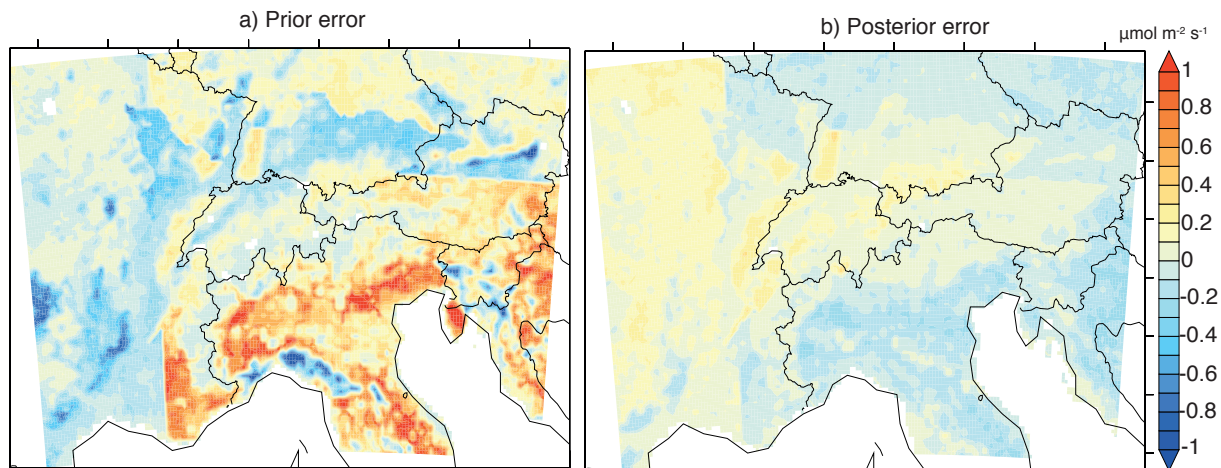


Figure 4.18 Map of annual mean fluxes biases relative to the truth with added fossil fuel biases (unit: $\mu\text{mol m}^{-2}\text{s}^{-1}$), calculated as average of prior or posterior fluxes minus true fluxes.

Both Frubuel and Lägern are affected by fossil fuel in summer, which makes it necessary to test how much these fossil fuel signals might affect the inverted NEE. The vertical distribution shows that JFJ could also see some regional NEE in summer time, hence it might bias the result if we just use the gradient of JFJ and other sites for the inverted NEE fluxes in summer time.

4.6.2 Assimilation method, network and correlation length

In this paper, the RMSE of posterior CO_2 mixing ratios and biases of posterior fluxes are significantly improved when considering the sub grid percentage information. This is in contrast to other pixel based assimilation from EnKF (Tolk et al., 2011; Peylin et al., 2013). Tolk et al. (2011) compared different methods in the Netherlands and found no significant difference of CO_2 mixing ratio RMSE from pixel-based inversion compared to the eco region inversion method over all hour analysis and the daytime analysis, and the information of sub grid information remained lost in both of these methods.

We assume that the inversion system would benefit from using percentage information also in a pixel based inversion. It's still questionable to define the correlation for the eco regions in each grid cell for the percentage assimilation methods. The 8 sites are enough for robust results in the footprint. The spatial sensitivity tests of the site LHW and BRM are similar and the observed CO_2 concentration at these sites are highly correlated (> 0.8), leading to the mismatch of the pace of improving uncertainty reduction and biases of posterior NEE fluxes. This study also shows that both RMSE of posterior CO_2 and biases of posterior NEE fluxes are reduced when increasing the spatial correlation length from 30km or 100km to 300km, similar to the regional inversion system from Lauvaux et al. (2012); Kadygrov et al. (2015). However, in some areas from Kadygrov et al. (2015), shorter correlation length decreases prior uncertainty and hence behaves better due to the different inversion method. Hence, we assume that CarbonTracker Switzerland might behave

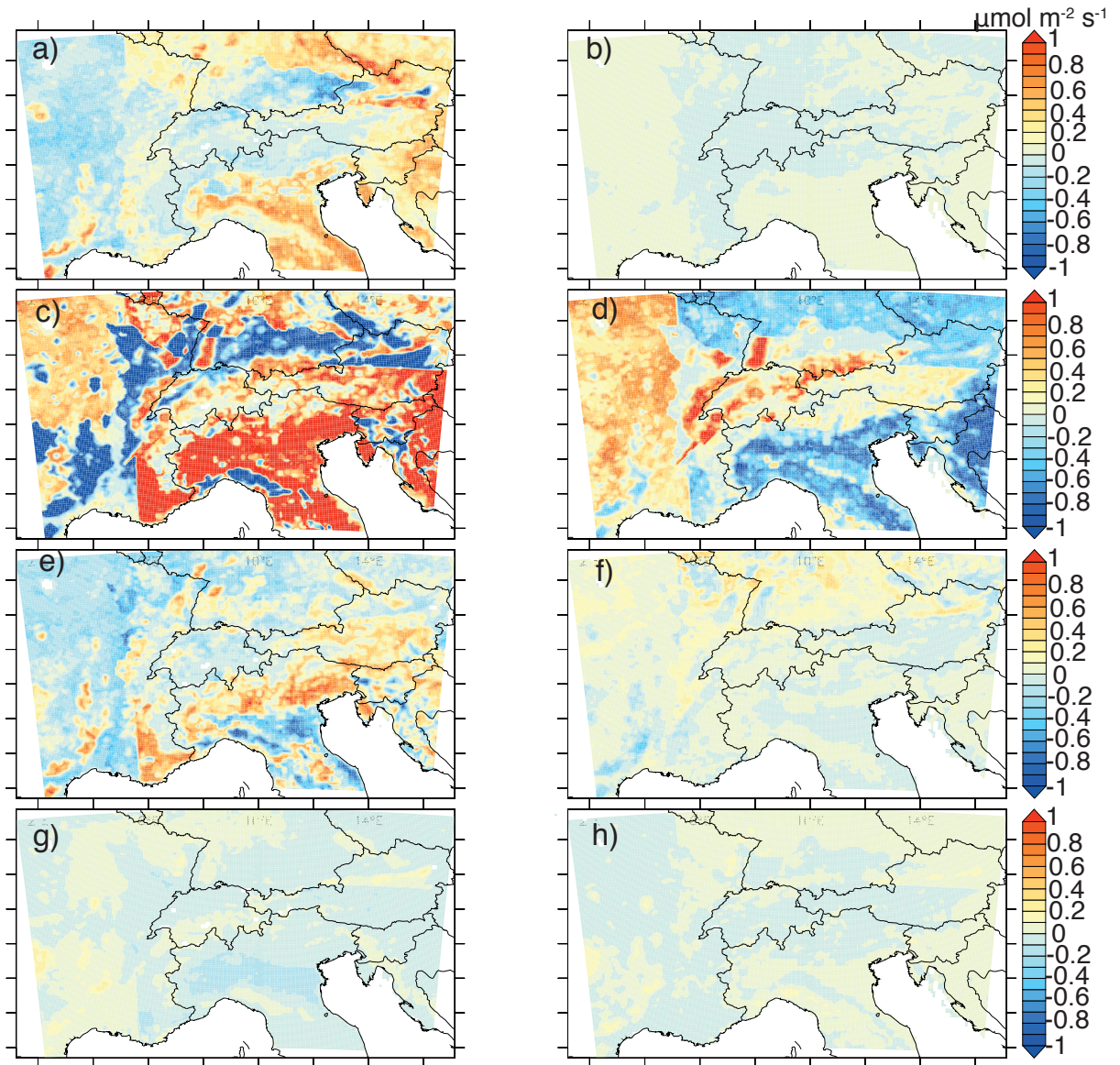


Figure 4.19 Seasonal mean fluxes biases relative to the truth with added fossil fuel biases (unit: $\mu\text{mol m}^{-2}\text{s}^{-1}$), calculated as average of prior or posterior fluxes minus true fluxes: the first column are seasonal error of prior NEE; the second column are error of posterior NEE; spring (March-May of 2013), summer (June-August of 2013), autumn (September-November of 2013), winter (December, January, February of 2013)

different at different areas if optimizing the scale factors at grid scale.

Different temporal smoothing window discussed by Peters et al. (2005) and Babenhauserheide et al. (2015) for global inversions. Babenhauserheide et al. (2015) showed that longer smooth windows could reduce the posterior error. Gourdji et al. (2010) and Basu et al. (2016) introduced temporal correlation in the prior error. We do not show different temporal windows here as more temporal windows require significantly more computation time, but by adding the temporal correlation function for scaling factors. We still found that longer smoothing window reduces the error of posterior fluxes, similar to Broquet et al. (2013) and Chevallier et al. (2012). It is still questionable how to generate the optimal weight for other simulations using different vegetation inventories, or for real observation data assimilation. As we did not test the night time

data with higher temporal window, the uncertainties from this part still remain unknown.

4.6.3 Data error

Based on the sensitivity test, the system could resolve the background error with standard deviation 2 ppm in summer time (July and August), which is higher than the constant error added by other studies (1 ppm), and also within the range of background error encountered in high resolution regional inversions (Lauvaux et al., 2012), implying that this system could generally remove the background error.

The footprint where we are focusing on in our project has very robust posterior fluxes no matter the given fossil fuel uncertainties (with just 7.95% posterior flux error from fossil fuel uncertainties, equivalent to $0.0034 \mu\text{mol m}^{-2}\text{s}^{-1}$, or given background biases or combination of them from May to December in 2013 (with just 2.6% posterior flux error relative to truth from combined fossil fuel and background errors, or $0.0011 \mu\text{mol m}^{-2}\text{s}^{-1}$). The offset between the combined fossil fuel uncertainties and background CO_2 errors results in smaller posterior error than the posterior error from just the fossil fuel uncertainty or background CO_2 error. This gives us some confidence about the posterior results in this assimilation system. In addition, the fluxes from Austria and eastern part of France are robust due to the high spatial correlation between the cropland in western part of the domain and inside footprint.

Although the combined fossil fuel uncertainties and background CO_2 error slightly bias the inverted fluxes in the footprint, the system generally produced a robust result from May to December in 2013. The error brought by the fossil fuel uncertainties is much lower than the error from Kadyrov et al. (2015), or the uncertainty target from CarbonSat (around $0.5 \text{ C m}^{-2} \text{ s}^{-1}$), and also much lower than 47% shift of NEE from Göckede et al. (2010).

This system could easily remove the NEE fluxes error with standard deviation 0.9, which including the range of the difference from different flux dataset (such as MTE or CLM data), implying that the robustness of system under current prior fluxes, the fossil fuel and background error are more important in these experiments. The main limitation of these tests is that we do not consider model transport error, which might require further constrain in the real observation assimilation system.

4.7 Conclusions

In this paper, we evaluated and tested the newly developed high-resolution CarbonTracker Switzerland system using both real observations (to evaluate the transport model and the priors) and synthetic data (to test the robustness of the inversion system). For the latter, we added as realistic

uncertainties as possible to the data.

The forward simulation shows that the model performs very well in predicting the CO₂ concentration compared to the amplitude and variability at all the new measurement sites in Switzerland, annually and seasonally. Summer biases are higher than during other seasons, due to too high NEE fluxes. The vertical distribution shows that the Lägern site is exposed to relatively high fossil fuel CO₂ (around 4.2 ppm), while Beromünster seems to be better suited for the inversion of NEE due to it being somewhat less polluted from fossil fuel CO₂.

The base run with all uncertainties and errors shows that the CarboCount CH system could remove most of the NEE fluxes error, particularly in the inner parts of the domain that are well covered by the CarboCount CH sites. The posterior fluxes are biased by the background CO₂ error with the croplands inside the footprint and the deciduous forests in the northern part of the domain suffering most from background CO₂ biases. The system could resolve the background error with a standard deviation of 2 ppm. Overall the base run in contrast to the control inversion without errors shows that the fossil fuel error and background error dominate the NEE error in the posterior results.

Sensitivity tests to the network density and localization method were conducted to check the assimilation's performance in the complex terrain. Five sites are enough to reduce the uncertainty inside the footprint, while 3 more sites outside help to reduce the biases of the posterior NEE fluxes, but even more sites would help to reduce the uncertainty in the western domain. Different spatial localization methods do not lead to statistically distinguishable differences for the total biases in the domain, but for robust cropland results, we recommend the CT2007 localization method, while the covariance location method appears to be a good choice for the other ecoregions. The sensitivity cases also reveal that the redistribution pattern of background CO₂ biases is affected by the spatial length and temporal correlation. Both higher spatial and temporal correlation could reduce the errors from the inside footprint cropland, whose error is most essential inside the footprint, implying both of them should be chosen for more robust posterior fluxes in the footprint.

In conclusion, the evaluation and synthetic tests of CarbonTracker Switzerland demonstrate that this system, together with the CarboCount CH and other observing sites, is potentially well suited to determine the net biospheric fluxes over central Europe and especially Switzerland.

Chapter 5

CarbonTracker Switzerland: Quantifying the net terrestrial biospheric carbon fluxes in central Europe and Switzerland for 2013

Abstract

We estimate the net CO₂ sources and sinks of the terrestrial biosphere, i.e., net ecosystem exchange (NEE), for 2013 in central Europe, especially Switzerland, using CarbonTracker Switzerland. This newly developed high resolution atmospheric CO₂ inversion system uses an Ensemble Kalman Filter to assimilate atmospheric CO₂ observations from 6 sites in central Europe and estimates twice-weekly NEE for a suite of 12 ecoregions in the domain. It uses the weather model COSMO as the atmospheric transport model, configured at 7 km resolution for the central European COSMO-2 domain. As prior, CarbonTracker CH uses the hourly photosynthesis and total ecosystem respiration fluxes from the Vegetation Photosynthesis and Respiration Model (VPRM).

The inversion system is evaluated using 3 independent atmospheric measurement sites that were not used in the assimilation, and the optimized fluxes for Switzerland are compared to the inventory data from the Swiss Federal Office for the Environment (BAFU). The inversion system successfully reduces the data-observations misfits at the independent sites by more than 50%, especially in summer, when the contribution of the biospheric fluxes to the total CO₂ variations is the largest. The error reduction is around 80% in the inner part of the domain, i.e., roughly the Swiss Plateau, and less in the other parts of the domain, largely due a much lower density of observing sites there. The optimized seasonal cycle of NEE is reduced by about 10% largely due a strong reduction in cropland NEE in July relative to the prior VPRM-based estimates, presumably due to harvest.

The total biospheric carbon sink in Switzerland estimated by CarbonTracker CH for 2013

amounts to about 1.4 Tg CO₂, in excellent agreement with inventory data for all ecoregions together. This substantial sink corresponds, however, only to 3% of the fossil fuel emissions in Switzerland for that year. The largest uptake is driven by cropland, followed by forests and grassland. In addition, the atmospheric CO₂ observation tell us that croplands absorb more CO₂ than prior VPRM and also substantially more than the bottom-up inventory would suggest. Mixed forests appear to have suffered more than the other vegetation types from the early hot summer in 2013.

5.1 Introduction

The increasing CO₂ levels in the atmosphere are the most important driver of current climate change, which is the motivation for the global efforts to reduce CO₂ emissions (Thompson et al., 2016). At the COP21 meeting in 2015, the EU committed itself to reduce its fossil fuel emissions by 40% by 2030 to alleviate the most dangerous effects of climate change. This CO₂ reduction policy requires a detailed understanding of the main sources and sinks country by country. This includes not only the CO₂ emissions from the burning of fossil fuels, but also the possible CO₂ sources and sinks from the terrestrial biosphere (Tian et al., 2016).

However, estimating the carbon exchange between the terrestrial biosphere and the atmosphere is a complicated and imprecise endeavor, largely due to the lack of a method to directly measure it over larger scale regions. As a result, one has to rely on non-direct methods to infer these fluxes, commonly grouped into two sets of methods. The first set are the bottom-up methods, in which the fluxes are estimated by in situ measurements (e.g., forest inventories or eddy covariance measurements) and then scaled up using various types of statistical models and large scale observations such as those determined by satellites. Alternatively one may just analyze the measured data to detect the changes of the fluxes (Ballantyne et al., 2012; Ciais et al., 2005; Piao et al., 2009; Jung et al., 2011; Beer et al., 2010). Different studies using this method have helped us to better understand the role of e.g., beetles and fires (Seidl et al., 2014), nutrient availability (Fernandez-Martinez et al., 2014), or droughts and other extreme events (Reichstein et al., 2013; Schwalm et al., 2012) for controlling the ecosystem and the carbon balance. The second set of methods are the top-down methods, wherein measured atmospheric CO₂ gradients are used to infer the surface biospheric fluxes, namely NEE, through various inversion techniques (Gurney et al., 2002; Peters et al., 2007; Peylin et al., 2013; Chevallier et al., 2014; Feng et al., 2016b). The results from such inversion systems have begun to converge recently on hemispheric scales, but still tend to diverge substantially at regional scales, especially in the tropics (Ciais et al., 2013b; Steinkamp and Gruber, 2013).

Recent studies have pushed the inversions towards regional scales. This was made possible by the increasing spatial density of atmospheric CO₂ measurements, reduced uncertainties in other

datasets (e.g., fossil fuel emissions) as well as improvements of transport models on regional and local scales and better parameterized land surface models (Peters et al., 2010; Jiang et al., 2016; Ciais et al., 2010). Such regional inversions share many of the same challenges as the global ones (e.g., time window for the inversion (Gourdji et al., 2012), prior error uncertainties (Chatterjee et al., 2012), different inversion methods (Meesters et al., 2012) or the choice of the observation network (Lauvaux et al., 2012)), but also a different set of challenges emerges. This includes biases in the background CO₂, i.e., that part of the total CO₂ that is transported into the domain from its boundaries (Lauvaux et al., 2012; Alden et al., 2016) and the influence of high temporal and spatial variations in the fossil fuel CO₂ source (Peylin et al., 2011), and the problem that stations may be assimilated twice in the local and regional model, and the system may be recirculated through the outer domain (Rödenbeck et al., 2009). Furthermore, despite a generally higher density of observing stations, regional inversions might be more sensitive to transport errors than global ones, owing to a stronger exposure to local to regional variations in both fluxes and transport.

While there still exists substantially less experience for regional-scale inversions compared to global-scale inversions, much progress in addressing these challenges has been made. In fact, Broquet et al. (2011) concluded from a series of synthetic tests that the inversion of the seasonal NEE variability by means of regional-scale atmospheric CO₂ inversions is by now robust at the scale of entire Europe. But estimates from different studies still diverge strongly.

Current estimates for the net carbon sink in Europe (Atlantic to Ural) fall into the range from near zero to 1.5 Pg C yr⁻¹ across all methods (Reuter et al., 2016, in press), with top-down methods tending to give higher sinks in general (Janssens et al., 2003; Turner et al., 2011; Piao et al., 2011; Kondo et al., 2015). The EU-25 countries have been found to take up CO₂, although with different amplitude from different methods (Ciais et al., 2013b; Schulze et al., 2009; Peters et al., 2010; Chevallier et al., 2014; Feng et al., 2016a). Most of the uptake is assumed to take place by the forests, with a smaller amount by grassland, while almost no uptake is assumed for croplands (Ciais et al., 2010). More uptake in Europe was inferred from an inversion system with satellite based measurements than with in-situ measurements (Reuter et al., 2014).

Most of the regional to local-scale inversions and comparisons between top-down and bottom-up methods have focused on flat regions, trying to avoid complex topography. In contrast, we focus here on a mountainous region, i.e., central Europe with Switzerland at its center (Luysaert et al., 2012; Ramonet et al., 2010). The atmospheric dynamics in this region is more complex, and includes mesoscale mountain flows such as Föhn, but also much smaller scale phenomena such as those associated with the diurnal mountain valley winds (Zardi and Whiteman, 2013). Then there is more orographic precipitation. It is also influenced by episodic maritime air masses, with lower evapotranspiration rates due to lower temperatures in the Alps. This adds to uncertainties not only in the modeled rates of photosynthesis and respiration from process models, but also in atmospheric transport models, owing to the interaction between evapotranspiration, air temper-

atures and atmospheric circulation (Imer et al., 2013). These contrasting environments result in different responses of the terrestrial biosphere to weather and climate fluctuations, depending on the altitude and location (FOEN, 2013; Etzold et al., 2011).

Switzerland's forestry and the harvested wood products absorbed 2.83 Tg CO₂ eq in 2013 (FOEN, 2015). The croplands were a source with contribution of 0.84 Tg CO₂, and forests is a strong sink of 2.26 Tg CO₂ in 2013 based on the bottom-up methods, with higher carbon sequestration intensity than average European forest (Etzold et al., 2011; FOEN, 2015).

The objectives of this chapter are: First, apply the high-resolution regional atmospheric CO₂ inversion system CarbonTracker Switzerland in order to quantify the terrestrial biospheric CO₂ fluxes in central Europe, especially in Switzerland, using atmospheric observations at 4 new measurement sites; Second, to compare the posterior fluxes with bottom-up methods to provide the first independent assessment of the biospheric sources and sinks in Switzerland.

This paper is structured as follows. First, the method and data used for this paper are introduced, followed by the evaluation with measured atmospheric CO₂ concentrations in Switzerland. Then we show the results from our inversion system. Finally, we discuss the results and end with our conclusions.

5.2 Method and data

5.2.1 CarbonTracker Switzerland

The regional atmospheric CO₂ inversion is undertaken using the newly developed CarbonTracker CH inversion system. Its main elements are described in chapter 2, while chapter 4 provides a detailed assessment of its performance with a set of synthetic observations. Here, we provide a summary as well as describe the more detailed choices needed for the assimilation of real observations.

CarbonTracker Switzerland uses the weather and climate model COSMO as its transport model (Baldauf et al., 2011). COSMO is a non-hydrostatic Regional Circulation Model developed by the Consortium for Small-scale Modeling (COSMO) and used as the weather prediction model by several weather services, including the German and Swiss Weather (MeteoSwiss) services. For the atmospheric CO₂ inversions, the COSMO-7 (7 km) configuration developed by MeteoSwiss is employed, but applied only for the central European COSMO-2 domain to limit the computational demand. COSMO is run in fully dynamic mode, i.e., atmospheric transport and mixing of CO₂ is computed online from COSMO's solving the main equation of motion given the initial and boundary conditions provided. The CO₂ is simulated at the same time with the weather in this fully coupled model, which is different from former inversion studies (Peters et al., 2010).

CarbonTracker Switzerland uses a merged product to prescribe the fossil fuel emissions inside its domain, namely a combination of a high resolution (500m*500m) inventory data developed by the company MeteoTest for the Swiss emissions and EDGAR v4.2-7T for the regions outside (see chapter 3). Diurnal, weekly and monthly time profiles based on different sectors or different countries were added in order to create hourly varying emissions for each grid cell of the model. The prior terrestrial biosphere fluxes, split into Gross Primary Production (GPP) and total ecosystem respiration (Ra) were taken from the high resolution Vegetation Photosynthesis and Respiration Model (VPRM), which is based on the assimilation of satellite based measurements of the fraction of the absorbed photosynthetically available radiation (FPAR) from the MODIS satellite.

The boundary conditions for the background CO₂ are taken from CarbonTracker EU, and updated every three hours (Peters et al., 2010). The ecotypes and the ecoregion map are taken from VPRM with some adjustments (see chapter 2). When creating the ecoregion map for COSMO at 7 km, we kept the detailed percentage information inside each grid cell, i.e., an attempt is made to represent the subgrid scale variability in ecoregions in the inversion. Table 5.1 shows the contribution of the different ecotypes to the grid cells where the measurement sites are located. The fluxes are proportionally adjusted based on this percentage.

As the footprint of the CarboCount CH network covers mostly the area of the Swiss Plateau and tapers off quickly thereafter, we separated the ecoregions also by geography, i.e., into a set of ecoregions that are located inside the main footprint, and another set located outside. The croplands dominate as an ecoregion in our domain, being responsible for nearly twice the fluxes than all the others. To account for spatial heterogeneity, we decomposed the original croplands into 4 different regions, due to similar behavior and species at different regions, such as rice primarily dominating in the southern part of our domain, while cropland tends to dominate in the dry land regions in the northern domain. The grassland is kept as one ecoregion in the whole domain due to its small contribution to total NEE.

Table 5.1 Percent contribution of ecotypes at the CO₂ measurement sites considered in the inversion

Site	Mixed forest [%] area	Deciduous forest [%] area	Grassland [%] area	Cropland [%] area	Others [%] area
Lägern Hochwacht (LHW)	-	18.8	-	68.9	12.3
Beromünster (BRM)	10.8	45.5	33.1	10.7	-
Früebüel (FRU)	14.5	19.9	-	19.8	45.9
Gimmiz (GIM)	-	17.4	-	82.6	-
Schauinsland (SSL)	64.4	35.6	-	-	-
Plateau Rosa (PRS)	-	-	28.6	-	71.5
Mounte Cimone (CMN)	-	86.6	-	13.4	-
Sonnblick (SNB)	11.2	-	50.2	-	38.58

The meteorological forcings at the boundaries of the COSMO-2 domain are extracted from the COSMO-7 analysis performed by MeteoSwiss. All these data were extracted and interpolated to the COSMO-2 domain at 7 km and hourly resolution using the Int2LM package. The background CO₂ data and the meteorological forcing data are read in by COSMO every 3 hours, while the fossil fuel emissions and terrestrial biospheric fluxes are fed hourly. The model is run from December 1st of 2012 onward until December 31 of that year in order to generate the initial CO₂ concentrations in the domain. In addition, we do not use the 2-way nested system because the driving data are from the European domain, and we assume that the amount of CO₂ re-entering to the domain after 8 days is negligible in the current domain.

5.2.2 Simulations

The inversion system was run for two different time periods in 2013: from January 1 until October and from September until December, with the initial CO₂ field taken from the one month simulation in December 2012. For the Ensemble Kalman Filter, an assimilation time step of 4 days and a 2 smoother windows were chosen. The choice of 4 days was based on the test from Lagrangian models (Oney et al., 2016, in review). This means that the scaling factors are optimized twice, while the daily observation (average in the afternoon) in each 4 days are used just once to optimize the fluxes in the 1 smooth window (4 days) before.

The time stepping in the Ensemble Kalman Filter consists of a number of concrete steps. First, an ensemble of scaling factors is generated. Thereafter the transport model is called and run to generate an ensemble of 3-D CO₂ concentration fields that is then sampled by the python code to do the inversion step. Finally, new runs are performed with a posterior ensemble. The CO₂ mixing ratio fields generated by the (ensemble of) fluxes is propagated every 3 hours.

The observation error matrix R is prescribed to evolve with time, with lower values in summer and higher ones in winter. But within each season this matrix is kept constant. The prior covariance matrix contains information about the prior assumption of the flux distribution and the correlations between different ecoregions. The spatial correlation length is chosen as 100 km, while the covariance inside each ecoregion is assumed to be 0.64. The off-diagonal for the correlation between ecoregions inside or outside the CarboCount CH footprint is a function of spatial correlation and percentage of the coverage, with the covariance between ecotypes in the same geographic area (such as inside footprint, or southern domain) are 0.49, and the covariance between the ecoregion in the same grid is 0.64, while the covariance between different ecotypes inside and outside the footprint is 0, except if it is the same ecotype. Although sensitivity tests indicated that no localization works best, here we would like to obtain more robust results from forests and croplands, and hence we kept the CT2007 localization method.

The number of CO₂ observing sites used for the assimilation is kept constant throughout

the inversion. In the present configuration, the system assimilates data from six stations inside the domain, namely Beromünster (BRM), Frübüel (FRU), Monte Cimone (CMN), Schauinsland (SSL), Plateau Rosa (PRS), and Sonnblick (SNB) (see Table 2.2 for details). The remaining three sites, namely Lägern Hochwacht (LHW), Gimmiz (GIM), and Jungfraujoch (JFJ) were used for validation. Average afternoon (13-16h local time) CO₂ concentration are used for the inversion and evaluation at the lower altitude sites, whereas the high altitude sites were sampled at night, i.e., from 0-6h local time. The former choice reflects the deep PBL during the afternoon, giving each site a much larger footprint (Oney et al., 2015).

Lägern Hochwacht is kept for the independent validation of the assimilation system due to its high correlation (over 0.8) with the CO₂ concentration at Lägern and at Beromünster. In addition, this site sits on an east-west ridge with some rather complex up-downwind slope circulations, which implies that COSMO will have difficulties to fully resolve the observations given its 7 km resolution. The reason of using Gimmiz as a validation site stems from the high misfits between the model and observations discussed in chapter 4. At the tall tower station Beromünster, only data from the top level are assimilated to avoid over-weighting information from this station and to avoid dealing with correlations in the model error between the top and the bottom levels of a given station. The top level is selected because it has the largest footprint.

The model-data mismatch matrix contains transport model error, representation errors, and observation error. Here we use the seasonal average error of observation and modeled CO₂ concentration (RMSE) from the forward run. During synoptic events, the highly variable measured CO₂ are less reliable due to the pollution by anthropogenic CO₂ signals. The model-data mismatch is usually smaller than the RMSE.

5.3 Results

5.3.1 Evaluation

Fig 5.1 shows a comparison of the observed and the modeled CO₂ concentration series at the sites LHW, GIM and JFJ, i.e., the sites that were not used in the assimilation. Both the prior and posterior modeled atmospheric CO₂ are able to reproduce the observed variations well. At Lägern und Gimmiz, the misfit as expressed by the Root Mean Square Error (RMSE) is reduced in the posterior substantially, particularly in summer (Table 5.2). However, in the annual mean, the RMSE reduction is less than 10%. This is because in wintertime, when the biospheric fluxes are low, the optimization can reduce the difference between prior and observed CO₂ concentration only by a minimal amount. Thus, for much of the seasonal cycle, the errors are retained. The posterior CO₂ concentrations tend to stay very close to the prior values at Jungfraujoch. This is expected since this very high altitude site is practically "blind" to the biospheric fluxes of the

domain, as it records primarily the background CO₂ variations. The low prior RMSE at JFJ means that the background CO₂ concentration is well reproduced, which suggests that the magnitude and vertical profile in the background signal is well captured by CarbonTracker, meaning that the potential bias from this component is likely low. This alleviates a major concern in regional atmospheric CO₂ inversion systems.

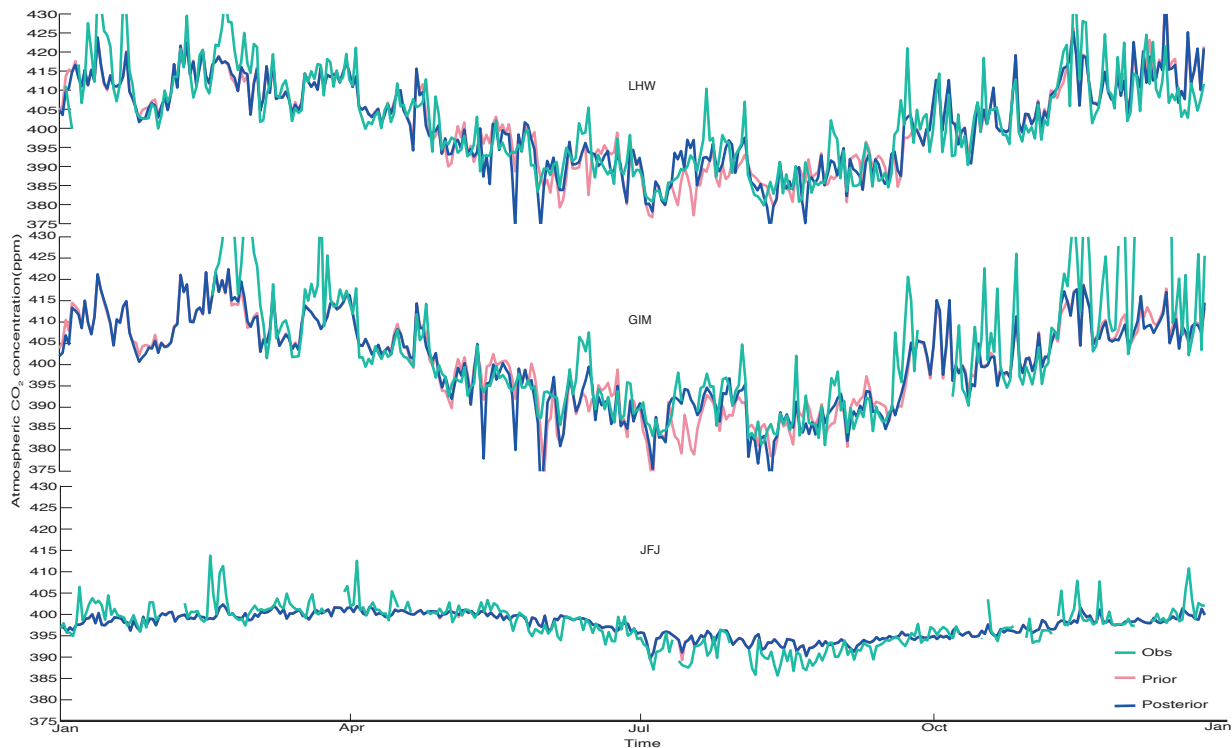


Figure 5.1 Comparison of modeled prior and posterior CO₂ concentration (ppm) with the observed one at 3 independent sites in 2013: LHW, GIM and JFJ. At LHW and GIM data are compared for the afternoon 12-15h local time, while for JFJ, the night time data are used, i.e., 0-6h local time.

Both, mean and variance are reduced significantly in the residuals of the posterior compared to prior CO₂ concentration in summer and autumn (Figure 5.2). In fact, the inversion is very successful in removing the prior bias at these validation sites, such that the median of the posterior residuals is mostly around 0.

The more complete assessment of the prior versus posterior misfits in Table 5.2 shows that especially in summer and autumn there are large biases in the prior CO₂ concentration, mostly stemming from the VPRM model overestimating the strength of the NEE (see also chapter 4). The inversion system is able to reduce this bias substantially, especially at FRU, SSL, and BRM. Transport errors, errors in the flux model (Tolk, 2013), and errors in fossil fuel emissions might contribute to the remaining residuals. Our tests with the synthetic data revealed that the errors introduced by the background CO₂ and fossil fuel emissions could significantly be reduced in the inner part of the domain. Hence, we attribute the remaining error to errors in the prior fluxes and transport error. The fact that the posterior biases are much smaller than the prior biases in CO₂ concentration, gives us confidence into the estimated posterior NEE fluxes.

Table 5.2 Comparison of modeled with observed CO₂ concentrations at the 9 observing sites within the domain : Difference between observed, prior and posterior CO₂ concentrations (daytime averaged) for all stations and seasons. All values are in ppm. The sites LHW, GIM and JFJ are used for independent evaluation.

Site	prior	posterior	prior	posterior	prior	posterior
	RMSE	RMSE	RMSE	RMSE	bias	bias
	annual	annual	summer	summer	summer	summer
Lägern (LHW)	6.4	6.0	6.5	5.6	-1.32	-1.12
Beromünster (BRM)	5.0	4.2	5.0	3.2	-1.01	-0.82
Früebüel (FRU)	5.6	5.1	5.3	4.2	-0.97	-0.004
Gimmiz (GIM)	11.1	11.0	5.5	4.2	-3.22	2.69
Monte Cimone (CMN)	4.1	3.7	6.3	5.5	-2.03	0.67
Schauinsland (SSL)	5.0	4.4	5.3	4.2	-0.38	0.62
Plateau Rosa (PRS)	3.4	3.4	4.3	4.2	4.32	4.28
Sonnblick (SNB)	3.3	3.3	3.9	3.8	3.28	3.22
Jungfrauoch (JFJ)	2.8	2.9	2.7	2.7	2.18	2.22

5.3.2 Source/sink behavior of CO₂ in the domain

5.3.2.1 Error reduction

Fig. 5.3 shows the relative improvement of the uncertainty obtained by CarbonTracker CH, plotted as the annual relative error reduction. The largest error reduction is achieved in the central part of the domain, i.e., in the footprint region of the CarboCount CO₂ measurement sites in Switzerland and of Schauinsland (SSL) in southern Germany. The strongest errors occurs for the mixed forests, deciduous forests, grasslands and the cropland in the inner part of the domain (Swiss Plateau). In contrast, the error reduction in the Alpine regions is very small. But this is largely due to the insensitivity of this ecoregion. This is a result of its small fluxes owing to much of it consisting of bare land and glacier.

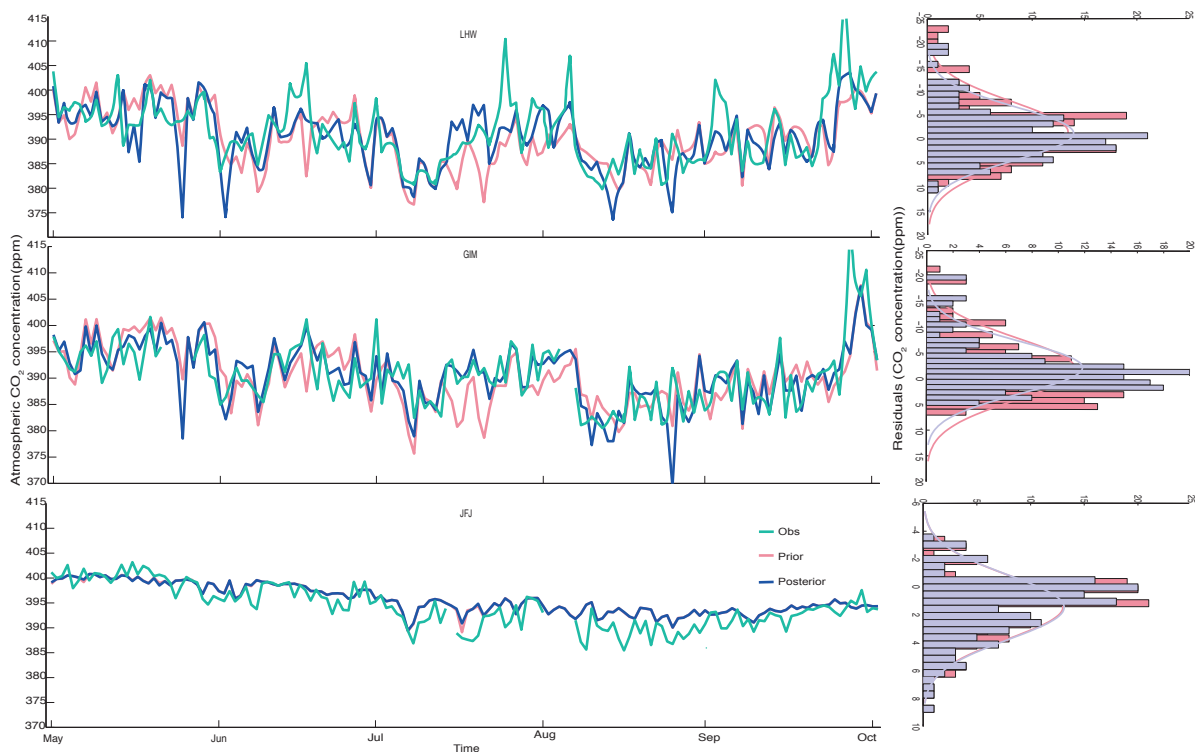


Figure 5.2 Comparison of prior and posterior CO₂ concentration (ppm) from May to September at the three independent sites, i.e., LHW, GIM and JFJ: the left column shows the time series of the CO₂ concentration, and the right column a histogram of the residuals.

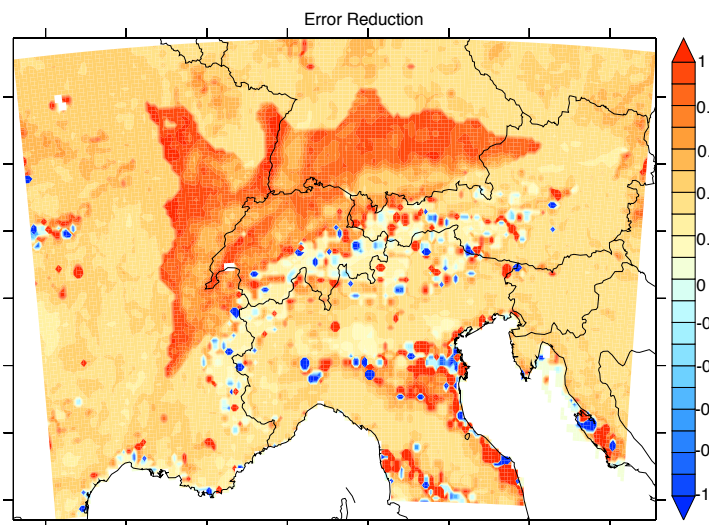


Figure 5.3 Relative measure of error reduction achieved by CarbonTracker CH by assimilating the CO₂ observation from 6 sites in the domain. The relative error reduction is obtained by computing $1 - \text{posterior variance}/\text{prior variance}$.

5.3.2.2 Annual and seasonal average NEE

The annual mean NEE maps indicate for both prior and posterior estimates relatively homogeneous sinks (see Fig. 5.4). The average uptake is reduced from $-0.79 \mu\text{mol m}^{-2}\text{s}^{-1}$ in the prior to $-0.75 \mu\text{mol m}^{-2}\text{s}^{-1}$ in the posterior (see Fig. 5.4). The inversion system also slightly reduces the magnitude of the spatial variations of the fluxes, with the average prior fluxes ranging from -2.3

to $0.8 \mu\text{mol m}^{-2}\text{s}^{-1}$, while the average posterior fluxes range from -2.3 to $0.7 \mu\text{mol m}^{-2}\text{s}^{-1}$.

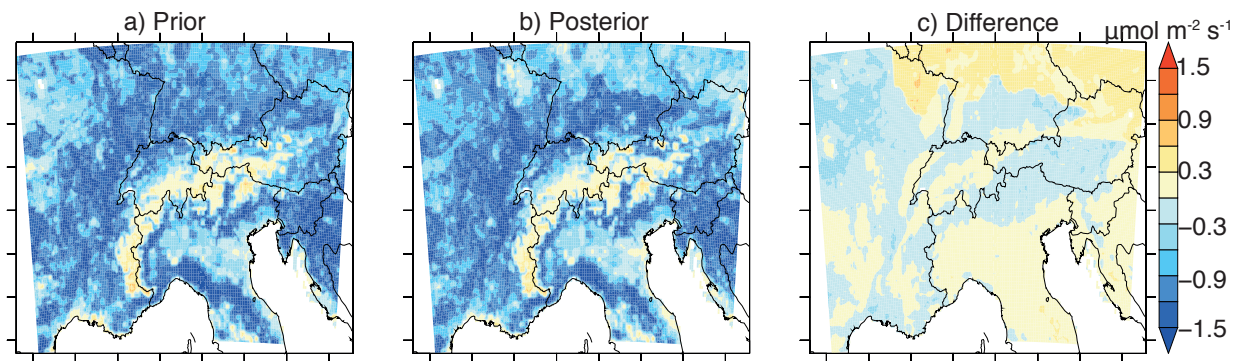


Figure 5.4 Annual mean NEE fluxes in 2013. (a) prior mean fluxes, (b) posterior mean fluxes, (c) absolute difference, with negative fluxes indicating a carbon sink. All panels have units of $\mu\text{mol m}^{-2}\text{s}^{-1}$.

The changes in the annual fluxes are located mainly in the northern and western part of the domain and inside the footprint of the domain. The sink is very small along the Alps and northern part of the domain, while it is strong in southern Italy and France. Compared to the prior VPRM data, the sinks in central Germany and northern Italy are smaller while they are stronger in the western part of France, and southern Germany. Although regions outside the footprint such as western France should remain mostly unchanged by the inversion system, there are still some correlations in the scaling factor of croplands, which caused the changes there. The spatial distribution of the posterior annual mean NEE is highly correlated with the prior NEE, with correlation coefficients over 0.9, indicating that the prior fluxes data might already match the annual atmospheric signal quite well and the system mainly allocate the fluxes inside of the domain. There are some ocean regions where prior and posterior fluxes appear, which might be caused by the interpolation of the land use map. Another explanation might be due to "leakage", i.e., the system redistributes the prior fluxes from land to coaster regions (Gurney, 2004).

Fig. 5.5 shows the seasonally averaged NEE fluxes over Switzerland. Larger seasonal changes can be observed in the western and northern parts of the domain. Spring shows strong uptake in the southern and western part of the footprint region (over $1.5 \mu\text{mol m}^{-2}\text{s}^{-1}$). The relatively large source in Italy presumably comes from the cultivation of rice, as the preparation and tilling of the land before the planting of rice tend to cause substantial CO_2 emissions. The land biosphere acts as a sink almost over the whole domain in summer. Our assimilation reduces the sinks in central Germany, Poland and part of Czech Republic. This suggests a stronger management or harvest in cropland and grassland than the process model VPRM predicts. The winter NEE flux map is dominated by sources in both prior and posterior results, with fewer sources in western part of the domain. Generally, the western domain shows larger changes and higher uncertainties which suggests that more constraints by observations are needed in this region.

Considering the monthly mean fluxes, we found the changes of posterior pattern from month to month to be similar to the prior fluxes. Generally, sources dominate the domain from October

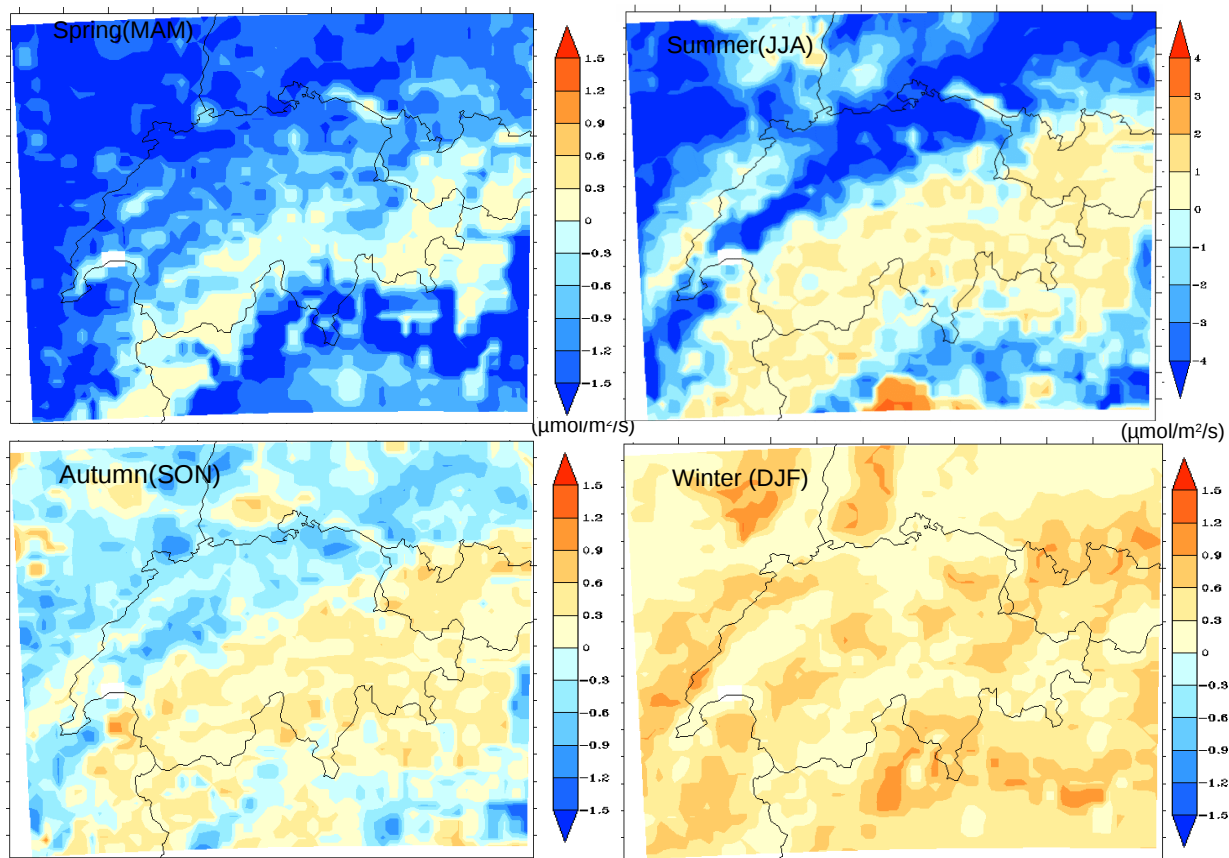


Figure 5.5 Seasonal mean fluxes ($\mu\text{mol m}^{-2}\text{s}^{-1}$) in 2013: upper left: spring (March, April, May); upper right: summer (June, July, August); lower left: autumn (September, October, November); lower right: winter (December, January, February).

until December and January until March. There are smaller sources in January in posterior fluxes (CarbonTracker-CH reduces the prior fluxes from 0.45 to $0.35 \mu\text{mol m}^{-2}\text{s}^{-1}$), while in April, there are stronger sinks in the posterior NEE (drag the fluxes from -0.33 to $-0.35 \mu\text{mol m}^{-2}\text{s}^{-1}$). In the northern and western part of Italy, there are strong sources, due to cropland management.

There is strong uptake in June, due to the very high uptake from cropland in the western part of the domain. Sensitivity tests show that the setup of the inversion system could affect the uptake in the western part of the domain. Whether the strong uptake in western part of the domain in June is real or not, and how large the uptake in this area is, still requires further investigation.

5.3.3 Carbon budget of Switzerland

The total NEE in Switzerland amounts to about $1.28 \text{ Tg CO}_2 \text{ yr}^{-1}$ (Figure 5.6), with about half of it stemming from croplands, followed by mixed and deciduous forests. The contribution of grasslands is relatively small. Even though the assimilation of the atmospheric CO_2 observations by CarbonTracker Switzerland does not change these annual integrated fluxes in a significant

manner, it reduces the uncertainty of these fluxes very substantially.

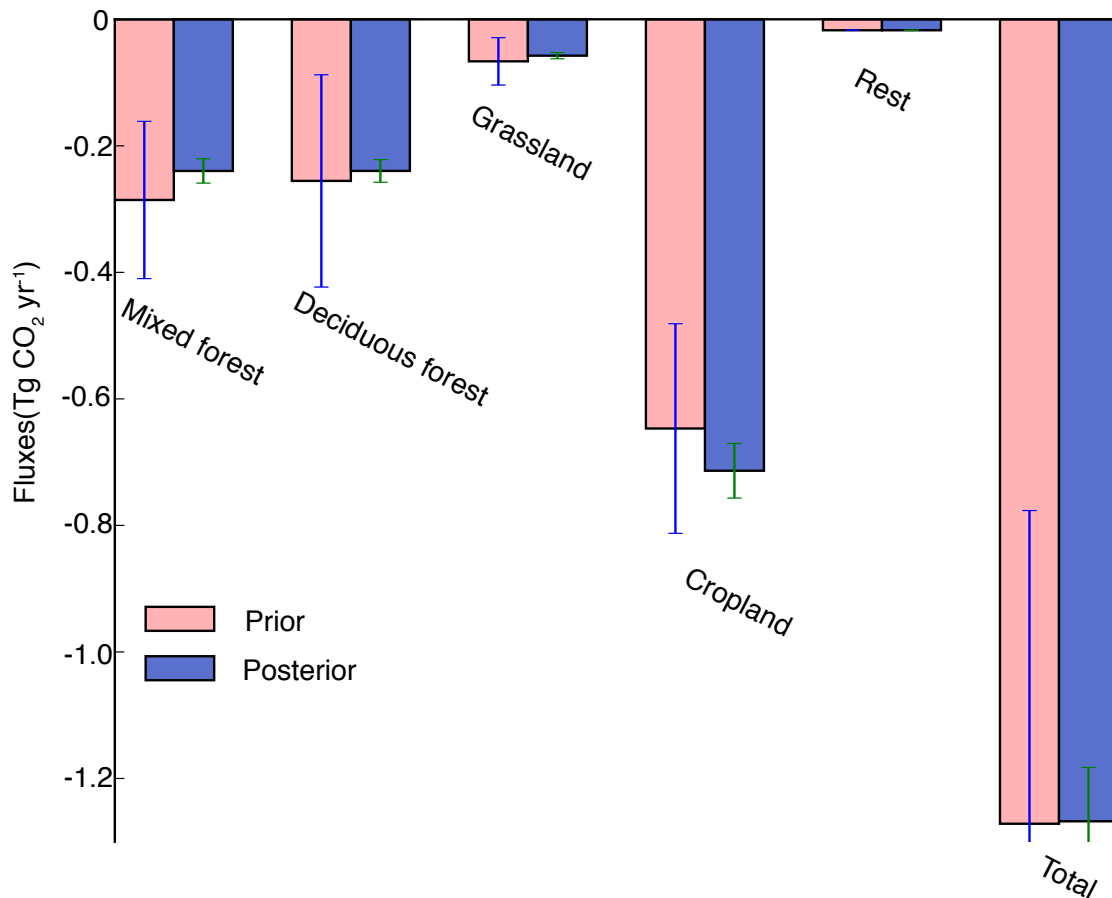


Figure 5.6 Integrated annual ecoregion fluxes in Tg CO₂ yr⁻¹ for Switzerland. Errorbars represent normalized 1 σ uncertainty.

While the annual mean NEE shift little between prior and posterior estimate, monthly NEE in Switzerland changes more substantially (see Fig. 5.7). The maximum NEE in Switzerland shifted from July to June, with a 0.29 Tg CO₂ reduction in the seasonality, i.e., 40% reduction compared to the prior fluxes. Additionally, even though May was colder than normal in 2013, the CO₂ in the atmosphere indicates large posterior fluxes than the prior NEE of the ecosystem model VPRM. In the other months, the shifts are minor. It is unlikely that the shift in seasonality is caused by the transport model, so we assume that this represents a true shift in NEE, driven by distinct changes in the observed CO₂.

Separated into the seasonal cycles for each ecoregion, the shifts become even more evident (Fig. 5.3.3). The posterior seasonal cycle of different ecosystems in Switzerland behave rather differently compared to the prior. For example, the mixed forest (including evergreen forest) have almost 0.06 Tg CO₂ less uptake than the prior estimate in June (corresponding to a halving of the prior fluxes), but then the uptake recovers to the prior level in July, resulting in almost no change in the annual uptake of this ecoregion. The deciduous forest behaves differently, with more

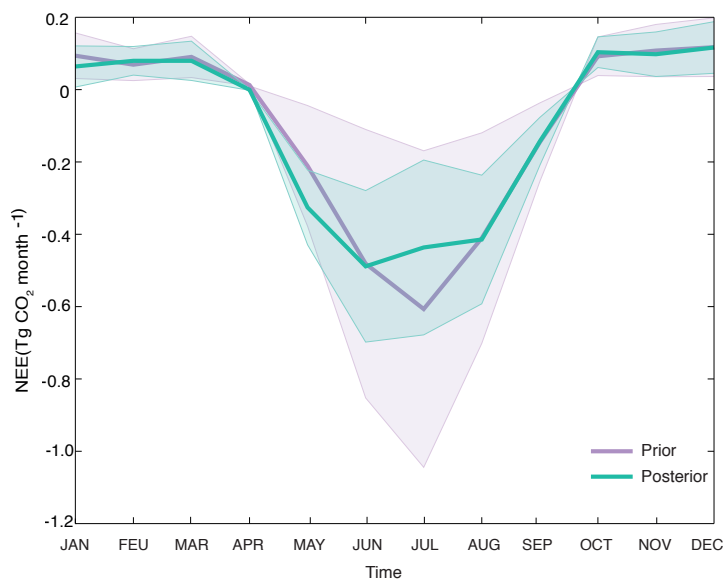


Figure 5.7 Seasonal cycle of NEE in Switzerland. Shown is the prior (purple) and posterior estimate (green), i.e., the estimate after the assimilation of the atmospheric CO₂ data.

uptake in June than July. These difference might reveal different sensitivities of the ecoregions to different controlling parameters, for example, the deciduous forest might be more sensitivity to the high temperatures in July, or there are other mechanisms causing a lag of drought impact on the NEE fluxes in deciduous forest.

The grasslands have a similar seasonal pattern as the deciduous forest, i.e., slightly larger sinks in June, with a 40% uptake reduction in July as compared to the prior. The most dramatic change occurs in cropland, with nearly 0.1 Tg CO₂ more uptake than the prior VPRM data in spring, i.e., the posterior fluxes almost doubled from the prior during this period. But in July, the reverse is diagnosed, i.e., a 68% reduction (=0.146 Tg CO₂) in sinks in July. The shift in seasonality among different ecoregions needs to be investigated further to see if our results are robust, such as assigning all the prior fluxes to forest, or cropland, or using other prior fluxes data and ecoregion maps, or zero prior fluxes.

Table 5.3 shows that the posterior annual terrestrial biospheric uptake integrated over Switzerland for the year 2013 is around -1.33 Tg CO₂, very close to the uptake from estimated the inventory data(FOEN, 2015). For comparison, the integrated fossil fuel emission for Switzerland is around 43 Tg, implying that the Swiss ecosystems could only absorb around 3% of the fossil fuel emissions emitted by Switzerland.

Both inventory data and the top-down method indicate that the forests in Switzerland are strong sinks. However, the annual integral posterior flux from forest is around -0.5 Tg CO₂ equivalent, strongly inconsistent with the inventory data (80% less than the inventory data). Both methods estimate grassland as close to neutral in Switzerland. In contrast, cropland is found to be a strong sink by the top-down method, while the inventory data suggests that it is a weak source.

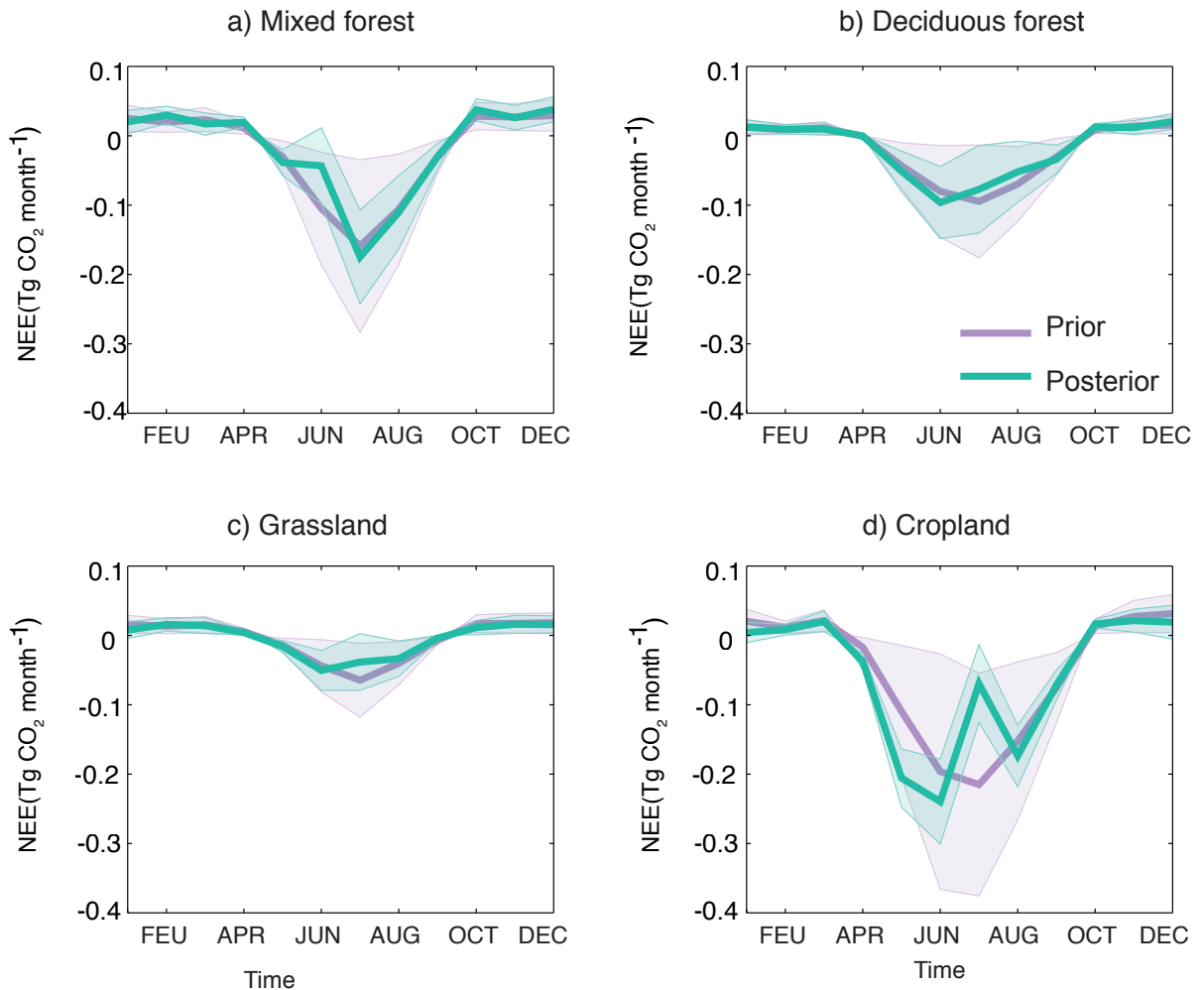


Figure 5.8 Seasonal cycle of NEE by different ecoregions in Switzerland: a) Mixed forest; b) Deciduous forest; c) Grassland; d) cropland.

Although there are large uncertainties after the inversion, the CarbonTracker CH estimates are far away from the inventories. Thus, further investigations are clearly required for this ecosystem.

5.4 Discussion

5.4.1 Posterior fluxes

This study is the first regional atmospheric CO₂-based inversion for terrestrial biospheric CO₂ fluxes for Switzerland. Although eddy covariance methods can measure these fluxes directly, their very limited spatial footprint makes it impossible to scale up these fluxes without sophisticated statistical methods.

Compared to the prior NEE provided by VPRM, there are shifts of the seasonality in the different ecoregions, such as a significant reduction of the uptake by mixed forests, which consists

Table 5.3 Carbon budget of Switzerland. Comparison of the CarbonTracker CH results with the inventory data (unit: Tg CO₂ yr⁻¹).

Ecoregion	Prior fluxes	Posterior fluxes	Inventory
Whole Switzerland	-1.28	-1.33	-1.48
Forests	-0.54	-0.5	-2.68
Grasslands	-0.07	-0.06	0.3
Croplands	-0.65	-0.75	0.87

in Switzerland primarily of conifers. Given their relatively high soil moisture sensitivity, this may reflect the impact of the dry June of 2013 affecting the NEE in this month, and subsequently for the entire year. The deciduous forest appears to have been less affected by the dry weather in June, but the dry weather in June may have had some influence on the posterior fluxes in later months.

The stronger sinks in April and May in the posterior cropland fluxes compared to the prior, might be due to the relatively wet conditions during these months, promoting their growth. However, there were also some rather cool days between March to April, but apparently, they did not leave a strong imprint.

Though the improvement of the total fluxes compared to the prior is not large, the uncertainties in the posterior fluxes are substantially reduced. The comparatively small improvement in the posterior for spring is mainly due to the low vegetation fluxes. Almost no improvement could be achieved in winter when NEE is low, thus requiring huge changes in the scaling factors to shift the predicted atmospheric CO₂ in a substantial manner.

5.4.2 Uncertainties related to the CarbonTracker CH system

In chapter 4, we showed that errors in the background CO₂ concentration affect the posterior fluxes only slightly in Switzerland even when they were combined with fossil fuel uncertainties. Thus, it is reasonable to assume that this is also the case here with the real observations, i.e., that the results here are reliable from May to December, with only a relatively small error stemming from fossil fuel in summer. Another potential bias may be caused by the meteorological forcing data, as errors in wind speed or direction might lead to errors in transport and thereafter fit of the observation to a false ecoregions (Lin and Gerbig, 2005; Miller et al., 2014). For this paper, we use the analysis data from MeteoSwiss who have worked for years with COSMO to improve its

skills owing to their use of this model for weather prediction. Although this error source cannot be excluded, we believe that no big bias is introduced through these means.

A good estimate of the planetary boundary layer is vital for the atmospheric CO₂ inversion, as an overestimate of the estimated PBL height during the day will result in higher sinks, because higher surface fluxes are needed to generate the same concentration level (Turner et al., 2011). Rossa et al. (2012) showed that COSMO-2 tends to indeed underestimate the PBL height during the day compared to observations, which would lead to an underestimation of the carbon sinks by our assimilation system. A mechanism different from Stephens et al. (2007), where the inversion system overestimated the sinks due to the positive mixed layer height in summer. However, the good comparison of total NEE fluxes in Switzerland compared to inventory data, and the well estimated GPP data alleviate such concerns.

While we do not think there is a large impact of errors in the fossil fuel emission in winter as shown by Tolk (2013), more sensitivity tests should be conducted in order to conclude more robust posterior fluxes for different ecoregions. These tests might include inversions with different prior fluxes, although the sensitivity test with synthetic data and a perfect transport model showed that the prior NEE does not matter much. There might be some bias in the posterior fluxes in cropland and forests, because we added the negligible coverage (i.e., ecoregions with coverage lower than 10%) to the ecoregions with highest coverage. The cropland is the dominated ecoregion in most grid, while the forests cover less than 10% in many grids (see chapter 2). In addition, we separate the prior total fluxes into different portions based on the coverage of different ecoregions by assuming that all the ecoregions in Switzerland has the same fluxes density all year around. In the future, we need to test the robustness with more extreme cases, such as distributing wrong portion to different ecoregions, or change the correlation function between different ecoregions, to check the possible uncertainties in the posterior fluxes from different ecoregions. Another test should consider the use of a different fossil fuel dataset, although the fossil fuel CO₂ does not contribute much to potential biases in NEE owing to its primary contribution being in winter when NEE is low. The last set of tests could concern the use of different settings in the inversion system, such as the values in the prior covariance matrix. However, the decreased spatial correlation or different localization methods won't change the posterior fluxes much as demonstrated with synthetic data presented in chapter4.

In this paper we explicitly considered the subgrid scale heterogeneity in the inversion by retaining the relative contribution of different ecotypes to any grid cell of the model. Of course, this inversion system only solve it by simply taking the ecoregion based inversion method, and the spatial correlation between ecotypes in the same grid cell or same ecotypes among different grid cells are difficult to quantify. However, the concept implemented here could be transferred or applied to other regional or global inversion system as well. In the future, the spatial correlation needs to be better described and pixel-based inversion might be adopted here for finer budgets, such as at the scale of states, or regions.

Some researchers are pushing inversion towards the parameter inversion with multi data sources, hoping to better constrain the inversion system. This system could be extended to use column data from high resolution satellite data, or adjusting the parameters in the fluxes field at the same time to constrain the system, and just need to carefully check the potential error or biases in the data to the system.

As Tolk (2013) shows that the pixel inversion to some extent kept the stochastic properties of the prior fluxes, this high resolution inversion might not help much to solve this problem. It is thus doubtful that the finer inversion method would lead to better improvement of the total fluxes than the cut-off domain method as we adopted here.

5.4.3 Top-down and bottom-up methods

Both the top-down and bottom-up methods agree that the forests in Switzerland are strong sink for atmospheric CO₂. This can be expected for a forest that is heavily managed, as the management keeps the mean age young, resulting in most trees growing fast and vigorously (Turner et al., 2011). The two methods also agree that grasslands are a small sink, in agreement with the expectation that grasslands are generally in steady state (Turner et al., 2011).

The inversion with CarbonTracker Switzerland reveals a large and unexpected difference from the inventory data for cropland. One reason might be due to the different consideration of atmospheric view of the CO₂ from cropland, i.e., the source is assigned to the regions with large consumption, while the cropland keeps as strong net uptake (Peters et al., 2007). Another explanation might be the underestimated soil variability from inventory data, as the amount of CO₂ absorbed by crops itself is small and consistent from year to year, while the soil carbon contributes to most of the changes. Besides the uncertainties in the top-down method we discussed before, the various sources of uncertainties in the bottom up method, such as errors in the mapping of parameterization of biogeochemistry, errors in estimating autotrophic and heterotrophic respiration would affect the result of the bottom-up method. The limitation in the bottom-up method lies in the data for the model inputs (such as high uncertainties in the satellite input data) and the uncertainties associated with the model parameters (Turner et al., 2011).

5.5 Summary and Conclusion

The high resolution assimilation system CarboCount CH was successfully applied to a new set of CO₂ concentration observation in order to estimate the biospheric CO₂ fluxes for the first time from such a top-down method.

We run the system for 2013 using six sites for the assimilation, while keeping another three

for validation. The system could optimize the CO₂ concentration at the three independent sites with an almost 50% improvement in summer, and with a 60% to 80% flux uncertainty reduction inside the footprint of the model, indicating that the current measurement setup is sufficient to estimate the CO₂ fluxes of Switzerland. A comparison of the posterior GPP data to MODIS confirms the good performance of the system.

The inversion system does not change the total fluxes in the domain, but it shifts the fluxes between different ecoregions. Northern and western domain fluxes are strong NEE sinks, and optimized by adjusting the cropland contribution in the system, while only minor changes are needed inside the footprint. The posterior seasonal cycle is estimated to be about 40% lower than the prior due to the management in cropland in July, comparing to prior VPRM data. The reduction of posterior fluxes in mixed forest in June partly offsets the seasonality of the total fluxes, which has very different pattern from other ecoregions. The grassland showed smaller seasonal change due to a reduced carbon uptake.

A shift occurs in the seasonal cycle of Switzerland, which is mainly due to an adjustment of the cropland, much smaller uptake in July in posterior due to the harvest or field management.

The total sink in Switzerland is about 1.3 Tg yr⁻¹ in 2013, consistent with the inventory data. In addition, the atmospheric CO₂ observation tells us that cropland absorbs more CO₂ than prior VPRM, while mixed forest suffered from the early hot summer more than other species with reduced posterior uptake in June, which is confirmed by in-situ surface observation. The grassland is mostly neutral, and forests are strong sinks in both methods, with much lower posterior fluxes compared the inventory data.

Chapter 6

Summary, conclusions and outlook

6.1 Background

The goal of this thesis was to develop CarbonTracker Switzerland, i.e., a system to provide high resolution estimates of a regional inversion system aimed at accurately quantifying the terrestrial biospheric fluxes in central Europe and, in particular Switzerland, and to compare this top-down based estimate with bottom-up based estimates, such as forest inventories. The long-term objective of the CarboCount CH project that this thesis is part of, is to track the response of the biospheric carbon fluxes to climate variations and to develop an understanding and ultimately predictive capability of the role of climate change on the carbon balance of Central European ecosystems.

Concretely, CarbonTracker Switzerland uses an Ensemble Kalman Filter (EnKF) technique to combine the atmospheric transport model COSMO with the new CarboCount CH based observations of atmospheric CO₂ in order to optimally estimate a set of scaling factors that determine the magnitude of the net exchange fluxes for a total of 12 discrete ecoregions.

The questions I tried to answer in this thesis are:

1. How well can the high resolution transport model COSMO reconstruct the atmospheric CO₂ concentration from the different components, especially that from fossil fuel emissions at different spatial scales, at individual measurement sites and across the entire domain, with high temporal resolution of the input data?
2. What are the key sources of error of the estimates of CO₂ fluxes, and how much do the input data uncertainties and biases, mainly those associated with the background CO₂ contribute to the uncertainties of inverted fluxes? How important are fossil fuel CO₂ errors in the local inversion system?

3. What are the sources and sinks of CO₂ in Switzerland and what causes differences between top-down and bottom-up systems?

I addressed the first question by conducting extensive forward simulations with the atmospheric transport model COSMO for both the (nearly) entire European domain as well as for the central European domain. The second and third questions were addressed through the use of the CarbonTracker system using synthetic observations from the forward run and then the new observations from the CarboCount CH project.

Although this is not the first high resolution atmospheric CO₂ inversion system in Europe (Tolk, 2013), it is the first focusing on central Europe and Switzerland. Further, it is the first study that uses the new CO₂ measurement data to assess the sources and sinks from different ecoregions from bottom-up inventory data. It represents a new regional inversion system method for characterizing and predicting regional CO₂ fluxes. Others have previously developed regional inversion systems with coarse temporal resolution (typically seasonal) and also often with spatial resolutions of more than 10 km (Meesters et al., 2012; Tolk et al., 2011). In this work I developed an EnKF-based system with a transport model that has a resolution of 7 km, i.e., one that is at the higher end of the spectrum of previous studies and also covers a more extensive domain compared to previous high-resolution studies. Further, my inversion system accounts for the transport of separate tracers for gross primary production and total ecosystem respiration taken from the high temporal and spatial resolution vegetation model VPRM.

The CarbonTracker CH system is based on previous versions of CarbonTracker (Peters et al., 2010), but had to be adjusted to the regional scale by explicitly considering the role and contribution of the lateral boundary conditions. In addition, several new elements have been implemented. First, hourly resolved variations in the high resolution fossil fuel emissions were implemented instead of the commonly assumed time constant, or just seasonally resolved emissions (Peylin et al., 2011). Second, a covariance localization method (Zupanski et al., 2007) (typically not adopted for such models) was implemented in this system to check the influence from the topography on the optimization process. Third, instead of using the approach of retaining a single dominant ecoregion within each grid cell (Peters et al., 2010; Tolk, 2013), I retained the ecological composition within each grid cell to explicitly account for the subgrid scale heterogeneity of the ecoregions. Fourth, I used a weighted average of the different smoothing windows to represent the temporal correlation in generating the prior scaling factor, and the system was tested with more realistic error structure, i.e., with varying biases following a Gaussian distribution for fossil fuel emissions and with a 5-day autocorrelation in the case of background CO₂ concentrations (representing the synoptic error).

6.2 Summary and general conclusions

In Europe, the fossil fuel component is the dominant contributor to the surface spatial gradients in atmospheric CO₂. The fossil fuel footprint contributes to more than half of the total temporal variations in atmospheric CO₂ in most areas of northern and western central Europe. Some of the largest variations tend to occur at diurnal scales owing to the combination of diurnal variations in emissions and atmospheric mixing/transport out of the surface layer. The covariations of these two factors, i.e., the fossil-fuel diurnal rectifier effect, leads to a difference as large as several ppm compared to a case with time-constant emissions. Each of the fossil fuel emission sector has its own distinct footprint, with that from fossil fuel fired power plant having the most distinguishable one owing to its stationarity and its extremely high emission density. Various simulations show that a reduction in fossil fuel emission by 30% from a given power plant is at the edge of detectability by the current generation of satellites (e.g., OCO₂), although changes in the variance could be seen already at lower levels of reduction. This indicates that changes in variability might provide an additional method for the monitoring and verification of changes in fossil fuel emissions. Increase in the frequency of satellite overpasses will enhance the possibility of detecting the fossil fuel emissions changes in the future.

Extensive tests with synthetic data fed to the CarbonTracker CH system reveal that the current CO₂ observation network is enough for removing more than 90% error from prior net biospheric (NEE) fluxes. This suggests that the complicated topographic region with patchy ecoregions does not prevent a successful application of a relatively standard inversion system. The tests also show that the biospheric fluxes are sensitive to a number of parameters and choices associated with the inversion system. For example, an inversion that accounts for the subgrid scale variability in ecoregions gives an around 20% higher error reduction and 10% less posterior error than an inversion that just accounts for the dominant ecoregion. Further, croplands in the core region, i.e., defined through the footprint of the CarboCount CH observing stations, and deciduous forests in the northern part of the domain suffer most from background CO₂ biases. Longer spatial and temporal correlations (1 month) are required to remove the biases in the background CO₂ for robust posterior fluxes, even though a background error with standard deviation as large as 2 ppm could be removed by the system. The influence of uncertainties from fossil fuel emissions on the posterior fluxes mainly occurs in summer, and this influence is relatively weaker than the background CO₂ biases. The tests of combining NEE error, fossil fuel error and background error imply that the fossil fuel error and background error dominate the NEE error in the posterior results. With combined biases from fossil fuel and background CO₂, the system underestimates the fluxes in the northern domain and overestimates in the southern part in summer, and produces robust results in the eastern and central part of the footprint from May to December in 2013.

Using real measured atmospheric CO₂ data to estimate the posterior fluxes for Switzerland with CarbonTracker CH resulted in high-confidence estimates owing to the significant improve-

ment in both posterior CO₂ concentration and posterior GPP comparing to the independent measurements or MODIS observation. The inversion system has a small impact on the total annual biospheric fluxes in the domain, but shifts the fluxes between different ecoregions and between seasons.

The fluxes in the northern and western domain are optimized due to the prevalence of cropland. However, the amplitude of the posterior seasonality from cropland inside the footprint is reduced by about 17% relative to the VPRM-based prior likely owing to the management of cropland in July. The reduction of the posterior fluxes in mixed forests in June partly offsets the seasonality of the total fluxes, the former having a very different seasonal pattern from other ecoregions. The grassland showed a smaller seasonal change due to lesser carbon uptake. The shift occurring in the seasonal cycle of Switzerland is mainly from cropland, with much less uptake in July in posterior fluxes comparing to the prior VPRM fluxes, due to harvest or field management.

The total sink in Switzerland is 1.33 Tg yr⁻¹ in 2013, commensurate with the inventory data. More than half of the carbon sink is contributed by cropland. The forest are sinks suggested by the top-down method, with posterior uptake of 0.5 Tg yr⁻¹. Possibly because mixed forest suffered from the early hot summer more than other ecoregions, their posterior uptake was reduced in June. The grassland is almost neutral.

6.3 Caveats and outlook

The CarbonTracker CH inversion system is an ecoregion-based inversion, that is, the entire ecoregion in a domain is adjusted at the same time. Even though we split the spatial domain into subregions using a combination of footprint sensitivity and climatic/topographic gradients, such an ecoregion based method might still bring some problems for complex topographic regions, e.g., the grassland in Switzerland at high altitude may behave differently from the grassland at lower altitudes, and hence sites such as Beromünster and Frübüel might act as different types of grassland. One way to solve this problem is to implement a pixel based inversion system, though the comparison from Tolk (2013) showed that the posterior fluxes did not differ much between a pixel and an ecoregion based inversion. Any future pixel and percentage based inversion method would require better description of the spatial correlation of fluxes in concert with the computational power, for example the problem of correlation of different ecoregions inside one pixel and correlation between neighbouring pixels to avoid inflating an already underdetermined problem given current observation density.

In addition, this thesis mainly focused on monthly or seasonal improvements of the prior biospheric fluxes. In the future, it would be highly attractive from an ecosystem point of view to take advantage of the high temporal resolution observations in order to improve the estimates

at shorter timescales, even down to the diurnal cycle. The latter would also help to improve our understanding of the seasonal cycle, which requires reducing inconsistencies with night time data in the inversion system, because night time CO₂ generally degrade the inverted results.

Furthermore, any transport model error is biasing the inverted fluxes, e.g. imperfectly estimated PBL can result in misinterpreted fluxes in the inversion system, or lead to the inaccurate determination of meteorological variables (primarily wind speed). As the mismatch between the observation and model is relatively small relative to the spread of the ensemble members, I did not quantify how such potential biases may influence the optimized results. The main reason is that this was viewed as being beyond the focus of this thesis.

Another source of error in the system are the boundary conditions. The boundary conditions used in this thesis for the COSMO-2 domain were taken directly from CarbonTracker Europe, which might be too coarse for its direct use in my regional inversion system and potentially bias the results, although available test results in chapter 4 suggest that the boundary condition do not lead to large biases in the budget of CO₂ inside the footprint when combined with fossil fuel uncertainties. One possible solution to improve the inverted fluxes is to optimize the background CO₂ using observations, which requires either aircraft measurements or other direct measurements that could provide accurate background CO₂ for the domain (Alden et al., 2016). This system follows the traditional way to deal with fossil fuel CO₂ with no associated uncertainty, which might result in spatial and temporal biases in posterior NEE, i.e., carryover bias (Basu et al., 2016). New approaches could be adopted where tracer based estimates are used to infer the fossil fuel footprint (Oney, 2016), having the potential to reduce the errors in regional NEE estimation in the inversion system with more realistic assumption about transport errors will affect the results.

More sensitivity tests to generate more robust results for different ecoregions would be worthwhile, such as how uncertainties in the fossil fuel emission inventory affect the inverted fluxes (Thompson et al., 2016; Peylin et al., 2011). In addition, although our tests in chapter 4 demonstrated that the inverted fluxes converge very well to the "truth", even when the priors are perturbed by up to 90%, these tests were done in a perfect transport setting. Thus we cannot exclude the potential biases in the fluxes from the land surface models or process models (since the spread of different transport models are significant at the regional scale (Geels et al., 2007)). More sensitivity tests yield more robust results using different prior fluxes or different transport models.

Multiple data streams could be assimilated into the system to reduce the uncertainties of fluxes and hence improve the optimization, such as the satellite data (from the recently launched OCO2). In addition, optimizing a set of model parameters related to photosynthesis in a process-based model that incorporates different data sources might benefit the whole inversion method as well (MacBean et al., 2016), such as by using eddy covariance flux measurements, FAPAR products, and soil moisture data. These multiple data streams might correct some poorly parametrized

processes or even help discover missing processes in the terrestrial ecosystem model.

The last issue in the data assimilation is that we found the residuals between the observations and the model to be non-Gaussian distributed. Some systems have already incorporated methods for accounting for the non-Gaussian distribution of residuals between models and observations, such as Gaussian Mixture method. We tested one extreme event that has a very large mean with small standard deviation outliers for one month (with standard 10 times less than mean errors), but further tests are necessary for the evaluation of more common scenarios, such as uniform noise with smaller mean and higher standard deviation; how would this noise affect the assimilation system in the growing period when the photosynthesis is strong, and so on.

Acknowledgements

I would really like to thank my supervisor Nicolas Gruber for guiding me through the past four years. I am grateful to him for introducing me into this field for helping getting started in the early stage of my PhD. I also appreciate that he introduced me into the science community by providing the opportunities for meeting with different scientists who visited ETH and by encouraging me to attend conferences and summer schools on different topics to broaden my horizon. It would have been hopeless without Nikis guidance and abundance of insightful ideas through this project. From him, I not only learned a lot about science, but also a lot of things in life. I am sure that I could not find a better supervisor than him.

I thank Dominik Brunner for leading this project and for organizing everything to make the project run successfully. Specially, I would like to thank him for spending time helping me with the model and data, and also for the insight of science. I really think I am really fortunate to have his supervision and contribution.

I thank Wouter Peters for providing a lot of help at the beginning of the PhD and sharing the experience of Ensemble Kalman Filter. Without this help, I wont make the work out faster. Thanks also go to Wouter for providing me the chance to visit the University of Wageningen and join in interesting group meetings and the TRANSCOM meeting. I am also thankful for the help from Ingrid van der Laan-Luijkx.

I am also grateful to Anne Roches fom C2SM for her contribution to set up the model at CSCS and help with the technical support with the model. Thanks also to the CSCS community for helping out with problems on the supercomputer and Katherine Osterried for the help in the past one year.

I would like to acknowledge the funding for my research from the Swiss National Science Foundation(SNSF). I was happy to be part of this project, especially as it involved working in a highly collaborative team, with many interactions and communication with Stephan Henne, Sonia Seneviratne, Edouard Davin. It was really great to work with other PhDs from this project: Brian and Stefanos, and a lot of fun with them.

I am grateful to all members in the group, especially for Bianca, Damian, Thomas, David, Matt. It was really a nice group with a lot of interesting events and fun together that enriched my

life. At last I would thank my family for supporting me all the way through my life.

Curriculum Vitae (CV)

Liu Yu

IBP, Environment Science, ETH

Mailbox: CHN, E29, Universitaestrasse 16, 8092 Zurich, Schweiz

Tel: +41 78 624 1343

Educational Background

1. 04.2012-8.2016 PhD. in Environmental physics at ETHz, Switzerland
Title of the dissertation: CarbonTracker Switzerland: A high resolution Ensemble Kalman Filter System to constrain biospheric CO₂ fluxes in central Europe
2. 09.2007-06.2010 M.S.c in Cartology and Geographic Information System(GIS) at Beijing Normal University, China
Title of Master thesis: An assimilation system to estimate snow via Ensemble kalman Filter using microwave remote sensing data
3. 09.2003-06.2007 First B.S.c in Geography at Central China Normal University
4. 09.2004-06.2007 Second B.S.c in Biology

Publications

1. Yu Liu, Lingmei Jiang, Jiancheng Shi, et al. Measurement And Simulation of The Snow Properties At An Alpine Valley Site, IGARSS, IGARSS 2009
2. Yu Liu, Lingmei Jiang, Jiancheng Shi, et al. Validation and sensitivity analysis of the snow thermal model(SNTHERM) at Binggou basin, Gansu. Journal of Remote Sensing (In English), 2011, 4

3. Y. Liu, N. Gruber, D. Brunner. Spatiotemporal patterns of the fossil-fuel CO₂ footprint in central Europe: Results from a high-resolution atmospheric transport model. Atmospheric chemistry and physics. (In review)
4. Y. Liu, N. Gruber, W. Peters, D. Brunner. CarbonTracker Switzerland: Quantifying the net terrestrial biospheric carbon fluxes in central Europe and Switzerland for 2013. JGR: Biogeosciences. (In preparation)
5. van der Laan-Luijkx, I. van der Velde, E. van der Veen, A. Tsuruta, K. Stanislawski, A. Babenhauserheide, H. Zhang, Y. Liu, W. He, H. Chen, K. A. Masarie, M. C. Krol, and W. Peters. The CarbonTracker Data Assimilation Shell (CTDAS) v1.0: implementation and demonstration of a versatile ensemble Kalman filter system. Geoscientific Model Development. (In review)

Teaching experience

1. 09.2013-09.2015 Teaching assistant of physics experiment
2. 09.2008-01.2009 Teaching assistant for Microwave Remote Sensing

Involved Projects

1. Participated in Key Project of Chinese National Programs for Fundamental Research and Development (973 Program), the third problem Reflect, radiation mechanisms, parametric inversion
In Situ Measurement and observation in synchronism with the satellite
2. The state high-tech research and development plans (863) research for method to inverse snow in the field of microwave remote sensing
Responsible for the assimilation system (using the Ensemble Kalman Filter (ENKF) to combine the snow process model and the microwave radiative transfer model with the remote sensing data)
3. National Natural Science Foundation: snow project Num. :40701115
Involved Model: the Snow Thermal Model (SNTHERM, a complex physic model developed by Jordan, U.S. Army Cold Regions Research and Engineering Laboratory)
Research of the technology and model for controlling of malignant invasive plant *Ageratina adenophora* Participated in design and implement the database of spectrum of *Ageratina adenophora*

Presentation

1. Poster in ICDC conference, 2013, Beijing: A high resolution regional CO₂ assimilation system for estimating terrestrial sources and sinks in central Europe
2. Oral presentation in Transcom meeting, 2014, Netherlands: Modeling anthropogenic CO₂ in Europe using a high resolution atmospheric model
3. Poster in EGU conference, 2015: Modeling anthropogenic CO₂ in Europe using a high resolution atmospheric model

Summer school

1. 13th International Swiss Climate Summer School 2014 "Linking land use, land cover and climate"
2. Data assimilation and carbon cycle, 2014
3. 14th Young Researchers Meeting Science and Communication, 2015

List of Figures

1.1	Schematic of the global carbon cycle taken from Ciais et al., (2013). The numbers are the stock of carbon (Pg C) in each reservoir, while the arrows show the fluxes (Pg C yr ⁻¹). The red arrows and numbers refer to the anthropogenic fluxes, while the black ones denote the "natural" fluxes.	9
1.2	Annual anthropogenic CO ₂ emissions and their partitioning among the atmosphere, land and ocean (Pg C yr ⁻¹) from 1750 to 2011. See Ciais et al. (2013b) for details.	11
2.1	A schematic flow diagram of a carbon data assimilation system using observed CO ₂ concentrations.	31
2.2	Schematic drawing of the time stepping used in an Ensemble Kalman Filter. . . .	31
2.3	The schematic draw of the assimilation system using observed CO ₂ concentration.	38
2.4	The geographic domain of CarbonTracker Switzerland. The domain is the same as that of the COSMO-2 setup used by MeteoSwiss, but with a resolution of 7 km.	40
2.5	The distribution of different eco regions: percentage of area in each pixel(%). . .	43
2.6	Map showing the CarboCount CH measurement sites for atmospheric CO ₂ in the context of other carbon related activities in Switzerland, such as FluxNet (Eddy Covariance Measurements) and the NABEL network (air quality).	45
3.1	Map of the fossil fuel emissions used in this study. Also depicted is the domain of the COSMO-7 setup employed here. Shown in transparent color are the fossil fuel CO ₂ emissions for different sectors in units of gC m ⁻² yr ⁻¹ . The colors from the different sector blend to a darker color when they are co- located as shown by the color mixing star at the bottom right.	52

3.2	Time dependence of fossil fuel CO ₂ emissions for different sectors and countries. (a) Time functions for the diurnal and weekly emissions for four sectors. (b) Annual evolution of the CO ₂ emission intensity for three different countries or group of countries. Shown are the daily minima and maxima for each country.	54
3.3	Comparison between modeled and observation-based estimates of the fossil fuel CO ₂ component. (a) Comparison at the Lutjewad site in the Netherlands (LUT, 6° 21'E, 53° 24'N, 1 m a.s.l.) (van der Laan et al., 2010; Bozhinova et al., 2014). (b) Comparison at Heidelberg (HEI, 49.417° N, 8.675° E, 116m a.s.l.) (Levin and Karstens, 2007). The observational estimates are based on concurrent observations of CO and ¹⁴ CO ₂	58
3.4	Maps of the model simulated annual mean components of atmospheric CO ₂ in the surface layer (10 m above ground). (a) fossil fuel component, (b) total atmospheric CO ₂ , (c) terrestrial biosphere component, and (d) background CO ₂ component. The results are shown as dry air mole fraction with units of ppm.	60
3.5	Instantaneous snapshot of the model simulated fossil fuel CO ₂ in the surface layer. (a) Snap shot on July 1st at 06 00 GMT, (b) as (a) but at 18 00 GMT, (c) snapshot on January 1st at 06 00 GMT, (d) as (c) but at 18 00 GMT.	61
3.6	As Figure 3.4, but for whole air column averaged dry air mole fraction in units of ppm.	62
3.7	Maps of the annual standard deviation of (a) the fossil fuel component and (b) atmospheric CO ₂ in the surface layer.	64
3.8	Maps of the contribution of fossil fuel CO ₂ variability to total atmospheric CO ₂ variability on various timescales in percent. (a) Contribution over all timescales; (b) contribution for the seasonal timescale only; (c) contribution for the synoptic timescale only; (d) contribution for the diurnal timescale only.	65
3.9	Maps of the impact of the consideration of time-varying fossil fuel emissions. (a) Difference in annual mean surface CO ₂ between the case with time varying and time-constant fossil fuel emissions. This difference represents the fossil fuel rectification effect. (b) Linear correlation between the fossil fuel emissions and the height of the planetary boundary layer height in the COSMO-7 model. Pixels with emissions smaller than 0.06 gC m ⁻² yr ⁻¹ are not plotted. The positive correlation implies high emissions when the PBL is deep, and vice versa. Most of this correlation stems from the diurnal time-scale, but the correlation is enhanced through the (mostly) positive correlation also on seasonal timescales.	67

- 3.10 Maps of the annual mean fossil fuel CO₂ generated by different countries/regions. (a) Surface pattern created by the emissions from Germany, (b) as (a), but for the France. (c) Column averaged pattern created by the emissions from Germany, and (d) as (c), but for France. 70
- 3.11 Pie charts depicting the origin of the fossil fuel CO₂ signal for each country/region. The percentages represent the contribution of each country/region of origin to the total fossil fuel signal in the averaged over the air column. The pie chart for Switzerland reveals, for example, that only 20% of the fossil fuel CO₂ signal over its territory stems from its territorial emission. Here, CH: Switzerland; DE: Germany; FR: France; IT: Italy; AT: Austria; NL: Netherlands; SW: countries in southwest of the domain; UK: United Kingdom; EA: countries in eastern domain; OT: the rest of countries. 71
- 3.12 Maps of the annual mean surface fossil fuel CO₂ stemming from different sectors in units of ppm. (a) fossil-fuel fired power plants, (b) residential heating, (c) industrial processes, and (d) road transportation. 72
- 3.13 Maps of the annual mean relative contribution of each sector to the total surface fossil fuel CO₂. a) fossil-fuel fired power plants, (b) residential heating, (c) industrial processes, and (d) road transportation. 73
- 3.14 Changes in annual mean atmospheric CO₂ and its standard deviations resulting from a 30% reduction in the fossil fuel emissions from all sectors. (a) Change in surface mean CO₂. (b) Change in the column averaged CO₂, i.e., $\overline{XCO_2}$. (c) Change in the standard deviation of surface CO₂ (all seasons). (d) Change in the standard deviation of the column averaged CO₂, i.e., $\overline{XCO_2}$. The standard deviation refers to the differences of the afternoon data (at 1:00 PM) to the annual afternoon average. 76
- 3.15 Impact of reductions in power plant emissions on the mean and standard deviation of the fossil fuel CO₂ signal . (a) probability density distribution of the surface atmospheric CO₂ for the present and for a case when the power plant emissions were reduced by 50% at a site in eastern Germany (50.32°N,13.19°E). (b) Relationship between the changes in the mean and the standard deviation of the column averaged CO₂ for a given reduction in power plant emissions, with different color representing representing different sites with different characteristics in their response to this reduction in emission: Blue (50.32°N, 13.19°E), Cyan (50.32°N, 6.59°E), Red (42.48°N, 6.51°W), Orange (49,28°N, 6.14°E) (Locations shown in Figure 14b with green circles). 77

- 4.1 Map showing the simulation domain of COSMO-2 and the dominant ecoregions at each grid cell of the model: 1-3: Mixed Forest; 4-6: Deciduous Forest; 7: grassland; 8-11: croplands, white area: others. The darker colors indicate the ecoregions that are inside the footprint of the observing sites of the CarboCount CH network, with the footprint boundary shown as a black line. While only the dominant ecoregion is shown, the inversion actually considers the relative contribution of each ecoregion present in a grid cell. The white areas belong to the group of 'others', which is not solved for in the inversion as their CO₂ fluxes are very small. 87
- 4.2 Comparison of average CO₂ concentration in the afternoon (from 12:00 to 15:00 UTC) between observation and model in 2013 at 8 different sites. 96
- 4.3 Time series of the different component contributing to atmospheric CO₂ (ppm) at daytime at the Beromünster site (selected from 12:00 to 15:00 UTC). 97
- 4.4 Spatial distribution of annual mean total CO₂ mole fraction (ppm) at height 10 meter (lowest level in the model) in 2013, with the 9 measurement sites indicated by symbols, i.e., 5 sites inside Switzerland (LHW, FRU, BRM, GIM, JFJ), 2 in Italy (PRS, CMN), 1 in Austria (SBN), and 1 in Germany (SSL). The solid line indicates the path for the north-south cross section along LHW, BRM and JFJ. . . 98
- 4.5 Modeled diurnal cycles of CO₂ concentration (ppm) from model simulation: difference between each site and site JFJ. a) annual mean diurnal cycle (January to December in 2013); b) Summer mean diurnal cycle (June to August in 2013); c) winter mean diurnal cycle (December, January and February in 2013). 99
- 4.6 Modeled seasonal cycle of atmospheric CO₂ at 6 sites within the model domain for the year 2013 (ppm). Shown is the difference between each site and JFJ. To emphasize the seasonal cycle, the records were smoothed with 1 month running mean filter. 100
- 4.7 North-south vertical section of the annual mean total CO₂ and its components along the line shown in Figure 4.4, i.e., connecting Lägern (LHW), Beromünster (BRM), and Jungfrauoch (JFJ) (ppm). (a) Total CO₂, (b) Background CO₂ component, (c) fossil fuel CO₂ component, and (d) biospheric CO₂ component. The vertical axis is plotted logarithmically to emphasize the strong vertical gradients in the lowest layers of the atmosphere. 101

- 4.8 Results from the base run for the period of the whole year in 2013. (a) Map of error reduction, calculated from the ratio between the posterior and prior variances, i.e., $1 - (\text{posterior variance} / \text{prior variance})$; (b) Map of mean NEE fluxes from VPRM, taken here as the true fluxes $\mu\text{mol m}^{-2}\text{s}^{-1}$; (c) bias of prior fluxes relative to true fluxes, calculated as prior - truth; (d) bias of posterior fluxes relative to true fluxes: calculated as posterior fluxes - truth fluxes. 103
- 4.9 Integrated fluxes per ecoregions for of the whole year in 2013 estimated by the base run in units of mol/region/s. 104
- 4.10 Seasonal mean flux biases relative to the truth (unit: $\mu\text{mol m}^{-2}\text{s}^{-1}$): the first row are errors of NEE, GPP, Ra in spring (March-May of 2013); the second row are errors of NEE, GPP, Ra in summer (June-August of 2013); the third row are errors of NEE, GPP, Ra in autumn (September-October of 2013); the fourth row are errors of winter (December, January, February of 2013). 105
- 4.11 Time series of weekly NEE fluxes at 5 measurement sites in 2013: unit ($\mu\text{mol m}^{-2}\text{s}^{-1}$). 107
- 4.12 Results of the control run (S2) for July to August, 2013. a) Map of error reduction, calculated as $1 - (\text{posterior variance} / \text{prior variance})$; b) Map of mean true fluxes $\mu\text{mol m}^{-2}\text{s}^{-1}$; c) bias of prior fluxes relative to true fluxes, calculated as prior - truth; d) bias of posterior fluxes relative to true fluxes: calculated as posterior fluxes - truth fluxes. 108
- 4.13 Integrated fluxes per eco regions, unit mol/region/s: over July to August in 2013. 109
- 4.14 Sensitivity test to different network choices from July to August. Different shape are from different simulations, and different color representing different eco regions. 110
- 4.15 Sensitivity tests to different localization methods for the months July to August. Different symbols indicate different simulations, and different colors represent different eco regions. 111
- 4.16 Sensitivity test to different eco region map: a) and c) error reduction from dominant or percentage eco region maps) and d) relative improvement comparing to the truth from dominant or percentage eco region maps, relative improvement is calculated as the $(\text{posterior} - \text{truth}) / \text{truth}$, unitless. 118
- 4.17 Sensitivity test to background CO_2 biases with 8 sites: unit: $\mu\text{mol m}^{-2}\text{s}^{-1}$: a) 100km spatial correlation and 8 days temporal correlation; b) 30km spatial correlation and 8 days temporal correlation; c) 300km spatial correlation and 8 days temporal correlation; d) 100km spatial correlation and 30 days temporal correlation. 119

4.18	Map of annual mean fluxes biases relative to the truth with added fossil fuel biases (unit: $\mu\text{mol m}^{-2}\text{s}^{-1}$), calculated as average of prior or posterior fluxes minus true fluxes.	119
4.19	Seasonal mean fluxes biases relative to the truth with added fossil fuel biases (unit: $\mu\text{mol m}^{-2}\text{s}^{-1}$), calculated as average of prior or posterior fluxes minus true fluxes: the first column are seasonal error of prior NEE; the second column are error of posterior NEE; spring (March-May of 2013), summer (June-August of 2013), autumn (June-August of 2013), winter (December, January, February of 2013)	120
5.1	Comparison of modeled prior and posterior CO_2 concentration (ppm) with the observed one at 3 independent sites in 2013: LHW, GIM and JFJ. At LHW and GIM data are compared for the afternoon 12-15h local time, while for JFJ, the night time data are used, i.e., 0-6h local time.	128
5.2	Comparison of prior and posterior CO_2 concentration (ppm) from May to September at the three independent sites, i.e., LHW, GIM and JFJ: the left column shows the time series of the CO_2 concentration, and the right column a histogram of the residuals.	130
5.3	Relative measure of error reduction achieved by CarbonTracker CH by assimilating the CO_2 observation from 6 sites in the domain. The relative error reduction is obtained by computing $1 - \text{posterior variance/prior variance}$	130
5.4	Annual mean NEE fluxes in 2013. (a) prior mean fluxes, (b) posterior mean fluxes, c) absolute difference, with negative fluxes indicating a carbon sink. All panels have units of $\mu\text{mol m}^{-2}\text{s}^{-1}$	131
5.5	Seasonal mean fluxes ($\mu\text{mol m}^{-2}\text{s}^{-1}$) in 2013: upper left: spring (March, April, May); upper right: summer (June, July, August); lower left: autumn (September, October, November); lower right: winter (December, January, February).	132
5.6	Integrated annual ecoregion fluxes in $\text{Tg CO}_2 \text{ yr}^{-1}$ for Switzerland. Errorbars represent normalized 1σ uncertainty.	133
5.7	Seasonal cycle of NEE in Switzerland. Shown is the prior (purple) and posterior estimate (green), i.e., the estimate after the assimilation of the atmospheric CO_2 data.	134
5.8	Seasonal cycle of NEE by different ecoregions in Switzerland: a	135

List of Tables

2.1	Summary and notation of variables used in the Ensemble Kalman Filter. M is the	34
2.2	The CO ₂ concentration measurement site information.	44
3.1	Evaluation of COSMO-7 based simulations of the atmospheric CO ₂ concentra- tion at 4 European sites (locations are shown in Figure 1). The comparison are shown for the 3 hourly means between 12 to 18 PM local time for the period April 2008 through April 2009. m.s.a.g.is the height above ground or relative height. . .	59
4.1	Settings of the base inversion.	92
4.2	Summary of inversions with CarbonTracker Switzerland, including control and sensitivity tests.	93
4.3	Comparison between observations and modeled CO ₂ concentration in the after- noon (from 12:00 to 15:00 UTC). Unit for RMSE and std are ppm.	95
5.1	Percent contribution of ecotypes at the CO ₂ measurement sites considered in the inversion	125
5.2	Comparison of modeled with observed CO ₂ concentrations at the 9 observing sites within the domain : Difference between observed, prior and posterior CO ₂ concentrations (daytime averaged) for all stations and seasons. All values are in ppm. The sites LHW, GIM and JFJ are used for independent evaluation.	129
5.3	Carbon budget of Switzerland. Comparison of the CarbonTracker CH results with the inventory data (unit: Tg CO ₂ yr ⁻¹).	135

Bibliography

- T. Aalto, P. Ciais, A. Chevallard, and C. Moulin. Optimal determination of the parameters controlling biospheric CO₂ fluxes over Europe using eddy covariance fluxes and satellite NDVI measurements. *Tellus, Ser. B Chem. Phys. Meteorol.*, 56(2):93–104, 2004. doi: 10.1111/j.1600-0889.2004.00096.x.
- C. B. Alden, J. B. Miller, L. V. Gatti, M. M. Gloor, K. Guan, A. M. Michalak, I. T. van der Laan-Luijkx, D. Touma, A. Andrews, L. S. Basso, C. S. C. Correia, L. G. Domingues, J. Joiner, M. C. Krol, A. I. Lyapustin, W. Peters, Y. P. Shiga, K. Thoning, I. R. van der Velde, T. T. van Leeuwen, V. Yadav, and N. S. Diffenbaugh. Regional atmospheric CO₂ inversion reveals seasonal and geographic differences in Amazon net biome exchange. *Global Change Biology*, 22(10):3427–3443, 2016. doi: 10.1111/gcb.13305.
- J. G. Alfieri, W. P. Kustas, J. H. Prueger, L. E. Hipps, J. L. Chavez, A. N. French, and S. R. Evett. Intercomparison of nine micrometeorological stations during the bearex08 field campaign. *Journal of Atmospheric and Oceanic Technology*, 28(11):1390–1406, 2011. doi: 10.1175/2011JTECH1514.1.
- M. R. Allen, D. J. Frame, C. Huntingford, C. D. Jones, J. A. Lowe, M. Meinshausen, and N. Meinshausen. Warming caused by cumulative carbon emissions towards the trillionth tonne. *Nature*, 458(7242):1163–1166, 2009. doi: 10.1038/nature08019.
- J. L. Anderson. An Ensemble Adjustment Kalman Filter for Data Assimilation. *Mon. Weather Rev.*, 129(12):2884–2903, 2001. doi: 10.1175/1520-0493(2001)129<textless2884:AEAKFF<textgreater2.0.CO;2.
- J. L. Anderson. An adaptive covariance inflation error correction algorithm for ensemble filters. *Tellus, Ser. A Dyn. Meteorol. Oceanogr.*, 59(2):210–224, 2007. doi: 10.1111/j.1600-0870.2006.00216.x.
- J. L. Anderson. Spatially and temporally varying adaptive covariance inflation for ensemble filters. *Tellus, Ser. A Dyn. Meteorol. Oceanogr.*, 61A:72–83, 2009. doi: 10.1111/j.1600-0870.2008.00361.x.
- J. L. Anderson. A Non-Gaussian Ensemble Filter Update for Data Assimilation. *Mon. Weather Rev.*, 138(11):4186–4198, 2010. doi: 10.1175/2010MWR3253.1.

- J. L. Anderson. Localization and Sampling Error Correction in Ensemble Kalman Filter Data Assimilation. *Mon. Weather Rev.*, 140:2359–2371, 2012. doi: 10.1175/MWR-D-11-00013.1.
- R. J. Andres, T. A. Boden, F.-M. Breon, P. Ciais, S. Davis, D. Erickson, J. S. Gregg, A. Jacobson, G. Marland, J. Miller, T. Oda, J. G. J. Olivier, M. R. Raupach, P. Rayner, and K. Treanton. A synthesis of carbon dioxide emissions from fossil-fuel combustion. *Biogeosciences*, 9(5): 1845–1871, may 2012. doi: 10.5194/bg-9-1845-2012.
- A. E. Andrews, K. A. Boering, B. C. Daube, S. C. Wofsy, M. Loewenstein, H. Jost, J. R. Podolske, C. R. Webster, R. L. Herman, D. C. Scott, G. J. Flesch, E. J. Moyer, J. W. Elkins, G. S. Dutton, D. F. Hurst, F. L. Moore, E. A. Ray, P. A. Romashkin, and S. E. Strahan. Mean ages of stratospheric air derived from in situ observations of CO₂, CH₄, and N₂O. *J. Geophys. Res. Atmos.*, 106(D23):32295–32314, 2001. doi: 10.1029/2001JD000465.
- A. E. Andrews, J. D. Kofler, M. E. Trudeau, J. C. Williams, D. H. Neff, K. A. Masarie, D. Y. Chao, D. R. Kitzis, P. C. Novelli, C. L. Zhao, E. J. Dlugokencky, P. M. Lang, M. J. Croswell, M. L. Fischer, M. J. Parker, J. T. Lee, D. D. Baumann, A. R. Desai, C. O. Stanier, S. F. J. De Wekker, D. E. Wolfe, J. W. Munger, and P. P. Tans. CO₂, CO, and CH₄ measurements from tall towers in the NOAA earth system research laboratorys global greenhouse gas reference network: Instrumentation, uncertainty analysis, and recommendations for future high-accuracy greenhouse gas monitoring efforts. *Atmos. Meas. Tech.*, 7:647–687, 2014. doi: 10.5194/amt-7-647-2014.
- A. Arneeth, S. P. Harrison, S. Zaehle, K. Tsigaridis, S. Menon, P. Bartlein, J. Feichter, A. Korhola, M. Kulmala, D. O'Donnell, G. Schurgers, S. Sorvari, and T. Vesala. Terrestrial biogeochemical feedbacks in the climate system. *Nat. Publ. Gr.*, 3(8):525–532, 2010. doi: 10.1038/ngeo905.
- A. Babenhauserheide, S. Basu, S. Houweling, W. Peters, and A. Butz. Comparing the Carbon-Tracker and M5-4DVar data assimilation systems for CO₂ surface flux inversions. *Atmos. Chem. Phys.*, 15:9747–9763, 2015. doi: 10.5194/acp-15-9747-2015.
- R. Bacastow. Modulation of atmospheric carbon dioxide by the southern oscillation. *Nature*, 261: 116–118, 1976.
- C. Bacour, P. Peylin, N. Macbean, P. J. Rayner, F. Delage, F. Chevallier, M. Weiss, J. Demarty, D. Santaren, F. Baret, D. Berveiller, E. Dufrêne, and P. Prunet. Joint assimilation of eddy covariance flux measurements and FAPAR products over temperate forests within a process-oriented biosphere model. pages 1–19, 2015. doi: 10.1002/2015JG002966.Received.
- D. F. Baker, R. M. Law, K. R. Gurney, P. Rayner, P. Peylin, A. S. Denning, P. Bousquet, L. Bruhwiler, Y. H. Chen, P. Ciais, I. Y. Fung, M. Heimann, J. John, T. Maki, S. Maksyutov, K. Masarie, M. Prather, B. Pak, S. Taguchi, and Z. Zhu. TransCom 3 inversion intercomparison: Impact of transport model errors on the interannual variability of regional CO₂ fluxes, 1988–2003. *Global Biogeochem. Cycles*, 20:1988–2003, 2006. doi: 10.1029/2004GB002439.

- M. Baldauf, A. Seifert, J. Förstner, D. Majewski, M. Raschendorfer, and T. Reinhardt. Operational convective-scale numerical weather prediction with the cosmo model: description and sensitivities. *Mon. Weather Rev.*, 139(12):3887–3905, 2011. doi: <http://dx.doi.org/10.1175/MWR-D-10-05013.1>.
- D. Baldocchi, E. Falge, L. Gu, R. Olson, D. Hollinger, S. Running, P. Anthoni, C. Bernhofer, K. Davis, R. Evans, J. Fuentes, A. Goldstein, G. Katul, B. Law, X. Lee, Y. Malhi, T. Meyers, W. Munger, W. Oechel, U. K. T. Paw, K. Pilegaard, H. P. Schmid, R. Valentini, S. Verma, T. Vesala, K. Wilson, and S. Wofsy. FLUXNET: A New Tool to Study the Temporal and Spatial Variability of Ecosystem-Scale Carbon Dioxide, Water Vapor, and Energy Flux Densities. *Bull. Am. Meteorol. Soc.*, 82(11):2415–2434, 2001.
- D. D. Baldocchi. Assessing the eddy covariance technique for evaluating carbon dioxide exchange rates of ecosystems: past, present and future. *Global Change Biology*, 9(4):479–492, 2003.
- A. P. Ballantyne, C. B. Alden, J. B. Miller, P. P. Tans, and J. W. C. White. Increase in observed net carbon dioxide uptake by land and oceans during the past 50 years. *Nature*, 488(7409):70–72, aug 2012. doi: 10.1038/nature11299.
- A. P. Ballantyne, R. Andres, R. Houghton, B. D. Stocker, R. Wanninkhof, W. Anderegg, L. A. Cooper, M. DeGrandpre, P. P. Tans, J. B. Miller, C. Alden, and J. W. C. White. Audit of the global carbon budget: Estimate errors and their impact on uptake uncertainty. *Biogeosciences*, 12(C):2565–2584, 2015. doi: 10.5194/bg-12-2565-2015.
- A. Bastos, R. M. Trigo, J. Peñuelas, I. Janssens, C. M. Gouveia, P. Ciais, F. Chevallier, C. Rodenbeck, S. Piao, P. Friedlingstein, and C. Vallès. European CO₂ sink influenced by NAO and East-Atlantic Pattern coupling Supplementary Information. *Nat. Geosci. Post_print*, 2016. doi: 10.1038/ncomms10315.
- S. Basu, S. Guerlet, A. Butz, S. Houweling, O. Hasekamp, I. Aben, P. Krummel, P. Steele, R. Langenfelds, M. Torn, S. Biraud, B. Stephens, A. Andrews, and D. Worthy. Global CO₂ fluxes estimated from GOSAT retrievals of total column CO₂. *Atmos. Chem. Phys.*, 13:8695–8717, 2013. doi: 10.5194/acp-13-8695-2013.
- S. Basu, J. B. Miller, and S. Lehman. Separation of biospheric and fossil fuel fluxes of CO₂ by atmospheric inversion of CO₂ and ¹⁴CO₂ measurements: Observation System Simulations. *Atmos. Chem. Phys.*, 16(9):5665–5683, 2016. doi: 10.5194/acp-16-5665-2016.
- C. Beer, M. Reichstein, E. Tomelleri, P. Ciais, M. Jung, N. Carvalhais, C. Rodenbeck, M. A. Arain, D. Baldocchi, G. B. Bonan, A. Bondeau, A. Cescatti, G. Lasslop, A. Lindroth, M. Lomas, S. Luyssaert, H. Margolis, K. W. Oleson, O. Roupsard, E. Veenendaal, N. Viovy, C. Williams, F. I. Woodward, and D. Papale. Terrestrial Gross Carbon Dioxide Uptake:

- Global Distribution and Covariation with Climate. *Science*, 329(5993):834–838, aug 2010. doi: 10.1126/science.1184984.
- B. A. Bergamaschi, R. Bernknopf, D. Clow, D. Dye, S. Faulkner, W. Forney, R. Gleason, T. Hawbaker, J. Liu, S.-G. Liu, et al. Public review draft: A method for assessing carbon stocks, carbon sequestration, and greenhouse-gas fluxes in ecosystems of the united states under present conditions and future scenarios. Technical report, US Geological Survey, 2010.
- M. Bocquet and L. Wu. Bayesian design of control space for optimal assimilation of observations. part ii: Asymptotic solutions. *Q. J. R. Meteorol. Soc.*, 137(658):1357–1368, 2011. doi: 10.1002/qj.841.
- B. Bolin and C. D. Keeling. Large-scale atmospheric mixing as deduced from the seasonal and meridional variations of carbon dioxide. *J. Geophys. Res.*, 68(13):3899–3920, 1963. doi: 10.1029/JZ068i013p03899.
- P. Bousquet, P. Peylin, P. Ciais, C. Le Quere, P. Friedlingstein, and P. P. Tans. Regional Changes in Carbon Dioxide Fluxes of Land and Oceans Since 1980. *Science*, 290(5495):1342–1346, 2000. doi: 10.1126/science.290.5495.1342.
- F. Bouttier and P. Courtier. Data assimilation concepts and methods. In *ECMWF lecture notes*, page 59. European Centre for Medium-Range Weather Forecasts, 1999.
- H. Bovensmann, M. Buchwitz, J. Burrows, M. Reuter, T. Krings, K. Gerilowski, O. Schneising, J. Heymann, A. Tretnner, and J. Erzingler. A remote sensing technique for global monitoring of power plant CO₂ emissions from space and related applications. *Atmos. Meas. Tech.*, 3(4): 781–811, 2010. doi: 10.5194/amt-3-781-2010.
- D. Bozhinova, M. K. Van Der Molen, I. R. van der Velde, M. C. Krol, S. van der Laan, H. A. J. Meijer, and W. Peters. Simulating the integrated summertime $\Delta^{14}\text{CO}_2$ signature from anthropogenic emissions over Western Europe. *Atmos. Chem. Phys.*, 14(14):7273–7290, 2014. doi: 10.5194/acp-14-7273-2014.
- B. H. Braswell, W. J. Sacks, E. Linder, and D. S. Schimel. Estimating diurnal to annual ecosystem parameters by synthesis of a carbon flux model with eddy covariance net ecosystem exchange observations. *Global Change Biology*, 11(2):335–355, 2005. doi: 10.1111/j.1365-2486.2005.00897.x.
- J. Brioude, W. M. Angevine, R. Ahmadov, S.-W. Kim, S. Evan, S. A. McKeen, E.-Y. Hsie, G. J. Frost, J. A. Neuman, I. B. Pollack, et al. Top-down estimate of surface flux in the Los Angeles Basin using a mesoscale inverse modeling technique: assessing anthropogenic emissions of CO, NO_x and CO₂ and their impacts. *Atmospheric Chemistry and Physics*, 13(7):3661–3677, 2013. doi: 10.5194/acp-13-3661-2013.

- F. Breon, G. Broquet, V. Puygrenier, F. Chevallier, I. Xueref-Remy, M. Ramonet, E. Dieudonne, M. Lopez, M. Schmidt, O. Perrussel, et al. An attempt at estimating Paris area CO₂ emissions from atmospheric concentration measurements. *Atmos. Chem. Phys.*, 15(4):1707–1724, 2015. doi: 10.5194/acp-15-1707-2015.
- G. Broquet, F. Chevallier, P. Rayner, C. Aulagnier, I. Pison, M. Ramonet, M. Schmidt, A. T. Vermeulen, and P. Ciais. A European summertime CO₂ biogenic flux inversion at mesoscale from continuous in situ mixing ratio measurements. *J. Geophys. Res. Atmos.*, 116:1–22, 2011. doi: 10.1029/2011JD016202.
- G. Broquet, F. Chevallier, F. M. BrEon, N. Kadyrov, M. Alemanno, F. Apadula, S. Hammer, L. Haszpra, F. Meinhardt, J. A. Morgui, J. Necki, S. Piacentino, M. Ramonet, M. Schmidt, R. L. Thompson, A. T. Vermeulen, C. Yver, and P. Ciais. Regional inversion of CO₂ ecosystem fluxes from atmospheric measurements: Reliability of the uncertainty estimates. *Atmos. Chem. Phys.*, 13:9039–9056, 2013. doi: 10.5194/acp-13-9039-2013.
- D. Brunner, N. Savage, O. Jorba, B. Eder, L. Giordano, A. Badia, A. Balzarini, R. Baro, R. Bianconi, C. Chemel, G. Curci, R. Forkel, P. Jimenez-Guerrero, M. Hirtl, A. Hodzic, L. Honzak, U. Im, C. Knote, P. Makar, A. Manders-Groot, E. van Meijgaard, L. Neal, J. L. Perez, G. Pirovano, R. San Jose, W. Schröder, R. S. Sokhi, D. Syrakov, A. Torian, P. Tuccella, J. Werhahn, R. Wolke, K. Yahya, R. Zabkar, Y. Zhang, C. Hogrefe, and S. Galmarini. Comparative analysis of meteorological performance of coupled chemistry-meteorology models in the context of AQMEII phase 2. *Atmos. Environ.*, 115:470–498, 2015. doi: 10.1016/j.atmosenv.2014.12.032.
- M. Buchwitz, M. Reuter, H. Bovensmann, D. Pillai, J. Heymann, O. Schneising, V. Rozanov, T. Krings, J. Burrows, H. Boesch, et al. Carbon Monitoring Satellite (CarbonSat): assessment of scattering related atmospheric CO₂ and CH₄ retrieval errors and first results on implications for inferring city CO₂ emissions. *Atmos. Meas. Tech.*, 6(12):3477–3500, 2013.
- M. Buchwitz, M. Reuter, O. Schneising, H. Boesch, S. Guerlet, B. Dils, I. Aben, R. Armante, P. Bergamaschi, T. Blumenstock, et al. The Greenhouse Gas Climate Change Initiative (GHG-CCI): Comparison and quality assessment of near-surface-sensitive satellite-derived CO₂ and CH₄ global data sets. *Remote Sens. Environ.*, 162:344–362, 2015.
- M. Buehner. Evaluation of a Spatial/Spectral Covariance Localization Approach for Atmospheric Data Assimilation. *Mon. Weather Rev.*, 140:617–636, 2012. doi: 10.1175/MWR-D-10-05052.1.
- H. K. Bugmann and A. M. Solomon. The use of a european forest model in north america: a study of ecosystem response to climate gradients. *Journal of Biogeography*, 22:477–484, 1995.

- J. Campbell, J. Berry, U. Seibt, S. Smith, S. Montzka, T. Launois, S. Belviso, L. Bopp, and M. Laine. Large historical growth in global terrestrial gross primary production. *Nature*, 544 (7648):84–87, 2017.
- J. G. Canadell and E. D. Schulze. Global potential of biospheric carbon management for climate mitigation. *Nat. Commun.*, 5:5282, 2014. doi: 10.1038/ncomms6282.
- J. G. Canadell, C. Le Quere, M. R. Raupach, C. B. Field, E. T. Buitenhuis, P. Ciais, T. J. Conway, N. P. Gillett, R. A. Houghton, and G. Marland. Contributions to accelerating atmospheric CO₂ growth from economic activity, carbon intensity, and efficiency of natural sinks. *Proc. Natl. Acad. Sci. U. S. A.*, 104(47):18866–70, 2007. doi: 10.1073/pnas.0702737104.
- C. Carouge, P. Peylin, P. J. Rayner, P. Bousquet, F. Chevallier, and P. Ciais. What can we learn from European continuous atmospheric CO₂ measurements to quantify regional fluxes Part 2: Sensitivity of flux accuracy to inverse setup. *Atmos. Chem. Phys. Discuss.*, 8:18621–18649, 2008. doi: 10.5194/acpd-8-18621-2008.
- E. Chan, D. Chan, M. Ishizawa, F. Vogel, J. Brioude, A. Delcloo, Y. Wu, and B. Jin. Investigation of error sources in regional inverse estimates of greenhouse gas emissions in Canada. *Atmos. Chem. Phys. Discuss.*, 15:22715–22779, 2015. doi: 10.5194/acpd-15-22715-2015.
- A. Chatterjee. Data Assimilation for Atmospheric CO₂: Towards Improved Estimates of CO₂ Concentrations and Fluxes. 2012.
- A. Chatterjee, A. M. Michalak, J. L. Anderson, K. L. Mueller, and V. Yadav. Toward reliable ensemble Kalman filter estimates of CO₂ fluxes. *J. Geophys. Res. Atmos.*, 117:1–17, 2012. doi: 10.1029/2012JD018176.
- F. Chevallier. Prior and posterior diagnostics in Autumn School: Data assimilation in biogeochemical cycles, Trieste. Technical report, Trieste, 2014.
- F. Chevallier, N. Viovy, M. Reichstein, and P. Ciais. On the assignment of prior errors in Bayesian inversions of CO₂ surface fluxes. *Geophys. Res. Lett.*, 33:1–5, 2006. doi: 10.1029/2006GL026496.
- F. Chevallier, F.-M. Bréon, and P. J. Rayner. Contribution of the Orbiting Carbon Observatory to the estimation of CO₂ sources and sinks: Theoretical study in a variational data assimilation framework. *Journal of Geophysical Research: Atmospheres*, 112(D9), 2007.
- F. Chevallier, S. Maksyutov, P. Bousquet, F.-M. Bron, R. Saito, Y. Yoshida, and T. Yokota. On the accuracy of the CO₂ surface fluxes to be estimated from the GOSAT observations. *Geophysical Research Letters*, 36(19):1–5, 2009. doi: 10.1029/2009GL040108.
- F. Chevallier, L. Feng, H. Bösch, P. I. Palmer, and P. J. Rayner. On the impact of transport model errors for the estimation of CO₂ surface fluxes from GOSAT observations. *Geophysical Research Letters*, 37(21), 2010.

- F. Chevallier, N. M. Deutscher, T. Conway, P. Ciais, L. Ciattaglia, S. Dohe, M. Fröhlich, A. Gomez-Pelaez, D. Griffith, F. Hase, et al. Global CO₂ fluxes inferred from surface air-sample measurements and from TCCON retrievals of the CO₂ total column. *Geophysical Research Letters*, 38(24), 2011.
- F. Chevallier, T. Wang, P. Ciais, F. Maignan, M. Bocquet, M. Altaf Arain, A. Cescatti, J. Chen, A. J. Dolman, B. E. Law, H. A. Margolis, L. Montagnani, and E. J. Moors. What eddy-covariance measurements tell us about prior land flux errors in CO₂-flux inversion schemes. *Global Biogeochem. Cycles*, 26:1–9, 2012. doi: 10.1029/2010GB003974.
- F. Chevallier, P. I. Palmer, L. Feng, H. Boesch, C. W. O'Dell, and P. Bousquet. Toward robust and consistent regional CO₂ flux estimates from in situ and spaceborne measurements of atmospheric CO₂. *Geophysical Research Letters*, 41(3):1065–1070, 2014. doi: 10.1002/2013GL058772. 2013GL058772.
- P. Ciais, M. Reichstein, N. Viovy, a. Granier, J. Ogee, V. Allard, M. Aubinet, N. Buchmann, C. Bernhofer, a. Carrara, F. Chevallier, N. De Noblet, A. D. Friend, P. Friedlingstein, T. Grünwald, B. Heinesch, P. Keronen, A. Knohl, G. Krinner, D. Loustau, G. Manca, G. Matteucci, F. Miglietta, J. M. Ourcival, D. Papale, K. Pilegaard, S. Rambal, G. Seufert, J. F. Sousa-sana, M. J. Sanz, E. D. Schulze, T. Vesala, and R. Valentini. Europe-wide reduction in primary productivity caused by the heat and drought in 2003. *Nature*, 437(7058):529–533, 2005. doi: 10.1038/nature03972.
- P. Ciais, P. Rayner, F. Chevallier, P. Bousquet, M. Logan, P. Peylin, and M. Ramonet. Atmospheric inversions for estimating CO₂ fluxes: Methods and perspectives. *Clim. Change*, 103(1-2):69–92, jul 2010. doi: 10.1007/s10584-010-9909-3.
- P. Ciais, T. Gasser, J. D. Paris, K. Caldeira, M. R. Raupach, J. G. Canadell, A. Patwardhan, P. Friedlingstein, S. L. Piao, and V. Gitz. Attributing the increase in atmospheric CO₂ to emitters and absorbers. *Nat. Clim. Chang.*, 3(10):926–930, 2013a. doi: 10.1038/nclimate1942.
- P. Ciais, C. Sabine, G. Bala, L. Bopp, V. Brovkin, J. Canadell, A. Chhabra, R. DeFries, J. Galloway, M. Heimann, C. Jones, C. L. Quere, R. B. Myneni, S. Piao, P. Thornton, P. C. France, J. Willem, P. Friedlingstein, and G. Munhoven. 2013: Carbon and Other Biogeochemical Cycles. *Clim. Chang. 2013 Phys. Sci. Basis. Contrib. Work. Gr. I to Fifth Assess. Rep. Intergov. Panel Clim. Chang.*, pages 465–570, 2013b. doi: 10.1017/CBO9781107415324.015.
- P. Ciais, A. Dolman, A. Bombelli, R. Duren, A. Peregon, P. Rayner, C. Miller, N. Gobron, G. Kinderman, G. Marland, et al. Current systematic carbon-cycle observations and the need for implementing a policy-relevant carbon observing system. *Biogeosciences*, 11:3547–3602, 2014. doi: 10.5194/bg-11-3547-2014.

- P. Ciais, D. Crisp, H. Van Der Gon, R. Engelen, M. Heimann, G. Janssens-Maenhout, and M. Scholze. Towards a European operational observing system to monitor fossil CO₂ emissions (Final Report from the expert group). *European Commission, JRC98161, Brussels*, 2015.
- P. M. Cox, R. A. Betts, C. D. Jones, S. A. Spall, and I. J. Totterdell. Acceleration of global warming due to carbon-cycle feedbacks in a coupled climate model. *Nature*, 408(6809):184187, nov 2000. doi: 10.1038/35041539.
- W. Cramer, A. Bondeau, F. I. Woodward, I. C. Prentice, R. A. Betts, V. Brovkin, P. M. Cox, V. Fisher, J. A. Foley, A. D. Friend, C. Kucharik, M. R. Lomas, N. Ramankutty, S. Sitch, B. Smith, A. White, and C. Young-Molling. Global response of terrestrial ecosystem structure and function to CO₂ and climate change: Results from six dynamic global vegetation models. *Glob. Chang. Biol.*, 7(4):357–373, 2001. doi: 10.1046/j.1365-2486.2001.00383.x.
- D. Crisp, R. M. Atlas, F. M. Breon, L. R. Brown, J. P. Burrows, P. Ciais, B. J. Connor, S. C. Doney, I. Y. Fung, D. J. Jacob, C. E. Miller, D. O'Brien, S. Pawson, J. T. Randerson, P. Rayner, R. J. Salawitch, S. P. Sander, B. Sen, G. L. Stephens, P. P. Tans, G. C. Toon, P. O. Wennberg, S. C. Wofsy, Y. L. Yung, Z. Kuang, B. Chudasama, G. Sprague, B. Weiss, R. Pollock, D. Kenyon, and S. Schroll. The Orbiting Carbon Observatory (OCO) mission. *Adv. Sp. Res.*, 34(4):700–709, 2004. doi: 10.1016/j.asr.2003.08.062.
- E. L. Davin, E. Maisonnave, and S. I. Seneviratne. Is land surface processes representation a possible weak link in current Regional Climate Models? *Environ. Res. Lett.*, 11(7):74027, 2016.
- F. Deng, D. Jones, T. Walker, M. Keller, K. Bowman, D. Henze, R. Nassar, E. Kort, S. Wofsy, K. Walker, et al. Sensitivity analysis of the potential impact of discrepancies in stratospheretro-posphere exchange on inferred sources and sinks of CO₂. *Atmospheric Chemistry and Physics*, 15(20):11773–11788, 2015.
- A. S. Denning, I. Y. Fung, D. Randall, et al. Latitudinal gradient of atmospheric CO₂ due to seasonal exchange with land biota. *Nature*, 376(6537):240–243, 1995. doi: 10.1038/376240a0.
- A. S. Denning, D. A. Randall, G. J. Collatz, and P. J. Sellers. Simulations of terrestrial carbon metabolism and atmospheric CO₂ in a general circulation model. *Tellus B*, 48(4):543–567, 1996. doi: 10.1034/j.1600-0889.1996.t01-1-00010.x.
- A. J. Dolman, C. Gerbig, J. Noilhan, C. Sarrat, and F. Miglietta. Detecting regional variability in sources and sinks of carbon dioxide: a synthesis. pages 1015–1026, 2009.
- A. J. Dolman, A. Shvidenko, D. Schepaschenko, P. Ciais, N. Tchepakova, T. Chen, M. K. Van Der Molen, L. Belelli Marchesini, T. C. Maximov, S. Maksyutov, and E. D. Schulze. An estimate of the terrestrial carbon budget of Russia using inventory-based, eddy covariance and inversion methods. *Biogeosciences*, 9(12):5323–5340, 2012. doi: 10.5194/bg-9-5323-2012.

- F. D'Ortenzio, D. Antoine, and S. Marullo. Satellite-driven modeling of the upper ocean mixed layer and air-sea CO₂ flux in the Mediterranean Sea. *Deep. Res. Part I Oceanogr. Res. Pap.*, 55:405–434, 2008. doi: 10.1016/j.dsr.2007.12.008.
- I. G. Enting, C. M. Trudinger, and R. J. Francey. A Synthesis Inversion of the Concentration and $\delta^{13}\text{C}$ of Atmospheric CO₂. *Tellus*, 47(1-2):35–52, 1995. doi: 10.1034/j.1600-0889.47.issue1.5.x.
- S. Etzold, N. K. Ruehr, R. Zweifel, M. Dobbertin, A. Zingg, P. Pluess, R. Häsler, W. Eugster, and N. Buchmann. The carbon balance of two contrasting mountain forest ecosystems in Switzerland: similar annual trends, but seasonal differences. *Ecosystems*, 14(8):1289–1309, 2011.
- G. Evensen. *Data Assimilation - The Ensemble Kalman Filter*. 2009. doi: 10.1007/978-3-642-03711-5.
- S. Fan. A Large Terrestrial Carbon Sink in North America Implied by Atmospheric and Oceanic Carbon Dioxide Data and Models. *Science*, 282(5388):442–446, 1998. doi: 10.1126/science.282.5388.442.
- S. M. Fan, T. L. Blaine, and J. L. Sarmiento. Terrestrial carbon sink in the Northern Hemisphere estimated from the atmospheric CO₂ difference between Mauna Loa and the South Pole since 1959. *Tellus, Ser. B Chem. Phys. Meteorol.*, 51:863–870, 1999. doi: 10.1034/j.1600-0889.1999.t01-4-00001.x.
- L. Feng, P. Palmer, H. Boesch, S. Dance, L. Feng, P. Palmer, H. Boesch, and S. Dance. Estimating surface CO₂ fluxes from space-borne CO₂ dry air mole fraction observations using an ensemble Kalman Filter. *Atmos. Chem. Phys.*, 9(8):2619–2633, 2009. doi: 10.5194/acp-9-2619-2009.
- L. Feng, P. I. Palmer, R. J. Parker, N. M. Deutscher, D. G. Feist, R. Kivi, I. Morino, and R. Sussmann. Estimates of European uptake of CO₂ inferred from GOSAT XCO₂ retrievals: sensitivity to measurement bias inside and outside Europe. *Atmos. Chem. Phys.*, 16:1289–1302, 2016a. doi: 10.5194/acp-16-1289-2016.
- S. Feng, T. Lauvaux, S. Newman, P. Rao, R. Ahmadov, A. Deng, L. I. Diaz-Isaac, R. M. Duren, M. L. Fischer, C. Gerbig, et al. Los Angeles megacity: a high-resolution land-atmosphere modelling system for urban CO₂ emissions. *Atmos. Chem. Phys.*, 16(14):9019–9045, 2016b. doi: 10.5194/acp-16-1289-2016.
- S. Feng, T. Lauvaux, S. Newman, P. Rao, R. Ahmadov, A. Deng, L. I. Diaz-Isaac, R. M. Duren, M. L. Fischer, C. Gerbig, et al. Los Angeles megacity: a high-resolution land-atmosphere modelling system for urban CO₂ emissions. *Atmos. Chem. Phys.*, 16(14):9019–9045, 2016c. doi: doi:10.5194/acp-16-9019-2016.

- M. Fernandez-Martinez, S. Vicca, I. A. Janssens, J. Sardans, S. Luysaert, M. Campioli, F. S. Chapin III, P. Ciais, Y. Malhi, M. Obersteiner, D. Papale, S. L. Piao, M. Reichstein, F. Rodà, and J. Peñuelas. Nutrient availability as the key regulator of global forest carbon balance. *Nat. Clim. Chang.*, 4(June):471–476, 2014. doi: doi:10.1038/nclimate2177.
- S. Ferrarese, F. Apadula, F. Bertiglia, C. Cassardo, A. Ferrero, L. Fialdini, C. Francone, D. Heltai, A. Lanza, A. Longhetto, et al. Inspection of highconcentration CO₂ events at the Plateau Rosa Alpine station. *Atmospheric Pollution Research*, 6(3):415–427, 2015.
- J. Finnigan and Y. Brunet. Turbulent airflow in forests on flat and hilly terrain. *Wind and trees*, pages 3–40, 1995.
- FOEN. Switzerland's sixth national communication and first biennial report under the unfccc, edited by federal office for the environment, 2013.
- FOEN. Switzerland's Greenhouse Gas Inventory 1990-2013, National Inventory Report Including reporting elements under the Kyoto Protocol Submission. (April):1–596, 2015.
- M. Forkel, N. Carvalhais, C. Rödenbeck, R. Keeling, M. Heimann, K. Thonicke, S. Zaehle, and M. Reichstein. Enhanced seasonal CO₂ exchange caused by amplified plant productivity in northern ecosystems. *Science*, 4971(January):1–9, 2016. doi: 10.1126/science.aac4971.
- C. Frankenberg, J. B. Fisher, J. Worden, G. Badgley, S. S. Saatchi, J. E. Lee, G. C. Toon, A. Butz, M. Jung, A. Kuze, and T. Yokota. New global observations of the terrestrial carbon cycle from GOSAT: Patterns of plant fluorescence with gross primary productivity. *Geophys. Res. Lett.*, 38:1–6, 2011. doi: 10.1029/2011GL048738.
- M. Frei and H. R. Künsch. Bridging the ensemble Kalman and particle filters. *Biometrika*, 100: 781–800, 2013. doi: 10.1093/biomet/ast020.
- P. Friedlingstein, R. M. Andrew, J. Rogelj, G. P. Peters, J. G. Canadell, R. Knutti, G. Luderer, M. R. Raupach, M. Schaeffer, D. P. van Vuuren, and C. Le Quere. Persistent growth of CO₂ emissions and implications for reaching climate targets. *Nat. Geosci.*, 7(10):709–715, 2014. doi: 10.1038/ngeo2248.
- R. Friedrich and S. Reis. *Emissions of Air Pollutants*. 2004. doi: 10.1787/data-00598-en.
- A. D. Friend, A. Arneeth, N. Y. Kiang, M. Lomas, J. Ogee, C. Roden beck, S. W. Running, J.-D. Santaren, S. Sitch, N. Viovy, et al. Fluxnet and modelling the global carbon cycle. *Global Change Biology*, 13(3):610–633, 2007.
- T. Frölicher, F. Joos, and C. Raible. Sensitivity of atmospheric CO₂ and climate to explosive volcanic eruptions. *Biogeosciences*, 8(8):2317–2339, 2011.

- T. L. Frölicher, F. Joos, C. C. Raible, and J. L. Sarmiento. Atmospheric CO₂ response to volcanic eruptions: the role of ENSO, season, and variability. *Global Biogeochemical Cycles*, 27(1): 239–251, 2013.
- R. Furrer and T. Bengtsson. Estimation of high-dimensional prior and posterior covariance matrices in Kalman filter variants. *J. Multivar. Anal.*, 98:227–255, 2007. doi: 10.1016/j.jmvA.2006.08.003.
- C. Gao, H. Wang, E. Weng, S. Lakshmivarahan, Y. Zhang, and Y. Luo. Assimilation of multiple data sets with the ensemble Kalman filter to improve forecasts of forest carbon dynamics. *Ecol. Appl.*, 21:1461–1473, 2011. doi: 10.1890/09-1234.1.
- G. Gaspari and S. E. Cohn. Construction of correlation functions in two and three dimensions. *Quarterly Journal of the Royal Meteorological Society*, 125(554):723–757, 1999.
- L. Gatti, J. Miller, M. Damelio, A. Martinewski, L. Basso, M. Gloor, S. Wofsy, and P. Tans. *Tellus B*, 62(5):581–594, 2010.
- C. Geels, S. C. Doney, R. Dargaville, J. Brandt, and J. H. Christensen. Investigating the sources of synoptic variability in atmospheric CO₂ measurements over the Northern Hemisphere continents: A regional model study. *Tellus, Ser. B Chem. Phys. Meteorol.*, 56:35–50, 2004. doi: 10.1111/j.1600-0889.2004.00084.x.
- C. Geels, M. Gloor, P. Ciais, P. Bousquet, P. Peylin, A. Vermeulen, R. Dargaville, T. Aalto, J. Brandt, J. Christensen, et al. Comparing atmospheric transport models for future regional inversions over EuropePart 1: mapping the atmospheric CO₂ signals. *Atmos. Chem. Phys.*, 7(13):3461–3479, 2007. doi: 10.5194/acp-7-3461-2007.
- C. Gerbig, J. Lin, S. Wofsy, B. Daube, A. Andrews, B. Stephens, P. Bakwin, and C. Grainger. Toward constraining regional-scale fluxes of CO₂ with atmospheric observations over a continent: 2. Analysis of COBRA data using a receptor-oriented framework. *Journal of Geophysical Research: Atmospheres*, 108(D24), 2003.
- C. Gerbig, J. Lin, J. Munger, and S. Wofsy. What can tracer observations in the continental boundary layer tell us about surface-atmosphere fluxes? *Atmospheric Chemistry and Physics*, 6(2):539–554, 2006.
- C. Gerbig, A. J. Dolman, and M. Heimann. On observational and modelling strategies targeted at regional carbon exchange over continents. *Biogeosciences*, 6(10):1949–1959, oct 2009. doi: 10.5194/bg-6-1949-2009.
- Gerbig, C. and Körner, S. and Lin, J. C. Vertical mixing in atmospheric tracer transport models: error characterization and propagation. *Atmos. Chem. Phys.*, 8(3):591–602, 2008. doi: 10.5194/acp-8-591-2008.

- M. Göckede, A. M. Michalak, D. Vickers, D. P. Turner, and B. E. Law. Atmospheric inverse modeling to constrain regional-scale CO₂ budgets at high spatial and temporal resolution. *J. Geophys. Res. Atmos.*, 115:1–23, 2010. doi: 10.1029/2009JD012257.
- M. Göckede, A. M. Michalak, D. Vickers, D. P. Turner, and B. E. Law. Atmospheric inverse modeling to constrain regional-scale CO₂ budgets at high spatial and temporal resolution. *Journal of Geophysical Research: Atmospheres*, 115(D15), 2010.
- S. M. Gourdjji, A. I. Hirsch, K. L. Mueller, V. Yadav, A. E. Andrews, and A. M. Michalak. Regional-scale geostatistical inverse modeling of North American CO₂ fluxes: A synthetic data study. *Atmos. Chem. Phys.*, 10:6151–6167, 2010. doi: 10.5194/acp-10-6151-2010.
- S. M. Gourdjji, K. L. Mueller, V. Yadav, D. N. Huntzinger, A. E. Andrews, M. Trudeau, G. Petron, T. Nehrkorn, J. Eluszkiewicz, J. Henderson, D. Wen, J. Lin, M. Fischer, C. Sweeney, and A. M. Michalak. North American CO₂ exchange: Inter-comparison of modeled estimates with results from a fine-scale atmospheric inversion. *Biogeosciences*, 9:457–475, 2012. doi: 10.5194/bg-9-457-2012.
- H. Graven, X. Xu, T. P. Guilderson, R. F. Keeling, S. E. Trumbore, and S. Tyler. Comparison of independent $\Delta^{14}\text{CO}_2$ records at point barrow, Alaska. *Radiocarbon*, 55(2-3):1541–1545, 2013a.
- H. D. Graven. Impact of fossil fuel emissions on atmospheric radiocarbon and various applications of radiocarbon over this century. *Proceedings of the National Academy of Sciences*, 112(31):9542–9545, 2015.
- H. D. Graven and N. Gruber. Continental-scale enrichment of atmospheric ¹⁴CO₂ from the nuclear power industry: Potential impact on the estimation of fossil fuel-derived CO₂. *Atmos. Chem. Phys.*, 11(23):12339–12349, 2011. doi: 10.5194/acp-11-12339-2011.
- H. D. Graven, R. F. Keeling, S. C. Piper, P. K. Patra, B. B. Stephens, S. C. Wofsy, L. R. Welp, C. Sweeney, P. P. Tans, J. J. Kelley, B. C. Daube, E. a. Kort, G. W. Santoni, and J. D. Bent. Enhanced seasonal exchange of CO₂ by northern ecosystems since 1960. *Science*, 341(September):1085–9, 2013b. doi: 10.1126/science.1239207.
- N. Gruber and J. N. Galloway. An Earth-system perspective of the global nitrogen cycle. *Nature*, 451(7176):293296, jan 2008. doi: 10.1038/nature06592.
- N. Gruber, P. Friedlingstein, C. Field, R. Valentini, M. Heimann, J. Richey, P. Lankao, E. Schulze, and C. Chen. The vulnerability of the carbon cycle in the 21st century : An assessment of carbon-climate-human interactions. *Glob. carbon cycle Integr. humans Clim. Nat. world*, 62: 45–76, 2004.

- K. R. Gurney. Transcom 3 inversion intercomparison: Model mean results for the estimation of seasonal carbon sources and sinks. *Glob. Biogeochem. Cycles*, 18, 2004. doi: 10.1029/2003GB002111.
- K. R. Gurney, R. M. Law, A. S. Denning, P. J. Rayner, D. Baker, P. Bousquet, L. Bruhwiler, Y.-H. Chen, P. Clals, S. Fan, I. Y. Fung, M. Gloor, M. Heimann, K. Higuchi, J. John, T. Maki, S. Maksyutov, K. Masarie, P. Peylin, M. Prather, B. C. Pak, J. Randerson, J. Sarmiento, S. Taguchi, T. Takahashi, and C.-W. Yuen. Towards robust regional estimates of CO₂ sources and sinks using atmospheric transport models. *Nature*, 415(6872):626–630, 2002. doi: 10.1038/415626a.
- F. Hase, M. Frey, T. Blumenstock, J. Groß, M. Kiel, R. Kohlhepp, G. Mengistu Tsidu, K. Schäfer, M. Sha, and J. Orphal. Application of portable FTIR spectrometers for detecting greenhouse gas emissions of the major city berlin. *Atmos. Meas. Tech.*, 8(7):3059–3068, 2015. doi: 10.5194/amt-8-3059-2015.
- L. Haszpra, M. Ramonet, M. Schmidt, Z. Barcza, Z. Patkai, K. Tarczay, C. Yver, J. Tarniewicz, and P. Ciais. Variation of CO₂ mole fraction in the lower free troposphere, in the boundary layer and at the surface. *Atmos. Chem. Phys.*, 12(18):8865–8875, 2012. doi: 10.5194/acp-12-8865-2012.
- M. Heimann and M. Reichstein. Terrestrial ecosystem carbon dynamics and climate feedbacks. *Nature*, 451(7176):289–292, 2008.
- T. W. Hilton, A. Zumkehr, S. Kulkarni, J. Berry, M. E. Whelan, and J. E. Campbell. Large variability in ecosystem models explains uncertainty in a critical parameter for quantifying GPP with carbonyl sulphide. *Tellus B*, 67:1–8, 2015. doi: 10.3402/tellusb.v67.26329.
- A. Holtslag, G. Svensson, P. Baas, S. Basu, B. Beare, A. Beljaars, F. Bosveld, J. Cuxart, J. Lindvall, G. Steeneveld, et al. Stable atmospheric boundary layers and diurnal cycles: challenges for weather and climate models. *B. Am. Meteorol. Soc.*, 94(11):1691–1706, 2013. doi: <http://dx.doi.org/10.1175/BAMS-D-11-00187.1>.
- R. A. Houghton, J. I. House, J. Pongratz, G. R. Werf, R. S. DeFries, M. C. Hansen, C. L. Quere, and N. Ramankutty. Carbon emissions from land use and land-cover change. *Biogeosciences*, 9(12):5125–5142, 2012.
- B. A. Hungate. ATMOSPHERIC SCIENCE: Nitrogen and Climate Change. *Science*, 302(5650):1512–1513, nov 2003. doi: 10.1126/science.1091390.
- B. R. Hunt, E. J. Kostelich, and I. Szunyogh. Efficient data assimilation for spatiotemporal chaos: A local ensemble transform Kalman filter. *Phys. D Nonlinear Phenom.*, 230:112–126, 2007. doi: 10.1016/j.physd.2006.11.008.

- D. Imer, L. Merbold, W. Eugster, and N. Buchmann. Temporal and spatial variations of soil CO₂, CH₄ and N₂O fluxes at three differently managed grasslands. *Biogeosciences*, 10 (SEPTEMBER):5931–5945, 2013. doi: 10.5194/bg-10-5931-2013.
- A. Indermühle, B. Stauffer, T. F. Stocker, D. Raynaud, and J.-M. Barnola. Early Holocene atmospheric CO₂ concentrations. *Science*, 286(5446):1815–1815, 1999.
- IPCC. *Climate Change 2014: Synthesis Report. Contribution of Working Groups I, II and III to the Fifth Assessment Report of the Intergovernmental Panel on Climate Change*. 2014. doi: 10.1017/CBO9781107415324.004.
- A. R. Jacobson, S. E. M. Fletcher, N. Gruber, J. L. Sarmiento, and M. Gloor. A joint atmosphere-ocean inversion for surface fluxes of carbon dioxide: 1. Methods and global-scale fluxes. *Global Biogeochem. Cycles*, 21(1), 2007. doi: 10.1029/2005GB002556.
- I. A. Janssens, A. Freibauer, P. Ciais, P. Smith, G.-J. Nabuurs, G. Folberth, B. Schlamadinger, R. W. A. Hutjes, R. Ceulemans, E.-D. Schulze, R. Valentini, and A. J. Dolman. Europe's terrestrial biosphere absorbs 7 to 12% of European anthropogenic CO₂ emissions. *Science*, 300(5625):1538–1542, 2003. doi: 10.1126/science.1083592.
- G. Janssens-Maenhout, F. Dentener, J. Van Aardenne, S. Monni, V. Pagliari, L. Orlandini, Z. Klimont, J. Kurokawa, H. Akimoto, T. Ohara, et al. Edgar-htap: a harmonized gridded air pollution emission dataset based on national inventories. *European Commission Publications Office, Ispra (Italy). JRC68434, EUR report No EUR*, 25:299–2012, 2012. doi: 10.2788/14069.
- F. Jiang, J. M. Chen, L. Zhou, W. Ju, H. Zhang, T. Machida, P. Ciais, W. Peters, H. Wang, B. Chen, L. Liu, C. Zhang, H. Matsueda, and Y. Sawa. A comprehensive estimate of recent carbon sinks in China using both top-down and bottom-up approaches. *Sci. Rep.*, 6(August 2015):22130, 2016. doi: 10.1038/srep22130.
- C. D. Jones and P. M. Cox. Modeling the volcanic signal in the atmospheric CO₂ record. *Global Biogeochem. Cycles*, 15(2):453–465, 2001. doi: 10.1029/2000GB001281.
- M. Jung, M. Reichstein, H. A. Margolis, A. Cescatti, A. D. Richardson, M. A. Arain, A. Arneth, C. Bernhofer, D. Bonal, J. Chen, D. Gianelle, N. Gobron, G. Kiely, W. Kutsch, G. Lasslop, B. E. Law, A. Lindroth, L. Merbold, L. Montagnani, E. J. Moors, D. Papale, M. Sottocornola, F. Vaccari, and C. Williams. Global patterns of land-atmosphere fluxes of carbon dioxide, latent heat, and sensible heat derived from eddy covariance, satellite, and meteorological observations. *J. Geophys. Res. Biogeosciences*, 116(3):1–16, 2011. doi: 10.1029/2010JG001566.
- N. Kadyrov, G. Broquet, F. Chevallier, L. Rivier, C. Gerbig, and P. Ciais. On the potential of the ICOS atmospheric CO₂ measurement network for estimating the biogenic CO₂ budget of Europe. *Atmos. Chem. Phys.*, 15(22):12765–12787, 2015. doi: 10.5194/acp-15-12765-2015.

- T. Kaminski, P. J. Rayner, M. Heimann, and I. G. Enting. On aggregation errors in atmospheric transport inversions. *Journal of Geophysical Research: Atmospheres*, 106(D5):4703–4715, 2001.
- J. Kang, E. Kalnay, J. Liu, and I. Fung. "Variable localization" in an ensemble Kalman filter: application to the carbon cycle data assimilation. *J. Geophys. Res. Atmos.*, pages 1–63, 2011.
- C. D. Keeling. The Concentration and Isotopic Abundances of Carbon Dioxide in the Atmosphere. *Tellus*, 12(2):200–203, 1960. doi: 10.1111/j.2153-3490.1960.tb01300.x.
- C. D. Keeling. The Suess effect: ¹³Carbon-¹⁴Carbon interrelations. *Environ. Int.*, 2(4-6):229–300, 1979. doi: 10.1016/0160-4120(79)90005-9.
- C. D. Keeling and R. Revelle. Effects of EL Nino/southern oscillation on the atmospheric content of carbon dioxide. 20:437–450, 1985.
- C. D. Keeling, R. B. Bacastow, A. F. Carter, S. C. Piper, T. P. Whorf, M. Heimann, W. G. Mook, and H. Roeloffzen. A three-dimensional model of atmospheric CO₂ transport based on observed winds: 1. Analysis of observational data, 1989.
- C. D. Keeling, J. F. S. Chin, and T. P. Whorf. Increased activity of northern vegetation inferred from atmospheric CO₂ measurements, 1996.
- R. F. Keeling and S. R. Shertz. Seasonal and interannual variations in atmospheric oxygen and implications for the global carbon cycle, 1992.
- E. D. Keller, J. C. Turnbull, and M. W. Norris. Detecting long-term changes in point-source fossil CO₂ emissions with tree ring archives. *Atmos. Chem. Phys.*, 16(9):5481–5495, 2016. doi: 10.5194/acp-16-5481-2016.
- G. Keppel-Aleks, P. O. Wennberg, C. W. O'Dell, and D. Wunch. Towards constraints on fossil fuel emissions from total column carbon dioxide. *Atmos. Chem. Phys.*, 13:4349–4357, 2013. doi: 10.5194/acp-13-4349-2013.
- J. Kim, H. M. Kim, and C.-H. Cho. Influence of CO₂ observations on the optimized CO₂ flux in an ensemble Kalman filter. *Atmos. Chem. Phys. Discuss.*, 14:13561–13602, 2014. doi: 10.5194/acpd-14-13561-2014.
- W. Kolby Smith, S. C. Reed, C. C. Cleveland, A. P. Ballantyne, W. R. L. Anderegg, W. R. Wieder, Y. Y. Liu, and S. W. Running. Large divergence of satellite and Earth system model estimates of global terrestrial CO₂ fertilization. *Nat. Clim. Chang.*, dec 2015. doi: 10.1038/nclimate2879.
- M. Kondo, K. Ichii, H. Takagi, and M. Sasakawa. Comparison of the data-driven top-down and bottom-up global terrestrial CO₂ exchanges: GOSAT CO₂ inversion and empirical eddy flux upscaling. *J. Geophys. Res. Biogeosciences*, 120(7):1226–1245, 2015. doi: 10.1002/2014JG002866.

- E. A. Kort, C. Frankenberg, C. E. Miller, and T. Oda. Space-based observations of megacity carbon dioxide. *Geophys. Res. Lett.*, 39(17):1–5, 2012. doi: 10.1029/2012GL052738.
- P. Kountouris, C. Gerbig, K.-U. Totsche, A.-J. Dolman, A.-G.-C.-A. Meesters, G. Broquet, F. Maignan, B. Gioli, L. Montagnani, and C. Helfter. An objective prior error quantification for regional atmospheric inverse applications. *Biogeosciences Discuss.*, 12(May):9393–9441, 2015. doi: 10.5194/bgd-12-9393-2015.
- R. Kretschmer, C. Gerbig, U. Karstens, and F.-T. Koch. Error characterization of CO₂ vertical mixing in the atmospheric transport model WRF-VPRM. *Atmos. Chem. Phys.*, 12:2441–2458, 2012. doi: 10.5194/acp-12-2441-2012.
- G. Krinner, N. Viovy, N. de Noblet-Ducoudre, J. Ogee, J. Polcher, P. Friedlingstein, P. Ciais, S. Sitch, and I. C. Prentice. A dynamic global vegetation model for studies of the coupled atmosphere-biosphere system. *Global Biogeochem. Cycles*, 19(1):133, 2005.
- J. J. P. Kuenen, A. J. H. Visschedijk, M. Jozwicka, and H. A. C. Denier Van Der Gon. TNO-MACC-II emission inventory; A multi-year (2003-2009) consistent high-resolution European emission inventory for air quality modelling. *Atmos. Chem. Phys.*, 14:10963–10976, 2014. doi: 10.5194/acp-14-10963-2014.
- S. S. Kulawik, D. B. a. Jones, R. Nassar, F. W. Irion, J. R. Worden, K. W. Bowman, T. MacHida, H. Matsueda, Y. Sawa, S. C. Biraud, M. L. Fischer, and A. R. Jacobson. Characterization of tropospheric emission spectrometer (TES) CO₂ for carbon cycle science. *Atmos. Chem. Phys.*, 10:5601–5623, 2010. doi: 10.5194/acp-10-5601-2010.
- I. Laan-Luijkx, I. Velde, M. Krol, L. Gatti, L. Domingues, C. Correia, J. Miller, M. Gloor, T. Leeuwen, J. Kaiser, et al. Response of the amazon carbon balance to the 2010 drought derived with carbontracker south america. *Global Biogeochemical Cycles*, 29(7):1092–1108, 2015.
- P. Landschützer, N. Gruber, D. C. E. Bakker, U. Schuster, S. Nakaoka, M. R. Payne, T. P. Sasse, and J. Zeng. A neural network-based estimate of the seasonal to inter-annual variability of the Atlantic Ocean carbon sink. *Biogeosciences*, 10:7793–7815, 2013. doi: 10.5194/bg-10-7793-2013.
- V. E. Larson and H. Volkmer. An idealized model of the one-dimensional carbon dioxide rectifier effect. *Tellus B*, 60(4):525–536, 2008. doi: 10.1111/j.1600-0889.2008.00368.x.
- T. Lauvaux, M. Uliasz, C. Sarrat, F. Chevallier, P. Bousquet, C. Lac, K. Davis, P. Ciais, A. Denning, and P. Rayner. Mesoscale inversion: first results from the ceres campaign with synthetic data. *Atmospheric Chemistry and Physics*, 8(13):3459–3471, 2008.
- T. Lauvaux, B. Gioli, C. Sarrat, P. J. Rayner, P. Ciais, F. Chevallier, J. Noilhan, F. Miglietta, Y. Brunet, E. Ceschia, H. Dolman, J. A. Elbers, C. Gerbig, R. Hutjes, N. Jarosz, D. Legain,

- and M. Uliasz. Bridging the gap between atmospheric concentrations and local ecosystem measurements. *Geophys. Res. Lett.*, 36(19):1–5, 2009. doi: 10.1029/2009GL039574.
- T. Lauvaux, A. E. Schuh, M. Bocquet, L. Wu, S. Richardson, N. Miles, and K. J. Davis. Network design for mesoscale inversions of CO₂ sources and sinks. *Tellus B*, 64:17980, 2012. doi: 10.3402/tellusb.v64i0.17980.
- T. Lauvaux, N. L. Miles, A. Deng, S. J. Richardson, M. O. Cambaliza, K. J. Davis, B. Gaudet, K. R. Gurney, J. Huang, D. OKeefe, et al. High-resolution atmospheric inversion of urban CO₂ emissions during the dormant season of the Indianapolis Flux Experiment (INFLUX). *J. Geophys. Res-Atmos.*, 121:5213–5236, 2016. doi: 10.1002/2015JD024473.
- C. Le Quere, R. M. Andrew, J. G. Canadell, S. Sitch, J. I. Korsbakken, G. P. Peters, A. C. Manning, T. A. Boden, P. P. Tans, R. A. Houghton, R. F. Keeling, S. Alin, O. D. Andrews, P. Anthoni, L. Barbero, L. Bopp, F. Chevallier, L. P. Chini, P. Ciais, K. Currie, C. Delire, S. C. Doney, P. Friedlingstein, T. Gkritzalis, I. Harris, J. Hauck, V. Haverd, M. Hoppema, K. Klein Goldewijk, A. K. Jain, E. Kato, A. Körtzinger, P. Landschützer, N. Lefèvre, A. Lenton, S. Lienert, D. Lombardozzi, J. R. Melton, N. Metzl, F. Millero, P. M. S. Monteiro, D. R. Munro, J. E. M. S. Nabel, S.-I. Nakaoka, K. O'Brien, A. Olsen, A. M. Omar, T. Ono, D. Pierrot, B. Poulter, C. Rödenbeck, J. Salisbury, U. Schuster, J. Schwinger, R. Seferian, I. Skjelvan, B. D. Stocker, A. J. Sutton, T. Takahashi, H. Tian, B. Tilbrook, I. T. van der Laan-Luijkx, G. R. van der Werf, N. Viovy, A. P. Walker, A. J. Wiltshire, and S. Zaehle. Global carbon budget 2016. *Earth System Science Data*, 8(2):605–649, 2016. doi: 10.5194/essd-8-605-2016.
- J. Lei and P. Bickel. A Moment Matching Ensemble Filter for Nonlinear Non-Gaussian Data Assimilation. *Mon. Weather Rev.*, 139:3964–3973, 2011. doi: 10.1175/2011MWR3553.1.
- H. Leng, J. Song, F. Lu, and X. Cao. A New Data Assimilation Scheme: The Space-Expanded Ensemble Localization Kalman Filter. *Adv. Meteorol.*, 2013:1–6, 2013. doi: 10.1155/2013/410812.
- I. Levin and U. Karstens. Inferring high-resolution fossil fuel CO₂ records at continental sites from combined ¹⁴CO₂ and CO observations. *Tellus B*, 59(2):245–250, 2007. doi: 10.1111/j.1600-0889.2006.00244.x.
- I. Levin and C. Rödenbeck. Can the envisaged reductions of fossil fuel CO₂ emissions be detected by atmospheric observations? *Naturwissenschaften*, 95(3):203208–, 2008.
- I. Levin, S. Hammer, E. Eichelmann, and F. R. Vogel. Verification of greenhouse gas emission reductions: the prospect of atmospheric monitoring in polluted areas. *Philos. T. Roy. Soc. A.*, 369(1943):1906–1924, 2011. doi: 10.1098/rsta.2010.0249.
- S. Levis. Modeling vegetation and land use in models of the Earth System. *Wiley Interdiscip. Rev. Clim. Chang.*, 1(6):840–856, 2010. doi: 10.1002/wcc.83.

- S. L. Lewis, P. M. Brando, O. L. Phillips, G. M. F. van der Heijden, and D. Nepstad. The 2010 Amazon drought. *Science*, 331(Ci):554, 2011. doi: 10.1126/science.1200807.
- J. C. Lin and C. Gerbig. Accounting for the effect of transport errors on tracer inversions. *Geophys. Res. Lett.*, 32(1):1–5, 2005. doi: 10.1029/2004GL021127.
- R. Lindenmaier, M. K. Dubey, B. G. Henderson, Z. T. Butterfield, J. R. Herman, T. Rahn, and S.-H. Lee. Multiscale observations of CO₂, ¹³CO₂, and pollutants at Four Corners for emission verification and attribution. *P. Natl. Acad. Sci. USA*, 111(23):8386–8391, 2014. doi: 10.1073/pnas.1321883111.
- B. Liu, B. Ait-El-Fquih, and I. Hoteit. Efficient kernel-based ensemble gaussian mixture filtering. *Monthly Weather Review*, 144(2):781–800, 2016.
- J. Liu, E. Kalnay, I. Fung, M. T. Chahine, and E. T. Olsen. AIRS CO₂ assimilation with an EnKF : preliminary results Motivation & Outline. pages 0–21, 2009.
- J. Liu, I. Fung, E. Kalnay, J. S. Kang, E. T. Olsen, and L. Chen. Simultaneous assimilation of AIRS XCO₂ and meteorological observations in a carbon climate model with an ensemble Kalman filter. *J. Geophys. Res. Atmos.*, 117:1–15, 2012. doi: 10.1029/2011JD016642.
- Y. Luo, B. O. Su, W. S. Currie, J. S. Dukes, A. Finzi, U. Hartwig, B. Hungate, R. E. Mc Murtrie, R. Oren, and W. J. Parton. Progressive nitrogen limitation of ecosystem responses to rising atmospheric carbon dioxide. *Bioscience*, 54(8):731–739, aug 2004.
- D. Lüthi, M. Le Floch, B. Bereiter, T. Blunier, J.-M. Barnola, U. Siegenthaler, D. Raynaud, J. Jouzel, H. Fischer, K. Kawamura, and T. F. Stocker. High-resolution carbon dioxide concentration record 650,000-800,000 years before present. *Nature*, 453(7193):379–382, 2008. doi: 10.1038/nature06949.
- S. Luyssaert, G. Abril, R. Andres, D. Bastviken, V. Bellassen, P. Bergamaschi, P. Bousquet, F. Chevallier, P. Ciais, M. Corazza, et al. The European land and inland water CO₂, CO, CH₄ and N₂O balance between 2001 and 2005. *Biogeosciences*, 9(8):3357–3380, 2012.
- N. MacBean, P. Peylin, F. Chevallier, M. Scholze, and G. Schürmann. Consistent assimilation of multiple data streams in a carbon cycle data assimilation system. *Geosci. Model Dev. Discuss.*, (March):1–44, 2016. doi: 10.5194/gmd-2016-25.
- P. Mahadevan, S. C. Wofsy, D. M. Matross, X. Xiao, A. L. Dunn, J. C. Lin, C. Gerbig, J. W. Munger, V. Y. Chow, and E. W. Gottlieb. A satellite-based biosphere parameterization for net ecosystem CO₂ exchange: Vegetation Photosynthesis and Respiration Model(VPRM). *Global Biogeochemical Cycles*, 22(2), apr 2008. doi: 10.1029/2006GB002735.
- A. D. McGuire, S. Sitch, J. S. Clein, R. Dargaville, G. Esser, J. Foley, M. Heimann, F. Joos, J. Kaplan, D. W. Kicklighter, R. A. Meier, J. M. Melillo, B. Moore, I. C. Prentice, N. Ramankutty,

- T. Reichenau, A. Schloss, H. Tian, L. J. Williams, and U. Wittenberg. Carbon balance of the terrestrial biosphere in the Twentieth Century: Analyses of CO₂, climate and land use effects with four process-based ecosystem models. *Glob. Biogeochem. Cycles*, 15(1):183–206, 2001. doi: 10.1029/2000GB001298.
- K. McKain, S. C. Wofsy, T. Nehrkorn, J. Eluszkiewicz, J. R. Ehleringer, and B. B. Stephens. Assessment of ground-based atmospheric observations for verification of greenhouse gas emissions from an urban region. *P. Natl. Acad. Sci. USA*, 109(22):8423–8428, may 2012. doi: 10.1073/pnas.1116645109.
- A. G. C. A. Meesters, L. F. Tolk, W. Peters, R. W. A. Hutjes, O. S. Vellinga, J. A. Elbers, A. T. Vermeulen, S. van der Laan, R. E. M. Neubert, H. A. J. Meijer, and A. J. Dolman. Inverse carbon dioxide flux estimates for the Netherlands. *J. Geophys. Res. Atmos.*, 117, 2012. doi: 10.1029/2012JD017797.
- M. Meinshausen, N. Meinshausen, W. Hare, S. C. B. Raper, K. Frieler, R. Knutti, D. J. Frame, and M. R. Allen. Greenhouse-gas emission targets for limiting global warming to 2 degrees C. *Nature*, 458(7242):1158–1162, 2009. doi: 10.1038/nature08017.
- A. M. Michalak, L. Bruhwiler, and P. P. Tans. A geostatistical approach to surface flux estimation of atmospheric trace gases. *Journal of Geophysical Research: Atmospheres*, 109(D14), 2004.
- A. M. Michalak, A. Hirsch, L. Bruhwiler, K. R. Gurney, W. Peters, and P. P. Tans. Maximum likelihood estimation of covariance parameters for Bayesian atmospheric trace gas surface flux inversions. *J. Geophys. Res. Atmos.*, 110:1–16, 2005. doi: 10.1029/2005JD005970.
- A. M. Michalak, R. Jackson, G. Marland, and C. Sabine. A U.S. Carbon Cycle Science Plan. *Eos, Trans. Am. Geophys. Union*, 90:81, 2011. doi: 10.1029/2009EO120003.
- J. B. Miller, S. Lehman, J. Turnbull, J. Southon, P. Tans, W. Peters, J. Elkins, and C. Sweeney. Using atmospheric ¹⁴CO₂ measurements to quantify fossil fuel emissions and evaluate atmospheric transport. *North*, 109(4):2004–2004, 2007. doi: 10.1029/2006JD008184.
- S. M. Miller, S. C. Wofsy, A. M. Michalak, E. A. Kort, A. E. Andrews, S. C. Biraud, E. J. Dlugokencky, J. Eluszkiewicz, M. L. Fischer, G. Janssens-Maenhout, et al. Anthropogenic emissions of methane in the united states. *Proceedings of the National Academy of Sciences*, 110(50):20018–20022, 2013.
- S. M. Miller, A. M. Michalak, and P. J. Levi. Atmospheric inverse modeling with known physical bounds: An example from trace gas emissions. *Geosci. Model Dev.*, 7:303–315, 2014. doi: 10.5194/gmd-7-303-2014.
- S. M. Miller, M. N. Hayek, A. E. Andrews, I. Fung, and J. Liu. Biases in atmospheric CO₂ estimates from correlated meteorology modeling errors. *Atmos. Chem. Phys.*, 15:2903–2914, 2015. doi: 10.5194/acp-15-2903-2015.

- K. Miyazaki, T. Maki, P. Patra, and T. Nakazawa. Assessing the impact of satellite, aircraft, and surface observations on CO₂ flux estimation using an ensemble-based 4-D data assimilation system. *J. Geophys. Res. Atmos.*, 116:1–20, 2011. doi: 10.1029/2010JD015366.
- T. Miyoshi and M. Kunii. The local ensemble transform kalman filter with the weather research and forecasting model: experiments with real observations. *Pure and applied geophysics*, 169(3):321–333, 2012.
- S. Mystakidis, E. L. Davin, N. Gruber, and S. I. Seneviratne. Constraining future terrestrial carbon cycle projections using observation-based water and carbon flux estimates. *Global change biology*, 2016.
- R. Nassar, L. Napier-Linton, K. R. Gurney, R. J. Andres, T. Oda, F. R. Vogel, and F. Deng. Improving the temporal and spatial distribution of CO₂ emissions from global fossil fuel emission data sets. *J. Geophys. Res-Atmos.*, 118(2):917–933, jan 2013. doi: 10.1029/2012JD018196.
- S. Newman, S. Jeong, M. L. Fischer, X. Xu, C. L. Haman, B. Lefer, S. Alvarez, B. Rappenglueck, E. a. Kort, a. E. Andrews, J. Peischl, K. R. Gurney, C. E. Miller, and Y. L. Yung. Diurnal tracking of anthropogenic CO₂ emissions in the Los Angeles basin megacity during spring 2010. *Atmos. Chem. Phys.*, 13:4359–4372, 2013. doi: 10.5194/acp-13-4359-2013.
- S. M. Ogle, K. Davis, T. Lauvaux, A. Schuh, D. Cooley, T. O. West, L. S. Heath, N. L. Miles, S. Richardson, F. J. Breidt, J. E. Smith, J. L. McCarty, K. R. Gurney, P. Tans, and A. S. Denning. An approach for verifying biogenic greenhouse gas emissions inventories with atmospheric CO₂ concentration data. *Environ. Res. Lett.*, 10(3):1–11, 2015. doi: 10.1088/1748-9326/10/3/034012.
- B. Oney, S. Henne, N. Gruber, M. Leuenberger, I. Bamberger, W. Eugster, and D. Brunner. The carbocount ch sites: characterization of a dense greenhouse gas observation network. *Atmos. Chem. Phys.*, 15(19):11147–11164, 2015. doi: 10.5194/acp-15-11147-2015.
- B. Oney, N. Gruber, S. Henne, M. Leuenberger, and D. Brunner. A CO₂-based method to determine the regional biospheric signal in atmospheric CO₂. *Tellus B*, 2016, in review.
- B. J. Oney. *Toward using atmospheric carbon dioxide observations to estimate the biospheric carbon flux of the Swiss Plateau*. PhD thesis, ETH ZURICH, 2016.
- E. Ott, B. R. Hunt, I. Szunyogh, A. V. Zimin, E. J. Kostelich, M. Corazza, E. Kalnay, D. Patil, and J. A. Yorke. A local ensemble kalman filter for atmospheric data assimilation. *Tellus A*, 56(5):415–428, 2004.
- S. W. Pacala, C. D. Canham, J. Saponara, J. A. Silander, R. K. Kobe, and E. Ribbens. Forest models defined by field measurements: estimation, error analysis and dynamics. *Ecological monographs*, 66(1):1–43, 1996.

- Y. Pan, R. A. Birdsey, J. Fang, R. Houghton, P. E. Kauppi, W. A. Kurz, O. L. Phillips, A. Shvidenko, S. L. Lewis, J. G. Canadell, P. Ciais, R. B. Jackson, S. W. Pacala, A. D. McGuire, S. Piao, A. Rautiainen, S. Sitch, and D. Hayes. A large and persistent carbon sink in the world's forests. *Science*, 333(6045):988–93, 2011. doi: 10.1126/science.1201609.
- P. K. Patra, M. Ishizawa, S. Maksyutov, T. Nakazawa, and G. Inoue. Role of biomass burning and climate anomalies for land-atmosphere carbon fluxes based on inverse modeling of atmospheric CO₂. *Global Biogeochemical Cycles*, 19(3), 2005.
- K. S.-H. Peh, R. T. Corlett, and Y. Bergeron. *Routledge Handbook of Forest Ecology*. Routledge, 2015.
- Z. Peng, M. Zhang, X. Kou, X. Tian, and X. Ma. A regional carbon flux data assimilation system and its preliminary evaluation in East Asia. *Atmos. Chem. Phys. Discuss.*, 14:20345–20381, 2014. doi: 10.5194/acpd-14-20345-2014.
- G. Peters, G. Marland, C. Le Quere, T. Boden, J. G. Canadell, and M. R. Raupach. Rapid growth in CO₂ emissions after the 2008-2009 global financial crisis. *Nat. Clim. Chang.*, 2:2–4, 2011. doi: 10.1038/nclimate1332.
- W. Peters, J. B. Miller, J. Whitaker, A. S. Denning, A. Hirsch, M. C. Krol, D. Zupanski, L. Bruhwiler, and P. P. Tans. An ensemble data assimilation system to estimate CO₂ surface fluxes from atmospheric trace gas observations. *J. Geophys. Res. Atmos.*, 110:1–18, 2005. doi: 10.1029/2005JD006157.
- W. Peters, A. R. Jacobson, C. Sweeney, A. E. Andrews, T. J. Conway, K. Masarie, J. B. Miller, L. M. P. Bruhwiler, G. Petron, A. I. Hirsch, D. E. J. Worthy, G. R. van der Werf, J. T. Randerson, P. O. Wennberg, M. C. Krol, and P. P. Tans. An atmospheric perspective on North American carbon dioxide exchange: CarbonTracker. *Proc. Natl. Acad. Sci. U. S. A.*, 104:18925–18930, 2007. doi: 10.1073/pnas.0708986104.
- W. Peters, M. Krol, G. Van Der Werf, S. Houweling, C. Jones, J. Hughes, K. Schaefer, K. Masarie, A. Jacobson, J. Miller, et al. Seven years of recent European net terrestrial carbon dioxide exchange constrained by atmospheric observations. *Glob. Chang. Biol.*, 16:1317–1337, 2010. doi: 10.1111/j.1365-2486.2009.02078.x.
- A. Petzold, A. Volz-Thomas, V. Thouret, J. Cammas, and C. Brenninkmeijer. Iagos-in-service aircraft for a global observing system. *3rd International Conference on Transport, Atmosphere and Climate, Germany*, pages 25–28, 2012.
- P. Peylin, D. Baker, J. Sarmiento, P. Ciais, and P. Bousquet. Influence of transport uncertainty on annual mean and seasonal inversions of atmospheric CO₂ data. *J. Geophys. Res. Atmos.*, 107, 2002. doi: 10.1029/2001JD000857.

- P. Peylin, P. Bousquet, C. Le Quere, S. Sitch, P. Friedlingstein, G. McKinley, N. Gruber, P. Rayner, and P. Ciais. Multiple constraints on regional CO₂ flux variations over land and oceans. *Global Biogeochem. Cycles*, 19(1):1–21, 2005. doi: 10.1029/2003GB002214.
- P. Peylin, S. Houweling, M. C. Krol, U. Karstens, C. Rödenbeck, C. Geels, A. Vermeulen, B. Badawy, C. Aulagnier, T. Pregger, F. Delage, G. Pieterse, P. Ciais, and M. Heimann. Importance of fossil fuel emission uncertainties over Europe for CO₂ modeling: Model intercomparison. *Atmos. Chem. Phys.*, 11:6607–6622, 2011. doi: 10.5194/acp-11-6607-2011.
- P. Peylin, R. M. Law, K. R. Gurney, F. Chevallier, A. R. Jacobson, T. Maki, Y. Niwa, P. K. Patra, W. Peters, P. J. Rayner, C. Rödenbeck, I. T. van der Laan-Luijkx, and X. Zhang. Global atmospheric carbon budget: results from an ensemble of atmospheric CO₂ inversions. *Biogeosciences*, 10(10):6699–6720, oct 2013. doi: 10.5194/bg-10-6699-2013.
- S. Piao, J. Fang, P. Ciais, P. Peylin, Y. Huang, S. Sitch, and T. Wang. The carbon balance of terrestrial ecosystems in China. *Nature*, 458(7241):1009–1013, 2009. doi: 10.1038/nature07944.
- S. Piao, P. Ciais, M. Lomas, C. Beer, H. Liu, J. Fang, P. Friedlingstein, Y. Huang, H. Muraoka, Y. Son, and I. Woodward. Contribution of climate change and rising CO₂ to terrestrial carbon balance in East Asia: A multi-model analysis. *Global and Planetary Change*, 75(34):133–142, feb 2011. doi: <http://dx.doi.org/10.1016/j.gloplachA.2010.10.014>.
- D. Pillai, C. Gerbig, R. Kretschmer, V. Beck, U. Karstens, B. Neininger, and M. Heimann. Comparing Lagrangian and Eulerian models for CO₂ transport a step towards Bayesian inverse modeling using WRF/STILT-VPRM. *Atmos. Chem. Phys. Atmos. Chem. Phys.*, 12:8979–8991, 2012. doi: 10.5194/acp-12-8979-2012.
- D. Pillai, M. Buchwitz, C. Gerbig, T. Koch, M. Reuter, H. Bovensmann, J. Marshall, and J. P. Burrows. Tracking city CO₂ emissions from space using a high resolution inverse modeling approach: A case study for Berlin, Germany. *Atmos. Chem. Phys. Discussions*, 16(15):9591–9610, 2016. doi: 10.5194/acp-16-9591-2016.
- E. Pinnington, E. Casella, S. Dance, A. Lawless, J. Morison, N. Nichols, M. Wilkinson, and T. Quaife. Investigating the role of background and observation error correlations in improving a model forecast of forest carbon balance using four dimensional variational data assimilation. In *EGU General Assembly Conference Abstracts*, volume 18, page 6189, 2016.
- A. Quillet, C. H. Peng, and M. Garneau. Toward dynamic global vegetation models for simulating vegetation-climate interactions and feedbacks: recent developments, limitations, and future challenges. *Environ. Rev.*, 18(April 2016):333–353, 2010. doi: 10.1139/a10-016.
- M. Ramonet, P. Ciais, T. Aalto, C. Aulagnier, F. Chevallier, D. Cipriano, T. J. Conway, L. Haszpra, V. Kazan, F. Meinhardt, et al. A recent build-up of atmospheric CO₂ over Europe. Part 1: observed signals and possible explanations. *Tellus B*, 62(1):1–13, 2010.

- M. R. Raupach, G. Marland, P. Ciais, C. Le Quere, J. G. Canadell, G. Klepper, and C. B. Field. Global and regional drivers of accelerating CO₂ emissions. *P. Natl. Acad. Sci. USA*, 104(24): 10288–10293, 2007. doi: 10.1073/pnas.0700609104.
- M. R. Raupach, M. Gloor, J. L. Sarmiento, J. G. Canadell, T. L. Frölicher, T. Gasser, R. A. Houghton, C. Le Quere, and C. M. Trudinger. The declining uptake rate of atmospheric CO₂ by land and ocean sinks. *Biogeosciences*, 11:3453–3475, 2014. doi: 10.5194/bg-11-3453-2014.
- D. Ray, S. Bathgate, D. Moseley, P. Taylor, B. Nicoll, S. Pizzirani, and B. Gardiner. Comparing the provision of ecosystem services in plantation forests under alternative climate change adaptation management options in wales. *Regional Environmental Change*, 15(8):1501–1513, 2015.
- J. Ray, V. Yadav, A. M. Michalak, B. van Bloemen Waanders, and S. A. McKenna. A multiresolution spatial parameterization for the estimation of fossil-fuel carbon dioxide emissions via atmospheric inversions. *Geoscientific Model Development*, 7:1277–1315, 2014. doi: 10.5194/gmdd-7-1277-2014.
- P. J. Rayner. Two decades of terrestrial carbon fluxes from a carbon cycle data assimilation system (CCDAS). *Global Biogeochem. Cycles*, 19(2), 2005. doi: 10.1029/2004GB002254.
- P. J. Rayner, M. R. Raupach, M. Paget, P. Peylin, and E. Koffi. A new global gridded data set of CO₂ emissions from fossil fuel combustion: Methodology and evaluation. *J. Geophys. Res.*, 115(D19):D19306, 2010. doi: 10.1029/2009JD013439.
- P. J. Rayner, E. Koffi, M. Scholze, T. Kaminski, and J.-L. Dufresne. Constraining predictions of the carbon cycle using data. *Philos. Trans. A. Math. Phys. Eng. Sci.*, 369(1943):1955–1966, 2011. doi: 10.1098/rsta.2010.0378.
- A. M. M. Rayner P. and F. Chevallier. Fundamentals of Data Assimilation. *Geosci. Model Dev. Discuss*, (Umr 7154):1–56, 2016. doi: 10.5194/gmd-2016-148.
- P. B. Reich, B. A. Hungate, and Y. Luo. Carbon-nitrogen interactions in terrestrial ecosystems in response to rising atmospheric carbon dioxide. *Annual Review of Ecology, Evolution, and Systematics*, pages 611–636, 2006.
- P. B. Reich, S. E. Hobbie, and T. D. Lee. Plant nitrogen limitation growth enhancement by elevated CO₂ eliminated by joint water and nitrogen limitation. *Nat. Geosci.*, 7(December): 920–924, 2014. doi: 10.1038/ngeo2284.
- M. Reichstein, E. Falge, D. Baldocchi, D. Papale, M. Aubinet, P. Berbigier, C. Bernhofer, N. Buchmann, T. Gilmanov, A. Granier, T. Grunwald, K. Havranek, H. Ilvesniemi, D. Janous, A. Knohl, T. Laurila, A. Lohila, D. Loustau, G. Matteucci, T. Meyers, F. Miglietta, J. M. Ourcival, J. Pumpanen, S. Rambal, E. Rotenberg, M. Sanz, J. Tenhunen, G. Seufert,

- F. Vaccari, T. Vesala, D. Yakir, and R. Valentini. On the separation of net ecosystem exchange into assimilation and ecosystem respiration: Review and improved algorithm. *Glob. Chang. Biol.*, 11(9):1424–1439, 2005. doi: 10.1111/j.1365-2486.2005.001002.x.
- M. Reichstein, D. Papale, R. Valentini, M. Aubinet, C. Bernhofer, A. Knohl, T. Laurila, A. Lindroth, E. Moors, K. Pilegaard, and G. Seufert. Determinants of terrestrial ecosystem carbon balance inferred from European eddy covariance flux sites. *Geophys. Res. Lett.*, 34(1), 2007. doi: 10.1029/2006GL027880.
- M. Reichstein, M. Bahn, P. Ciais, D. Frank, M. D. Mahecha, S. I. Seneviratne, J. Zscheischler, C. Beer, N. Buchmann, D. C. Frank, D. Papale, A. Rammig, P. Smith, K. Thonicke, M. van der Velde, S. Vicca, A. Walz, and M. Wattenbach. Climate extremes and the carbon cycle. *Nature*, 500(7462):287–295, 2013.
- M. Reuter, H. Bovensmann, M. Buchwitz, J. P. Burrows, B. J. Connor, N. M. Deutscher, D. W. T. Griffith, J. Heymann, G. Keppel-Aleks, J. Messerschmidt, J. Notholt, C. Petri, J. Robinson, O. Schneising, V. Sherlock, V. Velasco, T. Warneke, P. O. Wennberg, and D. Wunch. Retrieval of atmospheric CO₂ with enhanced accuracy and precision from SCIAMACHY: Validation with FTS measurements and comparison with model results. *Journal of Geophysical Research: Atmospheres*, 116(D4):1–13, 2011. doi: 10.1029/2010JD015047. D04301.
- M. Reuter, M. Buchwitz, M. Hilker, J. Heymann, O. Schneising, D. Pillai, H. Bovensmann, J. P. Burrows, H. Bösch, R. Parker, A. Butz, O. Hasekamp, C. W. O'Dell, Y. Yoshida, C. Gerbig, T. Nehrkorn, N. M. Deutscher, T. Warneke, J. Notholt, F. Hase, R. Kivi, R. Sussmann, T. Machida, H. Matsueda, and Y. Sawa. Satellite-inferred European carbon sink larger than expected. *Atmos. Chem. Phys.*, 14(24):13739–13753, 2014. doi: 10.5194/acp-14-13739-2014.
- M. Reuter, M. Buchwitz, M. Hilker, J. Heymann, H. Bovensmann, J. P. Burrows, S. Houweling, Y. Y. Liu, R. Nassar, F. Chevallier, P. Ciais, J. Marshall, and M. Reichstein. How much CO₂ is taken up by the European terrestrial biosphere? *Bull. Am. Meteorol. Soc.*, 2016, in press. doi: 10.1175/BAMS-D-15-00310.1.
- M. Rigby, A. Manning, and R. Prinn. Inversion of long-lived trace gas emissions using combined eulerian and lagrangian chemical transport models. *Atmospheric Chemistry and Physics*, 11(18):9887–9898, 2011.
- B. Ritter and J.-F. Geleyn. A comprehensive radiation scheme for numerical weather prediction models with potential applications in climate simulations. *Monthly Weather Review*, 120(2): 303–325, 1992.
- A. Roches and O. Fuhrer. Tracer module in the COSMO model. *COSMO Tech. Rep. No. 20*, (20), 2012.

- C. Rödenbeck, S. Houweling, M. Gloor, and M. Heimann. CO₂ flux history 1982-2001 inferred from atmospheric data using a global inversion of atmospheric transport. *Atmospheric Chemistry and Physics*, 3(6):1919–1964, 2003.
- C. Rödenbeck, C. Gerbig, K. Trusilova, and M. Heimann. A two-step scheme for high-resolution regional atmospheric trace gas inversions based on independent models. *Atmospheric Chemistry and Physics*, 9(14):5331–5342, 2009.
- C. D. Rodgers. Error Analysis and Characterisation. *Inverse methods Atmos. Sound. theory Pr.*, pages 43–63, 2000.
- A. Rossa, F. Domenichini, and B. Szintai. Selected cosmo-2 verification results over north-eastern italian veneto. *COSMO Newsletter*, 12:64–71, 2012.
- C. L. Sabine. The Oceanic Sink for Anthropogenic CO₂. *Science*, 305(5682):367–371, 2004. doi: 10.1126/science.1097403.
- S. R. Saleska, S. D. Miller, D. M. Matross, M. L. Goulden, S. C. Wofsy, H. R. Da Rocha, P. B. De Camargo, P. Crill, B. C. Daube, H. C. De Freitas, et al. Carbon in amazon forests: unexpected seasonal fluxes and disturbance-induced losses. *Science*, 302(5650):1554–1557, 2003.
- J. L. Sarmiento and N. Gruber. Sinks for anthropogenic carbon. *Phys. Today*, 55(8):30–36, aug 2002. doi: 10.1063/1.1510279.
- J. L. Sarmiento and G. Nicolas. *Ocean biogeochemical dynamics*. Princeton University Press, 2006.
- J. L. Sarmiento, M. Gloor, N. Gruber, C. Beaulieu, A. R. Jacobson, S. E. M. Fletcher, S. Pacala, and K. Rodgers. Trends and regional distributions of land and ocean carbon sinks. *Biogeosciences*, 7(2009):2351–2367, 2010. doi: 10.5194/bg-7-2351-2010.
- C. Sarrat, J. Noilhan, P. Lacarrere, S. Donier, C. Lac, J. Calvet, A. Dolman, C. Gerbig, B. Neininger, P. Ciais, et al. Atmospheric CO₂ modeling at the regional scale: Application to the CarboEurope Regional Experiment. *Journal of Geophysical Research: Atmospheres*, 112(D12), 2007.
- C. Sarrat, J. Noilhan, P. Lacarrere, E. Ceschia, P. Ciais, A. Dolman, J. Elbers, C. Gerbig, B. Gioli, T. Lauvaux, et al. Mesoscale modelling of the CO₂ interactions between the surface and the atmosphere applied to the April 2007 CERES field experiment. *Biogeosciences*, 6:633–646, 2009.
- E. Satar, T. A. Berhanu, D. Brunner, S. Henne, and M. Leuenberger. Continuous CO₂/CH₄/CO measurements (2012-2014) at Beromünster tall tower station in Switzerland. *Biogeosciences Discuss.*, (January):1–25, 2016. doi: 10.5194/bg-2015-593.

- D. Schimel, B. B. Stephens, and J. B. Fisher. Effect of increasing CO₂ on the terrestrial carbon cycle. *Proc. Natl. Acad. Sci.*, 112:436–441, 2015. doi: 10.1073/pnas.1407302112.
- O. Schneising, M. Buchwitz, J. P. Burrows, H. Bovensmann, P. Bergamaschi, and W. Peters. Three years of greenhouse gas column-averaged dry air mole fractions retrieved from satellite- Part 2: Methane. *Atmos. Chem. Phys.*, 8:8273–8326, 2008. doi: 10.5194/acpd-8-8273-2008.
- W. Schöner, L. Boeckli, H. Hausmann, J. C. Otto, S. Reisenhofer, C. Riedl, and S. Seren. Spatial patterns of permafrost at hoher sonnblick (Austrian Alps) - Extensive field-measurements and modelling approaches. *Austrian J. Earth Sci.*, 105(2):154–168, 2012.
- A. E. Schuh, T. Lauvaux, T. O. West, A. S. Denning, K. J. Davis, N. Miles, S. Richardson, M. Uliasz, E. Lokupitiya, D. Cooley, A. Andrews, and S. Ogle. Evaluating atmospheric CO₂ inversions at multiple scales over a highly inventoried agricultural landscape. *Glob. Chang. Biol.*, 19:1424–1439, 2013. doi: 10.1111/gcb.12141.
- E. D. Schulze, S. Luyssaert, P. Ciais, A. Freibauer, I. A. Janssens, J. F. Soussana, P. Smith, J. Grace, I. Levin, B. Thiruchittampalam, M. Heimann, A. J. Dolman, R. Valentini, P. Bousquet, P. Peylin, W. Peters, C. Rodenbeck, G. Etiope, N. Vuichard, M. Wattenbach, G. J. Nabuurs, Z. Poussi, J. Nieschulze, and J. H. Gash. Importance of methane and nitrous oxide for Europes terrestrial greenhouse-gas balance. 2(November), 2009. doi: 10.1038/ngeo741.
- C. R. Schwalm, C. A. Williams, K. Schaefer, D. Baldocchi, T. A. Black, A. H. Goldstein, B. E. Law, W. C. Oechel, K. T. Paw U, and R. L. Scott. Reduction in carbon uptake during turn of the century drought in western North America. *Nat. Geosci.*, 5(8):551–556, 2012. doi: 10.1038/ngeo1529.
- R. Seidl, M.-J. Schelhaas, W. Rammer, and P. J. Verkerk. Increasing forest disturbances in europe and their impact on carbon storage. *Nature climate change*, 4(9):806–810, 2014.
- S. I. Seneviratne, D. Lüthi, M. Litschi, and C. Schär. Land-atmosphere coupling and climate change in Europe. *Nature*, 443(7108):205–209, 2006. doi: 10.1038/nature05095.
- Y. Shiga, A. Michalak, S. M. Gourджи, K. L. Mueller, and V. Yadav. Detecting fossil fuel emissions patterns from subcontinental regions using North American insitu CO₂ measurements. *Geophys. Res. Lett.*, 41:1–8, 2014. doi: 10.1002/2014GL059684.
- D. M. Sigman and E. A. Boyle. Glacial/Interglacial Variations In Atmospheric Carbon Dioxide. *Nature*, 407(6806):859–869, 2000. doi: 10.1038/35038000.
- D. M. Sigman, M. P. Hain, and G. H. Haug. The polar ocean and glacial cycles in atmospheric CO₂ concentration. *Nature*, 466(7302):47–55, 2010. doi: 10.1038/nature09149.
- S. Sitch, P. M. Cox, W. J. Collins, and C. Huntingford. Indirect radiative forcing of climate change through ozone effects on the land-carbon sink. *Nature*, 448(August):791–794, aug 2007. doi: 10.1038/nature06059.

- S. Solomon, G.-K. Plattner, R. Knutti, and P. Friedlingstein. Irreversible climate change due to carbon dioxide emissions. *Proc. Natl. Acad. Sci. U. S. A.*, 106(6):1704–9, 2009. doi: 10.1073/pnas.0812721106.
- T. Sondergaard and P. F. J. Lermusiaux. Data Assimilation with Gaussian Mixture Models Using the Dynamically Orthogonal Field Equations. Part II: Applications. *Mon. Weather Rev.*, 141(6):1761–1785, 2013. doi: Doi10.1175/Mwr-D-11-00296.1.
- M. Steinacher, F. Joos, and T. F. Stocker. Allowable carbon emissions lowered by multiple climate targets. *Nature*, 499(7457):197–201, 2013. doi: 10.1038/nature12269.
- K. Steinkamp. *Inverse modeling of the sources and sinks of atmospheric CO₂ : joint constraints from the ocean and atmosphere*. PhD thesis, ETH Zurich, 2011.
- K. Steinkamp and N. Gruber. A joint atmosphere-ocean inversion for the estimation of seasonal carbon sources and sinks. *Glob. Biogeochem. Cycles*, 27(August):732–745, 2013. doi: 10.1002/gbc.20064.
- B. B. Stephens, K. R. Gurney, P. P. Tans, C. Sweeney, W. Peters, L. Bruhwiler, P. Ciais, M. Ramonet, P. Bousquet, T. Nakazawa, S. Aoki, T. Machida, G. Inoue, N. Vinnichenko, J. Lloyd, A. Jordan, M. Heimann, O. Shibistova, R. L. Langenfelds, L. P. Steele, R. J. Francey, and a. S. Denning. *Science*, 316(2007):1732–1735, 2007. doi: 10.1126/science.1137004.
- B. Stocker, R. Roth, and F. Joos. Multiple greenhouse-gas feedbacks from the land biosphere under future climate change scenarios. *Nat. Clim. Chang.*, 3(7):666–672, 2013a. doi: 10.1038/nclimate1864.
- T. F. Stocker, Q. Dahe, G.-K. Plattner, L. V. Alexander, S. K. Allen, N. L. Bindoff, F.-M. Breon, J. A. Church, U. Cubash, S. Emori, P. Forster, P. Friedlingstein, L. D. Talley, D. G. Vaughan, and S.-P. Xie. Technical Summary. *Clim. Chang. 2013 Phys. Sci. Basis. Contrib. Work. Gr. I to Fifth Assess. Rep. Intergov. Panel Clim. Chang.*, pages 33–115, 2013b. doi: 10.1017/CBO9781107415324.005.
- A. Tarantola. *Inverse problem theory and methods for model parameter estimation*. Society for Industrial and Applied Mathematics, 2005.
- A. J. Teuling, S. I. Seneviratne, R. Stöckli, M. Reichstein, E. Moors, P. Ciais, S. Luysaert, B. van den Hurk, C. Ammann, C. Bernhofer, et al. Contrasting response of european forest and grassland energy exchange to heatwaves. *Nature Geoscience*, 3(10):722–727, 2010.
- R. L. Thompson, P. K. Patra, F. Chevallier, S. Maksyutov, R. M. Law, T. Ziehn, I. T. van der Laan-Luijkx, W. Peters, A. Ganshin, R. Zhuravlev, T. Maki, T. Nakamura, T. Shirai, M. Ishizawa, T. Saeki, T. Machida, B. Poulter, J. G. Canadell, and P. Ciais. Topdown assessment of the Asian carbon budget since the mid 1990s. *Nat. Commun.*, 7:10724, 2016. doi: 10.1038/ncomms10724.

- K. Thonicke, A. Spessa, I. C. Prentice, S. P. Harrison, L. Dong, and C. Carmona-Moreno. The influence of vegetation, fire spread and fire behaviour on biomass burning and trace gas emissions: Results from a process-based model. *Biogeosciences*, 7(6):1991–2011, 2010. doi: 10.5194/bg-7-1991-2010.
- P. E. Thornton and N. E. Zimmermann. An improved canopy integration scheme for a Land Surface Model with prognostic canopy structure. *J. Clim.*, 20(15):3902–3923, 2007. doi: 10.1175/JCLI4222.1.
- H. Tian, C. Lu, P. Ciais, A. M. Michalak, J. G. Canadell, E. Saikawa, D. N. Huntzinger, K. R. Gurney, S. Sitch, B. Zhang, J. Yang, P. Bousquet, L. Bruhwiler, G. Chen, E. Dlugokencky, P. Friedlingstein, J. Melillo, S. Pan, B. Poulter, R. Prinn, M. Saunio, C. R. Schwalm, and S. C. Wofsy. The terrestrial biosphere as a net source of greenhouse gases to the atmosphere. *Nature*, 531(7593):225–228, 2016. doi: 10.1038/nature16946.
- L. Tolk, A. Meesters, A. Dolman, and W. Peters. Modelling representation errors of atmospheric CO₂ mixing ratios at a regional scale. *Atmospheric chemistry and physics*, 8(22):6587–6596, 2008.
- L. F. Tolk. The carbon balance from an atmospheric perspective: inverse modeling of regional biospheric CO₂ fluxes. 2013.
- L. F. Tolk, W. Peters, A. G. C. A. Meesters, M. Groenendijk, A. T. Vermeulen, G. J. Steeneveld, and A. J. Dolman. Modelling regional scale surface fluxes, meteorology and CO₂ mixing ratios for the Cabauw tower in the Netherlands. *Biogeosciences*, 6(June):2265–2280, 2009. doi: 10.5194/bg-6-2265-2009.
- L. F. Tolk, A. J. Dolman, A. G. C. a. Meesters, and W. Peters. A comparison of different inverse carbon flux estimation approaches for application on a regional domain. *Atmos. Chem. Phys.*, 11:10349–10365, 2011. doi: 10.5194/acp-11-10349-2011.
- A. Tsuruta, T. Aalto, L. Backman, J. Hakkarainen, I. T. Laan-Luijkx, M. C. Krol, R. Spahni, S. Houweling, M. Laine, E. Dlugokencky, et al. Global methane emission estimates for 2000–2012 from CarbonTracker Europe-CH₄ v1.0. *Geoscientific Model Development*, 10(3):1261–1289, 2017.
- J. C. Turnbull, J. B. Miller, S. J. Lehman, P. P. Tans, R. J. Sparks, and J. Southon. Comparison of ¹⁴CO₂, CO, and SF₆ as tracers for recently added fossil fuel CO₂ in the atmosphere and implications for biological CO₂ exchange. *Geophys. Res. Lett.*, 33:2–6, 2006. doi: 10.1029/2005GL024213.
- J. C. Turnbull, P. P. Tans, S. J. Lehman, D. Baker, T. J. Conway, Y. S. Chung, J. Gregg, J. B. Miller, J. R. Southon, and L. X. Zhou. Atmospheric observations of carbon monoxide and fossil fuel CO₂ emissions from East Asia. *J. Geophys. Res.-Atmos.*, 116:1–14, 2011. doi: 10.1029/2011JD016691.

- J. C. Turnbull, C. Sweeney, A. Karion, T. Newberger, S. J. Lehman, P. P. Tans, K. J. Davis, T. Lauvaux, N. L. Miles, S. J. Richardson, et al. Toward quantification and source sector identification of fossil fuel CO₂ emissions from an urban area: Results from the INFLUX experiment. *J. Geophys. Res-Atmos.*, 120(1):292312, 2015. doi: 10.1002/2014JD022555.
- J. C. Turnbull, E. D. Keller, M. W. Norris, and R. M. Wiltshire. Independent evaluation of point source fossil fuel CO₂ emissions to better than 10%. *P. Natl. Acad. Sci. USA*, 113(37): 1028710291, 2016. doi: 10.1073/pnas.1602824113.
- A. J. Turner and D. J. Jacob. Balancing aggregation and smoothing errors in inverse models. *Atmos. Chem. Phys.*, 15:7039–7048, 2015. doi: 10.5194/acp-15-7039-2015.
- D. P. Turner, M. Göckede, B. E. Law, W. D. Ritts, W. B. Cohen, Z. Yang, T. Hudiburg, R. Kennedy, and M. Duane. Multiple constraint analysis of regional land-surface carbon flux. *Tellus, Ser. B Chem. Phys. Meteorol.*, 63:207–221, 2011. doi: 10.1111/j.1600-0889.2011.00525.x.
- S. van der Laan, U. Karstens, R. E. M. Neubert, I. T. van der Laan-Luijkx, and H. Meijer. Observation-based estimates of fossil fuel-derived CO₂ emissions in the Netherlands using $\Delta^{14}\text{C}$, CO and ²²²Radon. *Tellus B*, 62(5):389–402, nov 2010. doi: 10.1111/j.1600-0889.2010.00493.x.
- I. R. van der Laan-Luijkx, M. C. Krol, L. V. Gatti, L. G. Domingues, C. S. C. Correia, J. B. Miller, M. Gloor, T. T. Leeuwen, J. W. Kaiser, C. Wiedinmyer, S. Basu, C. Clerbaux, and W. Peters. Global Biogeochemical Cycles drought derived with CarbonTracker South America. pages 1092–1108, 2015. doi: 10.1002/2014GB005082.Received.
- I. T. van der Laan-Luijkx, I. R. van der Velde, E. van der Veen, A. Tsuruta, K. Stanislawski, A. Babenhauserheide, H. F. Zhang, Y. Liu, W. He, H. Chen, et al. The CarbonTracker Data Assimilation Shell (CTDAS) v1.0: implementation and global carbon balance 2001–2015. *Geosci. Model Dev. Discuss.*, pages 1–30, 2017. doi: 10.5194/gmd-2017-45.
- I. van der Velde. *Studying biosphere-atmosphere exchange of CO₂ through Carbon-13 stable isotopes*. Wageningen University, 2015.
- S. Vardag, C. Gerbig, G. Janssens-Maenhout, and I. Levin. Estimation of continuous anthropogenic CO₂: Model-based evaluation of CO₂, CO, $\delta^{13}\text{C}(\text{CO}_2)$ and $\Delta^{14}\text{C}(\text{CO}_2)$ tracer methods. *Atmos. Chem. Phys.*, 15(22):12705–12729, 2015. doi: 10.5194/acp-15-12705-2015.
- V. A. Velasco, M. Buchwitz, H. Bovensmann, M. Reuter, O. Schneising, J. Heymann, T. Krings, K. Gerilowski, and J. P. Burrows. Towards space based verification of CO₂ emissions from strong localized sources: Fossil fuel power plant emissions as seen by a CarbonSat constellation. *Atmos. Meas. Tech.*, 4:2809–2822, 2011. doi: 10.5194/amt-4-2809-2011.

- F. R. Vogel, B. Thiruchittampalam, J. Theloke, R. Kretschmer, C. Gerbig, S. Hammer, and I. Levin. Can we evaluate a fine-grained emission model using high-resolution atmospheric transport modelling and regional fossil fuel CO₂ observations? *Tellus B*, 65:1–16, 2013. doi: 10.3402/tellusb.v65i0.18681.
- K. J. Wecht, D. J. Jacob, C. Frankenberg, Z. Jiang, and D. R. Blake. Mapping of north american methane emissions with high spatial resolution by inversion of sciamachy satellite data. *Journal of Geophysical Research: Atmospheres*, 119(12):7741–7756, 2014.
- L. R. Welp, R. F. Keeling, H. A. J. Meijer, A. F. Bollenbacher, S. C. Piper, K. Yoshimura, R. J. Francey, C. E. Allison, and M. Wahlen. Interannual variability in the oxygen isotopes of atmospheric CO₂ driven by El Nino. *Nature*, 477(7366):579–582, sep 2011. doi: 10.1038/nature10421.
- P. Weston, W. Bell, and J. Eyre. Accounting for correlated error in the assimilation of high-resolution sounder data. *Quarterly Journal of the Royal Meteorological Society*, 140(685): 2420–2429, 2014.
- J. S. Whitaker and T. M. Hamill. Ensemble data assimilation without perturbed observations. *Monthly Weather Review*, 130(7):1913–1924, 2002.
- L. J. Wicker and W. C. Skamarock. Time-Splitting Methods for Elastic Models Using Forward Time Schemes. *Mon. Weather Rev.*, 130(8):2088–2097, 2002.
- S. Wofsy and R. Harris. The North American Carbon Program (NACP): Report of the NACP Committee of the US Interagency Carbon Cycle Science Program, US Global Change Res. Program, Washington, DC, 2002.
- S. C. Wofsy. Hiaper pole-to-pole observations (hippo): fine-grained, global-scale measurements of climatically important atmospheric gases and aerosols. *Philosophical Transactions of the Royal Society of London A: Mathematical, Physical and Engineering Sciences*, 369(1943): 2073–2086, 2011.
- L. Wu, M. Bocquet, T. Lauvaux, F. Chevallier, P. Rayner, and K. Davis. Optimal representation of source-sink fluxes for mesoscale carbon dioxide inversion with synthetic data. *J. Geophys. Res. Atmos.*, 116:1–16, 2011. doi: 10.1029/2011JD016198.
- D. Wunch, G. C. Toon, P. O. Wennberg, S. C. Wofsy, B. B. Stephens, M. L. Fischer, O. Uchino, J. B. Abshire, P. Bernath, S. C. Biraud, et al. *Atmospheric Measurement Techniques*, 3(5): 1351–1362, 2010.
- D. Wunch, P. O. Wennberg, G. C. Toon, B. J. Connor, B. Fisher, G. B. Osterman, C. Frankenberg, L. Mandrake, C. ODell, P. Ahonen, S. C. Biraud, R. Castano, N. Cressie, D. Crisp, N. M. Deutscher, A. Eldering, M. L. Fisher, D. W. T. Griffith, M. Gunson, P. Heikkinen, G. Keppel-Aleks, E. Kyrö, R. Lindenmaier, R. Macatangay, J. Mendonca, J. Messerschmidt, C. E. Miller,

- I. Morino, J. Notholt, F. A. Oyafuso, M. Rettinger, J. Robinson, C. M. Roehl, R. J. Salawitch, V. Sherlock, K. Strong, R. Sussmann, T. Tanaka, D. R. Thompson, O. Uchino, T. Warneke, and S. C. Wofsy. A method for evaluating bias in global measurements of CO₂ total columns from space. *Atmos. Chem. Phys.*, 11:12317–12337, 2011. doi: 10.5194/acp-11-12317-2011.
- F. S. Yang, T. Miyoshi, H. Li, J. Liu, C. Danforth, J.-s. Kang, S. Penny, and S. Greybush. Recent Advances in EnKF. Technical Report September, 2011.
- S. Zaehle. Terrestrial nitrogen-carbon cycle interactions at the global scale. *Philos. Trans. R. Soc. B-Biological Sci.*, 368(ii):1–9, jul 2013. doi: 10.1098/rstb.2013.0125.
- D. Zardi and C. D. Whiteman. Diurnal mountain wind systems. In *Mountain Weather Research and Forecasting*, pages 35–119. Springer, 2013.
- C. Zellweger, L. Emmenegger, M. Firdaus, J. Hatakka, M. Heimann, E. Kozlova, T. G. Spain, M. Steinbacher, M. V. van der Schoot, and B. Buchmann. Assessment of recent advances in measurement techniques for atmospheric carbon dioxide and methane observations. *Atmos. Meas. Tech. Discussions*, 9(9):4737–4757, 2016. doi: 10.5194/amt-9-4737-2016.
- S. Zhang, X. Zheng, Z. Chen, B. Dan, J. M. Chen, X. Yi, L. Wang, and G. Wu. A Global Carbon Assimilation System using a modified EnKF assimilation method. *Geosci. Model Dev. Discuss.*, 7:6519–6547, 2014. doi: 10.5194/gmdd-7-6519-2014.
- X. Zhang, K. R. Gurney, P. Rayner, D. Baker, and Y.-P. Liu. Sensitivity of simulated CO₂ concentration to sub-annual variations in fossil fuel CO₂ emissions. *Atmos. Chem. Phys. Discuss.*, 15:20679–20708, 2016. doi: 10.5194/acpd-15-20679-2015.
- D. Zupanski, A. S. Denning, M. Uliasz, M. Zupanski, A. E. Schuh, P. J. Rayner, W. Peters, and K. D. Corbin. Carbon flux bias estimation employing Maximum Likelihood Ensemble Filter (MLEF). *J. Geophys. Res. Atmos.*, 112:1–18, 2007. doi: 10.1029/2006JD008371.
- M. Zupanski, S. J. Fletcher, I. M. Navon, B. Uzunoglu, R. P. Heikes, D. A. Randall, T. D. Ringler, and D. Daescu. Initiation of ensemble data assimilation. *Tellus, Ser. A Dyn. Meteorol. Oceanogr.*, 58(2):159–170, 2006. doi: 10.1111/j.1600-0870.2006.00173.x.

